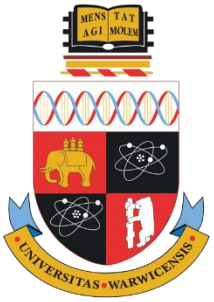

Development of an All-Diamond Conductivity Sensor for Aquatic Environments

by

Lee Simcox

Thesis submitted to the University of Warwick for the degree of Doctor of Philosophy

---

Supervisor: Prof. Julie Macpherson

Molecular Analytical Science Centre for Doctoral Training

December 2019

MAS CDT
Molecular Analytical Science Centre for Doctoral Training

WARWICK
THE UNIVERSITY OF WARWICK

“But man is not made for defeat,” he said. “A man can be destroyed but not defeated.”

— Ernest Hemingway, *The Old Man and the Sea*

Contents

List of Figures

List of Tables

Abbreviations

3D	three dimensional
ABS	acrylonitrile butadiene styrene
AC	alternating current
ADC	analogue-to-digital converter
AFM	atomic force microscopy
AI	analogue input
BDD	boron doped diamond
CFU	colony forming units
CLSM	confocal laser scanning microscopy
CV	crystal violet
CVD	chemical vapour deposition
CVM	cyclic voltammetry
DAQ	data acquisition
DC	direct current
EPS	extracellular polymeric substance
FE	field emission
FEM	finite element method
FIFO	first in first out
H-BDD	hydrogen terminated boron doped diamond
LB	Luria-Bertani
NDC	non-diamond carbon
NTC	negative temperature coefficient
O-BDD	oxygen terminated boron doped diamond

RAM	random access memory
RMS	root mean square
RTD	resistance temperature detector
PC	personal computer
PSD	power spectral density
PVC	polyvinyl chloride
SD	standard deviation
SE	secondary electron
SEM	scanning electron microscopy
SPC	screen printed carbon
TDMS	technical data management streaming
VI	virtual instrument

List of Symbols

Symbol	Meaning
α	temperature coefficient of conductivity
δ	skin depth
ε_r	relative permittivity of solution
ε_0	absolute permittivity of free space
η	viscosity
θ	measured temperature
K	cell constant
κ	solution conductivity
κ_{meas}	measured solution conductivity
κ_{25}	solution conductivity corrected to 25 °C
$\overline{\kappa}$	time average solution conductivity
κ'	fluctuations in solution conductivity
λ_i	ion mobility
μ	permeability
ρ	fluid density
ρ	resistivity
τ	lag (time interval)
χ	temperature dissipation rate
ω	angular frequency
A	area of electrode
A_{595}	absorbance of solubilised stain at 595 nm
a	cross-sectional area

C	capacitance
C_{cell}	cell capacitance
C_{ext}	capacitance of external factors
C_{p}	parasitic capacitance
C_{dl}	double layer capacitance
c_i	concentration of ions
$\mathbf{D}$	electric displacement field vector
D	thermal diffusivity
d	thickness
d_{p}	pipe diameter
$\mathbf{E}$	electric field vector
E	electric field strength
E	spectral distribution function
F	Faraday’s constant
f	frequency
f_{25}	temperature correction factor
G	conductance
I	current
$\mathbf{J}$	current density vector
j	current density
j	marker fluid injection position
$\boldsymbol{k}$	wavenumber
k	frequency
k'	roll-off frequency

l	electrode length
$\mathbf{n}$	normal vector
OD_{600}	optical density at 600 nm
P	wetted perimeter
Re	Reynolds number
R	resistance
R_{el}	polarisation resistance
R_{sol}	solution resistance
R_a	arithmetical mean surface roughness
R_T	autocorrelation function
r	radius of bubble
r_i	ion radius
s	electrode separation
t	time
u	flow velocity
V	voltage
v	marker fluid injection flow rate
W	electrode width
w	width
x	centre position of bubble in x direction
Z	impedance
Z_{cell}	cell impedance
Z_{ext}	impedance of external factors
Z_{dl}	double layer impedance

Z_{meas}	measured impedance
Z_p	parasitic impedance
z	centre position of bubble in z direction
z_i	ion charge

Acknowledgements

First and foremost, I would like to thank my supervisor Julie Macpherson for giving me the opportunity to undertake a PhD and form part of the Warwick Electrochemistry and Interfaces Group. I would also like to thank Pat Unwin, and my industrial supervisors from DSTL: Tom Fleming and Owen Griffiths; as well as Elizabeth Wellington for the collaboration in Life Sciences. I could not have completed this PhD alone, and I have been fortunate enough to have had the opportunity to work with some amazing people throughout my studies, for which I am extremely grateful.

I would like to thank Maxim Joseph, who was working on this project before I started. His mentorship, help and knowledge, to say nothing of his patience, friendliness and good nature, made the start of my PhD so much easier. Max's support and guidance laid the foundations for my success, and for this he has all my gratitude. I would also like to thank Rui Abreu Pereira, whose mentorship and friendship made it so enjoyable to work in Life Sciences, and who I credit with making me a much stronger scientist and person overall.

I am indebted to both Rod Wesson and Ian Baylis, for their vast expertise which has aided me considerably during my work. Rod's continuous assistance and genius—but above all, his friendliness, kindness, and willingness to help—has been an asset throughout my entire PhD, and I cannot thank him enough. Ian's support, not to mention his good humour, made it a pleasure to work in Engineering, and made the closing period of my PhD far less stressful than it could have been. I also acknowledge the skills and expertise of Alex Colburn, Lee Butcher, and Marcus Grant.

I want to express my thanks to Rob Johnson and Shrina Bhagat, for helping me through some of the most difficult times of my life. Of course, thanks go to Haytham Hussein, Faduma Maddar, and Nicole Reily for the coffee breaks.

I want to thank all the members of WEIG, in particular Harriet Pearce, Ashley Page, Roy Meyler, Georgia Wood, Emily Braxton, Zoë Ayres, Slava Shkirskiy, Bryn Jones, Lingcong Meng, and Anthony Lucio. In addition, I want to thank Victoria Clark, and everyone in the first year of MAS CDT, as well as Naomi Grew, Nikola Chmel, Anne Maynard, and Hugo van den Burg.

Declaration

This thesis is submitted to the University of Warwick in support of my application for the degree of Doctor of Philosophy. It has been composed by myself and has not been submitted in any previous application for any degree.

The work presented (including data generated and data analysis) was carried out by the author except in the cases outlined below:

The design and production of the instruments used in Chapters 3 and 5 to operate the conductivity sensor (AC conductance meter and differential voltmeter) was by Alex Colburn (Chemistry, Warwick).

The design and fabrication of the experimental setups in Chapter 5 was by Ian Baylis (Engineering, Warwick). The data generated in Figures 5.16–5.17 and some of the data analysis in Section 5.4.2 was carried out with the help of Tom Fleming (Defence Science and Technology Laboratory, Salisbury).

In Chapter 6, the design and fabrication of the 3D printed biofilm activity sensor was by Craig Stracey (Process Instruments, Burnley). The experimental design and data generated in Figures 6.2–6.3 was carried out by Kathryn Burrill (Process Instruments, Burnley).

Parts of this thesis have been published by the author:

Chapter 4 was published as:

"Boron Doped Diamond as a Low Biofouling Material for Aquatic Environments: Assessment of *Pseudomonas aeruginosa* Biofilm Formation"

L. J. Simcox, R. P. A. Pereira, E. M. H. Wellington, J. V. Macpherson, *ACS Appl. Mater. Inter.*, **2019**, 11, 28, 25024-25033.

Abstract

Solution conductivity sensors are widely used in industrial and research settings to make measurements across the wide range of conductivities found in aqueous solutions. However, in many natural aquatic environments, direct contact with solution means that exposed sensor electrodes are susceptible to surface fouling, mechanical wear, or corrosion. This thesis explores the development of a synthetic all-diamond conductivity sensor, comprised of conducting diamond electrodes encapsulated in an insulating diamond substrate. Due to the extreme chemical robustness of diamond it opens up application in more challenging corrosive, abrasive, and natural aquatic environments. The capability of the sensor as a working device allowing accurate measurements of solution conductivity with simultaneous temperature measurement is demonstrated herein through validation in a laboratory environment. In addition, progression from laboratory to simulated environments occurs by the assessment of the performance of the all-diamond conductivity sensor in both an environmental natural river water system as well as a pilot test rig suitable for industrial application.

For long-term measurement in such natural aquatic applications, biofouling is a major issue faced by sensors as it often causes deterioration in stability and performance. Therefore, the biofouling properties of conducting diamond in relation to microbial biofilm formation were investigated, and found to be a low biofouling material when compared to other common electrode and packaging materials. Clearly, this has favourable implication when utilising this material as a sensing electrode in real-world aquatic environments.

In summary, this thesis explores not only the development and application of a synthetic all-diamond conductivity sensor, but also provides a greater understanding of conducting diamond electrodes for real-world sensor applications. Moreover, the work discussed herein demonstrates the capacity for long term *in situ* placement of an all-diamond conductivity sensor for monitoring in a range of aquatic environments.

1 Introduction

1.1 Theory of conductivity

1.1.1 Solution conductivity

Conductivity is the ability of a material to carry an electric current. Electronic conductors or semiconductors will predominantly conduct current using electrons or positive holes as charge carriers. In contrast, in aqueous electrolyte solutions, this current is conducted by the transport of ions; therefore, this is referred to as solution conductivity or electrolytic conductivity.[1]

A solution conductivity measurement returns information on the ionic constituents of a solution, as it is a property of the chemical nature and composition of the electrolyte.[2] Note that the ionic constituents of a solution refers to the ion-forming portion of an electrolyte, regardless of the extent of dissociation, association with other complexes, or solvation. Electrolytes are categorised as strong or weak, where strong electrolytes will fully dissociate in aqueous solution, such as HCl and KNO_3, whilst weak electrolytes such as ethanoic acid dissociate according to their equilibrium dissociation constant. In this thesis, we will consider only strong electrolytes, since the quantitative relationships used in the study of weak electrolytes are not applicable herein.[3]

The conductivity, κ, of a solution can therefore be explained as the conductance (reciprocal of resistance, R) through a unit cube of electrolyte solution, as illustrated in **Figure 1.1**.[4] Since the conductance depends on the number of charge carriers, it becomes apparent that the conductivity of an electrolyte solution is a function of the concentration, c_i, of all the ions present.[5]

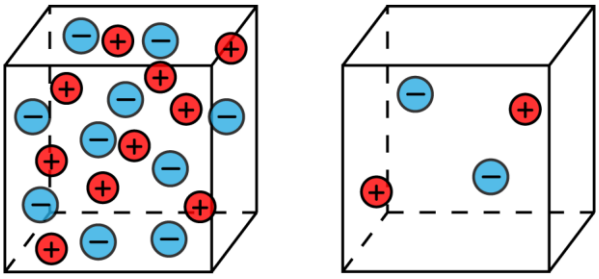

Figure 1.1. Schematic explanation of the variation of conductivity with electrolyte concentration.

In addition, the conductivity varies with the relative mobility, λ_i, of the ions present in solution, leading to Equation (1.1):

$$\kappa = \sum_i c_i \lambda_i \tag{1.1}$$

The mobility of an ion is generally governed by its size, its charge, and the viscosity of the solvent that it is dissolved in:

$$\lambda_i = \frac{z_i e}{6\pi\eta r_i} \tag{1.2}$$

where z_i is the charge on the ion, e is the charge on an electron, η is the solvent viscosity, and r_i is the radius of the ion.[2] However, due to ion-ion interactions the ion mobility is not constant, and it is also a function of concentration and temperature.[4]

In aqueous solution, the lowest measurable conductivity is defined by the dissociation of water (~5×10^{-2} µS cm^{-1} at 25°C).[6] The addition of dissolved ions increases the conductivity of aqueous solutions, until a conductivity maximum is achieved using concentrated acids, *e.g.* 30% H_2SO_4 (~8×10^{5} µS cm^{-1} at 25°C).[7]

1.1.2 Principles of conductivity measurement

Consider two electrodes, each of area *A* and separated by a distance *s*, placed into an electrolytic solution, as demonstrated in **Figure 1.2**. If a voltage is applied between the electrodes, then a current will flow. In the volume of solution between the electrodes, an electric field is generated, and the ions present will drift through the bulk medium at a given velocity. Anions will move towards the positive electrode, whilst cations will move towards the negative electrode.

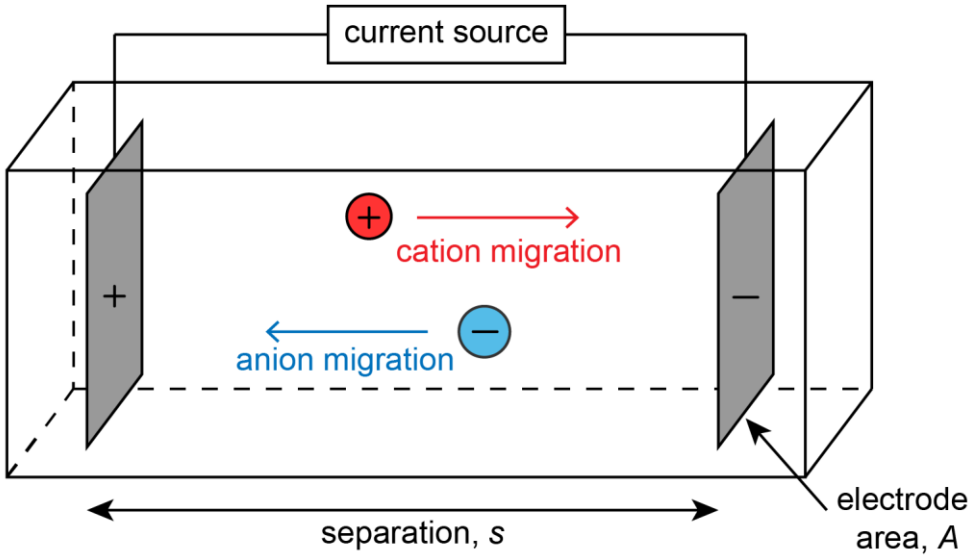

Figure 1.2. The movement of ions in solution between electrodes.

This permits the measurement of solution resistance, R_{sol}, with either direct or alternating current, *I*, driven by a voltage, *V*, through Equation (1.3), Ohm's law.

$$V = IR_{sol} \tag{1.3}$$

The bulk electrolyte conductivity obeys the following relationship:

$$\kappa = \frac{s}{R_{sol}A} \tag{1.4}$$

The term $1/R_{sol}$ is also known as conductance, G, since it is the reciprocal of R; similarly, the conductivity is the reciprocal of resistivity, ρ. The ratio s/A is a characteristic of the conductance cell used to make the conductance measurement, and is known as the cell constant, K:

$$K = \frac{s}{A} \tag{1.5}$$

These relationships mean that Equation (1.4) can be altered into Equation (1.6):

$$\kappa = \frac{1}{R_{sol}} \times K \tag{1.6}$$

The cell constant can be readily obtained experimentally by calibrating the conductance cell using standard solutions of known conductivity. Thus, K is the effective length and cross sectional area of the conducting path, rather than the geometric value.[1] Typical K values range from 0.01 to 10 cm^{-1}, with low K sensors being used to measure low conductivity solutions, and *vice versa*.[7]

Ions in an electrolyte undergo random motion due to their thermal energy, but in the presence of an applied voltage they are subjected to an additional force which accelerates them towards a particular electrode. Under an applied electric field or potential gradient, E, the ion migrates at a drift velocity v_i which is proportional to E:

$$v_i = \lambda_i E \tag{1.7}$$

Therefore, the flux of i ions under an applied potential gradient is $c_i v_i$ and consequently the total charge carried by all ions across a unit plane perpendicular to the flow direction, per second, is the current density, j:

$$j = F \sum_i z_i c_i v_i \tag{1.8}$$

where z_i is the charge of the ion and F is Faraday's constant.[3,4] Thus, by maintaining a constant E whilst measuring j, or conversely, by maintaining constant j whilst measuring the resultant E, then a measurement of R_{sol} and κ can be obtained (Equations (1.3)–(1.4)).

When a direct current (DC) is applied to the electrodes of the conductivity measuring cell, migration of the ions in solution will over time lead to the accumulation of ions at the electrode surface (**Figure 1.3a**), which can subsequently lead to chemical reactions taking place. These electrolysis reactions will alter the composition of the solution, and therefore also the conductivity. In order to avoid this, an alternating current (AC) is applied instead of DC. With AC, there is no net migration of ions in one direction; individual ions oscillate about their positions with the applied frequency (**Figure 1.3b**).[1,4]

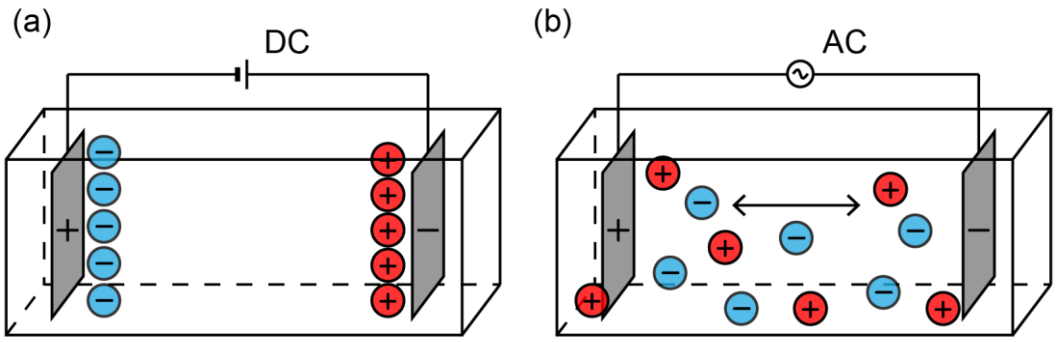

Figure 1.3. Migration of ions in solution when (a) DC and (b) AC is applied to the measuring cell.

Consequently, AC instead of DC is used in solution conductivity determination. Note that the frequency employed is generally on the order of 1 kHz, so that the polarity of the electrodes changes 2000 times per second.[2] This period of time is too short for electrons to be transferred in or out of solution phase species to or from the electrode,[2] though some electron transfer must happen at the solution/electrode

interface in order to maintain a complete electrical circuit.[4] The chief role of the rapidly fluctuating voltage is to sequentially attract and repel ions from the electrodes (**Figure 1.3b**); this movement constitutes an AC in the solution.[2]

1.1.3 Conductivity sensors

There are three types of conductivity sensors that are used to constitute a conductance measuring cell: 2-point, 4-point, and inductive.

1.1.3.1 2-point sensors

In a traditional 2-point conductivity sensor, the AC is applied between two electrodes and the resulting voltage is measured (**Figure 1.4**). The aim is to measure R_{sol} only, using Equation (1.3). This method of measuring conductivity has been used since the early 20th Century.[8,9] Indeed, Kohlrausch pioneered this field from the 1870s by demonstrating that an electrolyte solution has a definite and constant electrical resistance.[1]

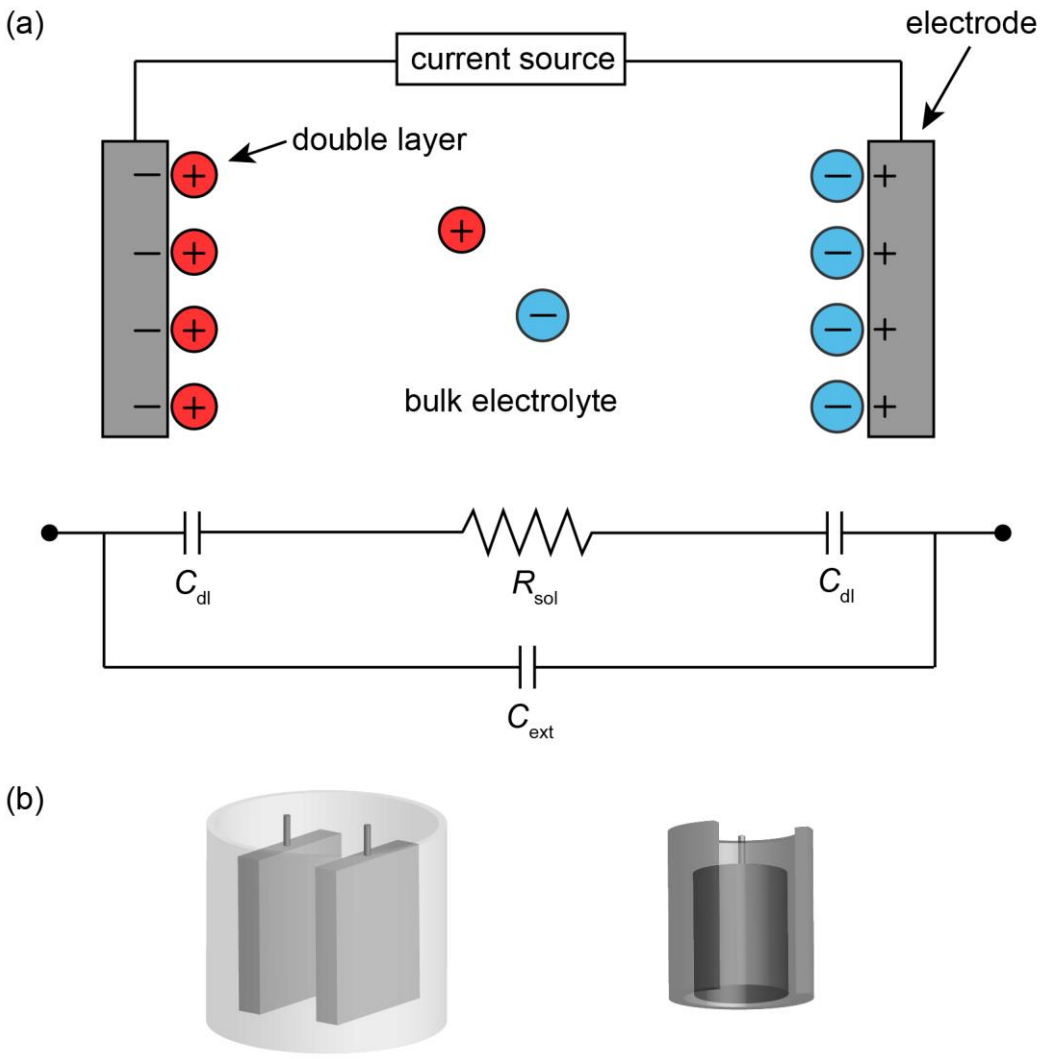

Figure 1.4. (a) Schematic of a 2-point conductivity sensor and its electrical equivalent circuit. (b) Possible electrode arrangements of 2-point conductivity sensors.

Typically, the two electrodes are positioned parallel to each other, and are surrounded by an outer insulating tube which protects them from mechanical damage and keeps the measurement cell contained.[10] Alternatively, one electrode can be constructed as a pin which is encircled by the second electrode. Both of these sensors are usually manufactured from robust materials like metals (*e.g.* stainless steel or titanium) so that they are less susceptible to mechanical damage.

A sinusoidal AC at any one frequency is employed with a Wheatstone bridge circuit to provide an absolute impedance and a phase shift.[1,11] The evaluation of solution

conductivity is then determined through calibration using the cell constant. However, balancing the Wheatstone bridge generally contains not only R_{sol} but also capacitance effects in the system. The accumulation and dissipation of ions at the electrode surface constitutes a capacitance known as the double layer, C_{dl}. This capacitance is in series with R_{sol}.[1,12] Cell capacitance occurs as a result of the medium between the two electrodes; the corresponding impedance is in parallel with R_{sol}. Similarly, parasitic effects arising from stray capacitance in leads, connections, *etc.* create a parallel impedance, which can be minimised with appropriate cell design.[13] Both of these capacitances are termed C_{ext} in **Figure 1.4a**.

1.1.3.2 4-point sensors

4-point conductivity sensors utilise four electrodes to create a measuring cell (**Figure 1.5**).[14] A pair of outer electrodes pass an applied AC through the solution (often termed current injection electrodes), in the same manner as the 2-point sensor. The potential difference between two points in solution is measured by a pair of inner probe (potential sensing) electrodes. The inner potential sensing electrodes must be placed within the electric field of the current injection electrodes, and the voltage is measured using a high impedance voltmeter.

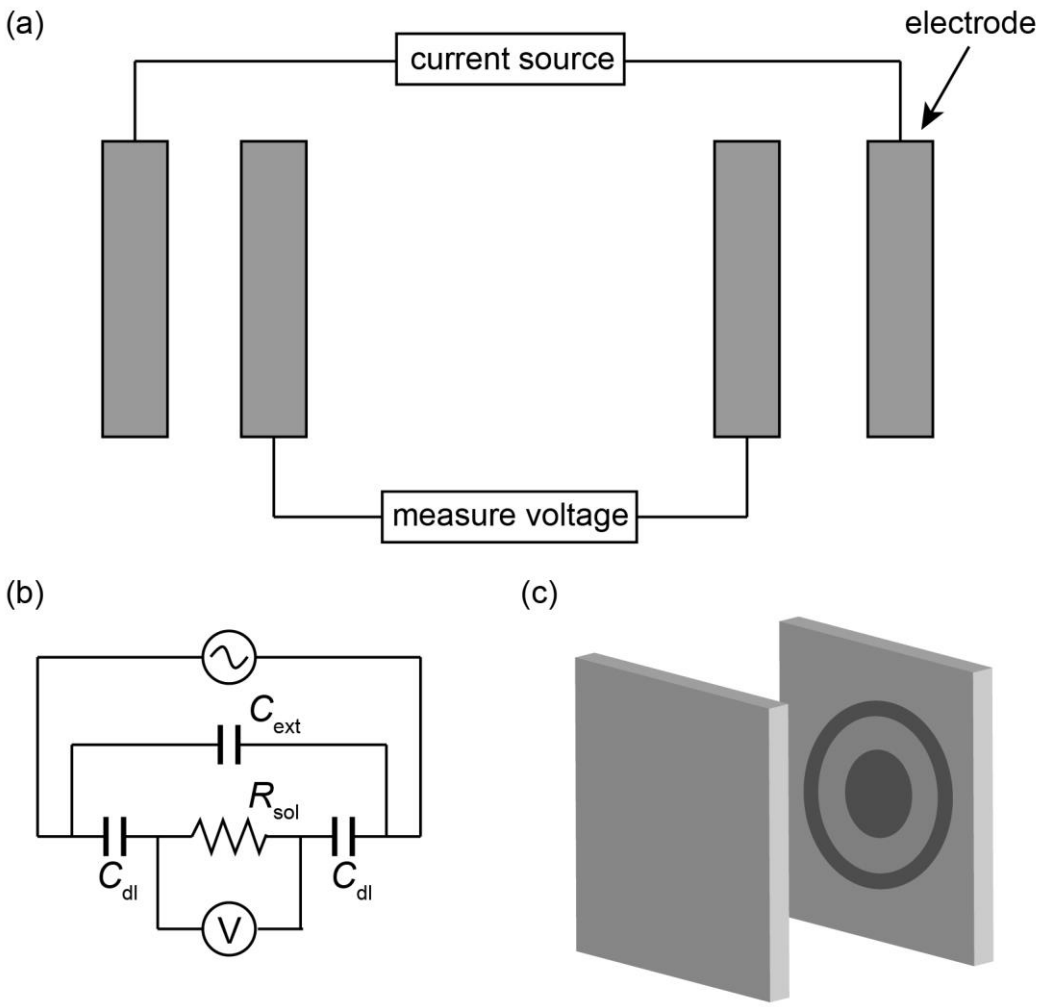

Figure 1.5. (a) Schematic of a 4-point conductivity sensor and (b) its electrical equivalent circuit. (c) Typical electrode arrangement of a 4-point conductivity sensor.

The 4-point conductivity cell was originally explored in the 1940s and developed further in the 1960s.[15–17] Different arrangements of the four electrodes are possible including bands and squares, but typically concentric circles are used where the potential sensing electrode is within the current injection electrode, with the electrode pairs facing each other (**Figure 1.5b**).[10] Generally, electrodes of any material or dimension can be employed unless they are attacked by the sample solution.[14]

One of the main advantages of the 4-point sensor over the 2-point sensor is that it is capable of measuring higher conductivity solutions, can aid in eliminating electrode polarisation contributions, and can be used when coating or fouling of electrodes is a concern.[10] This is because C_{dl} is not in the equivalent circuit of the R_{sol} measurement, hence the measurement is not limited by Z_{dl} (see **Sections 1.1.4.1** and **1.1.4.2**). However, because of geometrical considerations 4-point sensors are less capable of being miniaturised, making them unsuitable for handling small sample volumes (*e.g.* biological samples).

1.1.3.3 Inductive sensors

Both 2-point and 4-point conductivity sensors are known as direct contact sensors, since they employ electrodes that are in contact with the electrolyte solution.[7] An alternative technique is the inductive conductivity sensor, also referred to as toroidal or electrodeless conductivity sensors.[7,10] This measuring system utilises a probe consisting of two toroids in close proximity to each other (**Figure 1.6**).[18] Note that the toroids will generally be encased together in a polymeric material.

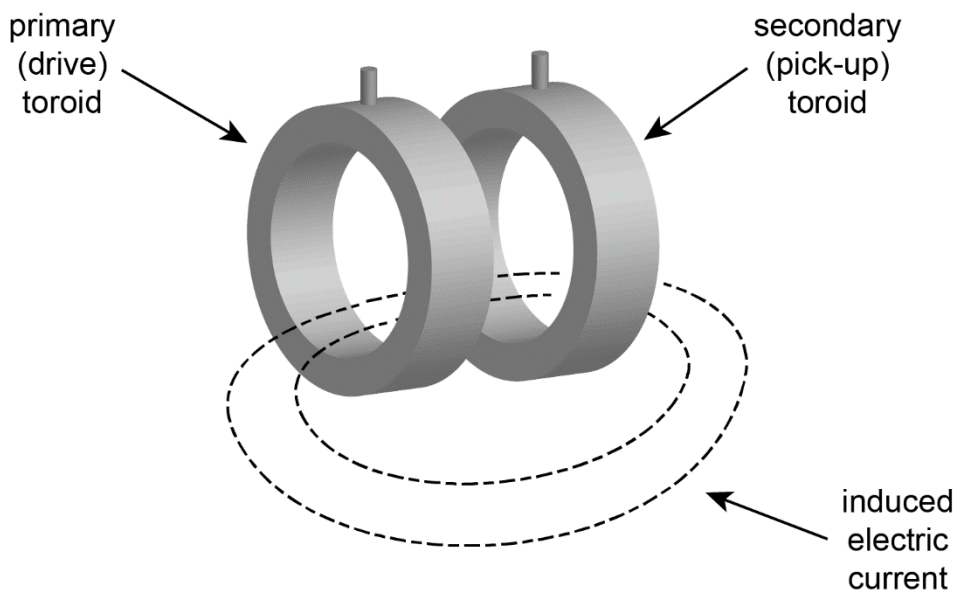

Figure 1.6. Principle of operation of an inductive conductivity sensor.

An AC voltage is passed through the primary drive coil, which induces a current in the electrolyte solution. In turn, this induced solution current will induce a current in the secondary pick-up coil. The amount of coupling between the two coils is proportional to the solution conductivity.[7,18]

Inductive conductivity sensing was developed in the 1950s, and has now become popular primarily in the chemical process industry.[18] This is because the major advantage of inductive sensors is that the sensing coils are not in contact with the solution. The material housing the toroids can be any desired insulating, chemically resistant material, and the sensor can be incorporated into flow through configurations.[7] Furthermore, inductive sensors are less susceptible to fouling effects. Coatings or contamination can build up to a substantial thickness before a decrease in sensor performance is observed. However, inductive sensors can have an order of magnitude lower sensitivity (accuracy) than direct contact sensors. Inductive sensors are typically much larger (at least 4 cm in diameter), and the induced solution current must occupy a large volume around the sensor to ensure that there is a

complete loop without obstruction. Consequently, a minimum sample volume of several hundred millilitres is required, and because of their geometric mounting considerations, inductive sensors do not lend themselves well to many applications.[7,18]

1.1.4 Factors influencing conductivity measurement

The accuracy of a conductivity measurement can be affected by several factors, including polarisation, contamination/fouling, and electrode geometry/field effects.

1.1.4.1 Polarisation

Applying an electrical current to electrodes in solution may cause an accumulation of ionic species near the electrode surfaces and chemical reactions at the surfaces.[1,19] Several factors then influence the interdependence of applied current and electrode potential, and their collective effect is known as electrode polarisation.[20] Specifically, kinetic polarisation, which originates due to the kinetics of the chemical reaction,[20] causes a polarisation resistance to arise on the electrode surface, which may lead to erroneous results as it is a parasitic component to the solution resistance.[1,19]

In earlier literature, polarisation errors were usually minimised by the use of AC for measurements, and by coating the electrodes with a heavy deposit of platinum black, a system initiated by Kohlrausch.[21,22] By applying an AC, the measuring current will flow through the double layer capacitance (C_{dl}) of the electrodes instead of building up a voltage drop across the electrode surface due to the solution resistance (R_{sol}). Polarisation resistance, R_{el}, is then much smaller than R_{sol}.[22] Increasing the active

surface area of the electrodes with a layer of platinum black reduces the current density and consequently the polarisation effect.[23] However, the extent of platinisation was variable, and was often found to catalyse undesired reactions in solution.

The 4-point sensing technique aids in eliminating electrode polarisation contributions.[17,24] Polarisation does not occur if the current passing through the measuring electrodes is zero.[16] Therefore, by measuring the potential between the inner potential sensing electrodes of a 4-point sensor without drawing any current, *i.e.* using a high impedance voltmeter, then no AC boundary potentials can develop at these electrodes and the measured potential will not be influenced by polarisation.[24,25] The ratio of the observed potential and the current which passes through the solution is identical with the impedance of the solution and independent of the polarisation impedance of the current electrodes.

1.1.4.2 Fouling

Fouling is the undesired deposition of liquid borne material onto a surface. If deposited on the electrodes of a direct contact sensor, this layer can cause poor sensor response and erroneous readings. A classic example of this is biofouling, which is the adhesion of microorganisms to surfaces followed by biofilm development. Though, a wide range of fouling types can occur: deposition of inorganic material due to undissolved or slowly precipitating solids; organic substances such as oils and proteins; not to mention particle deposition from silica or clay, for example.[26–28]

Deposits on the electrode surface of a 2-point conductivity sensor have a similar effect to polarisation errors, *i.e.* the conductivity reading is lower than usual. Fouling affects the measurement response to the extent that it alters the geometry, and hence the cell constant, of the probe. In addition, surface fouling will affect the electrode capacitance C_{dl}. The magnitude of C_{dl} will generally decrease (and therefore Z_{dl} will increase) causing the voltage across R_{sol} to increase and hence the effective R_{sol} to increase (through Equation (1.3)) leading to an apparent lower κ measurement. These effects can be reduced with a 4-point conductivity cell, or even further with the use of an inductive conductivity sensor.[7,10]

Nevertheless, after extended periods of time fouling will always become a problem. Correct cleaning procedures (where feasible) will prevent this, and many different approaches to fouling protection have been developed.[29,30] These include mechanical devices like wipers, scrapers, meshes, and shutters. Non-toxic (*e.g.* silicone greases) and toxic (*e.g.* tributyl tin) barriers have both been used for biofilm prevention, as well as the use of copper coatings and implementation of biocide generation systems.

1.1.4.3 Field effects

In the ideal case, there is a uniform electric field distribution between the electrodes of a conductivity sensor, since the measured resistance (and ultimately κ) is determined by the 3D current distribution (conducting volume of solution). However, in practice often considerable spreading of the electric field occurs, known as fringing (**Figure 1.7**). Fringing is exclusively dependent on the electrode configuration, and mostly occurs at electrode edges.[31,32]

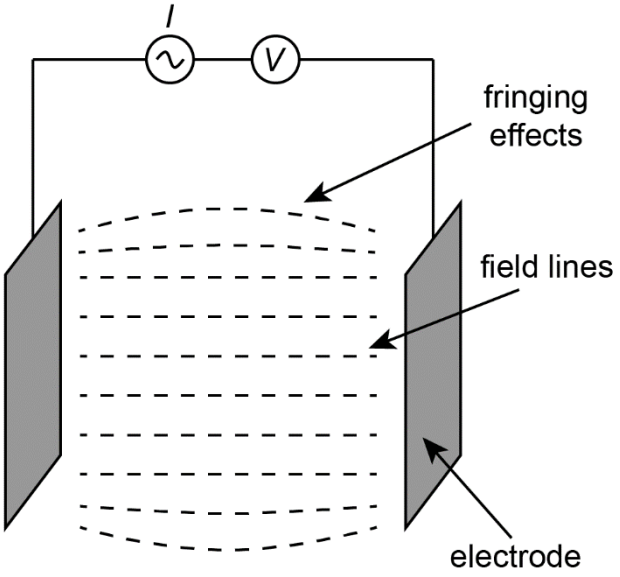

Figure 1.7. 2-point conductivity cell, illustrating the electric field distribution where fringing effects can occur at the electrode edges.

Errors are also caused by field effects: the part of the measuring field that falls outside the geometric space of the conductivity cell. These fringing field lines can affect the measurement if something interferes with the electric field, such as beaker walls, pipe walls, or other external objects. 4-point conductivity sensors are often designed to minimise this effect. If the entire measuring field is contained within the body of the cell, then field errors cannot be caused by external bodies. Otherwise, simulations can yield the 3D electric field distribution, for the investigation of the influence of several parameters, such as the distance of the electrodes from a non-conducting wall.[7,31,32]

1.1.4.4 Dissolution of gaseous substances

Gaseous substances can be dissolved in the sample and form ionic species which influence the conductivity measurement. Carbon dioxide (CO_2) is the main gas in

ambient air that has a significant influence. In water, whilst the majority of CO_2 remains dissolved, it exists in chemical equilibrium with carbonic acid (H_2CO_3) which dissociates rapidly in a first step to hydrogen carbonate (HCO_3^-) and in a second slow step to carbonate (CO_3^{2-}).[33] This can particularly affect the results from low conductivity solutions.[7,34]

Moreover, air bubbles which adhere to the electrode surface or enter the sensor's measuring field will increase the resistance of the sample within the cell and lower the conductivity reading. Dissolved air in cold water becomes less soluble when it gets warmer, which may produce bubbles within a measuring cell if the sample experiences changes in temperature. Consequently, air bubbles often cause unstable signals or inaccurate measurements.[7,35]

1.1.4.5 Parasitic components

Stray capacitances and resistances in various components of the electronics of a conductivity sensor, *e.g.* cables and connections, create a current path in parallel to the electrolyte solution (C_p, a component of C_{ext} in **Figure 1.4a**). This particularly impacts the measurement of low conductivity solutions, where the electrolyte is capacitively coupled to ground through the high cell impedance.[1] Also, this affects measurement at high AC frequencies since as f increases, the impedance from the parasitic components (Z_p) decreases, creating a short circuit path. These issues are unavoidable but can be minimised with appropriate design.[36–38]

1.2 Temperature measurement

1.2.1 Effect of temperature on conductivity

Solution conductivity is strongly temperature dependent. The temperature variation of solution conductivity is large, often involving a five- or six-fold change over the range 0–100 °C.[21] As the temperature of a sample increases, the viscosity (η) of the sample decreases and hence the ion mobility (λ) increases. On a side note, the monatomic ions K^+ and Cl^- are of similar mobility and show a linear variation of the product $\lambda\eta$ with temperature; for this reason potassium chloride solutions are used as standards to calibrate conductivity cells.[39,40]

In most cases, conductivity sensors will report a conductivity value corrected to the value it would have been at a certain reference temperature, usually 25 °C.[41] Alternatively, the conductivity measured at the sample temperature can be reported. Generally it is not possible to adjust the sample temperature to the reference temperature, especially in the case of *in situ* conductivity sensors. Hence, both of these methods require measurement of the temperature of the sample simultaneous to the conductivity measurement.[7]

1.2.1.1 Temperature correction

If it is desired to find the conductivity of a solution at a temperature from measurements made at another temperature, it is necessary to know the change in solution conductivity per degree of temperature. This is known as the temperature coefficient of conductivity, α:

$$\alpha = \frac{1}{\kappa_{25}}\left(\frac{\kappa_\theta - \kappa_{25}}{\theta - 25}\right) \tag{1.9}$$

where 25 and θ °C are the temperatures at which the conductivities κ_{25} and κ_θ were measured, respectively. The coefficient is usually expressed as a conductivity variation in % °C^{-1}.[40–42]

Linear temperature correction is most often used, for moderate to highly conductive solutions of salts, acids, and bases, using Equation (1.10):

$$\kappa_{25} = \frac{\kappa_\theta}{1 + {}^{\alpha}\!/_{100\%} \times (\theta - 25)} \tag{1.10}$$

The α value is generally determined empirically, by taking two conductivity measurements at two temperatures: one at the reference temperature, the other at a typical sample temperature. Though, the greater the difference between these temperatures, the higher the risk of error. Indeed, due to the possible errors caused by temperature correction, pharmaceutical standards often prohibit the use of temperature corrected measurements.[43] Temperature coefficients of common electrolytes generally fall into the ranges shown in **Table 1.1**.

Table 1.1. Temperature coefficients of common electrolytic solutions.

Electrolyte solution	**α / % °C^{-1}**
Acids	1.0 – 1.6
Bases	1.8 – 2.2
Salts	2.2 – 3.0
Drinking water	2.0
Ultrapure water	5.2

However, linear temperature correction is not suitable for many aqueous solutions under test and the temperature dependency can only be described by non-linear functions; such is the case for the non-linear function for natural waters, *e.g.* ground water, surface water, and waste water.[44]

The principle of non-linear correction remains the same as linear correction, whereby the conductivity measured at the sample temperature is corrected to 25°C to give κ_{25}:

$$\kappa_{25} = f_{25}(\theta) \times \kappa_{\theta} \tag{1.11}$$

$f_{25}(\theta)$ is the temperature correction factor used for the conversion of conductivity values of natural water from θ to 25°C. The need for non-linear correction arises from the fact that α is, like conductivity itself, not constant and the factors governing its variation can be complex. The coefficient differs with various electrolytes, and with different concentrations and mixtures of electrolytes, and with temperature.[41,42,44–46]

1.2.2 Temperature sensors

Because of the key role that temperature plays in determining a conductivity measurement, it is imperative to measure the temperature of a sample simultaneously with the conductivity measurement. As a result most, if not all, conductivity sensors combine a temperature sensing element into their construction. An extensive range of techniques for the measurement of temperature is available, but the three types of temperature sensors currently in widespread use are platinum resistance temperature detectors (RTD), thermistors, and thermocouples (**Figure 1.8**).[47]

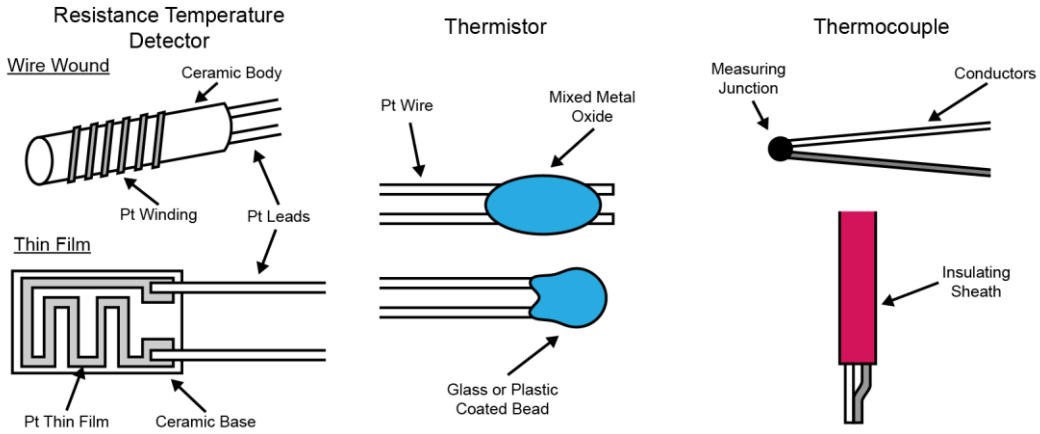

Figure 1.8. Common temperature sensing elements: (a) metal resistive temperature detector, illustrating wire wound and thin film designs, (b) thermistor, and (c) thermocouple.

1.2.2.1 Metal resistance temperature detector

In 1821, Sir Humphrey Davey demonstrated that the electrical resistivity of a metal is related to temperature. By the 1930s, work by Callendar, Van Dusen, and Meyers saw platinum being used in the first RTDs. The resistance of most metals increases reasonably linearly with temperature, which is the fundamental physical principle of RTDs. As the temperature of a metal increases, the amplitudes of the thermodynamic vibrations of its atomic nuclei increase. Correspondingly, the probability of collisions between its free electrons and bound ions increases. These interruptions of the motion of the free electrons, due to collisions, cause the resistance of the metal to increase.[47–49]

Consider the general case where an RTD, with a resistance $R_{\theta,}$ is measuring a temperature with respect to a reference temperature, θ_0, usually 0 °C. A Taylor series expansion gives the resistance of the RTD at the temperature θ:[50]

$$R_\theta = R_0(1 + A\Delta\theta + B\Delta\theta^2) \tag{1.12}$$

where R_0 is the resistance at the reference temperature, and $\Delta\theta = \theta - \theta_0$. The coefficients A and B, which are assumed to be independent of temperature, are defined by:

$$A = \frac{1}{R_0}\left(\frac{\partial R}{\partial \theta}\right)_{\theta=\theta_0} \tag{1.13}$$

$$B = \frac{1}{2!R_0}\left(\frac{\partial^2 R}{\partial \theta^2}\right)_{\theta=\theta_0} \tag{1.14}$$

Usually, third order terms and higher can be neglected.[48]

RTDs consist of a metal conductor either wound round, or deposited as a thin film onto, an insulating support. For most commercial RTDs, platinum is preferred* because it is chemically inert, has linear and highly repeatable resistance-temperature characteristics, and can be used over a wide temperature range. Also, it can be refined to a high degree of purity, ensuring that variations in resistance at the same temperature are small. The most commonly used RTDs have a nominal resistance of either 100 Ω or 1000 Ω at 0 °C, thereby named Pt100 or Pt1000 RTDs, respectively.[47,51]

RTDs are the most accurate of the three temperature sensors described here, and offer the highest long-term stability (±0.05 °C per year) due to the stable physical properties of platinum.[48] The response time is on the order of a few seconds in water.[47] However, care must be taken in the operation of an RTD (the electronics) to use an excitation current as low as possible (<1 mA) so as not to cause errors from self-heating.[52]

* Nickel and copper are also used.

1.2.2.2 Thermistor

Whilst research into the thermal properties of semiconductors was first reported by Faraday in 1834, semiconductor thermometers were only realised later on in the 20th Century. Similar to metal RTDs, thermistors also exploit the fact that a material's resistance is temperature dependent. In practice, only thermistors with a negative temperature coefficient (NTC type) are used for temperature measurement. NTC thermistors utilise mixtures of oxides of transition metals such as Mn, Fe, Ni, Cu, Ti, Zn, and Co. Upon raising the temperature, the number of active charge carriers in the thermistor increases by promoting them into the conduction band. Therefore, the resistance of an NTC thermistor decreases with increasing temperature, is non-linear, and can be described by the following relationship:[47,48]

$$R_\theta = R_0 e^{\left[\alpha \cdot \Delta\theta\left(\theta_0 / \theta\right)\right]} \tag{1.15}$$

where α is a constant depending on the thermistor material.

The characteristics of a thermistor vary substantially, depending on the materials used and method of manufacture. Typically, thermistors are bead shaped, where drops of metal oxide slurry are placed upon two parallel Pt wires, then dried and sintered before being hermetically sealed in glass or plastic.[48,49] Compared with metal RTDs, thermistors can be smaller, and offer higher temperature sensitivity. Since they operate at higher resistances, the possibility of measuring smaller temperature differences is advantageous.

1.2.2.3 Thermocouple

In 1821, Seebeck discovered that a voltage is created when the ends of two dissimilar metals are joined and placed at different temperatures. Peltier realised that this effect is reversible, thus creating a thermocouple. Today, thermocouples are the most commonly used temperature sensor. Thermocouples consist of a closed thermoelectric circuit, composed of two homogeneous dissimilar metals joined at the ends, creating a measuring junction. The resultant thermal electromotive force is a function only of the two metal types and of the temperature.[47,48]

A thermocouple sensor will be mounted in an insulating protective sheath, which can then be placed in a host of assemblies (terminals, adapters, *etc.*) and in different geometries. Thermocouples are commonly used because of their low cost, small size, and wide temperature detection range. However, in comparison to metal RTDs and thermistors, their sensitivity is adequate and their accuracy is much lower.[48,49]

1.3 Sensor applications

1.3.1 Applications for conductivity sensors

Conductivity sensors have found widespread use in many different applications. The scale of aqueous solution conductivity spans over eight orders of magnitude (**Figure 1.9**). Conductivity is a nonspecific measurement, hence the majority of applications revolve around the detection of a certain bulk concentration of electrolytes.[7]

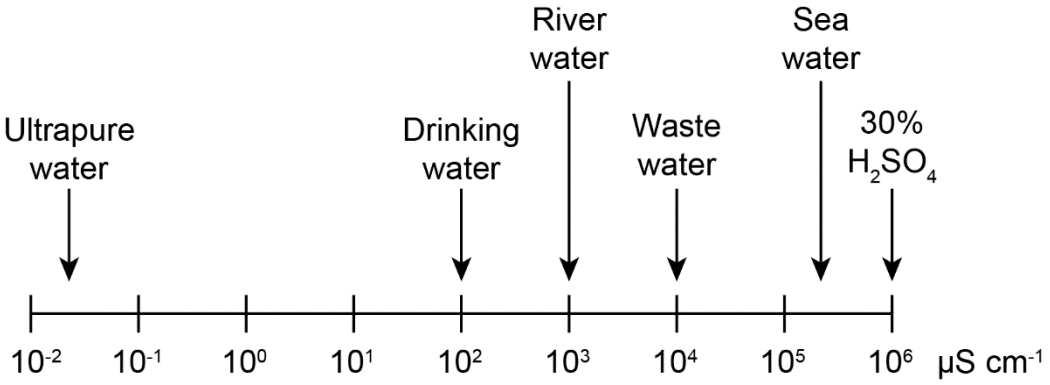

Figure 1.9. Solution conductivity scale, highlighting common aqueous solutions.

Conductivity measurements are extensively used in industrial applications, generally to measure or control solution quality of either input or output streams. For example, this is utilised in chemical plants, food processing, pulp and paper industry, and other manufacturing processes. Boilers and cooling towers monitor conductivity to help control build-up of dissolved solids to prevent scaling and corrosion. Any processes involving deionisation, reverse osmosis, or ion exchange will likely monitor conductivity. These measurements are also heavily used in the pharmaceutical industry, for ultrapure water analysis as well as impurity detection during manufacturing.[7,10,53]

Interface detection can be achieved using conductivity measurements. This involves the detection of an interface between two solutions of dissimilar conductivities, *e.g.* water and a hydrocarbon. Most commonly employed in food processing, such as dairy and brewing, this allows pipes to be cleaned while minimising time spent off-line. Similarly, conductivity can be used for leak detection, where the leak of a contaminant into a sample can be detected through a difference in conductivity between the two.[7,10]

Whilst conductivity is nonspecific, it can sometimes be applied to concentration measurements if the composition of the solution and its conductivity behaviour are known. As long as there is a known, measurable change in conductivity which solely increases or decreases over the desired concentration range, then concentrations can be measured.[7,54]

Conductivity sensors can have extensive applications in biological testing, and miniaturised probes have been developed for compatibility with the small sample volumes available (< mL) and insertion into tissues.[53] Measurements have been taken in blood, in order to monitor red blood cell concentration and that of other indicators.[55,56] Analysis of urine,[57] sweat,[58] and human cerebrospinal fluid[59] have also been utilised using conductivity measurements.

1.3.2 Aquatic environments

Conductivity is a water quality parameter often monitored for environmental testing. Aquatic environments cover a wide range of natural waters, from seawater and river water, through to geothermal waters, mountain waters and snow, and acid mine drainage waters.[60]

Marine coastal environments contain some of the world's most important ecosystems and represent significant resources for human industry and recreation. Water quality in the coastal environment is important for a number of reasons, from the protection of marine organisms and ecosystems to the health of people in the region and the safety of industries such as aquaculture. However, growing populations and industrial pressures in the coastal zone lead to activities such as dumping of waste, construction of harbours, dredging, and extraction processes which all contribute to

changes in environmental quality of the coastal zone. As a result it is essential that environmental health in coastal environments is monitored.[30,61]

Ocean processes span a vast range of scales, both temporal and spatial, from the sub-second and sub-millimetre scale of molecular processes to large scale tidal processes and climate change spanning decades. Traditionally, environmental monitoring involved the collection of discrete samples periodically, followed by analysis in a laboratory, research vessel, *etc*. To investigate such a wide range of processes, a large volume of data has to be gathered from an incredibly harsh environment. Consequently, *in situ* instruments are needed that operate on time scales at least comparable to the physical parameters, and to high precision and accuracy standards.[61–63]

However, the major issue faced by the prolonged direct operation of any *in situ* sensor in a natural aquatic environment of interest is that of long term stability, as mentioned previously. Surface fouling of the sensor leads to deterioration of performance over time, which provides a significant obstacle to obtaining reliable long-term measurements.[29,62,64,65] Moreover, sensors need to be resilient and withstand a variety of natural conditions that can rapidly change, such as turbulent flow, temperature, suspended solids, and weather conditions.[65,66]

1.4 Diamond as a sensor material

1.4.1 Boron doped diamond as an electrode material

Whilst traditionally thought of as a rare gemstone, diamond possesses a multitude of remarkable properties (**Table 1.2**). It is incredibly hard and mechanically stable,

making it extremely resistant to mechanical wear and chemical attack. Moreover, it has a very high thermal conductivity. However, it is also a very strong electrical insulator.[67,68] In order to produce electrical conductivity, diamond can be doped with either boron (p-type dopant) or nitrogen (n-type dopant), though the former is more common, thus yielding boron doped diamond (BDD). At moderate doping levels (~10^{18} boron atoms cm^{-3}) BDD is a p-type semiconductor, where the boron atoms accept electrons from the valence band leading to holes conducting in the valence band. At high doping levels (~10^{20} boron atoms per cm^{-3}) these holes overlap resulting in a boron impurity band and metallic conduction behaviour. This doping is also accompanied by a colour change from colourless through blue (semiconducting) to black (metallic-like) with increasing levels of doping.[69,70]

Table 1.2. Physical properties of diamond and BDD.[71,72]

Property	**Value**
Hardness	56–102 (Knoop) 85–100 (Vickers)
Toughness[†]	7.5–10 MPa $m^{-0.5}$
Thermal conductivity	2200 W m^{-1} K^{-1}
Low thermal expansion	0.9 ppm K^{-1}
Electrical resistivity	10^{13}–10^{15} Ω m (diamond) 10^{-2}–10^{-3} Ω m (BDD)

[†] Ability to resist breakage from forceful impact.

As a result, these extreme properties of diamond and BDD, in combination with advances in methods for the artificial synthesis of these materials, has enabled their usage in a range of devices, in particular as an electrode material for sensing applications and electrochemical processes.[73–75] Several methods are available for synthetic diamond growth, with chemical vapour deposition (CVD)[76,77] and high pressure high temperature[78,79] being the most common. CVD is the most popular technique for highly doped diamond due to its high level of control over the growth process, leading to its ability to produce high quality large structured polycrystalline diamond films.[77,80]

Diamond is formed from tetrahedral, sp^3 bonded carbon atoms which create a face centred cubic (fcc) lattice (**Figure 1.10a**). All bonds between atoms are covalent σ bonds, and this structure gives diamond most of its fundamental properties, as described above. Doping diamond replaces a small number of carbon atoms in the lattice with the dopant, hence for highly doped "metallic" BDD around 1 in 1000 carbon atoms are replaced with boron.[81]

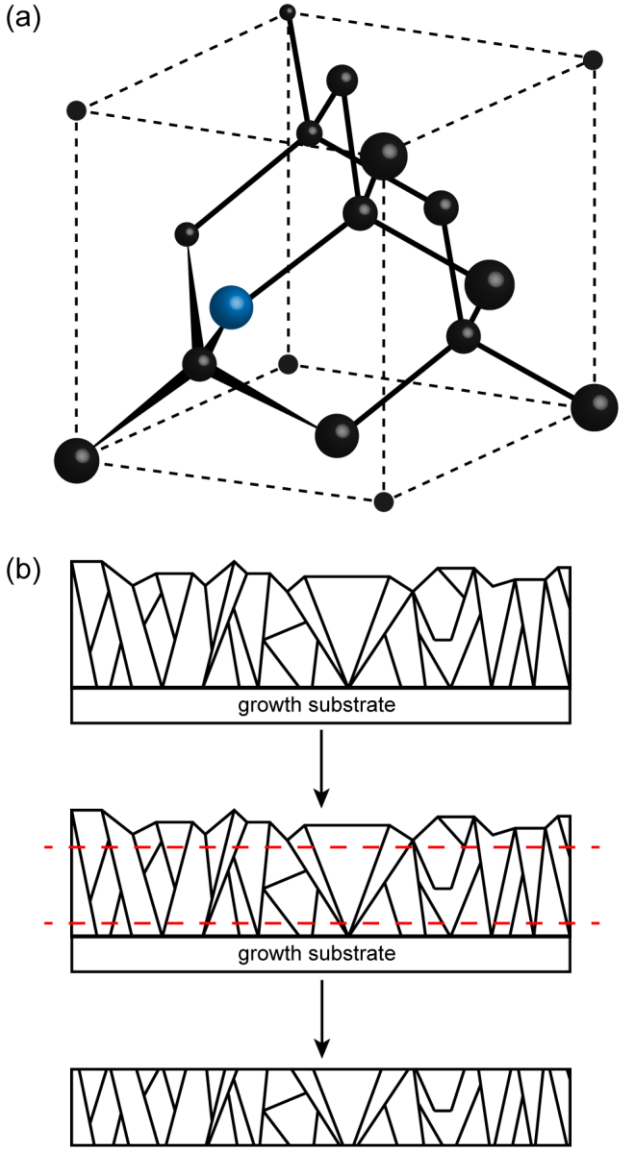

Figure 1.10. Schematic presentation of structure and growth of polycrystalline BDD. (a) Structure of diamond, showing sp^3 bonded C atoms (coloured black) in a tetrahedral lattice. BDD structure is formed by replacing one C atom with one B atom (coloured blue). (b) Illustration of the growth process. Polycrystalline BDD film is grown to a certain thickness, which is then cut and polished from both sides, resulting in a freestanding BDD substrate.[82]

Polycrystalline BDD growth using CVD begins with a plasma typically generated by either microwaves or a hot filament over a substrate such as tungsten or silicon, which is impregnated with diamond nanoparticles. A gaseous carbon source such as methane is then added to the reactor, along with an excess of hydrogen gas and a

gaseous boron source such as B_2H_6.[76,83,84] Under high temperature (>1000 K) diamond nucleates from the seed particles, growing in all directions forming grains within a thin film across the substrate (**Figure 1.10b**). The diamond sp^3 structure is then grown slowly atom by atom; as the grains continue to grow at different rates, they increase in size as the film becomes thicker.[84] Depending on the growth conditions, this can lead to the resultant BDD being either nanocrystalline or microcrystalline, existing as a thin film or a freestanding wafer.[78,80] During growth, the primary crystalline facets are (111), (110) and (100) which uptake boron to different degrees. As an electrode material, polycrystalline BDD will exhibit an average behaviour with contributions from all the differently doped grains.[82,84]

BDD as an electrode material offers a number of advantages over other commonly used materials, such as gold or platinum. BDD has a catalytically inactive surface, benefits from low background currents, and has a wide potential range over which negligible water electrolysis occurs, meaning that an assortment of analytes can be investigated.[80,85,86] The applications of BDD electrodes are extensive,[87,88] from wastewater treatment,[89,90] to the electroanalysis of neurotransmitters,[91,92] metal ions,[93,94] and organics.[95]

1.4.2 All-diamond sensor fabrication

In order to use any electrode in a given system, the electrode must be packaged in such a way as to expose only the required electrode geometry whilst insulating the remainder. Freestanding BDD electrodes, *i.e.* where the BDD has been removed from the growth support, are usually cut to size and then sealed or encapsulated in either glass or epoxy.[96,97] In contrast, thin film BDD electrodes remain attached to

the support substrate and an electrochemical cell is clamped on the top surface to define the electrode area.[98] However, both of these approaches present some difficulties. For thin film electrodes, it is impractical to use this set-up for *in situ* applications, *e.g.* natural aquatic environments. For encapsulated electrodes, few insulating materials will be as mechanically hard as the BDD, so over time with use the former will always degrade or erode at a faster rate. This causes the electrode to become recessed or protruding, leading to changing electrode geometries and therefore changing electrochemical signals, which can complicate analysis or cause the sensor to drift from its calibration. This effect is exacerbated when using BDD electrodes in harsh environments, such as extreme solution pH or high temperatures or pressures.

A more ideal solution to these issues is to create all-diamond devices, whereby the BDD electrode is encapsulated with insulating undoped diamond, thus both components offer identical material properties. Both single microelectrodes and microelectrode arrays have been created, using lithographic processes including electron beam lithography and optical photolithography masking.[99–101] However, with these devices electrodes were not individually addressable, and electrical contact was made on the top face. Ideally, contact will be made from the rear face in order to present only an all-diamond surface to solution. Recent work in the development of electrode fabrication methodology has enabled the manufacture of co-planar BDD electrodes with controlled geometries encapsulated within insulating diamond (**Figure 1.11**).[102]

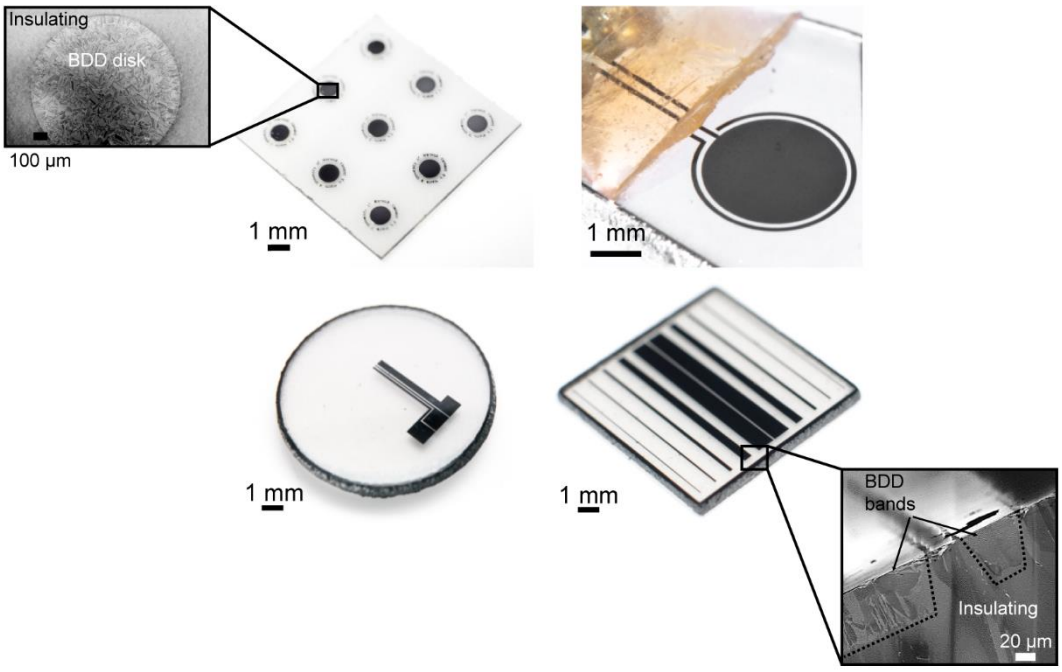

Figure 1.11. Family of example all-diamond electrodes, each displaying black BDD electrodes embedded into transparent insulating diamond. Clockwise from top-left: multiple individual macro electrodes; ring disc electrode; band electrodes with top contacts; band electrodes of varying dimensions (rear contacted). Insets show scanning electron microscope images of the all-diamond electrodes, (top left) from the top face of the device, showing a BDD macro disk embedded in insulating diamond, (bottom right) a cut-through slice of the device revealing two BDD bands at the top of the insulating diamond substrate.[102–104]

This method allows for the fabrication of bands, disks, and rings with a minimum size of around 50 µm each.[93,102–104] Using a laser micromachining approach, material is removed from an insulating diamond substrate to produce trenches. BDD is overgrown on the patterned surface, and then a polishing step is necessary to reveal the filled-in trenches. To obtain an all-diamond surface, contacting must be done through the rear of the insulating diamond, revealing the inner face of the BDD electrode. Any 2D electrode geometry is feasible, and multiple electrodes are individually addressable, with minimal offset (~10 nm recess) between electrode and packaging.[102]

Earlier work in developing this methodology saw the all-diamond device fabricated in reverse: insulating diamond overgrown into laser micromachined BDD.[105,106] Whilst multiple electrodes can be created in this fashion, they are not individually addressable. Along a similar vein, individual all-diamond microelectrode probes have been demonstrated using a comparable fabrication approach and tungsten wire.[107]

1.5 Microbial biofilm formation

1.5.1 Biofouling

In both natural aquatic environments and industrial applications there is a critical need to monitor water quality, analysing parameters such as pH, dissolved gases, organic content, and heavy metals in order to fulfil quality control, environmental management, or regulatory compliance.[108] The use of continuous *in situ* (or on-line) monitoring is considered most beneficial as it allows automatic, real-time measurements directly at the water source of interest.[63,108] Electrode based sensors are ideal for such analysis, as they can be low cost, automated, and miniaturised.[30,62]

However, one of the biggest challenges with *in situ* monitoring is the deterioration of sensor performance over time due to biofouling, which provides a significant obstacle to obtaining reliable long-term measurements.[29,62,64] Biofouling is the accumulation of unwanted biological matter (**Figure 1.12**), and in aquatic environments (whether natural or man-made) this is often due to the formation of microbial biofilms.[26,109,110] Biofilms are complex and dynamic communities of microorganisms attached to a surface.[111] Colonisation of a surface with the formation

of a biofilm may then subsequently attract larger macrofouling organisms.[27,112] Moreover, fouling from abiotic components such as inorganic particles or organic matter can support biofouling indirectly by aiding the growth of biomass.[26]

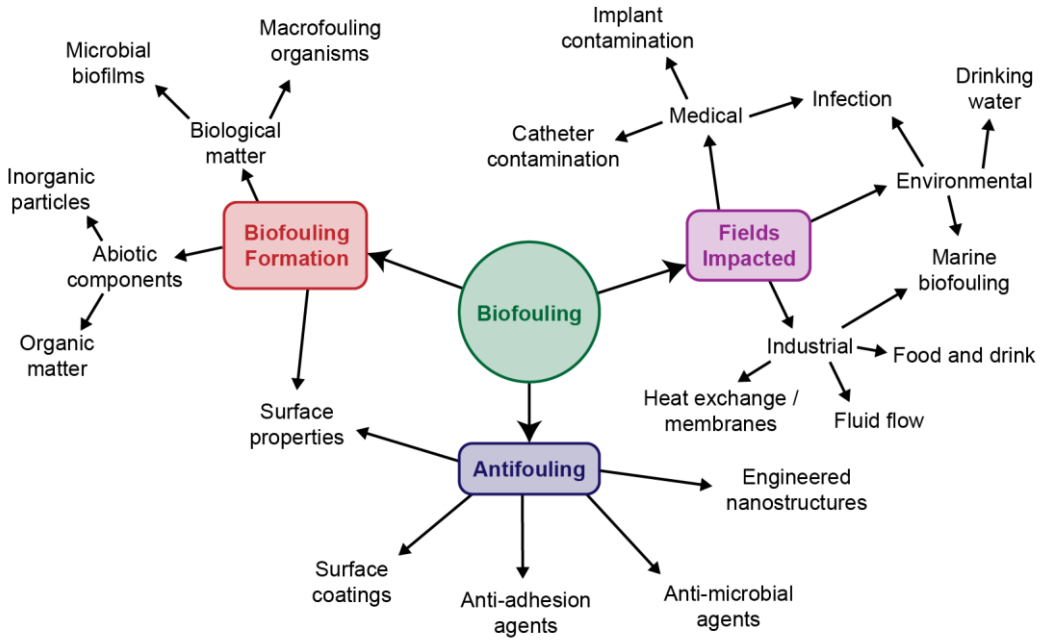

Figure 1.12. Overview of main types of biofouling, fields impacted by biofouling, and antifouling strategies. Adapted from Bixler and Bhushan.[27]

Biofouling is a problem prevalent in a wide variety of medical, environmental, and industrial fields. Biofouling on medical devices and implants in the human body will often lead to device failure or infection from pathogenic microorganisms. Biofilms colonise a wide range of structures in the marine environment, which leads to problems such as increased costs, increased ship fuel consumption, and corrosion. Industrial biofouling affects a range of applications from water utility systems and food production, to power plants and industrial processes.[26–28,64,109,113–118]

Given the negative implications of biofouling and biofilm formation, there is a vast amount of research into strategies for the prevention and control of surface

biofouling. These surface modifications range from the development of surface coatings and anti-bacterial adhesion agents, to the incorporation of silver or copper nanoparticles and antimicrobial agents, to engineering nanostructured materials.[119–124] However, for sensing applications, it is not always possible to modify the sensor surface without adversely affecting the performance properties. This is especially true of devices where the sensing element, *e.g.* an electrode, is directly exposed to the solution.[29]

1.5.2 Bacterial adherence and biofilm formation

Bacteria tend to attach to any surface, regardless of whether it is living or inanimate, in both static and dynamic environments.[111] Once attached, bacteria proliferate and produce a matrix of extracellular polymeric substance (EPS), forming a matured biofilm.[116,125,126] Biofilms in aquatic ecosystems pose environmental concerns and a significant threat to human health, since they can act as reservoirs for antibiotic resistance, and aid the transmission of human pathogens.[113,127] In humans, biofilms can lead to persistent and life-threatening infections, often through the contamination of medical devices, catheters, implants, and prosthetics. Also, the exposure of patients and staff in clinical settings to bacterial pathogens has been associated to bacterial colonisation and biofilm formation in water systems. Indeed, more than 45% of hospital-related infections can be traced back to biofilms.[111,128–130] Despite the ready use of biocides and antimicrobial agents in clinical environments, the biofilm mode of life provides superior bacterial protection against physical (*e.g.* hydrodynamic shear, UV radiation) and chemical (*e.g.* chlorine, acid) stresses.[128,131]

Biofilm formation has been investigated for some time, beginning from the late 17th Century when van Leeuwenhoek first observed oral biofilms.[132] Work carried out in the 1930s by early pioneers of biofilm formation, including Zobell, demonstrated that not only are a large number of bacteria capable of attaching to a surface and proliferating, but also that this attachment appeared to consist of two stages.[133,134] Advances in microscopy and microbiological techniques have contributed greatly to understanding biofilm structure and mechanisms of biofilm formation.[110,126,132]

The formation of bacterial biofilms must, necessarily, begin with the adhesion of a small number of bacterial cells to a surface. Once upon the surface, the cells may then commit to the active process of adhesion and begin to synthesize new EPS material. Then the biofilm develops, through further colonisation and the growth and division of bacterial cells on the surface.[118,132,135,136] Though a useful description of biofilm formation, the processes involved are considerably more intimate, and so in 1990 Characklis and Marshal described an eight step process for biofilm formation (**Figure 1.13**), from an initial conditioning layer through to the eventual development of a mature biofilm.[137]

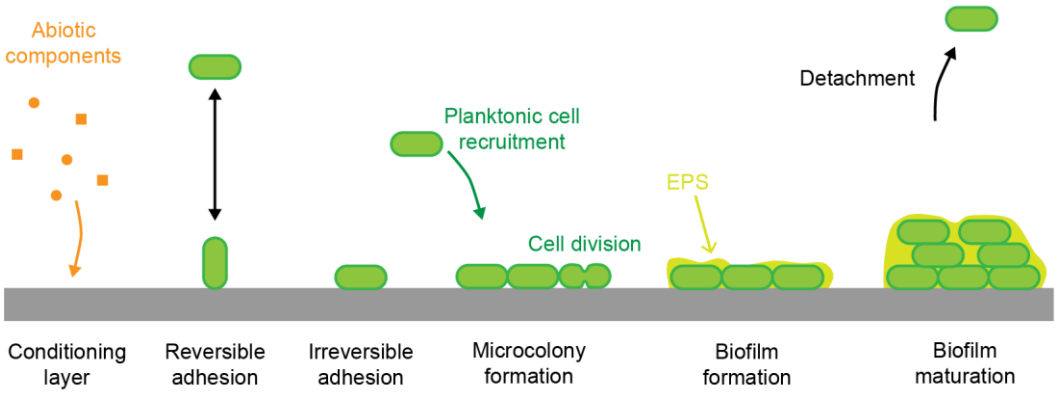

Figure 1.13. Schematic illustration of biofilm formation. Adapted from Simões, and Kjelleberg.[132,138]

The conditioning layer is the foundation on which a biofilm grows, and can be composed of many particles, organic or inorganic. Anything that may be present within the bulk fluid can settle onto a substrate and become part of a conditioning layer. The substrate provides anchorage and nutrients facilitating growth of the bacterial community.[118,139]

Initially, planktonic (free-floating) microbial cells are transported from bulk liquid to the surface either by physical forces or by bacterial appendages such as flagella. A fraction of the cells reaching the surface reversibly adsorbs. Many factors contribute to bacterial adhesion, based on the properties of the surface such as functionality, hydrophobicity, roughness, and charge, as well as local environmental variables like available nutrients, bacterial orientation, temperature and pressure conditions.[118,139,140] If repulsive forces are greater than the attractive forces, the bacteria will detach from the surface. Physical forces associated to bacterial adhesion include the van der Waals forces, steric interactions, electrostatic interactions, and hydrophobic interactions.[118,141]

In order for bacteria to react to a surface or an interface, these cells must be able to sense their proximity to these surfaces or interfaces. Bacteria appear to 'explore' the area of the surface that they first encounter in a species-specific series of behaviours. Cells of some species move very little on the surface before initiating their adhesion behaviour, and cells of other species congregate in certain locations.[125,135,142,143]

A number of the reversibly adsorbed cells remain immobilised and become irreversibly adsorbed. Chemical reactions are stimulated based on adhesins and protein recognition, thus consolidating the bond between bacteria and surface.[118,144,145] As mentioned above, the process of reversible attachment allows an

individual bacterial cell to sample the surface, and either release from the surface or trigger the transition to irreversible attachment.[131,132]

As the stationary cells divide (binary division), daughter cells spread outward and upward from the attachment point to form clusters.[112] At the same time, planktonic cells from bulk liquid continue to be recruited, forming microcolonies on the surface.[132,146] Consequently, a rapid increase in population is observed. This depends on the nature of the environment, both physically and chemically, and occurs at the expense of the surrounding nutrients from the bulk fluid and the substrate. At this stage the physical and chemical contribution to the initial attachment cease and the biological processes begin to dominate.[118] Formation of EPS and the presence of cations interact to form stronger bonding between cells and builds up the biofilm matrix. The biofilm matrix is composed of the microbial cells embedded in a hydrated gel, itself containing polysaccharides (*e.g.* alginate), ions, and trace proteins.[118,147–149]

Bacterial cells communicate with each other: quorum sensing describes a process where numerous auto inducers (chemical and peptide signals in high concentrations) are used to alter the state of neighbouring cells. Signals might be used to alter the distribution of species, protein expression, induce genetic changes, attract cells into the biofilm, or even act as lethal agents towards competing bacterial species.[146,150] The last stage in biofilm development is dispersal. This is an important step in the biofilm life cycle, as it enables exiting cells to seek out and colonise new resources. A mature biofilm is now developed.[125,142,146,151]

1.6 Methods of quantifying & visualising biofilm formation

Biofilm research has been an active field of study since the late 1970s.[152] Since then, the development and advancement of a host of imaging technologies and biochemical methods (**Figure 1.14**) has enabled a deeper understanding of the biofilm and how it interplays with the surrounding environment.[153,154]

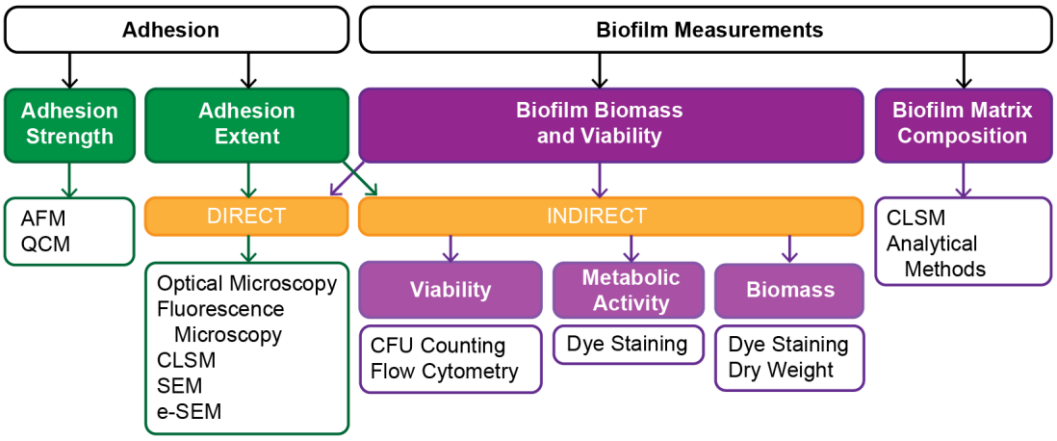

Figure 1.14. Overview of methods to characterise biofilms.[153]

1.6.1 Quantification of biofilm formation

Biofilm biomass and viability can be assessed by different techniques that rely on microbiological and molecular methods, or on physical or chemical properties of the biofilm. Microscopy methods are also important tools for assessing biofilm biomass properties as they allow describing biofilm spatial organisation in a direct way (**Section 1.6.2**).

1.6.1.1 Chemical methods

Chemical methods make use of dyes or stains that are able to bind to or adsorb onto biofilm components. They are indirect methods and can be used to measure specific biofilm components, such as those comprising EPS. Crystal Violet (CV) staining for biofilm quantification remains the most frequently used quantification technique in microtiter plate assays. Originally developed in the 1970s, it has now proved to be compatible with the study of bacterial attachment and sessile development.[153,155,156]

In the classical procedure, bacterial cells are grown in the wells of a polystyrene microtiter plate. At different time points, the wells are emptied and washed to remove planktonic cells before staining the biomass attached to the surface of the wells, which can then be quantified by detachment or stain solubilisation. Whilst being an indirect method for the estimation of the adhered biomass, the microtiter plate dye staining method offers three main advantages: (1) versatility, since it can be used with a broad range of different bacterial species (as well as eukaryotic cells); (2) microorganisms do not need to be detached from the microtiter plates, avoiding biased estimation of the number of cells in the biofilm; and (3) the high-throughput capability of the method allows testing of many different conditions simultaneously. Limitations include possible bias of the estimate of sessile development capability of microorganisms forming loose biofilms, due to the washing steps. Since the assay correlates with all attached bacterial biomass, which can result both from sessile bacteria development at the surface and from sedimentation of planktonic cells due to gravity. Appropriate washing steps can remove sedimented non-attached cells, reducing this problem. Furthermore, the nonspecific nature of CV does not allow species differentiation in multispecies microbial communities.[153]

Moreover, colourimetric methods have been used to assess cellular physiology and metabolic activity within biofilms. Assays utilising dyes such as XTT and resazurin (Alamur Blue) are being increasingly used to study microbial biofilms, through the quantification of metabolic activity, though there is a higher limit of quantification making it less sensitive.[153,157,158]

1.6.1.2 Physical methods

Total biofilm biomass can be obtained from dry or wet weight measurements. Biofilm biomass can be quantified as a weight difference between the dried sample with biofilm and the cleaned substrate before biofilm formation. Also, the volumetric biofilm density as a unit of dry biofilm mass per unit of wet volume can be determined. Using another approach to assess biofilm biomass, substrates with attached cells were vortexed and the released biofilm components were then filtered. Biofilm biomass was expressed as a weight of a dried filter containing biofilm components against the weight of the sterile control filter. However, both methods can underestimate biofilm biomass if the whole biofilm is not removed from the test surface. These methods also present several limitations related to time consumption and lack of sensitivity when detecting small changes in biofilm production.[153]

1.6.1.3 Microbiological methods

The most widely used technique to estimate biofilm cell viability is the determination of colony forming units (CFU) on agar media. Based on the universal dilution series approach used to quantify cells, this technique is available in every microbiological

laboratory. However, this method presents serious limitations. The fraction of detached live cells may not be representative of the initial biofilm population, and a subpopulation of biofilm cells may be viable but non-culturable and hence would not be detected by the CFU approach. Alternatively, flow cytometry, coupled with a few possible fluorophores, have been used to quickly and accurately determine biofilms cell viability. While more expensive, flow cytometry resolves both limitations of CFU counting by allowing differentiation between total, dead, and viable cells.[153]

1.6.2 Visualisation of biofilm formation

Microscopy is by far the most popular technique for imaging components of biofilm systems. It encompasses a variety of techniques for image formation, which can broadly be divided into three categories: (1) optical microscopy, which uses the visible and UV parts of the spectrum, (2) electron microscopy, which uses electron beams, and (3) scanning probe microscopy, which uses a physical probe.

1.6.2.1 Optical and fluorescence microscopy

Optical microscopy refers to the techniques that use mainly the visible part of the electromagnetic radiation spectrum to illuminate an object and magnify an image of it using optical lenses. Optical microscopy was classically used in the early days of biofilm research, generally to image biofilm distribution across a surface.[110]

In fluorescence microscopy, the external light is used to stimulate secondary illumination which is emitted by the sample itself. Samples may exhibit natural fluorescence, or usually microscopists attach fluorescent stains. Among the many

possible ways of staining biofilm components, four are now popular: fluorescent *in situ* hybridisation probes, fluorescent proteins, live/dead stains, and EPS staining. These techniques have revolutionised microbiology and have had a pronounced impact on biofilm research.[110,159]

Confocal laser scanning microscopy (CLSM), whilst not inherently fluorescence microscopy, is now often used in conjunction with the above mentioned fluorescent dyes and probes to enhance the imaging of various biofilm components (typically, microbial cells and EPS). CLSM is currently a tool of choice in biofilm research, as it can provide sharp images of fully hydrated biofilms in 3D.[110,154,159,160]

1.6.2.2 Electron microscopy

Electron microscopy uses beams of electrons to illuminate a sample. There are two basic types: transmission electron microscopy (TEM) and scanning electron microscopy (SEM). In both, images are formed as a result of the interaction between the beam of primary electrons and the sample; however, in TEM this beam penetrates the sample whereas in SEM it is reflected from the sample.[110]

SEM is a method of choice for imaging microbial biofilms, in particular when investigating the substrate surface and comparing the location of microorganisms with topographical features of the surface. SEM offers a much higher resolution than optical and fluorescence microscopy. TEM can obtain even higher resolution, and may be used when analysis at a scale smaller than individual microbial cells are required.[110,161]

However, both TEM and SEM require the use of a high vacuum, meaning that biofilm samples must be carefully dehydrated to prepare them for imaging. This may degrade the EPS matrix, generate artefacts, and alter the biofilm structure. Environmental SEM is a variety of SEM that allows for a gaseous environment in the sample chamber, thus enabling hydrated biofilms to be imaged without losing structural information.[110,162,163]

1.6.2.3 Scanning probe microscopy

Atomic force microscopy (AFM) has been the most common variation of scanning probe technique applied to microorganism and biofilm studies. Here, a cantilever with a sharp tip is scanned over the surface of a sample positioned by a piezoelectric scanner. The attractive force between the tip and the surface affects the position of the cantilever and is detected. In biofilm research, AFM has helped document the initial stages of biofilm formation. It gives images of single microorganisms attached to surfaces with incredible clarity and resolution. Moreover, it can yield quantitative information on adhesion forces between cell and surface.[164–169]

1.7 Aims and objectives

This thesis is concerned with the development of an all-diamond solution conductivity sensor and accompanying software, with simultaneous temperature measurement, that is capable of making accurate measurements in a range of natural aquatic environments under both static and turbulent flow conditions. The impact of biofouling by means of biofilm formation on the diamond material used for sensor

development is also explored. Firstly, Chapter 2 describes a brief overview of the materials, instrumentation, and experimental techniques used to accomplish these objectives.

In Chapter 3, we aim to develop an all-diamond conductivity sensor that is capable of working across a wide range of solution conductivity, but in particular the higher conductivity range that is associated with aquatic and especially marine waters. We consider an assessment of 2-point *vs.* 4-point sensor designs. The sensor is required to perform for extended periods of time (> weeks) in an environment where the flow conditions are likely to change. We also investigate the integration of a temperature sensor into the device for simultaneous conductivity and temperature measurement.

Chapter 4 looks at a more fundamental study into bacterial attachment onto BDD. We aim to assess the biofilm formation (biofouling) capabilities of both BDD and diamond against other materials commonly employed as either the sensing or packaging component in water quality sensors. We focus on *Pseudomonas aeruginosa* and other bacterial species commonly found in both natural and man-made aquatic environments. We comparatively evaluate the extent of *P. aeruginosa* monospecies and multispecies biofilm formation on these test surfaces and explore the surface properties that yield beneficial effects practical for an applied sensor.

In Chapter 5, we aim to further the application of the developed all-diamond conductivity sensor through the assessment of its performance properties in a water (aquatic) flume test rig. In particular, we focus on sensor performance in natural waters and biofouling resistance over extended testing time periods (>30 days), in addition to the examination of properties such as time resolution of the sensor,

response under turbulent flow conditions, as well as situations involving rapidly changing conductivity or temperature.

Finally, in Chapter 6 we aim to initially investigate the preliminary development of an associated sensor for monitoring biofilm formation. Such a sensor would be highly beneficial in a host of environmental, medical, and industrial applications. To conclude, the final chapter summarises all these studies and provides an insight into the possible future development of the work contained herein.

1.8 References

(1) Braunstein, J.; Robbing, G. D. Electrolytic Conductance Measurements and Capacitive Balance. *J. Chem. Educ.* **1971**, *48* (1), 52.

(2) Compton, R. G.; Sanders, G. H. W. *Electrode Potentials*, 1st ed.; Oxford University Press Inc.: New York, 1996.

(3) Robbins, J. Electrolytic Conduction. In *Ions in Solution (2): An Introduction to Electrochemistry*; Oxford University Press Inc.: Oxford, 1972; pp 16–41.

(4) Bockris, J. O.; Reddy, A. K. N. Ion Transport in Solutions. In *Modern Electrochemistry (1): Ionics*; Kluwer Academic Publishers: Boston, 2002; pp 361–600.

(5) Glasstone, S. *An Introduction to Electrochemistry*, 10th ed.; Affiliated East-West Press: New Delhi, 1942.

(6) Bandura, A. V.; Lvov, S. N. The Ionization Constant of Water over Wide Ranges of Temperature and Density. *J. Phys. Chem. Ref. Data* **2006**, *35* (1), 15–30.

(7) Gray, J. R. Conductivity Analyzers and Their Application. In *Environmental Instrumentation and Analysis Handbook*; Down, R. D., Lehr, J. H., Eds.; John Wiley & Sons, Inc., 2004; pp 491–510.

(8) Northrup, E. F. *Methods of Measuring Electrical Resistance*, 1st ed.; McGraw-Hill: New York, 1912.

(9) Washburn, E. W. The Measurement of Electrolytic Conductivity. I. The Theory of the Design of Conductivity Cells. *J. Am. Chem. Soc.* **1916**, *38* (11), 2431–2460.

(10) Lipták, B. G. *Instrument Engineers' Handbook. Volume I: Process Measurement and Analysis*, 4th ed.; CRC Press: Boca Raton, 2003.

(11) Stout, M. B. *Basic Electrical Measurements*, 1st ed.; Prentice-Hall, Inc.: New Jersey, 1960.

(12) Grahame, D. C. Properties of the Electrical Double Layer at a Mercury Surface. II. The Effect of Frequency on the Capacity and Resistance of Ideal Polarized Electrodes. *J. Am. Chem. Soc.* **1946**, *68* (2), 301–310.

(13) Jones, G.; Bollinger, G. M. The Measurement of the Conductance of Electrolytes. III. The Design of Cells. *J. Am. Chem. Soc.* **1931**, *53* (2), 411–451.

(14) Tamamushi, R.; Takahashi, K. Instrumental Study of Electrolytic Conductance Measurements Using Four-Electrode Cells. *J. Electroanal. Chem.* **1974**, *50* (2), 277–284.

(15) Gunning, H. E.; Gordon, A. R. The Conductance and Ionic Mobilities for Aqueous Solutions of Potassium and Sodium Chloride at Temperatures from 15° to 45°C. *J. Chem. Phys.* **1942**, *10* (2), 126–131.

(16) Barendrecht, E.; Janssen, N. G. L. M. Use of Four-Electrode Conductometry for the Automatic Determination of Carbon Dioxide and Ammonia in Concentrated Scrubbing Water of Coke Oven Gas. *Anal. Chem.* **1961**, *33* (2), 199–203.

(17) Anderson, F. P.; Brookes, H. C.; Hotz, M. C. B.; Spong, A. H. Measurement of Electrolyte Conductance with a Four-Electrode Alternating Current Potentiometer. *J. Phys. E.* **1969**, *2* (6), 499–502.

(18) Light, T. S.; McHale, E. J.; Fletcher, K. S. Electrodeless Conductivity. *Talanta* **1989**, *36* (1–2), 235–241.

(19) Hills, G. J.; Djordjević, S. Electrode Polarization in Conductance Measurements, with Special Reference to Molten Salt Systems. *Electrochim. Acta* **1968**, *13* (7), 1721–1726.

(20) Oldham, K. B.; Myland, J. C.; Bond, A. M. *Electrochemical Science and Technology: Fundamentals and Applications*, 1st ed.; John Wiley & Sons, Inc.: Chichester, 2012.

(21) Robinson, R. A.; Stokes, R. H. *Electrolyte Solutions*, 2nd ed.; Butterworths Publications: London, 1965.

(22) Jones, G.; Christian, S. M. The Measurement of the Conductance of Electrolytes. VI. Galvanic Polarization by Alternating Current. *J. Am. Chem. Soc.* **1935**, *57* (2), 272–280.

(23) Jones, G.; Bollinger, D. M. The Measurement of the Conductance of Electrolytes. VII. On Platinization. *J. Am. Chem. Soc.* **1935**, *57* (2), 280–284.

(24) Schwan, H. P. Alternating Current Electrode Polarization. *Biophysik* **1966**, *3* (2), 181–201.

(25) Schwan, H. P.; Ferris, C. D. Four-Electrode Null Techniques for Impedance Measurement with High Resolution. *Rev. Sci. Instrum.* **1968**, *39* (4), 481–485.

(26) Flemming, H. C. Biofouling in Water Systems - Cases, Causes and Countermeasures. *Appl. Microbiol. Biotechnol.* **2002**, *59* (6), 629–640.

(27) Bixler, G. D.; Bhushan, B. Biofouling: Lessons from Nature. *Philos. Trans. R. Soc. A Math. Phys. Eng. Sci.* **2012**, *370* (1967), 2381–2417.

(28) Walker, J.; Surman, S.; Jass, J. *Industrial Biofouling: Detection, Prevention and Control*, 1st Ed.; Wiley: Chichester, 2000.

(29) Delauney, L.; Compère, C.; Lehaitre, M. Biofouling Protection for Marine Environmental Sensors. *Ocean Sci.* **2010**, *6* (2), 503–511.

(30) Mills, G.; Fones, G. A Review of in Situ Methods and Sensors for Monitoring the Marine Environment. *Sens. Rev.* **2012**, *32* (1), 17–28.

(31) Jacobs, P.; Varlan, A.; Sansen, W. Design Optimisation of Planar Electrolytic Conductivity Sensors. *Med. Biol. Eng. Comput.* **1995**, *33* (6), 802–810.

(32) Kordas, N.; Manoli, Y.; Mokwa, W.; Rospert, M. A CMOS-Compatible Monolithic Conductivity Sensor with Integrated Electrodes. *Sensors Actuators A. Phys.* **1994**, *43* (1–3), 31–37.

(33) Bunce, N. J. *Environmental Chemistry*, 1st ed.; Wuerz Publishing Ltd: Canada, 1991.

(34) Park, K. Electrolytic Conductance of Sea Water: Effect of Calcium Carbonate Dissolution. *Science (80-.).* **1964**, *146* (3640), 56–57.

(35) Sigrist, L.; Dossenbach, O.; Ibl, N. On the Conductivity and Void Fraction of Gas Dispersions in Electrolyte Solutions. *J. Appl. Electrochem.* **1980**, *10* (2), 223–228.

(36) Mazzeo, B. A. Parasitic Capacitance Influence of Potential-Sensing Electrodes on Four-Electrode Liquid Impedance Measurements. *J. Appl. Phys.* **2009**, *105* (9).

(37) Holler, F. J.; Enke, C. G. Conductivity and Conductometry. In *Laboratory Techniques in Electroanalytical Chemistry*; Kissinger, P. T., Heineman, W. R., Eds.; Marcel Dekker: New York, 1996; pp 237–266.

(38) Mysels, E. K.; Scholten, P. C.; Mysels, K. J. The Anomalous Frequency Effect in Conductometric Measurements at High Dilution. *J. Phys. Chem.* **1970**, *74* (5), 1147–1150.

(39) Wu, Y. C.; Koch, W. F. Absolute Determination of Electrolytic Conductivity for Primary Standard KCl Solutions from 0 to 50°C. *J. Solution Chem.* **1991**, *20* (4), 391–401.

(40) Barthel, J.; Feuerlein, F.; Neueder, R.; Wachter, R. Calibration of Conductance Cells at Various Temperatures. *J. Solution Chem.* **1980**, *9* (3), 209–219.

(41) ISO-7888. *Water Quality - Determination of Electrical Conductivity. International Organization for Standardization: 6.*; Geneva, Switzerland, 1985.

(42) Tower, O. F. *The Conductivity of Liquids*, 1st ed.; Chemical Publishing Company: Easton, 1905.

(43) United States Pharmacopeial Convention. *USP 645 Water Conductivity*;

Rockville, United States, 2015.

(44) Smith, S. H. Temperature Correction in Conductivity Measurements. *Limnol. Oceanogr.* **1962**, *7* (3), 330–334.

(45) Talbot, J. D. R.; House, W. A.; Pethybridge, A. D. Prediction of the Temperature Dependence of Electrical Conductance for River Waters. *Water Res.* **1990**, *24* (10), 1295–1304.

(46) Wagner, R. Temperaturkorrekturfaktoren Für Die Elektrischen Leitfähigkeit von Wässern. *Z. Wasser- Abwasserforsch.* **1980**, *2*.

(47) Bentley, J. P. Temperature Sensor Characteristics and Measurement System Design. *J. Phys. E.* **1984**, *17*, 430–439.

(48) Michalski, L.; Eckersdorf, K.; Kucharski, J.; McGhee, J. *Temperature Measurement*, 2nd ed.; John Wiley & Sons, Inc.: Chichester, 2001.

(49) Childs, P. R. N.; Greenwood, J. R.; Long, C. A. Review of Temperature Measurement. *Rev. Sci. Instrum.* **2000**, *71* (8).

(50) Callendar, H. L. On the Practical Measurement of Temperature: Experiments Made at the Cavendish Laboratory, Combridge. *Philos. Trans. R. Soc. A Math. Phys. Eng. Sci.* **1887**, *178*, 161–230.

(51) Clayton, W. A. Thin-Film Platinum for Appliance Temperature Control. *IEEE Trans. Ind. Appl.* **1988**, *24* (2), 332–336.

(52) Tong, A. Improving the Accuracy of Temperature Measurements. *Sens. Rev.* **2001**, *21* (3), 193–198.

(53) He, D.; Shannon, M. A.; Miller, N. R. Micromachined Silicon Electrolytic Conductivity Probes with Integrated Temperature Sensor. *IEEE Sens. J.* **2005**, *5* (6), 1185–1196.

(54) Laxen, D. P. H. A Specific Conductance Method for Quality Control in Water Analysis. *Water Res.* **1977**, *11* (1), 91–94.

(55) Hirsch, F. G.; Texter, E. C.; Wood, L. A.; Ballard, W. C.; Horan, F. E.; Wright, I. S. The Electrical Conductivity of Blood. *Blood* **1950**, No. 5, 1017–1035.

(56) Trautman, E. D.; Newbower, R. S. A Practical Analysis of the Electrical Conductivity of Blood. *IEEE Trans. Biomed. Eng.* **1983**, *BME-30* (3), 141–154.

(57) Jacobs, P.; Suls, J.; Sansen, W. Performance of a Planar Differential-Conductivity Sensor for Urea. *Sensors Actuators B. Chem.* **1994**, *20* (2–3), 193–198.

(58) Liu, G.; Ho, C.; Slappey, N.; Zhou, Z.; Snelgrove, S. E.; Brown, M.; Grabinski, A.; Guo, X.; Chen, Y.; Miller, K.; Edwards, J.; Kaya, T. A Wearable Conductivity Sensor for Wireless Real-Time Sweat Monitoring. *Sensors Actuators, B Chem.* **2016**, *227*, 35–42.

(59) Baumann, S. B.; Wozny, D. R.; Kelly, S. K.; Meno, F. M. The Electrical Conductivity of Human Cerebrospinal Fluid at Body Temperature. *IEEE*

Trans. Biomed. Eng. **1997**, *44* (3), 220–223.

(60) McCleskey, R. B.; Kirk Nordstrom, D.; Ryan, J. N. Electrical Conductivity Method for Natural Waters. *Appl. Geochemistry* **2011**, *26* (SUPPL.), S227–S229.

(61) Bierman, P.; Lewis, M.; Ostendorf, B.; Tanner, J. A Review of Methods for Analysing Spatial and Temporal Patterns in Coastal Water Quality. *Ecol. Indic.* **2011**, *11* (1), 103–114.

(62) Prien, R. D. The Future of Chemical in Situ Sensors. *Mar. Chem.* **2007**, *107* (3), 422–432.

(63) Howell, K. A.; Achterberg, E. P.; Braungardt, C. B.; Tappin, A. D.; Worsfold, P. J.; Turner, D. R. Voltammetric in Situ Measurements of Trace Metals in Coastal Waters. *TrAC - Trends Anal. Chem.* **2003**, *22* (11), 828–835.

(64) Klahre, J.; Flemming, H. C. Monitoring of Biofouling in Papermill Process Waters. *Water Res.* **2000**, *34* (14), 3657–3665.

(65) Hanrahan, G.; Patil, D. G.; Wang, J. Electrochemical Sensors for Environmental Monitoring: Design, Development and Applications. *J. Environ. Monit.* **2004**, *6* (8), 657.

(66) Bourgeois, W.; Romain, A. C.; Nicolas, J.; Stuetz, R. M. The Use of Sensor Arrays for Environmental Monitoring: Interests and Limitations. *J. Environ. Monit.* **2003**, *5* (6), 852–860.

(67) May, P. W. Diamond Thin Films: A 21st-Century Material. *Philos. Trans. R. Soc. London. Ser. A Math. Phys. Eng. Sci.* **2000**, *358* (1766), 473–495.

(68) Falcao, E. H.; Wudl, F. Carbon Allotropes: Beyond Graphite and Diamond. *J. Chem. Technol. Biotechnol.* **2007**, *82* (6), 524–531.

(69) Williams, A. W. S.; Lightowlers, E. C.; Collins, A. T. Impurity Conduction in Synthetic Semiconducting Diamond. *J. Phys. C Solid State Phys.* **1970**, *3* (8), 1727–1735.

(70) Lagrange, J. P.; Deneuville, A.; Gheeraert, E. Activation Energy in Low Compensated Homoepitaxial Boron-Doped Diamond Films. *Diam. Relat. Mater.* **1998**, *7* (9), 1390–1393.

(71) Balmer, R. S.; Brandon, J. R.; Clewes, S. L.; Dhillon, H. K.; Dodson, J. M.; Friel, I.; Inglis, P. N.; Madgwick, T. D.; Markham, M. L.; Mollart, T. P.; Perkins, N.; Scarsbrook, G. A.; Twitchen, D. J.; Whitehead, A. J.; Wilman, J. J.; Woollard, S. M. Chemical Vapour Deposition Synthetic Diamond: Materials, Technology and Applications. *J. Phys. Condens. Matter* **2009**, *21* (36).

(72) Field, J. E. The Mechanical and Strength Properties of Diamond. *Reports Prog. Phys.* **2012**, *75* (12).

(73) Xu, J.; Granger, M. C.; Chen, Q.; Strojek, J. W.; Lister, T. E.; Swain, G. M. Peer Reviewed: Boron-Doped Diamond Thin-Film Electrodes. *Anal. Chem.* **2011**, *69* (19), 591A-597A.

(74) Compton, R. G.; Foord, J. S.; Marken, F. Electroanalysis at Diamond-like and

Doped-Diamond Electrodes. *Electroanalysis* **2003**, *15* (17), 1349–1363.

(75) Panizza, M.; Cerisola, G. Application of Diamond Electrodes to Electrochemical Processes. *Electrochim. Acta* **2005**, *51* (2), 191–199.

(76) Bachmann, P. K.; Leers, D.; Lydtin, H. Towards a General Concept of Diamond CVD. *Diam. Relat. Mater.* **1991**, *1*.

(77) May, P. W. CVD Diamond: A New Technology for the Future? *Endeavour* **1995**, *19* (3), 101–106.

(78) Yan, B.; Jia, X.; Fang, C.; Chen, N.; Li, Y.; Sun, S.; Ma, H. A. The Effect of Phosphorus and Nitrogen Co-Doped on the Synthesis of Diamond at High Pressure and High Temperature. *Int. J. Refract. Met. Hard Mater.* **2016**, *54*, 309–314.

(79) Bundy, F. P. Direct Conversion of Graphite to Diamond in Static Pressure Apparatus. *J. Chem. Phys.* **1963**, *38* (3), 631–643.

(80) Macpherson, J. V. A Practical Guide to Using Boron Doped Diamond in Electrochemical Research. *Phys. Chem. Chem. Phys.* **2015**, *17* (5), 2935–2949.

(81) Davies, G. *Properties and Growth of Diamond*, 1st ed.; Institution of Electrical Engineers: London, 1994.

(82) Wilson, N. R.; Clewes, S. L.; Newton, M. E.; Unwin, P. R.; Macpherson, J. V. Impact of Grain-Dependent Boron Uptake on the Electrochemical and Electrical Properties of Polycrystalline Boron Doped Diamond Electrodes. *J. Phys. Chem. B* **2006**, *110* (11), 5639–5646.

(83) Butler, J. E.; Mankelevich, Y. A.; Cheesman, A.; Ma, J.; Ashfold, M. N. R. Understanding the Chemical Vapor Deposition of Diamond: Recent Progress. *J. Phys. Condens. Matter* **2009**, *21* (36), 364201.

(84) Celii, F. G.; Butler, J. E. Diamond Chemical Vapor Deposition. *Annu. Rev. Phys. Chem.* **1991**, *42* (1), 643–684.

(85) Brillas, E.; Martinez-Huitle, C. A. *Synthetic Diamond Films: Preparation, Electrochemistry, Characterization and Applications*, 1st ed.; John Wiley & Sons, Inc.: New Jersey, 2011.

(86) Pleskov, Y. V. Electrochemistry of Diamond: A Review. *Russ. J. Electrochem.* **2002**, *38* (12), 1275–1291.

(87) Luong, J. H. T.; Male, K. B.; Glennon, J. D. Boron-Doped Diamond Electrode: Synthesis, Characterization, Functionalization and Analytical Applications. *Analyst* **2009**, *134* (10), 1965–1979.

(88) Hupert, M.; Muck, A.; Wang, J.; Stotter, J.; Cvackova, Z.; Haymond, S.; Show, Y.; Swain, G. M. Conductive Diamond Thin-Films in Electrochemistry. *Diam. Relat. Mater.* **2003**, *12* (10–11), 1940–1949.

(89) Comninellis, C.; Chen, G. *Electrochemistry for the Environment*, 1st ed.; Springer-Verlag: New York, 2010.

(90) Cañizares, P.; Lobato, J.; Paz, R.; Rodrigo, M. A.; Sáez, C. Electrochemical

Oxidation of Phenolic Wastes with Boron-Doped Diamond Anodes. *Water Res.* **2005**, *39* (12), 2687–2703.

(91) Sarada, B. V.; Rao, T. N.; Tryk, D. A.; Fujishima, A. Electrochemical Oxidation of Histamine and Serotonin at Highly Boron- Doped Diamond Electrodes. *Anal. Chem.* **2000**, *72* (7), 1632–1638.

(92) Patel, A. N.; Unwin, P. R.; MacPherson, J. V. Investigation of Film Formation Properties during Electrochemical Oxidation of Serotonin (5-HT) at Polycrystalline Boron Doped Diamond. *Phys. Chem. Chem. Phys.* **2013**, *15* (41), 18085–18092.

(93) Read, T. L.; Bitziou, E.; Joseph, M. B.; Macpherson, J. V. In Situ Control of Local Ph Using a Boron Doped Diamond Ring Disk Electrode: Optimizing Heavy Metal (Mercury) Detection. *Anal. Chem.* **2014**, *86* (1), 367–371.

(94) Dragoe, D.; Spătaru, N.; Kawasaki, R.; Manivannan, A.; Spătaru, T.; Tryk, D. A.; Fujishima, A. Detection of Trace Levels of Pb 2+ in Tap Water at Boron-Doped Diamond Electrodes with Anodic Stripping Voltammetry. *Electrochim. Acta* **2006**, *51* (12), 2437–2441.

(95) Rao, T. N.; Sarada, B. V.; Tryk, D. A.; Fujishima, A. Electroanalytical Study of Sulfa Drugs at Diamond Electrodes and Their Determination by HPLC with Amperometric Detection. *J. Electroanal. Chem.* **2000**, *491* (1–2), 175–181.

(96) Hutton, L.; Newton, M. E.; Unwin, P. R.; Macpherson, J. V. Amperometric Oxygen Sensor Based on a Platinum Nanoparticle-Modified Polycrystalline Boron Doped Diamond Disk Electrode. *Anal. Chem.* **2009**, *81* (3), 1023–1032.

(97) Ayres, Z. J.; Borrill, A. J.; Newland, J. C.; Newton, M. E.; Macpherson, J. V. Controlled Sp2 Functionalization of Boron Doped Diamond as a Route for the Fabrication of Robust and Nernstian PH Electrodes. *Anal. Chem.* **2016**, *88* (1), 974–980.

(98) Granger, M. C.; Witek, M.; Xu, J.; Wang, J.; Hupert, M.; Hanks, A.; Koppang, M. D.; Butler, J. E.; Lucazeau, G.; Mermoux, M.; Strojek, J. W.; Swain, G. M. Standard Electrochemical Behavior of High-Quality, Boron-Doped Polycrystalline Diamond Thin-Film Electrodes. *Anal. Chem.* **2000**, *72* (16), 3793–3804.

(99) Hees, J.; Hoffmann, R.; Yang, N.; Nebel, C. E. Diamond Nanoelectrode Arrays for the Detection of Surface Sensitive Adsorption. *Chem. - A Eur. J.* **2013**, *19* (34), 11287–11292.

(100) Smirnov, W.; Yang, N.; Hoffmann, R.; Hees, J.; Obloh, H.; Müller-Sebert, W.; Nebel, C. E. Integrated All-Diamond Ultramicroelectrode Arrays: Optimization of Faradaic and Capacitive Currents. *Anal. Chem.* **2011**, *83* (19), 7438–7443.

(101) Rusinek, C. A.; Becker, M. F.; Rechenberg, R.; Schuelke, T. Fabrication and Characterization of Boron Doped Diamond Microelectrode Arrays of Varied Geometry. *Electrochem. commun.* **2016**, *73*, 10–14.

(102) Joseph, M. B.; Bitziou, E.; Read, T. L.; Meng, L.; Palmer, N. L.; Mollart, T. P.; Newton, M. E.; MacPherson, J. V. Fabrication Route for the Production of

Coplanar, Diamond Insulated, Boron Doped Diamond Macro- and Microelectrodes of Any Geometry. *Anal. Chem.* **2014**, *86* (11), 5238–5244.

(103) Channon, R. B.; Joseph, M. B.; Bitziou, E.; Bristow, A. W. T.; Ray, A. D.; Macpherson, J. V. Electrochemical Flow Injection Analysis of Hydrazine in an Excess of an Active Pharmaceutical Ingredient: Achieving Pharmaceutical Detection Limits Electrochemically. *Anal. Chem.* **2015**, *87* (19), 10064–10071.

(104) Joseph, M. B.; Colburn, A.; Mollart, T. P.; Palmer, N.; Newton, M. E.; Macpherson, J. V. A Synthetic Diamond Conductivity Sensor: Design Rules and Applications. *Sensors Actuators, B Chem.* **2017**, *238*, 1128–1135.

(105) Pagels, M.; Hall, C. E.; Lawrence, N. S.; Meredith, A.; Jones, T. G. J.; Godfried, H. P.; Pickles, C. S. J.; Wilman, J.; Banks, C. E.; Compton, R. G.; Jiang, L. All-Diamond Microelectrode Array Device. *Anal. Chem.* **2005**, *77* (11), 3705–3708.

(106) Colley, A. L.; Williams, C. G.; Johansson, U. D. H.; Newton, M. E.; Unwin, P. R.; Wilson, N. R.; Macpherson, J. V. Examination of the Spatially Heterogeneous Electroactivity of Boron-Doped Diamond Microarray Electrodes. *Anal. Chem.* **2006**, *78* (8), 2539–2548.

(107) Silva, E. L.; Gouvêa, C. P.; Quevedo, M. C.; Neto, M. A.; Archanjo, B. S.; Fernandes, A. J. S.; Achete, C. A.; Silva, R. F.; Zheludkevich, M. L.; Oliveira, F. J. All-Diamond Microelectrodes as Solid State Probes for Localized Electrochemical Sensing. *Anal. Chem.* **2015**, *87* (13), 6487–6492.

(108) *In Situ Monitoring of Aquatic Systems: Chemical Analysis and Speciation*, 1st ed.; Buffle, J., Horvai, G., Eds.; John Wiley & Sons, Inc.: Chichester, 2001.

(109) Flemming, H. C. Microbial Biofouling: Unsolved Problems, Insufficient Approaches, and Possible Solutions. In *Biofilm Highlights*; Flemming, H. C., Wingender, J., Szewzyk, U., Eds.; Springer-Verlag: Berlin, 2011; pp 81–110.

(110) Lewandowski, Z.; Beyenal, H. *Fundamentals of Biofilm Research*, 2nd Ed.; CRC Press: Boca Raton, 2017.

(111) Donlan, R. M. Biofilm Formation: A Clinically Relevant Microbiological Process. *Clin. Infect. Dis.* **2001**, *33* (8), 1387–1392.

(112) Stoodley, P.; Sauer, K.; Davies, D. G.; Costerton, J. W. Biofilms as Complex Differentiated Communities. *Annu. Rev. Microbiol.* **2002**, *56* (1), 187–209.

(113) Wingender, J.; Flemming, H. C. Biofilms in Drinking Water and Their Role as Reservoir for Pathogens. *Int. J. Hyg. Environ. Health* **2011**, *214* (6), 417–423.

(114) *Biofilms - Science and Technology*, 1st Ed.; Melo, L. F., Bott, T. R., Fletcher, M., Capdeville, B., Eds.; Plenum Publishing Corporation, 1992.

(115) Liu, S.; Gunawan, C.; Barraud, N.; Rice, S. A.; Harry, E. J.; Amal, R. Understanding, Monitoring, and Controlling Biofilm Growth in Drinking Water Distribution Systems. *Environ. Sci. Technol.* **2016**, *50* (17), 8954–8976.

(116) Costerton, J. W.; Cheng, K.-J.; Greesy, G. G.; Ladd, T. I.; Nickel, J. C.; Dasgupta, M.; Marrie, T. J. Bacterial Biofilms in Nature and Disease. *Ann.*

Rev. Microbiol. **1987**, *41*, 435–464.

(117) Carpentier, B.; Cerf, O. Biofilms and Their Consequences, with Particular Reference to Hygiene in the Food Industry. *J. Appl. Bacteriol.* **1993**, *75* (6), 499–511.

(118) Garrett, T. R.; Bhakoo, M.; Zhang, Z. Bacterial Adhesion and Biofilms on Surfaces. *Prog. Nat. Sci.* **2008**, *18* (9), 1049–1056.

(119) Kostakioti, M.; Hadjifrangiskou, M.; Hultgren, S. J. Bacterial Biofilms: Development, Dispersal, and Therapeutic Strategies in the Dawn of the Postantibiotic Era. *Cold Spring Harb. Perspect. Med.* **2013**, *3* (4), a010306–a010306.

(120) Chen, M.; Yu, Q.; Sun, H. Novel Strategies for the Prevention and Treatment of Biofilm Related Infections. *Int. J. Mol. Sci.* **2013**, *14* (9), 18488–18501.

(121) Banerjee, I.; Pangule, R. C.; Kane, R. S. Antifouling Coatings: Recent Developments in the Design of Surfaces That Prevent Fouling by Proteins, Bacteria, and Marine Organisms. *Adv. Mater.* **2011**, *23* (6), 690–718.

(122) Gu, H.; Ren, D. Materials and Surface Engineering to Control Bacterial Adhesion and Biofilm Formation: A Review of Recent Advances. *Front. Chem. Sci. Eng.* **2014**, *8* (1), 20–33.

(123) Tripathy, A.; Sen, P.; Su, B.; Briscoe, W. H. Natural and Bioinspired Nanostructured Bactericidal Surfaces. *Adv. Colloid Interface Sci.* **2017**, *248*, 85–104.

(124) Chamsaz, E. A.; Mankoci, S.; Barton, H. A.; Joy, A. Nontoxic Cationic Coumarin Polyester Coatings Prevent Pseudomonas Aeruginosa Biofilm Formation. *ACS Appl. Mater. Interfaces* **2017**, *9* (8), 6704–6711.

(125) O'Toole, G.; Kaplan, H. B.; Kolter, R. Biofilm Formation as Microbial Development. *Annu. Rev. Microbiol.* **2000**, *54* (1), 49–79.

(126) Costerton, J. W.; Lewandowski, Z.; Caldwell, D. E.; Korber, D. R.; Lappin-Scott, H. M. Microbial Biofilms. *Annu. Rev. Microbiol.* **1995**, *49* (1), 711–745.

(127) Balcázar, J. L.; Subirats, J.; Borrego, C. M. The Role of Biofilms as Environmental Reservoirs of Antibiotic Resistance. *Front. Microbiol.* **2015**, *6*, 1–9.

(128) Hall-Stoodley, L.; Costerton, J. W.; Stoodley, P. Bacterial Biofilms: From the Natural Environment to Infectious Diseases. *Nat. Rev. Microbiol.* **2004**, *2* (2), 95–108.

(129) Costerton, J. W. Bacterial Biofilms: A Common Cause of Persistent Infections. *Science (80-.).* **1999**, *284* (5418), 1318–1322.

(130) Emmerson, A. M. Emerging Waterborne Infections in Health-Care Settings. *Emerg. Infect. Dis.* **2001**, *7* (2), 272–276.

(131) Tuson, H. H.; Weibel, D. B. Bacteria-Surface Interactions. *Soft Matter* **2013**, *9* (17), 4368–4380.

(132) MacEachran, D. P.; O'Toole, G. A. Do Not Fear Commitment: The Initial Transition to a Surface Lifestyle by Pseudomonads. In *The Biofilm Mode of Life: Mechanisms and Adaptations*; Kjelleberg, S., Givskov, M., Eds.; Horizon Bioscience, 2007; pp 23–35.

(133) Zobell, C. E.; Allen, E. C. The Significance of Marine Bacteria in the Fouling of Submerged Surfaces. *J. Bacteriol.* **1935**, *29* (3), 239–251.

(134) Zobell, C. E. The Effect of Solid Surfaces Upon Bacterial Activity. *J. Bacteriol.* **1943**, *46* (1), 39–56.

(135) Costerton, J. W. Introduction to Biofilm. *Int. J. Antimicrob. Agents* **1999**, *11* (3–4), 217–221.

(136) Fletcher, M. *Microbial Adhesion to Surfaces*, 1st ed.; Ellis-Horwood: Chichester, 1980.

(137) Characklis, W. G.; Marshall, K. C. *Biofilms*, 1st ed.; John Wiley & Sons, Inc.: New York, 1990.

(138) Simões, M.; Simões, L. C.; Vieira, M. J. A Review of Current and Emergent Biofilm Control Strategies. *LWT - Food Sci. Technol.* **2010**, *43* (4), 573–583.

(139) Donlan, R. M. Biofilms: Microbial Life on Surfaces. *Emerg. Infect. Dis.* **2002**, *8* (9), 881–890.

(140) Song, F.; Koo, H.; Ren, D. Effects of Material Properties on Bacterial Adhesion and Biofilm Formation. *J. Dent. Res.* **2015**, *94* (8), 1027–1034.

(141) Renner, L. D.; Weibel, D. B. Physiochemical Regulation of Biofilm Formation. *MRS Bull* **2011**, *36* (5), 347–355.

(142) Teschler, J. K.; Zamorano-Sánchez, D.; Utada, A. S.; Warner, C. J. A.; Wong, G. C. L.; Linington, R. G.; Yildiz, F. H. Living in the Matrix: Assembly and Control of Vibrio Cholerae Biofilms. *Nat. Rev. Microbiol.* **2015**, *13* (5), 255–268.

(143) O'Toole, G. A.; Wong, G. C. L. Sensational Biofilms: Surface Sensing in Bacteria. *Curr. Opin. Microbiol.* **2016**, *30* (1999), 139–146.

(144) Caiazza, N. C.; O'Toole, G. A. SadB Is Required for the Transition from Reversible to Irreversible Attachment during Biofilm Formation by Pseudomonas Aeruginosa PA14. *J. Bacteriol.* **2004**, *186* (14), 4476–4485.

(145) Berne, C.; Ducret, A.; Hardy, G. G.; Brun, Y. V. Adhesins Involved in Attachment to Abiotic Surfaces by Gram-Negative Bacteria. *Microbiol. Spectr.* **2015**, *3* (4), 1–45.

(146) Watnick, P.; Kolter, R. Biofilm, City of Microbes. *J. Bacteriol.* **2000**, *182* (10), 2675–2679.

(147) Dunne, W. M. Bacterial Adhesion: Seen Any Good Biofilms Lately? *Clin. Microbiol. Rev.* **2002**, *15* (2), 155–166.

(148) Sutherland, I. W. The Biofilm Matrix - An Immobilized but Dynamic Microbial Environment. *Trends Microbiol.* **2001**, *9* (5), 222–227.

(149) Flemming, H.-C.; Wingender, J. The Biofilm Matrix. *Nat. Rev. Microbiol.* **2010**, *8* (9), 623–633.

(150) Lazar, V. Quorum Sensing in Biofilms - How to Destroy the Bacterial Citadels or Their Cohesion/Power? *Anaerobe* **2011**, *17* (6), 280–285.

(151) McDougald, D.; Rice, S. A.; Barraud, N.; Steinberg, P. D.; Kjelleberg, S. Should We Stay or Should We Go: Mechanisms and Ecological Consequences for Biofilm Dispersal. *Nat. Rev. Microbiol.* **2012**, *10* (1), 39–50.

(152) Costerton, J. W.; Geesey, G. G.; Cheng, K.-J. How Bacteria Stick. *Sci. Am.* **1978**, *238* (1), 86–95.

(153) Azeredo, J.; Azevedo, N. F.; Briandet, R.; Cerca, N.; Coenye, T.; Costa, A. R.; Desvaux, M.; Di Bonaventura, G.; Hébraud, M.; Jaglic, Z.; Kačániová, M.; Knøchel, S.; Lourenço, A.; Mergulhão, F.; Meyer, R. L.; Nychas, G.; Simões, M.; Tresse, O.; et al. Critical Review on Biofilm Methods. *Crit. Rev. Microbiol.* **2017**, *43* (3), 313–351.

(154) Neu, T. R.; Lawrence, J. R. Innovative Techniques, Sensors, and Approaches for Imaging Biofilms at Different Scales. *Trends Microbiol.* **2015**, *23* (4), 233–242.

(155) Kwasny, S. M.; Opperman, T. J. Static Biofilm Cultures of Gram-Positive Pathogens Grown in a Microtiter Format Used for Anti-Biofilm Drug Discovery. *Curr. Protoc. Pharmacol.* **2010**, 1–27.

(156) O'Toole, G. A. Microtiter Dish Biofilm Formation Assay. *J. Vis. Exp.* **2011**, No. 47, 10–11.

(157) Chandra, J.; Mukherjee, P. K.; Ghannoum, M. A. In Vitro Growth and Analysis of Candida Biofilms. *Nat. Protoc.* **2008**, *3* (12), 1909–1924.

(158) Peeters, E.; Nelis, H. J.; Coenye, T. Comparison of Multiple Methods for Quantification of Microbial Biofilms Grown in Microtiter Plates. *J. Microbiol. Methods* **2008**, *72* (2), 157–165.

(159) Jerome, W. G. (Jay); Price, R. L. *Basic Confocal Microscopy*, 2nd ed.; Springer Nature: Switzerland, 2018; Vol. 9.

(160) Inoué, S. Foundations of Confocal Scanned Imaging in Light Microscopy. In *Handbook of Biological Confocal Microscopy*; Pawley, J. B., Ed.; Springer: New York, 2006.

(161) Angert, I.; Böker, C.; Edelman, M.; Hiller, S.; Merkle, A.; Zeitler, D. ZEISS Scanning Electron Microscopes for Biological Applications. In *Biological Field Emission Scanning Electron Microscopy*; Fleck, R. A., Humbel, B. M., Eds.; John Wiley & Sons, Inc.: New Jersey, 2019; pp 117–142.

(162) Little, B.; Wagner, P.; Ray, R.; Pope, R.; Scheetz, R. Biofilms: An ESEM Evaluation of Artifacts Introduced during SEM Preparation. *J. Ind. Microbiol.* **1991**, *8* (4), 213–221.

(163) Reimer, R.; Eggert, D.; Hohenberg, H. Environmental Scanning Electron Microscopy. In *Biological Field Emission Scanning Electron Microscopy Volume II*; Fleck, R. A., Humbel, B. M., Eds.; John Wiley & Sons, Inc.: New

Jersey, 2019; pp 439–460.

(164) Beech, I. B.; Smith, J. R.; Steele, A. A.; Penegar, I.; Campbell, S. A. The Use of Atomic Force Microscopy for Studying Interactions of Bacterial Biofilms with Surfaces. *Colloids Surfaces B Biointerfaces* **2002**, *23* (2–3), 231–247.

(165) Boyd, R. D.; Verran, J.; Jones, M. V.; Bhakoo, M. Use of the Atomic Force Microscope to Determine the Effect of Substratum Surface Topography on Bacterial Adhesion. *Langmuir* **2002**, *18* (6), 2343–2346.

(166) Dorobantu, L. S.; Gray, M. R. Application of Atomic Force Microscopy in Bacterial Research. *Scanning* **2010**, *32* (2), 74–96.

(167) Fang, H. H. P.; Chan, K. Y.; Xu, L. C. Quantification of Bacterial Adhesion Forces Using Atomic Force Microscopy (AFM). *J. Microbiol. Methods* **2000**, *40* (1), 89–97.

(168) Huang, Q.; Wu, H.; Cai, P.; Fein, J. B.; Chen, W. Atomic Force Microscopy Measurements of Bacterial Adhesion and Biofilm Formation onto Clay-Sized Particles. *Sci. Rep.* **2015**, *5* (June), 1–12.

(169) Wright, C. J.; Shah, M. K.; Powell, L. C.; Armstrong, I. Application of AFM from Microbial Cell to Biofilm. *Scanning* **2010**, *32* (3), 134–149.

2 Experimental

2.1 Chemicals

All solutions were prepared using ultrapure water with a resistivity of ≥18.2 MΩ cm at 25 °C (Merck Millipore, Watford, UK). All chemicals were used as received (**Table 2.1**), and weighed using an analytical balance (A200S, Sartorius, Göttingen, Germany).

Table 2.1. List of chemicals used in this thesis.

Chemical	**Supplier**	**Details**
Acetic acid	Fisher Scientific	Analysis grade, ≥99.7%
Acetone	Sigma-Aldrich Acros Organics	≥99% 99.5%, MOS grade‡, residue free
Acid Blue 9	Cole Parmer	—
Crystal violet solution	Sigma-Aldrich	1% in H_2O
Dark red colouring	Brake Bros	Carmoisine E122
Ethanol absolute	VWR Chemicals	Reagent grade, ≥99.8%
Glucose	Sigma-Aldrich	≥99.5%
Glutaraldehyde solution	Sigma-Aldrich	Grade I§, 50% in H_2O
Hexaammineruthenium(III) chloride	Strem Chemicals	99%
Hexamethyldisilazane	Technic	VLSI grade‡
Hydrochloric acid	Technic	ULSI grade‡
Isopropanol	Sigma-Aldrich Fisher Scientific	≥99.5% ≥99.8%, MOS grade

‡ MOS: metal oxide semiconductor < VLSI: very large scale integration < ULSI: ultra large scale integration.
§ Specially purified for use as an electron microscopy fixative.

Microposit MF-319 developer	Rohm & Haas Electronic Materials	—
Microposit S1818 positive photoresist	Rohm & Haas Electronic Materials	—
Nitric acid	Technic	VLSI grade‡
Potassium chloride	Sigma-Aldrich Acros Organics	Reagent grade, ≥99% Analysis grade, >99%
Potassium nitrate	Sigma-Aldrich	Reagent grade, ≥99.0%
Propidium iodide solution	Sigma-Aldrich	1% in H_2O, ≥94%
Sodium alginate	Vickers Laboratories	—
Sulfuric acid	Sigma-Aldrich	Reagent grade, 95–98%

Materials used as substrates for Chapter 4, along with items used to fabricate sensors and experimental setups in Chapters 3, 5 and 6, are listed in **Table 2.2**.

Table 2.2. List of materials used in this thesis.

Material	**Supplier**	**Details**
Alumina	CoorsTek	—
Alumina micropolish	Buehler	0.05 µm
Boron doped diamond	Element Six	Electrochemical processing grade
Conductive adhesive Ag epoxy	Chemtronics	—
Copper	Goodfellow Cambridge	99.9%, annealed, 0.3 mm thickness
Diamond	Element Six	Thermal grade
Epoxy resin RX771C	Robnor Resin Lab	—
Kapton film 500 HN	Du Pont de Nemours	127 µm thickness
Polyvinyl chloride	Goodfellow Cambridge	Unplasticised

Pt wire	Goodfellow Cambridge	—
Saturated calomel electrode (SCE)	—	Manufactured in-house
Screen printed carbon	Gwent Electronic Materials	C2130307D1 carbon/graphite paste
Silicone sealant	Dow Corning	732
Stainless steel	Goodfellow Cambridge	AISI 304, hard

2.2 Sensor fabrication and measurement

2.2.1 All-diamond sensor fabrication

A co-planar, all-diamond conductivity sensor was fabricated in accordance with procedures described previously.[1,2] The BDD and intrinsic diamond substrates/electrodes used in this work were synthesised using microwave chemical vapour deposition (CVD). Trench structures were patterned by laser micromachining (A-series, Oxford Lasers, Didcot, UK) into a polished (<1 nm R_a roughness) insulating polycrystalline intrinsic diamond substrate (optical grade; Element Six, Didcot, UK). High quality BDD containing minimal non-diamond carbon (NDC) and with metal-like conductivity (boron dopant level $>10^{20}$ B atoms cm^{-3}) was overgrown by CVD onto the substrate.[3] The BDD was subsequently polished back[4] to reveal bands of conducting diamond (<1 nm roughness) embedded in insulating diamond (bands recessed by ~10 nm).

Contact to the conducting diamond was made by laser micromachining (A-series, Oxford Lasers, Didcot, UK) vias from the rear face of the diamond substrate until

contact was made to the rear of the conducting diamond band. Each BDD band was contacted with at least two separate vias. The entire diamond substrate was acid cleaned by exposure to a solution of 96% sulfuric acid (Sigma-Aldrich, St. Louis, USA) saturated with potassium nitrate (Sigma-Aldrich, St. Louis, USA) heated to a temperature of approximately 200 °C for 30 min.[5] Next, electrical contact to the BDD bands was made by sputtering (Minilab 060, Moorfield Nanotechnology, Knutsford, UK) layers of Ti and then Au (thicknesses 10 nm and 400 nm, respectively) and then annealing in a tube furnace for 5 h at 450 °C, during which titanium carbide is formed to provide an Ohmic contact to the BDD.[6,7]

Finally, contact was made to tinned Cu wires using conductive Ag epoxy (Chemtronics, Kennesaw, USA). Insulating epoxy resin (Robnor Resin Lab, Swindon, UK) was used to seal the wires in place and encapsulate the diamond sensor.

2.2.2 Temperature sensor fabrication

Temperature sensing was incorporated into the all-diamond sensor platform by integrating a commercial Pt resistance temperature detector (RTD) onto the rear face of the diamond substrate. A thin film Pt RTD (F2020, Omega Engineering, Manchester, UK) was mounted onto the rear (lapped) face of an insulating polycrystalline diamond substrate (thermal grade; Element Six, Didcot, UK) using a thin layer of conductive Ag epoxy (Chemtronics, Kennesaw, USA). The sensor was then encapsulated in insulating epoxy resin (Robnor Resin Lab, Swindon, UK) such that only the front (polished) face of the diamond was revealed to solution, whilst lead wires from the RTD were exposed from the rear for electrical connection. This

assembly ensured that the RTD was in thermal contact with the diamond substrate, but was electrically isolated from solution.

2.2.3 Conductivity sensor characterisation

Optical microscopy and measurements were made through an Olympus BH2 light microscope (Olympus Corporation, Japan) with magnification capabilities in the range 50–1000×.

Electrochemical impedance spectroscopy (FAS-2, Gamry Instruments, Warminster, USA) was employed to determine C_{dl} for each band electrode. The potential of the band electrode was cycled around 0 ± 0.01 V *vs.* a saturated calomel reference electrode over the *f* range 0.1–100,000 Hz.

2.2.4 Conductivity sensor measurement

An AC conductance meter (for 2-point probe operation) and a differential voltmeter (for 4-point probe operation) were custom built in-house to drive the sensor with minimal internal capacitance. The AC conductance meter was designed to drive alternating currents of 1 µA – 1 mA at frequencies of 1–100 kHz, whilst measuring the alternating voltage required to attain the desired current amplitude. Control of the two instruments was achieved using a custom written LabVIEW script (v. 14, National Instruments, Austin, USA) and a USB-6002 DAQ card (National Instruments, Austin, USA). This system was able to switch between applied frequencies and currents, recording the voltages which were then converted to solution conductivities *via* a calibration curve.

2.2.5 Temperature sensor measurement

Operation of the commercial Pt RTD temperature sensor was achieved using a custom written LabVIEW script (v. 14, National Instruments, Austin, USA) and a cDAQ-9171 equipped with 9217 input module (National Instruments, Austin, USA). Connection from the RTD lead wires to the input module was made in a 3-wire configuration. A commercial Pt RTD temperature probe (HH376, Omega Engineering, Manchester, UK) was also employed, with accuracy ±0.12°C.

2.3 Instrumentation, analysis and characterisation

2.3.1 Contact angle measurement

Water contact angles measurements were utilised to distinguish surface hydrophobicity/hydrophilicity.[8,9] Contact angle values were measured by the static sessile drop method, using a KRÜSS DSA100 drop shape analysis system (KRÜSS GmbH, Hamburg, Germany) at 20 °C with 3 µL droplets of ultrapure water (Merck Millipore, Watford, UK). The contact angle arises from the equilibrium between three phases (**Figure 2.1**): the solid phase (substrate surface), the liquid phase (droplet), and the gas phase (ambient air). The contact angle was measured between the baseline, defined by the droplet solid interface, and the tangent line for the ellipse fitted for the droplet shape profile.

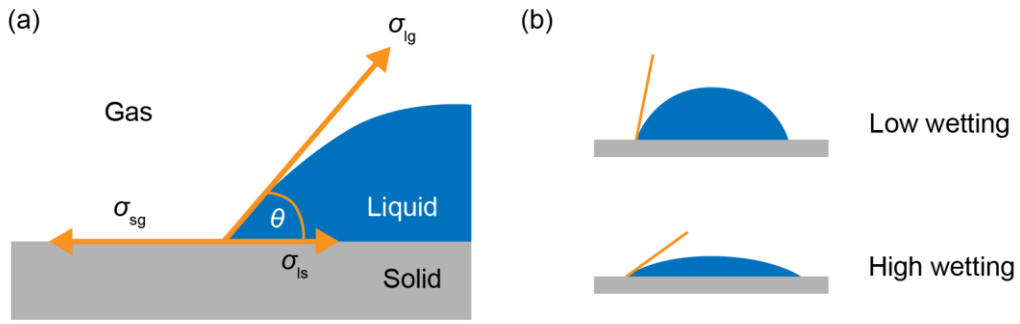

Figure 2.1. Schematic of contact angle measurement. (a) Measured contact angle, θ, is determined from the solid/liquid baseline to the tangent for the ellipse fitted for the droplet shape at the three phase point. (b) The contact angle is a measure of the wettability of a solid by a liquid.

2.3.2 Atomic force microscopy

Atomic force microscopy (AFM) is an imaging technique capable of providing topographical information with nanometre resolution. The principle is based on a very sharp tip or probe being scanned across a surface, with the feedback from interaction forces between the tip and the surface being recorded in order to provide the topography of the surface (**Figure 2.2**). This is achieved by mounting the tip on a cantilever which is deflected by attractive and repulsive forces generated between the tip and surface. Movement in the cantilever is detected with a laser focused onto the cantilever which then reflects the beam onto a photodiode detector, thereby providing a feedback mechanism where the sample is repositioned during scanning as to maintain a constant force between tip and sample.[10]

An AFM instrument is commonly operated in tapping mode. Here, the tip is oscillated at the resonant frequency of the cantilever while being scanned across the surface. The oscillation amplitude of the cantilever is high enough that the tip makes an intermittent contact with the surface to sample short-range repulsive forces, allowing high resolution imaging of surface topography. Contact with the surface

causes a dampening in the cantilever oscillation amplitude. This dampening is used as a feedback mechanism whereby the damping amplitude is kept constant in order to track the surface. The lateral resolution of an AFM is limited to the radius of curvature of the tip apex, but offers highly accurate vertical measurements (< nm).[10]

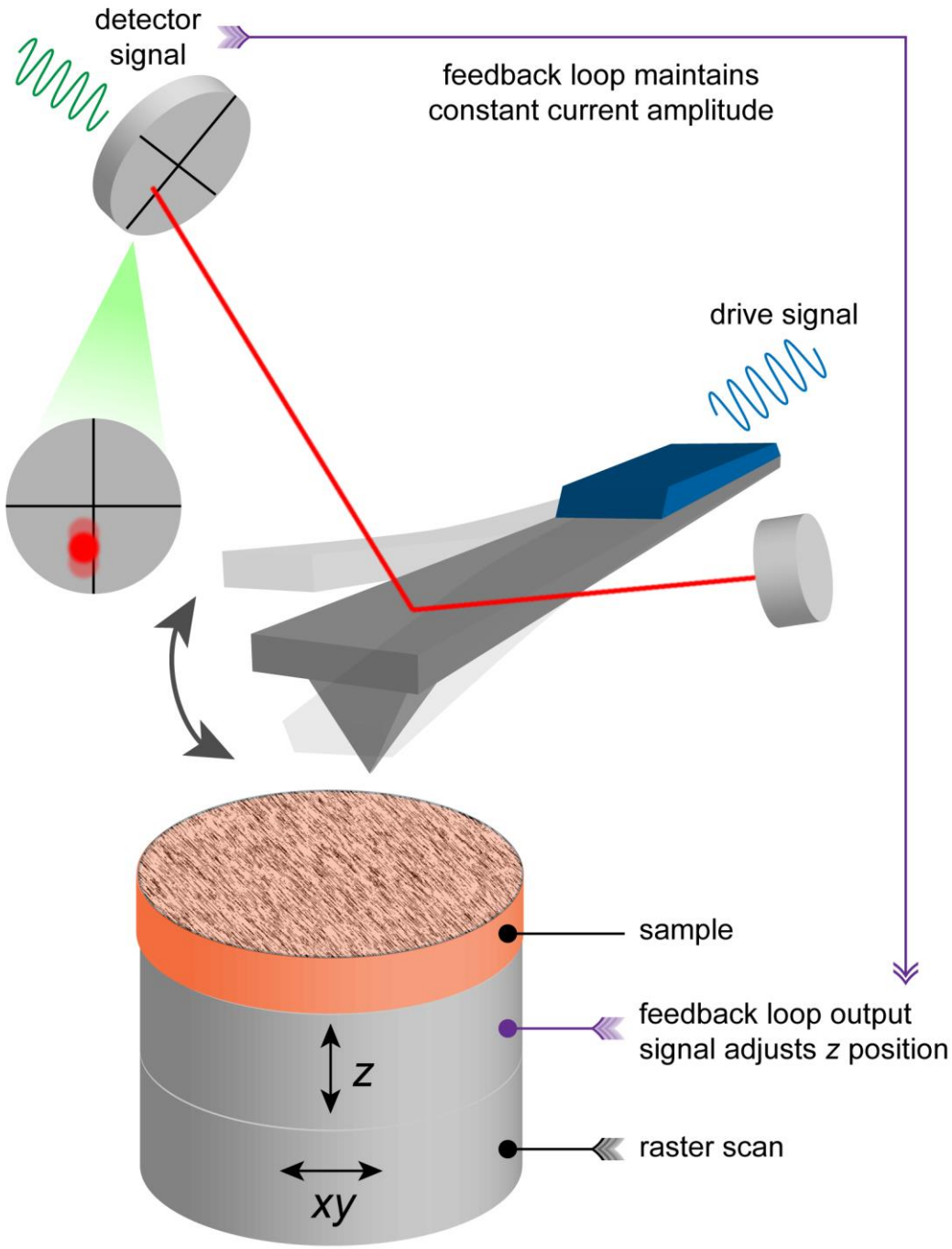

Figure 2.2. Schematic of the principle of operation of an atomic force microscope.

AFM was performed using an Innova system (Bruker, Coventry, UK) operating in tapping mode using an antimony doped silicon probe with a spring constant of 3 N m^{-1}.

2.3.3 Multititer plate assay for biofilm formation

Ten waterborne or water-based biofilm-producing bacterial strains were included in this thesis (**Table 2.3**). All of these strains have been widely used for biofilm studies, are known to be moderate to strong biofilm producers, and are well characterised for genotype and phenotype.[11–14]

Table 2.3. List of bacterial strains used in this thesis.

Species	**Strain**
Acinetobacter baumannii	DSM 30008
Aeromonas hydrophila	DSM 30187
Klebsiella pneumoniae	DSM 30104
Pseudomonas aeruginosa	MPAO1
	NPAO1
	PA14
	LESB58
	ΔwspF
	ΔPsl ΔPel
Staphylococcus aureus	ATCC 29213

Bacterial strains were transferred from frozen stock cultures to LB agar plates and incubated aerobically at 37 °C for 18 to 24 h. All strains were subcultured to LB broth and incubated at 37 °C, 120 rpm. The optical density of the bacterial cultures was monitored at 600 nm (OD_{600}) using a Jenway 7200 spectrophotometer (Cole-Parmer, Staffordshire, UK) to ensure that all cultures reached a mid-exponential growth phase, with an OD_{600} corresponding to approximately 10^8 cells mL^{-1} (strain-dependent OD_{600} range: 0.15–0.2). The strain *P. aeruginosa* ΔPsl ΔPel was used solely for validation of the microtiter plate biofilm assay, as this strain should not produce biofilm and therefore acts as a negative control. All other *Pseudomonas* strains were studied as monospecies biofilm producers. *P. aeruginosa* MPAO1 and the four non-*Pseudomonas* strains were used to generate multispecies biofilms.

Bacterial strains were tested for their ability to form biofilm on the substrates in the presence of two different media: LB broth (pH = 6.9 ± 0.1), and filtered tap drinking water (pH = 6.8 ± 0.1) collected from University of Warwick, Coventry, UK and filtered using a 0.2 µm pore-size membrane filter (Sartorius Stedim Biotech, Göttingen, Germany). For the assay with LB growth medium, a 200 µL bacterial inoculum was added to each well (2×10^7 cells $well^{-1}$) of the multititer plate. For the assay with drinking water as the growth medium, the inoculum was centrifuged at 7,500 rpm for 10 min, the supernatant was removed and the bacterial pellet resuspended in the filtered tap water. The inoculum with a volume of 200 µL was then added to each well (2×10^7 cells $well^{-1}$). For multispecies biofilms, a similar procedure was followed with equal cell concentrations of each strain being mixed together to attain the final inoculum of approximately 2×10^7 cells $well^{-1}$. For every assay, the microtiter plate was incubated under static conditions at either 37 °C or 20 °C for 2 days.

After the 2 day incubation, 150 µL of the liquid culture comprising planktonic cells were carefully aspirated from each well. Next, wells containing the substrate were washed once with sterile water, then the biofilm was fixed either by incubation at 70 °C for 1 h (for CV assay, Section 2.3.4) or by chemical fixation with 1% glutaraldehyde (Grade I, 50% in H_2O; Sigma Aldrich, St Louis, USA) for 1 h followed by a three-step washing with sterile water to remove excess glutaraldehyde (for both microscopy techniques, Section 2.3.5–2.3.6). An overview of the process flow for biofilm formation and subsequent analysis is shown in **Figure 2.3**.

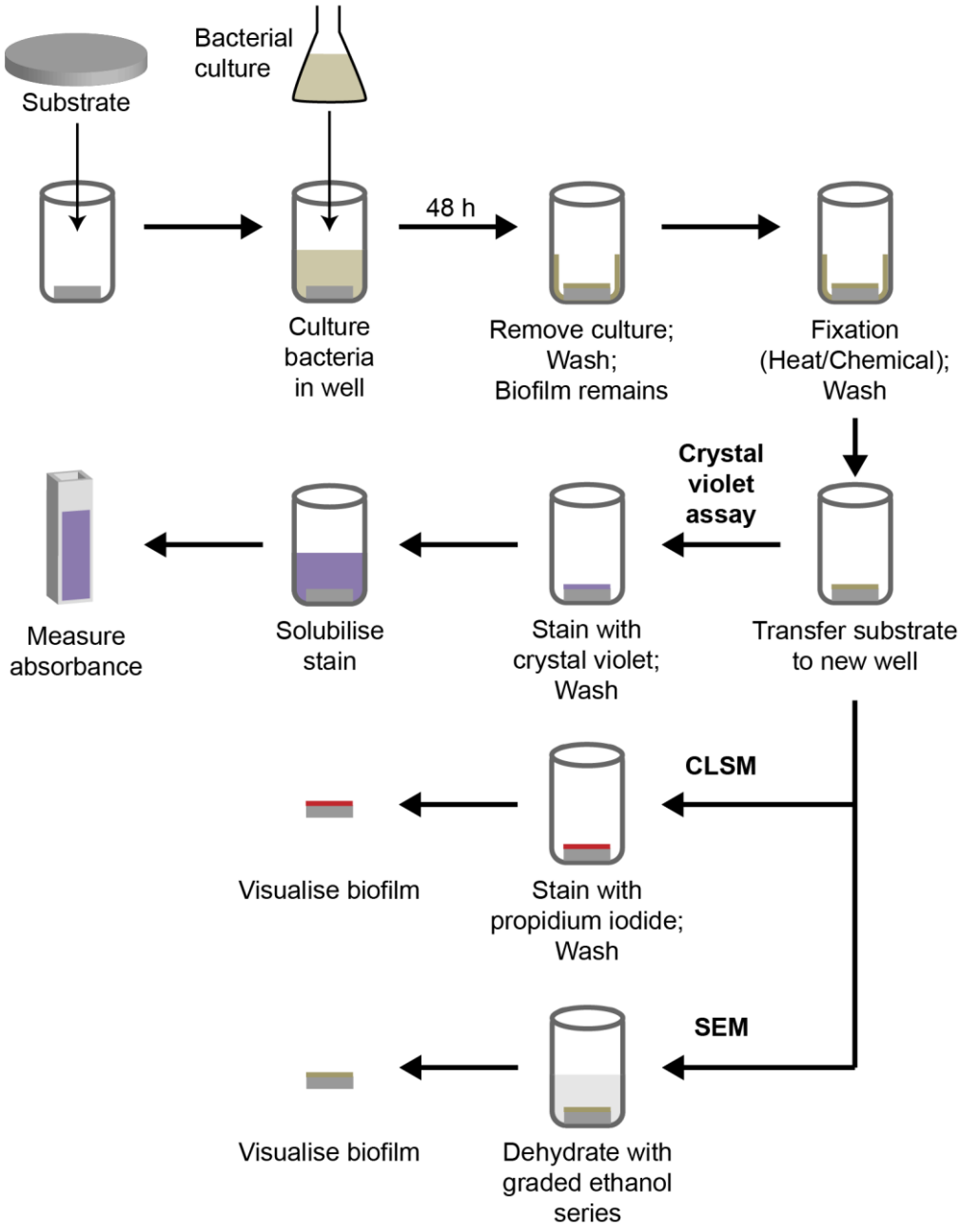

Figure 2.3. Schematic overview of processes utilised in this thesis for formation of biofilm on test substrates, followed by methods of analysis of biofilm formation on substrates.

2.3.4 Crystal violet assay

The assay was adapted from previously described protocols.[12,15,16] Samples were transferred using sterile tweezers to a new multititer plate, before being stained with 0.1% crystal violet aqueous solution (1% in H_2O; Sigma Aldrich, St Louis, USA) for

15 min. The stain was removed from the wells and washed three times with sterile water to remove excess. Stained biofilm was solubilised in 30% acetic acid (≥99.7%; Fisher Scientific, Loughborough, UK) for 15 min. The solubilised stain was transferred to a new 96-well plate and the absorbance at 595 nm (A_{595}) measured using a Multiskan FC Microplate Photometer (Fisher Scientific, Loughborough, UK).

2.3.5 Confocal laser scanning microscopy

Confocal laser scanning microscopy (CLSM) was developed in the 1980s, and is a microscopy technique with the ability to generate clear, thin optical sectioned images, which is totally free from out-of-focus fluorescence. Consequently, its application quickly expanded throughout the biological fields.[17]

During a CLSM experiment the sample is scanned in a series of points using a laser beam, and the resulting image is reconstructed digitally to produce 2D images or 3D profiles. A laser is directed through an aperture (also called a pinhole) and the objective lens, where it is focused on a point of the sample. When a fluorochrome is present in any fluorescently labelled sample, laser excitation at a particular wavelength causes a fluorescent signal to be emitted. A pinhole is used to filter the emitted signal wavelength and remove any background fluorescence before detection. The pinhole is pivotal in achieving the essential feature of CLSM, so that only light from the focal point of the objective is used in image formation. Thus, the focused point of the specimen and detection of the signal is in conjugate focus (confocal) resulting in the resolution, contrast, and signal to noise ratio characteristic of confocal images.[18,19]

In this work, biofilm cells were stained by the addition of 150 µL of 0.1 mg mL^{-1} propidium iodide (≥94%; Sigma Aldrich, St Louis, USA) for 15 min at room temperature, followed by a washing step with sterile water.[20] Samples were transferred using sterile tweezers onto a microscope slide. The dead stained biofilm cells were visualised on a Zeiss LSM710 microscope (Carl Zeiss Ltd., Cambridge, UK). A diode-pumped solid-state laser with maximum emission at 561 nm was used as the excitation source, whilst the detection range was 566–718 nm. Images were analysed using ImageJ software (v. 1.51n, National Institutes of Health, USA) by individually thresholding each image slice of the *z* stack, summing the slices, and calculating the mean fluorescence intensity across the resultant image.

2.3.6 Scanning electron microscopy

To investigate the surface of a sample, scanning electron microscopy (SEM) was employed. A high energy electron beam is generated by an accelerating voltage (0 – 30 kV) which is focused and scanned across the surface of the sample. Interactions between the electron beam and sample result in several types of signals, including secondary electrons (SEs) and backscattered electrons. SEs are a good representation of the surface structure and provide topographical information. Images are collected using a SE detector.[21]

SEM has been under constant development and are now well established for most biological systems. Though, biological samples must be subject to careful preparation and imaging conditions. In this work, samples were dehydrated by a graded series of ethanol (50, 75, 90, 95, and 100%) for 10 min each. Images were obtained using the secondary electron detector on a Zeiss Gemini field emission (FE)

instrument (Carl Zeiss Ltd., Cambridge, UK) operating at 1 kV. Operating in a low energy regime (1 kV) offers the advantages of minimised specimen damage and increased surface sensitivity.[22–24]

2.4 References

(1) Joseph, M. B.; Bitziou, E.; Read, T. L.; Meng, L.; Palmer, N. L.; Mollart, T. P.; Newton, M. E.; MacPherson, J. V. Fabrication Route for the Production of Coplanar, Diamond Insulated, Boron Doped Diamond Macro- and Microelectrodes of Any Geometry. *Anal. Chem.* **2014**, *86* (11), 5238–5244.

(2) Joseph, M. B.; Colburn, A.; Mollart, T. P.; Palmer, N.; Newton, M. E.; Macpherson, J. V. A Synthetic Diamond Conductivity Sensor: Design Rules and Applications. *Sensors Actuators, B Chem.* **2017**, *238*, 1128–1135.

(3) Yokoya, T.; Nakamura, T.; Matsushita, T.; Muro, T.; Takano, Y.; Nagao, M.; Takenouchi, T.; Kawarada, H.; Oguchi, T. Origin of the Metallic Properties of Heavily Boron-Doped Superconducting Diamond. *Nature* **2005**, *438* (7068), 647–650.

(4) Van Bouwelen, F. M. Diamond Polishing from Different Angles. *Diam. Relat. Mater.* **2000**, *9* (3), 925–928.

(5) Hutton, L.; Newton, M. E.; Unwin, P. R.; Macpherson, J. V. Amperometric Oxygen Sensor Based on a Platinum Nanoparticle-Modified Polycrystalline Boron Doped Diamond Disk Electrode. *Anal. Chem.* **2009**, *81* (3), 1023–1032.

(6) Tachibana, T.; Williams, B. E.; Glass, J. T. Correlation of the Electrical Properties of Metal Contacts on Diamond Films with the Chemical Nature of the Metal-Diamond Interface. I. Gold Contacts: A Non-Carbide-Forming Metal. *Phys. Rev. B* **1992**, *45* (20), 11968–11974.

(7) Tachibana, T.; Williams, B. E.; Glass, J. T. Correlation of the Electrical Properties of Metal Contacts on Diamond Films with the Chemical Nature of the Metal-Diamond Interface. II. Titanium Contacts: A Carbide-Forming Metal. *Phys. Rev. B* **1992**, *45* (20), 11975–11981.

(8) Marmur, A. Soft Contact: Measurement and Interpretation of Contact Angles. *Soft Matter* **2006**, *2* (1), 12–17.

(9) Yuan, Y.; Lee, T. R. Contact Angle and Wetting Properties. In *Springer Series in Surface Sciences*; 2013; Vol. 51, pp 3–34.

(10) Binnig, G.; Quate, C. F.; Gerber, C. Atomic Force Microscope. *Phys. Rev. Lett.* **1986**, *56* (9), 930–933.

(11) Kukavica-Ibrulj, I.; Bragonzi, A.; Paroni, M.; Winstanley, C.; Sanschagrin, F.; O'Toole, G. A.; Levesque, R. C. In Vivo Growth of *Pseudomonas Aeruginosa*

Strains PAO1 and PA14 and the Hypervirulent Strain LESB58 in a Rat Model of Chronic Lung Infection. *J. Bacteriol.* **2008**, *190* (8), 2804–2813.

(12) Andreozzi, E.; Barbieri, F.; Ottaviani, M. F.; Giorgi, L.; Bruscolini, F.; Manti, A.; Battistelli, M.; Sabatini, L.; Pianetti, A. Dendrimers and Polyamino-Phenolic Ligands: Activity of New Molecules Against *Legionella Pneumophila* Biofilms. *Front. Microbiol.* **2016**, *7* (289), 1–16.

(13) Rendueles, O.; Ghigo, J. M. Multi-Species Biofilms: How to Avoid Unfriendly Neighbors. *FEMS Microbiol. Rev.* **2012**, *36* (5), 972–989.

(14) Mah, T. C.; O'Toole, G. A. Mechanisms of Biofilm Resistance to Antimicrobial Agents. *Trends Microbiol.* **2001**, *9* (1), 34–39.

(15) Merritt, J. H.; Kadouri, D. E.; O'Toole, G. A. Growing and Analyzing Static Biofilms. *Curr. Protoc. Microbiol.* **2005**, *0* (1), 1B.1.1-1B.1.17.

(16) Chandra, J.; Mukherjee, P. K.; Ghannoum, M. A. In Vitro Growth and Analysis of Candida Biofilms. *Nat. Protoc.* **2008**, *3* (12), 1909–1924.

(17) Inoué, S. Foundations of Confocal Scanned Imaging in Light Microscopy. In *Handbook of Biological Confocal Microscopy*; Pawley, J. B., Ed.; Springer: New York, 2006.

(18) Jerome, W. G. (Jay); Price, R. L. *Basic Confocal Microscopy*, 2nd ed.; Springer Nature: Switzerland, 2018; Vol. 9.

(19) Sheppard, C. J. R.; Shotton, D. M. *Confocal Laser Scanning Microscopy*, 1st ed.; BIOS Scientific Publishers: Oxford, 1997.

(20) Palmer, R. J.; Haagensen, J. A. J.; Neu, T. R.; Sternberg, C. Confocal Microscopy of Biofilms — Spatiotemporal Approaches. In *Handbook of Biological Confocal Microscopy*; Pawley, J. B., Ed.; Springer: New York, 2006.

(21) Goldstein, J. I.; Newbury, D. E.; Michael, J. R.; Ritchie, N. W. M.; Scott, J. H. J.; Joy, D. C. *SEM Microscopy and X-Ray Microanalysis*, 4th ed.; Springer Nature: New York, 2018.

(22) Angert, I.; Böker, C.; Edelman, M.; Hiller, S.; Merkle, A.; Zeitler, D. ZEISS Scanning Electron Microscopes for Biological Applications. In *Biological Field Emission Scanning Electron Microscopy*; Fleck, R. A., Humbel, B. M., Eds.; John Wiley & Sons, Inc.: New Jersey, 2019; pp 117–142.

(23) Humbel, B. M.; Schwarz, H.; Tranfield, E. M.; Fleck, R. A. Chemical Fixation. In *Biological Field Emission Scanning Electron Microscopy*; Fleck, R. A., Humbel, B. M., Eds.; John Wiley & Sons, Inc.: New Jersey, 2019; pp 191–211.

(24) Echlin, P. *Handbook of Sample Preparation for Scanning Electron Microscopy and X-Ray Microanalysis*, 1st ed.; Springer US: New York, 2009.

3 Development of an all-diamond conductivity sensor for aquatic environments

3.1 Aims

Solution conductivity sensors are widely used in industrial and research settings to make measurements across the wide range of conductivities found in aqueous solutions, from distilled water to concentrated salts and acids. However, changes in electrode geometry as a result of mechanical wear, surface fouling, or chemical attack result in deterioration of sensor performance, necessitating regular recalibration and cleaning. We describe a corrosion resistant, mechanically robust all-diamond conductivity sensor fabricated from synthetically grown insulating and conducting diamond. Using a two-step growth procedure, pairs of co-planar conducting boron doped diamond (BDD) band electrodes embedded into an insulating diamond platform are produced in 2-point and 4-point probe configurations. Both designs are comparatively assessed; the latter being optimised for performance over the higher conductivity range as applicable for natural aquatic and marine environments. Since it is of paramount importance to measure sample temperature along with conductivity, we investigate methods of integrating a temperature sensor into the conductivity sensor platform. In addition, we discuss the development of software (using LabVIEW) to allow operation of the sensor to obtain and record real-time measurements. Overall, we examine the development and application of synthetic all-diamond conductivity sensors for use over extended periods of time, *in situ* in aquatic and marine environments.

3.2 Introduction

3.2.1 Solution conductivity measurements

Solution conductivity is a measure of total ion concentration in aqueous solutions, ranging orders of magnitude from low conductivity deionised water to highly conductive concentrated acids (~ 5×10^{-2} – 1×10^{6} µS cm^{-1}).[1] Conductivity measurements have found widespread use, typically as a water quality parameter, in a variety of industrial and environmental applications, in addition to laboratory based measurements.[2] The former are often highly corrosive or fouling environments, *e.g.* chemical or waste streams, boilers and cooling towers, food processing, and rivers and seawater. Therefore, sensors exposed to such solutions require resistance to mechanical wear, surface fouling, and chemical attack, especially if long-term continuous measurements are required.

Boron doped diamond (BDD) is advantageous as a sensor material when such properties are required.[3] In fact, by using a combination of laser micromachining and BDD overgrowth procedures it is possible to produce co-planar, individually addressable BDD electrodes of any geometry which are encapsulated in insulating intrinsic diamond, thus presenting an all-diamond surface for direct contact with the solution of interest.[4] Recent work has shown that it is possible to produce an all-diamond solution conductivity device, which operates in a 2-point sensing configuration, in this way (**Figure 3.1**).[5]

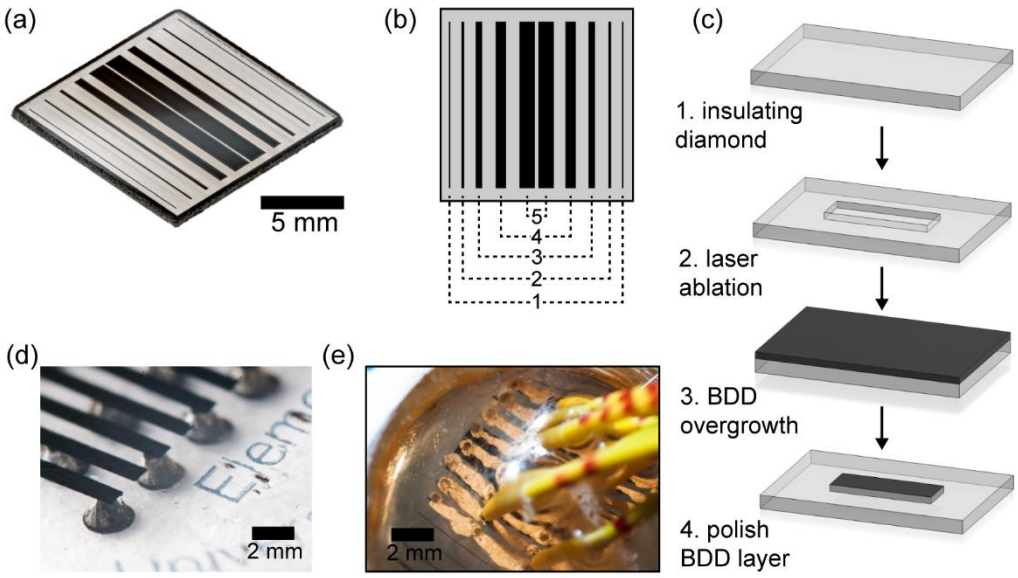

Figure 3.1. Overview of all-diamond conductivity sensor fabrication. (a) Optical image of the all-diamond sensor, consisting of five pairs of BDD bands on the insulating diamond front face. (b) Diagram of the labelled electrode pairs. (c) Schematic describing the step-by-step fabrication of the all-diamond electrodes. (d) Vias are made from the rear face to the internal surface of the electrode by laser micromachining. (e) Au contact tracks are deposited onto the vias for electrical connection to Cu wires. The whole assembly is then cast into epoxy resin. Adapted from Joseph *et al*.[4,5]

Measurements of conductivity are most simply made by applying a fixed alternating current (AC) between two electrodes (typically arranged facing each other) in contact with solution—known as 2-point probe operation—and then measuring the resulting alternating voltage and calculating the impedance. From this, the solution resistance (R_{sol}) can be determined. By calibrating the sensor with solutions of known conductivity, the cell constant (K) can be derived which allows conversion to solution conductivity, κ.[5,6]

Considering a conductivity sensor consisting of two co-planar electrodes, the sensor can be modelled with the equivalent circuit shown in **Figure 3.2a**. Upon the application of a fixed AC, three current flow paths exist between the electrodes: (1) through R_{sol} and the capacitance of the double layer, C_{dl}; (2) through the capacitance of the electrodes that make up the cell, C_{cell}; (3) through other parasitic capacitances

arising from the measurement electronics and wiring, C_p. Since C_{cell} and C_p are in parallel, they can be summed to produce a single value termed the capacitance of external factors, C_{ext}.

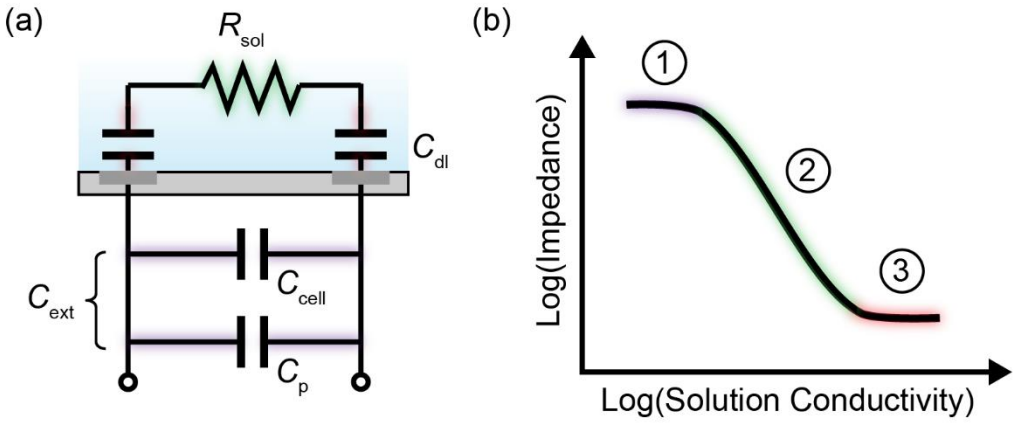

Figure 3.2. (a) Equivalent circuit of the all-diamond conductivity sensor. (b) Example theoretical response of the equivalent circuit as a function of solution conductivity, where the measured impedance is controlled by three domains. Adapted from Joseph *et al*.[5]

These three capacitors—C_{dl}, C_{cell}, and C_p—have characteristic impedances (Z_{dl}, Z_c, and Z_p, respectively) defined by:

$$Z = \frac{1}{j\omega C} \tag{3.1}$$

where $j^2 = -1$, ω is the angular frequency equal to $2\pi f$, and f is the frequency of the applied AC. The response of the experimentally measured impedance, Z_{meas}, to changing solution conductivity is shown qualitatively in **Figure 3.2b**. Overall, there are three possible conditions for the response of Z_{meas}:

When $Z_{ext} < R_{sol} \leq Z_{dl}$;

When $Z_{ext} > R_{sol} > Z_{dl}$;

When $Z_{ext} > R_{sol} < Z_{dl}$.

Under condition 2, $Z_{meas} \propto R_{sol}$ and the sensor is able to make accurate measurements of solution conductivity. However, under conditions 1 and 3 the sensor is insensitive to solution conductivity, limited by the magnitude of either Z_{ext} or Z_{dl}, respectively. Consequently, in order to maximise the working range of the sensor (domain 2) C_{ext} should be minimised and C_{dl} maximised.

3.2.2 Determination of C_{cell}

To determine the cell capacitance C_{cell}, equations (3.2) to (3.4) can be used:[7,8]

$$C_{cell} = \frac{\varepsilon_r \varepsilon_0 l}{2} \frac{K\left(\sqrt{1-g^2}\right)}{K(g)} \tag{3.2}$$

where K is the cell constant for a pair of coplanar electrodes, ε_r is the relative permittivity of solution (here assumed to be 80 for water[9]), ε_0 is the absolute permittivity of free space, l is the electrode length, $K(g)$ is the complete elliptical of the first kind:

$$K(g) = \int_{t=0}^{1} \frac{dt}{\sqrt{(1-t^2)(1-g^2t^2)}} \tag{3.3}$$

and g relates to the geometry of the electrodes:

$$g = \frac{s}{s+w} \tag{3.4}$$

where s is the electrode separation and w is the electrode width. In equation (3.3), $t = \sin\theta$ where θ refers to an angle used in the mathematical treatment of the applied conformal transformation.[10]

3.2.3 Analytical expression for the measured impedance

In order to analytically determine the measured impedance, Z_{meas}, of the circuit in **Figure 3.2**, equation (3.5) applies:

$$Z_{meas} = Z_{cell} + Z_p + x \tag{3.5}$$

The impedance Z_p is the collective term for the parasitic capacitances (C_p), Z_{cell} is the impedance from C_{cell}, and x is the impedance of the solution resistance, R_{sol}, and the double layer capacitance, C_{dl} in series, expressed as:

$$x = R_{sol} + 2Z_{dl} \tag{3.6}$$

Since we know the relationship between Z and C, equation (3.1), we can then rearrange equations (3.5) and (3.6):[5,8,11]

$$Z_{meas} = \frac{2 + j\omega\alpha}{j\omega\beta + \omega^2\gamma} \tag{3.7}$$

where $\alpha = C_{dl} \times R_{sol}$, $\beta = C_{dl} + 2 \times (C_{cell} + C_p)$ and $\gamma = (C_{cell} + C_p) \times C_{dl} \times R_{sol}$. In order to obtain a physically relevant form of equation (3.7), we take the modulus and expand to:[8,12,13]

$$|Z_{meas}| = \frac{\sqrt{\omega^4(\alpha\beta - 2\gamma)^2 + (2\gamma\beta + \omega^3\alpha\gamma)^2}}{\omega^2\beta^2 + \omega^4\gamma^2} \tag{3.8}$$

We can now predict, for a given C_{cell}, C_p, C_{dl}, and R_{sol}, the total measured impedance of a conductivity cell of a co-planar two electrode band geometry. Equation (3.8) is used to generate the theoretical plots shown later in this chapter.

3.2.4 Extension to 4-point probe operation

Up to now, discussion of conductivity measurements has comprised solely 2-point probe operation, and the previously fabricated all-diamond conductivity sensor[5] was designed for this method. However, this configuration of conductivity sensor is non-ideal for measuring the wide range of solution conductivities available, in particular highly conductive solutions such as concentrated salts, acids, and alkalis, as well as natural aquatic environments such as river water and seawater.[1,2]

Under a 4-point probe operation, four electrodes are utilised in the conductivity cell. A fixed AC is applied across two outer current injection electrodes (similar to 2-point) and the potential drop through the solution is measured between two inner potential sensing electrodes.[2] In this way, polarisation at the potential sensing electrodes does not occur and therefore there is no effect of C_{dl} (region 3 in **Figure 3.2b**).[14] Consequently, 4-point measurements are considered more suitable for higher conductivity solutions. We investigate the extension of the co-planar all-diamond conductivity sensor to a 4-point probe arrangement, taking into account geometrical design considerations.

3.2.5 Conductivity and temperature

The temperature variation of solution conductivity is large, often involving a five- or six-fold change over the range 0–100 °C.[15] This is due to increasing ion mobility (λ) and decreasing viscosity (η). The monatomic ions K^+ and Cl^- are of similar mobility and show a linear variation of the product $\lambda\eta$ with temperature, hence this is the reason that potassium chloride solutions are used as standard solutions to calibrate conductivity cells.[16,17]

Therefore, in most cases conductivity sensors will report a conductivity value corrected to the value it would have been at a certain reference temperature, usually 25 °C.[18] Alternatively, the conductivity measured at the sample temperature can be reported. Both of these methods require measurement of the temperature of the sample simultaneous to the conductivity measurement.[1] As a result, we also explore integration of a temperature sensor into the all-diamond conductivity sensor platform.

3.2.6 Sensor operation and data acquisition

Whilst the electronics that operate the conductivity sensor can be used manually, it is advantageous to be able to operate the sensor using a software-based system of control. Key reasons are that it allows long-term operation such as environmental monitoring, high-speed operation in which a large amount of data is collected quickly, and automated real-time data processing.[19] Data acquisition (DAQ) is the process of measuring a real-world signal (voltage, in this case) and bringing that information into a computer in digital form for further analysis and storage. LabVIEW is a graphical programming environment designed to imitate actual instruments and is popular for sensor data acquisition,[20,21] therefore we choose to use this software to create a program—known as a virtual instrument (VI)—which allows control of the sensor and acquires data.

There are two co-dependent aspects to reading data: how quickly the real-world signal is digitised, and how much data is retrieved by the software at any given time from the hardware (**Figure 3.3**). The conductivity sensor outputs an analogue voltage signal, which is sampled by the DAQ device and digitised by its analogue-to-digital

converter (ADC). Data is stored in the device's buffer (FIFO buffer) before being transferred to the PC's memory and entering the LabVIEW VI.[22]

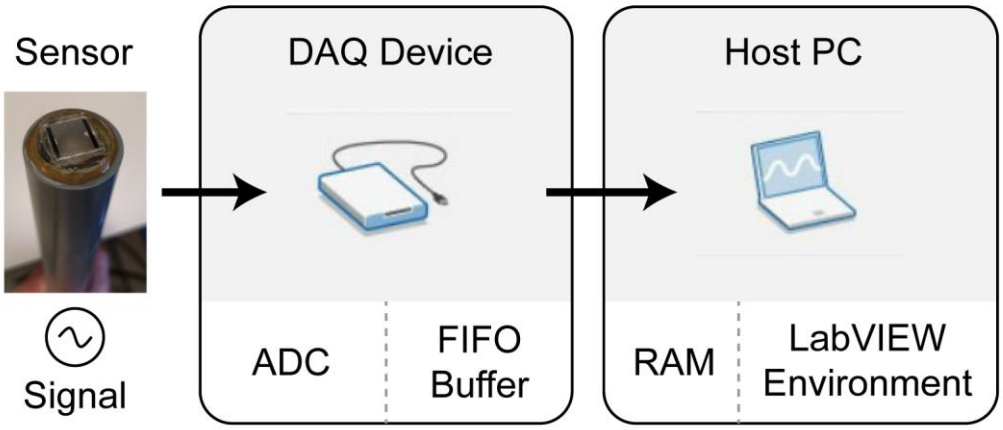

Figure 3.3. Elements of the data acquisition system.

Also, the DAQ device is input/output meaning that as well as acquiring data from the sensor (device input), it can output a signal to control the conductivity sensor electronics. Therefore we can use LabVIEW to create a VI that allows full PC operation of the conductivity sensor. In this chapter we discuss the application of a DAQ device for this purpose, along with the development of a VI and user interface that builds up in functionality.

3.3 Experimental

3.3.1 Conductivity sensor fabrication

A co-planar, all-diamond conductivity sensor was fabricated in accordance with procedures described previously.[4,5] Briefly, trench structures were patterned by laser micromachining (A-series, Oxford Lasers, Didcot, UK) into a polished (<1 nm

roughness) insulating polycrystalline diamond substrate (optical grade; Element Six, Didcot, UK). High quality BDD containing minimal non-diamond carbon (NDC) and with metal-like conductivity was overgrown onto the substrate. The BDD was subsequently polished back to reveal bands of conducting diamond (<1 nm roughness) embedded in insulating diamond (bands recessed by ~10 nm), as shown in **Figure 3.1c**. Contact to the conducting diamond was made by laser micromachining (A-series, Oxford Lasers, Didcot, UK) vias from the rear face of the diamond substrate until contact was made to the rear of the conducting diamond band (**Figure 3.1d**). Each BDD band was contacted with at least two separate vias. The entire diamond substrate was acid cleaned by exposure to a solution of 96% sulfuric acid (Sigma-Aldrich, St. Louis, USA) saturated with potassium nitrate (Sigma-Aldrich, St. Louis, USA) heated to a temperature of approximately 200 °C for 30 min. Next, electrical contact to the BDD bands was made by firstly sputtering (Minilab 060, Moorfield Nanotechnology, Knutsford, UK) layers of Ti and then Au (thicknesses 10 nm and 400 nm respectively) and then annealing in a tube furnace for 5 h at 450 °C. Final contact was made to tinned Cu wires using conductive Ag epoxy (Chemtronics, Kennesaw, USA). Insulating epoxy resin (Robnor Resin Lab, Swindon, UK) was used to seal the wires in place and encapsulate the diamond sensor (**Figure 3.1e**). For calibration experiments, the sensor was mounted in the lid of a Falcon tube using silicone sealant (732, Dow Corning, Michigan, USA); this allowed easy transfer of the sensor between solutions.

An AC conductance meter (for 2-point probe operation) and a differential voltmeter (for 4-point probe operation) were custom built in-house[**] to drive the sensor with minimal internal capacitance. The AC conductance meter was designed to drive

[**] Refer to Appendix A for detailed circuit diagrams for the instrumentation used.

alternating currents of 1 µA – 1 mA at frequencies of 1–100 kHz, whilst measuring the alternating voltage required to attain the desired current amplitude. Control of the two instruments was achieved using a custom written LabVIEW script (v. 14, National Instruments, Austin, USA) and a USB-6002 DAQ card (National Instruments, Austin, USA). This system was able to switch between applied frequencies and currents, recording the voltages which were then converted to solution conductivities *via* a calibration curve.

3.3.2 Conductivity sensor characterisation and measurement

Electrochemical impedance spectroscopy (FAS-2, Gamry Instruments, Warminster, USA) was employed to determine C_{dl} for each band electrode. The potential of the band electrode was cycled around 0 ± 0.01 V *vs.* a saturated calomel reference electrode over the *f* range 0.1–100,000 Hz.

A commercial 4-point probe graphite electrode conductivity sensor (InLab 731, Mettler Toledo, Leicester, UK) was also employed. This sensor was specified for 10^1 – 10^6 µS cm^{-1} with a nominal *K* of 0.57 cm^{-1}, with the electrodes arranged as two pairs of concentric circles facing each other.

The commercial sensor was operated with automatic temperature correction enabled throughout, whilst the all-diamond sensor was operated either in temperature controlled or temperature corrected modes depending on the experiments. Calibration experiments were conducted under temperature controlled conditions (air temperature ± 0.1°C).

3.3.3 Temperature sensor fabrication

Temperature sensing was incorporated into the all-diamond sensor platform by integrating a commercial Pt RTD onto the rear face of the diamond substrate. A thin film Pt RTD (F2020, Omega Engineering, Manchester, UK) was mounted onto the rear (lapped) face of an insulating polycrystalline diamond substrate (thermal grade; Element Six, Didcot, UK) using a thin layer of conductive Ag epoxy (Chemtronics, Kennesaw, USA). The sensor was then encapsulated in insulating epoxy resin (Robnor Resin Lab, Swindon, UK) such that only the front (polished) face of the diamond was revealed to solution, whilst lead wires from the RTD were exposed from the rear for electrical connection. This assembly ensured that the RTD was in thermal contact with the diamond substrate but was electrically isolated from solution.

Integration of temperature sensing was also investigated by fabrication of a custom designed RTD pattern by Pt deposition directly onto the diamond surface, using two methods: shadow masking and photolithography (**Figure 3.4**). For both approaches, the insulating diamond substrate was first cleaned using acetone (99.5%, Acros Organics, Geel, Belgium) and isopropanol (99.8%, Fisher Scientific, Loughborough, UK), and then dried with purified N_2.

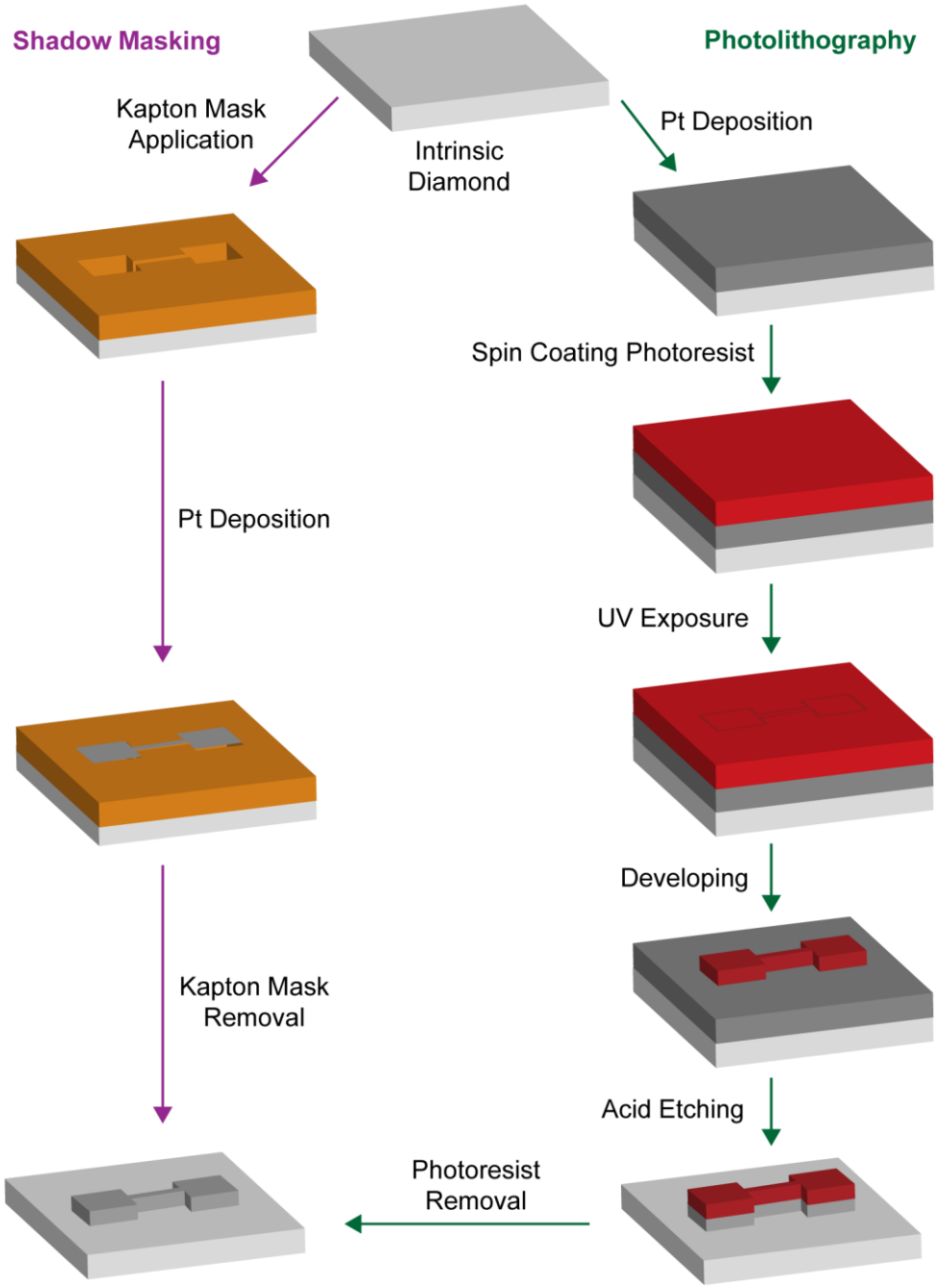

Figure 3.4. Schematic overview of the shadow masking and photolithography processes for custom RTD fabrication on diamond.

For shadow masking, the desired mask pattern was cut from a sheet of 127 µm thick Kapton film (500 HN; Du Pont de Nemours, Contern, Luxembourg) using laser micromachining (A-Series, Oxford Lasers, Didcot, UK) to create a negative image mask. This mask was placed over the insulating diamond substrate for evaporation

(e2000LL electron beam evaporator, Scientific Vacuum Systems, Wokingham, UK) of layers of Ti and then Pt (thicknesses 5 nm and 52 nm, respectively).

For photolithography, the desired mask pattern was obtained as a photomask (quartz substrate coated with chrome film) from the manufacturer (Compugraphics, Fife, UK). The insulating diamond substrate was baked on a hotplate for 3 min at 115 °C, before being primed with hexamethyldisilazane (Technic, Chalon-sur-Saône, France) for 1 min. Three drops of S1818 positive photoresist (Rohm & Haas Electronic Materials, Marlborough, USA) were spin coated (WS-650MZ-23NPP/UD2/US2B, Laurell Technologies, Philadelphia, USA) at 300 rpm for 5 s and then 4000 rpm for 20 s, followed by a bake for 3 min at 115 °C. The substrate was aligned underneath the chrome mask on a MA8 mask aligner (Süss Microtec, Garching, Germany) and exposed to 130 mJ cm^{-2} of ultraviolet light. After exposure, the substrate was developed using MF-319 developer (Rohm & Haas Electronic Materials, Marlborough, USA) for 35 s, rinsed with ultrapure water, and then dried with purified N_2. The exposed Pt was removed by etching in aqua regia (3:1 mixture of hydrochloric acid (Technic, Chalon-sur-Saône, France) and nitric acid (Technic, Chalon-sur-Saône, France)). The substrate was immersed in freshly prepared aqua regia which was heated to 80 °C for 20 min. Finally, the patterned photoresist layer was removed by dissolving in acetone (99.5%, Acros Organics, Geel, Belgium) while wiping with lint-free cloth, and then the substrate rinsed with ultrapure water and dried with purified N_2.

Deposited Pt RTD patterns were visualised by optical microscopy on a Leica Polylite microscope (Leica Microsystems, Milton Keynes, UK). Connections were tested with a 6½ digit multimeter (34401A, Agilent Technologies, Wokingham, UK).

3.3.4 Temperature sensor measurement

Operation of the commercial Pt RTD temperature sensor was achieved using a custom written LabVIEW script (v. 14, National Instruments, Austin, USA) and a cDAQ-9171 equipped with 9217 input module (National Instruments, Austin, USA). Connection from the RTD lead wires to the input module was made in a 3-wire configuration. In addition, a commercial Pt RTD temperature probe (HH376, Omega Engineering, Manchester, UK) was also employed, with accuracy ±0.12°C.

For the conductivity *vs.* temperature experiments, sensors were placed in a heated circulating bath with cooling coil (T100, Grant Instruments, Cambridge, UK) filled with tap water (University of Warwick, Coventry, UK). The temperature of the water was maintained (±0.05 °C stability, ±0.1 °C uniformity) for 10 min each at 30, 27, 24, 21, 18, and 15 °C.

3.3.5 Data handling and theoretical modelling

Data analysis and curve fitting was conducted using Excel (v. 2013, Microsoft Corporation, Washington, USA) and OriginPro (v. 9.1, OriginLab Corporation, Massachusetts, USA). To evaluate model fit (the variance in the dependent variable accounted for by the independent variables), R^2 (coefficient of determination) was used for linear fits, and adjusted R^2 was used for non-linear fits (five parameter logistic model).

Modelling of the theoretical sensor behaviour was completed using MATLAB (v. 2013b, MathWorks, Massachusetts, USA). Simulations were performed using the finite element modelling package COMSOL Multiphysics (v. 5.3a, COMSOL AB,

Stockholm, Sweden). Statistical analysis was performed using Past3 (v. 3.16, Oslo, Norway). Differences were considered statistically significant at a probability $p < 0.05$.

3.4 Results and discussion

3.4.1 Design and fabrication of a four-point planar all-diamond conductivity sensor

Previous work[5] has shown it possible to fabricate a conductivity sensor consisting of five pairs of two polarised co-planar electrodes, shown in **Figure 3.1a–b** and referred to as "Barcode" sensor. The dimensions of the electrode pairs that comprise this sensor (in terms of electrode width, length, and separation) are listed in **Table 3.1**. Since the response of the sensor is controlled by three domains (**Figure 3.2b**) we investigated the behaviour of these regions, in particular with a view to improve the performance capabilities by moving from a 2-point to a 4-point sensor.

Table 3.1. Dimensions of the five electrode pairs present on the Barcode device.

Electrode pair	Width / mm	Length / mm	Separation / mm
1	1.00	10.00	0.08
2	0.50	10.00	3.98
3	0.20	10.00	5.98
4	0.10	10.00	7.98
5	0.05	10.00	8.98

3.4.1.1 Determination of C_{dl}

Whilst C_{dl} should be essentially independent of applied AC frequency (ideally capacitive behaviour), in practice slight deviation can occur (known as capacitance dispersion); moreover, it is important to evaluate the magnitude of C_{dl} for this system for an analytical determination (**Section 3.2.3**).[6,23–25] Therefore, this parameter was determined at a range of frequencies using electrochemical impedance spectroscopy (**Figure 3.5**) in a solution of 0.1M KNO_3. The capacitance was calculated from the measured impedance of each individual electrode band through rearrangement of equation (3.1), and then normalised to the electrode area.

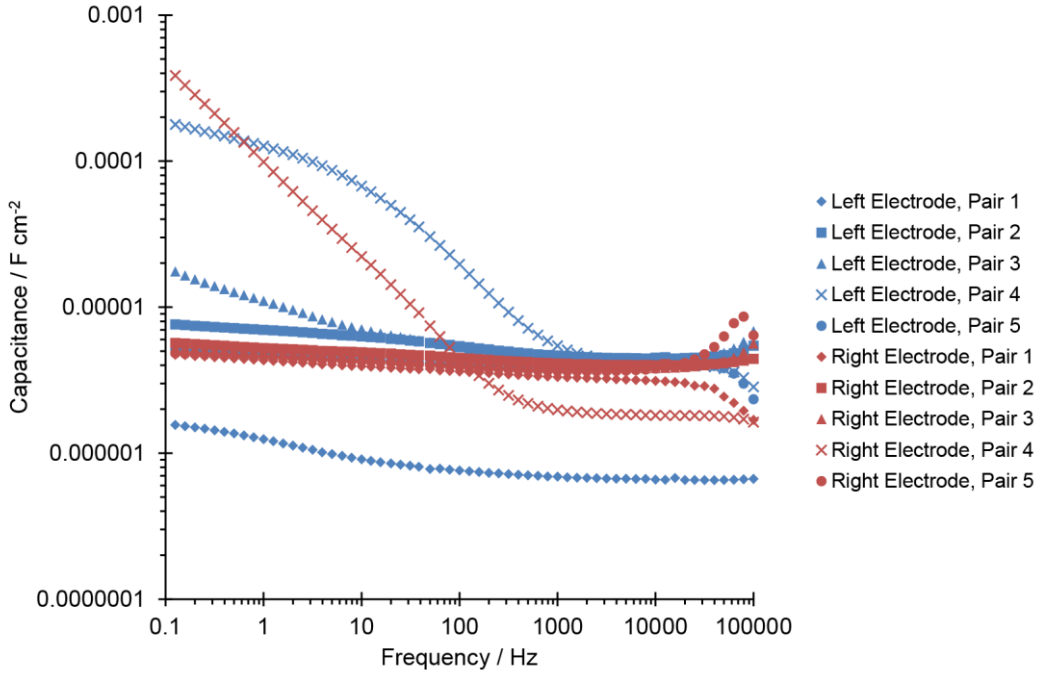

Figure 3.5. Capacitance of the double layer at each electrode of the Barcode sensor with varying applied frequency.

Most of the electrodes exhibit a constant capacitance, generally ranging from 1–8 µF cm^{-2} (range over all electrodes) between 0.1–100 kHz. Ideally capacitive behaviour has been observed previously on polycrystalline smooth electrodes,[25,26] such as those

in use here (the BDD electrodes have a surface roughness R_a < 1 nm)[4]. Deviation from purely capacitive behaviour (capacitance dispersion) was seen on both the left and right electrodes of pair 4 (red and blue cross) at lower frequencies (< 1000 Hz). This may be due to defects, *e.g.* scratches or pits, observed by optical microscopy in the surface of these electrodes, since capacitance dispersion depends strongly on the state of the surface and the presence of surface inhomogeneities increases this phenomenon.[25–27] Furthermore, the slight deviations of some electrodes at higher frequencies (> 30000 Hz) may be due to the finite rate of rearrangement of either the double layer or the adsorbed water layer.[27] Nonetheless, the overall frequency-independence of eight of the ten electrodes enables us to take a specific capacitance value for each electrode.

3.4.1.2 Testing the electronics

The sensor instruments (**Figure 3.6b**) consist of an AC conductance meter for 2-point operation and a differential voltmeter for 4-point operation (refer to Appendix A for more details). Having these separate instruments offers the advantage that both 2-point and 4-point conductivity measurements can be made simultaneously.

In order to ensure that the electronics in the sensor instruments work appropriately, a dummy cell was produced to replicate the conductivity sensor (**Figure 3.6a**). Known resistors were used to represent R_{sol}, whilst ceramic capacitors were used to represent C_{dl} and C_{ext}. The AC conductance meter was connected on the outside of the circuit to encompass all these elements, to record a 2-point conductivity measurement and simulate the current injection electrodes for the 4-point measurement. The differential voltmeter was connected inside the circuit such that it would only

measure R_{sol}, thus simulating the potential sensing electrodes and recording a 4-point measurement. As the value of R_{sol} was changed, the impedance measured by the sensor instruments was recorded (**Figure 3.6c–d**).

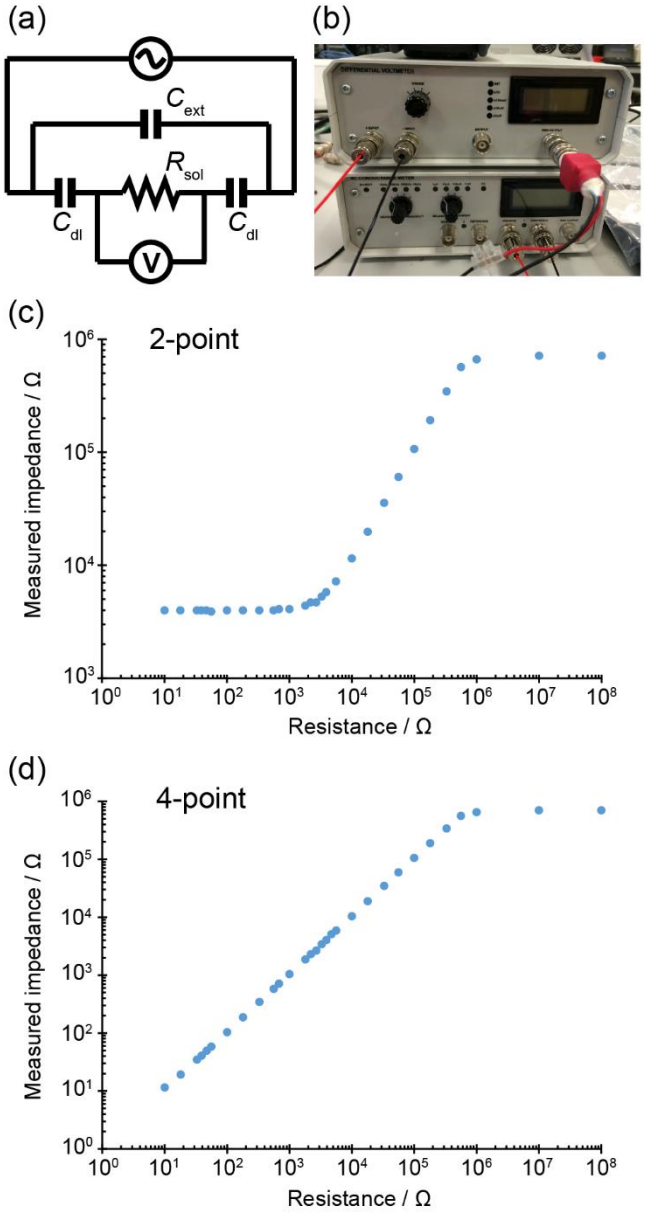

Figure 3.6. Characterisation of conductivity sensor electronics. (a) Equivalent circuit for the 2-point and 4-point measurements. (b) Photograph of the electronic instruments used to operate the sensor: AC conductance meter (bottom) and differential voltmeter (top). Impedance measured by the sensor electronics of the dummy circuit shown in (a), in both (c) 2-point and (d) 4-point configuration. Data points are measured using known resistors to represent varying solution resistance, R_{sol}. C_{dl} = 220 nF and C_{ext} = 47 pF.

In both cases, there is a plateau at the high resistance/low solution conductivity region. This is because the measured impedance is limited by Z_{ext} (the condition where $Z_{ext} < R_{sol} \leq Z_{dl}$), in particular the capacitance of the electronics, C_p, which can never be eliminated. The 2-point measurement also plateaus in the low resistance/high solution conductivity region. Here, the measurement is limited by Z_{dl} (the condition where $Z_{ext} > R_{sol} < Z_{dl}$) because this is included in the circuit in which the measurement is taken. An R_{sol} range of ~ 5×10^4 – 1×10^6 Ω is measurable. In contrast, the 4-point measurement does not plateau in this region, since it is not limited by Z_{dl} as only the voltage drop across the resistor is being measured, not any other part of the circuit. In this case a wider R_{sol} range can be accessed: 10^1 – 10^6 Ω. Translating this dummy circuit to the actual conductivity sensor, this experiment confirms that using the 4-point approach, the impedance of the potential sensing electrodes is not significant for the conductivity measurement.[28]

3.4.1.3 Solution calibration with Barcode sensor

Having assessed the performance of the sensor electronics and instrumentation, we now move forward to the evaluation of solution conductivity measurements using the Barcode all-diamond sensor. A calibration experiment was performed (**Figure 3.7**) using KCl solutions of known conductivity. Despite the Barcode sensor originally being designed solely for 2-point measurements, it does have the capability to operate in a 4-point configuration in particular with the electronics previously tested (**Section 3.4.1.2**). Therefore we investigated both 2-point and 4-point measurements. Electrode pair 4 was used as the current injection electrodes for the 2-point

measurement, and electrode pair 5 was used as the potential sensing electrodes for the 4-point measurement.[††]

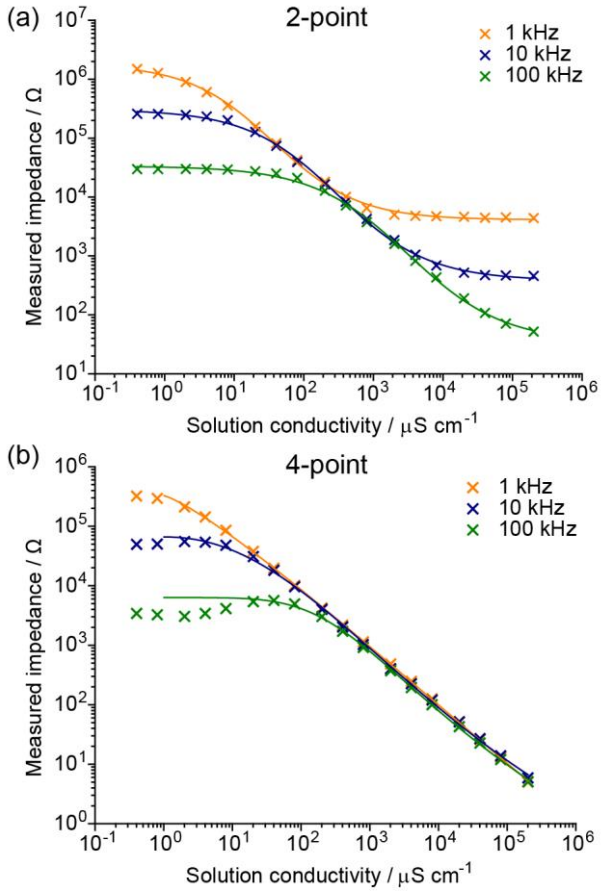

Figure 3.7. Barcode conductivity sensor calibration. (a) 2-point and (b) 4-point measured impedance of solutions of known conductivity, at applied AC frequencies of 1 (orange), 10 (blue) and 100 (green) kHz. Data points indicate experimental values, with fitted model.

For the 2-point measurement, at each AC frequency (f) tested the curves plateau at the lower and higher conductivities, due to C_{ext} and C_{dl}, respectively. These asymptotes occur at decade intervals as f increases ten-fold, as expected in equation (3.1). Using a combination of all AC frequencies, a linear relationship between Z_{meas} and κ is generally observed between ~ 10 – 100,000 μS cm^{-1}. Similarly, for the 4-point measurement a plateau is observed at the lower conductivities, with the lowest

[††] Refer to **Figure 3.1b** for electrode numbering and Table 3.1 for electrode dimensions.

measurable κ of 5 μS cm^{-1} at f = 1 kHz, but then the linear behaviour extends to the highest conductivity of 200,000 μS cm^{-1}. As discussed earlier, this is due to the potential sensing electrodes being uninfluenced by polarisation.[29,30]

In order to use the calibration to attain an unknown conductivity of a solution from the measured impedance, a model was fitted to the experimental curve obtained. Because of the sigmoidal response observed, the five parameter logistic equation was chosen:[31]

$$y = A_{\text{min}} + \frac{A_{\text{max}} - A_{\text{min}}}{\left(1 + \left(\frac{x}{x_0}\right)^h\right)^b} \tag{3.9}$$

A_{min} and A_{max} represent the positions of the lower and upper plateaus, respectively. The value x_0 is the x position of the inflection point of the curve. The parameters h and b work in conjunction with each other to control the rate of approach of the curve to the two asymptotes. As a general interpretation, h controls the slope of the curve, and b is a symmetry factor.

Rearrangement of equation (3.9) yields:

$$x = x_0 \times \left(\left(\frac{A_{\text{max}} - A_{\text{min}}}{y - A_{\text{min}}}\right)^{1/b} - 1\right)^{1/h} \tag{3.10}$$

which allows the conversion of the impedance measured by the sensor, y, to the conductivity of the solution, x. Fitted parameters for the Barcode conductivity sensor calibration curves (**Figure 3.7**) are listed in **Table 3.2**.

Table 3.2. Fitted parameters for the calibration curves of the Barcode conductivity sensor.

Parameter	A_{min}	A_{max}	x_0	h	b	**Adjusted R^2**
2-point calibration						
1 kHz	4109	1803225	37	−0.71	2.64	0.99869
10 kHz	383	305984	309	−0.67	2.90	0.99896
100 kHz	34	33514	3149	−0.63	2.99	0.99957
4-point calibration						
1 kHz	5×10^{-32}	322589	630695	−1.24	0.052	0.99983
10 kHz	0.002	65962	100512	−2.54	0.034	0.99931
100 kHz	1×10^{-27}	6310	555	−4.93	0.032	0.99047

Notice that for the 4-point model fit, the values of A_{min} are close to zero, due to the absence of a lower asymptote.

3.4.1.4 Theoretical sensor behaviour and evaluation of C_{cell}

Through equation (3.8), we can now predict the total measured impedance of a co-planar two electrode band conductivity cell, and hence the range of expected conductivity values. Therefore, we now investigate the theoretical sensor behaviour using the analytical expression in comparison with the experimentally obtained Z_{meas} *vs* κ values in **Figure 3.7**, as well as exploring the impact of C_{cell} on the region 1 of the sensor response curve (**Figure 3.2b**).

Using the series of equations (3.2)–(3.8), a MATLAB script[‡‡] was developed to output the theoretically determined impedance that would be measured by a conductivity cell given specific parameters. **Table 3.3** lists the parameter definitions applicable to the Barcode conductivity sensor.

Table 3.3. Sensor design parameters used for theoretical plots.

Sensor	**2-point**			**4-point**		
Width / mm	0.2			0.5		
Length / mm	10			10		
Separation / mm	5.60			3.08		
Frequency / kHz	1	10	100	1	10	100
Capacitance / μF cm^{-2}	4.17	4.06	6.23	3.71	2.95	2.24

Previous work has experimentally found a value of $C_{cell} = 5\times10^{-11}$ F.[5] However, this value can also be determined analytically through equation (3.2). Consequently, we decided to run the MATLAB model, using the parameter definitions given in **Table 3.3**, using either the fixed value of C_{cell} previously determined and defining it as a constant, or by allowing it to vary as MATLAB solves the relevant equations. **Figure 3.8** shows the theoretical sensor response curves under these two conditions for both the 2-point and 4-point configurations.

[‡‡] Refer to Appendix B for the code used in this script.

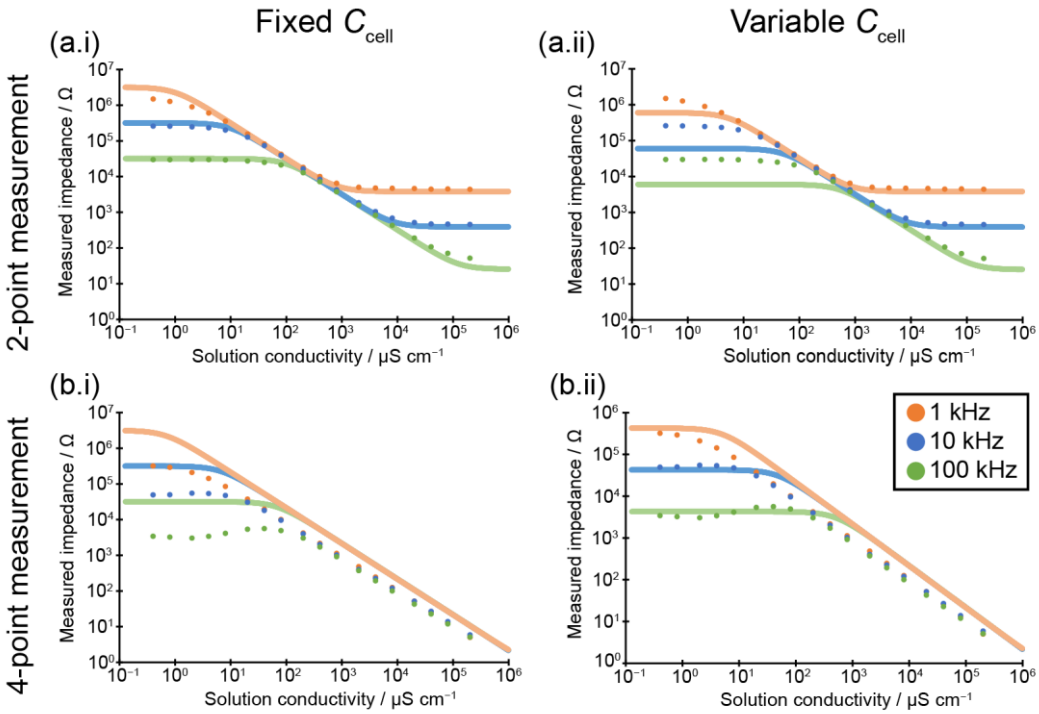

Figure 3.8. Experimental and theoretical response of all-diamond conductivity sensor to changing solution conductivity. Data points show experimental results, previously reported in **Figure 3.7**, from (a) 2-point and (b) 4-point measurements, at f = 1, 10 and 100 kHz. Theoretical response demonstrates the effect of changing cell capacitance, C_{cell}, in the model by (i) keeping it fixed, or (ii) allowing it to vary in the model equations.

Values of C_{dl} were taken from experimental data (**Figure 3.5**). To remove the effects of C_{dl} from the 4-point model, this value was defined as a very high value (1000 μF) so that the asymptote is shifted downwards. Calculated values of C_{cell} from the model were 2.7×10^{-10} F for 2-point and 3.7×10^{-10} F for 4-point configurations. For the 2-point configuration, the model fits the experimental results well when the value of C_{cell} is fixed (**Figure 3.8a.i**). Yet, when this value is allowed to vary, it is calculated to be almost an order of magnitude smaller, resulting in a lower theoretical Z_{meas} at the plateau (**Figure 3.8a.ii**). This could be due to fringing effects not being accounted for in the model, as the capacitance is not estimated to be high enough. For the 4-point configuration, the opposite result is observed: the variable C_{cell} value causes the model to fit the experimental results better than when it is kept fixed

(**Figure 3.8b**). This is not unexpected, because the value of C_{cell} = 5×10^{-11} F was determined only for the 2-point configuration.

Different C_{cell} values were measured using the AC conductance meter and differential voltmeter, since the current injection and potential sensing electrodes have different geometries. However, the C value that is measured is in fact C_{ext}:

$$C_{ext} = C_p + C_{cell} \tag{3.11}$$

C_{ext} is the in-air measurement (essentially infinitely high R_{sol}), C_{cell} is calculated with MATLAB, and C_p depends on the electronic equipment. In-air measurements on different electrode pairs with each electronics at each frequency allow the determination of C_p for each instrument (**Table 3.4**). Therefore the measured C does not match the theoretical C_{cell}, hence $C = C_{ext}$.

Table 3.4. Capacitance values of the conductivity cell. C_p is determined from the experimentally measured C_{ext} and the theoretically calculated C_{cell}.

Frequency / kHz	C_{ext} **/ F**	C_{cell} **/ F**	C_p **/ F**
Current injection electrodes (2-point)			
1	6.10×10^{-10}	2.70×10^{-10}	3.40×10^{-10}
10	6.14×10^{-10}	2.70×10^{-10}	3.44×10^{-10}
100	5.18×10^{-10}	2.70×10^{-10}	2.48×10^{-10}
Potential sensing electrodes (4-point)			
1	5.40×10^{-9}	3.70×10^{-10}	5.03×10^{-9}
10	2.44×10^{-9}	3.70×10^{-10}	2.07×10^{-9}
100	1.72×10^{-9}	3.70×10^{-10}	1.35×10^{-9}

Now, we have obtained greater understanding of the effect of C_{dl} and C_{ext} on the response of the conductivity cell, as well as demonstrated that the Barcode sensor and the electronics of the sensor instruments are capable of recording 2-point and 4-point measurements of solution conductivity.

3.4.1.5 Sensor design parameters

Seawater has relatively high conductivity (~5 S m^{-1})[1] therefore the conductivity sensor response needs to be linear in this region so that accurate measurements can be made (*i.e.* $Z_{meas} \propto R_{sol}$). We have observed that the Barcode sensor is only linear up to 2 S m^{-1} with a 2-point arrangement. To measure higher solution conductivities in 2-point mode, the cell geometry must be modified. This can be achieved by (a) increasing the electrode area or (b) decreasing the separation between electrodes; (c) increasing the frequency of applied AC; or (d) increasing C_{dl}, as demonstrated in **Figure 3.9** for six different 2-point sensor designs given in **Table 3.5**.

Table 3.5. Design parameters used for demonstrating the effect of varying the sensor design in **Figure 3.9**.

Sensor	**1**	**2**	**3**	**4**	**5**	**6**
Width / mm	0.1	0.5	0.1	0.1	0.1	0.1
Length / mm	5	5	10	5	5	5
Separation / mm	10	10	10	1	10	10
Frequency / kHz	10	10	10	10	100	10
Capacitance / µF cm^{-2}	3	3	3	3	3	10

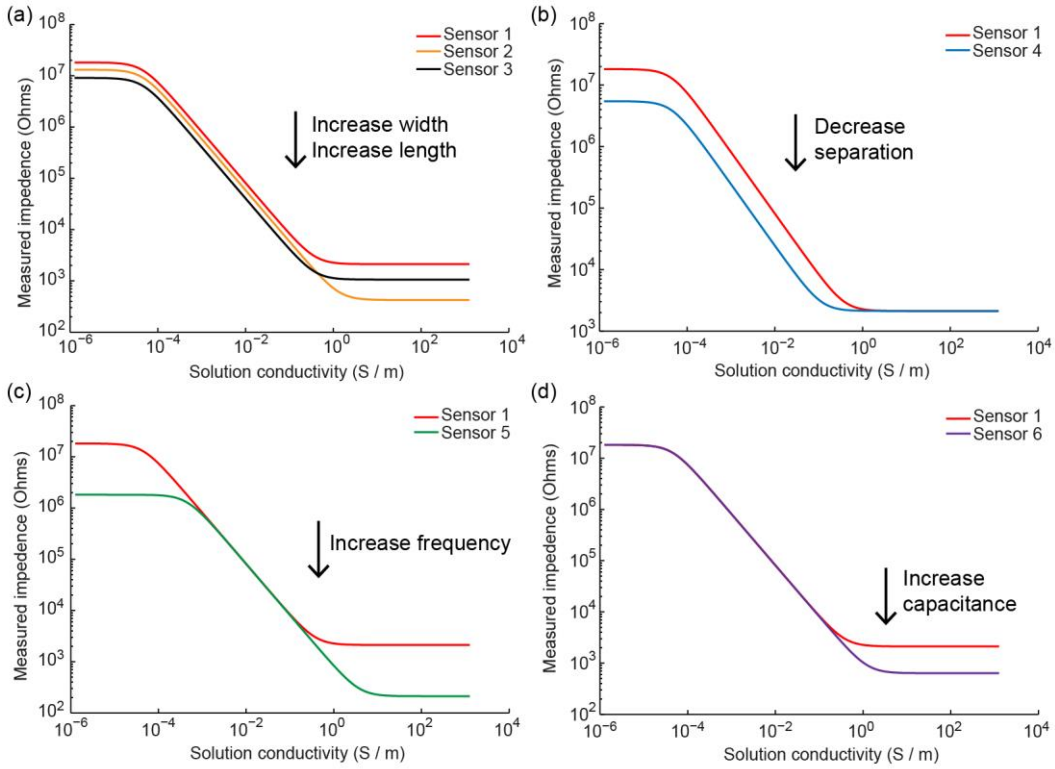

Figure 3.9. Theoretical models of the response of the all-diamond conductivity sensor showing the effect of changing the following design parameters: (a) electrode width and length, (b) separation between electrodes, (c) frequency of applied current, and (d) capacitance of the double layer at the electrodes.

Note that these design parameters are illustrative only. The aim was to shift the curve such that the response is linear at higher κ, namely by lowering Z_{meas} for a given κ. Increasing the electrode width and length, has an effect on both C_{cell} and C_{dl} which consequently effects Z_{meas}. Decreasing the electrode separation has a major effect only on C_{cell}. Increasing the applied AC frequency results in a proportional decrease to Z_{meas}, hence the curve shifts downwards. Finally, increasing C_{dl} has only an effect on the lower asymptote of the curve, since this domain is limited by Z_{dl}.

Applying these concepts to the design of the new sensor, various combinations of cell geometries were trialled in the MATLAB model to obtain an optimal geometry of 2-point electrodes which was linear at higher κ values. Subsequently, this design

was used to fabricate a new all-diamond conductivity sensor, henceforth called Seacon (**Figure 3.10**).

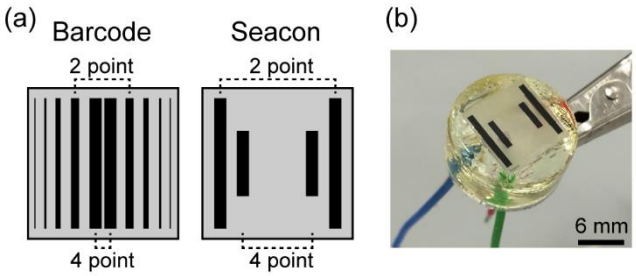

Figure 3.10. New all-diamond conductivity sensor design, Seacon. (a) Comparison of sensor design with Barcode sensor. (b) Photograph of Seacon sensor, encapsulated in epoxy resin and back contacted.

A comparison of the Seacon cell design *vs.* Barcode is shown in **Figure 3.10a**. Barcode sensor was originally designed to be linear across as wide a conductivity range as possible, operating in 2-point mode, hence its many electrode pairs of different widths and separations.[5] Though, the sensor can also operate in a 4-point configuration, as we have seen in the experimental comparison (**Section 3.4.1.3**), and the electrode pairs used for 2-point measurement and current injection, along with the potential sensing electrodes for 4-point measurement, are detailed in **Figure 3.10a**.

Since Seacon was focused at the higher conductivity range, it consists of only two electrode pairs. Furthermore, these electrodes pairs were optimised for a 4-point arrangement. The 2-point approach using the MATLAB model was used to define the geometry of the outer current injection electrodes. The inner potential sensing electrodes were designed to be half the length of the outer electrodes, so that the potential sensing electrodes would not encounter any electric field fringing effects[7,8] and thus would place a uniform potential distribution across the electrode.[29]

3.4.2 Performance of 4-point sensor design

The performance of the Seacon conductivity sensor was evaluated through a calibration experiment using KCl solutions of known conductivity (**Figure 3.11**). Solutions ranged from distilled water (0.055 µS cm^{-1}) up to 400,000 µS cm^{-1}, and the impedance of these solutions measured by the sensor in both 2-point and 4-point measurements simultaneously.

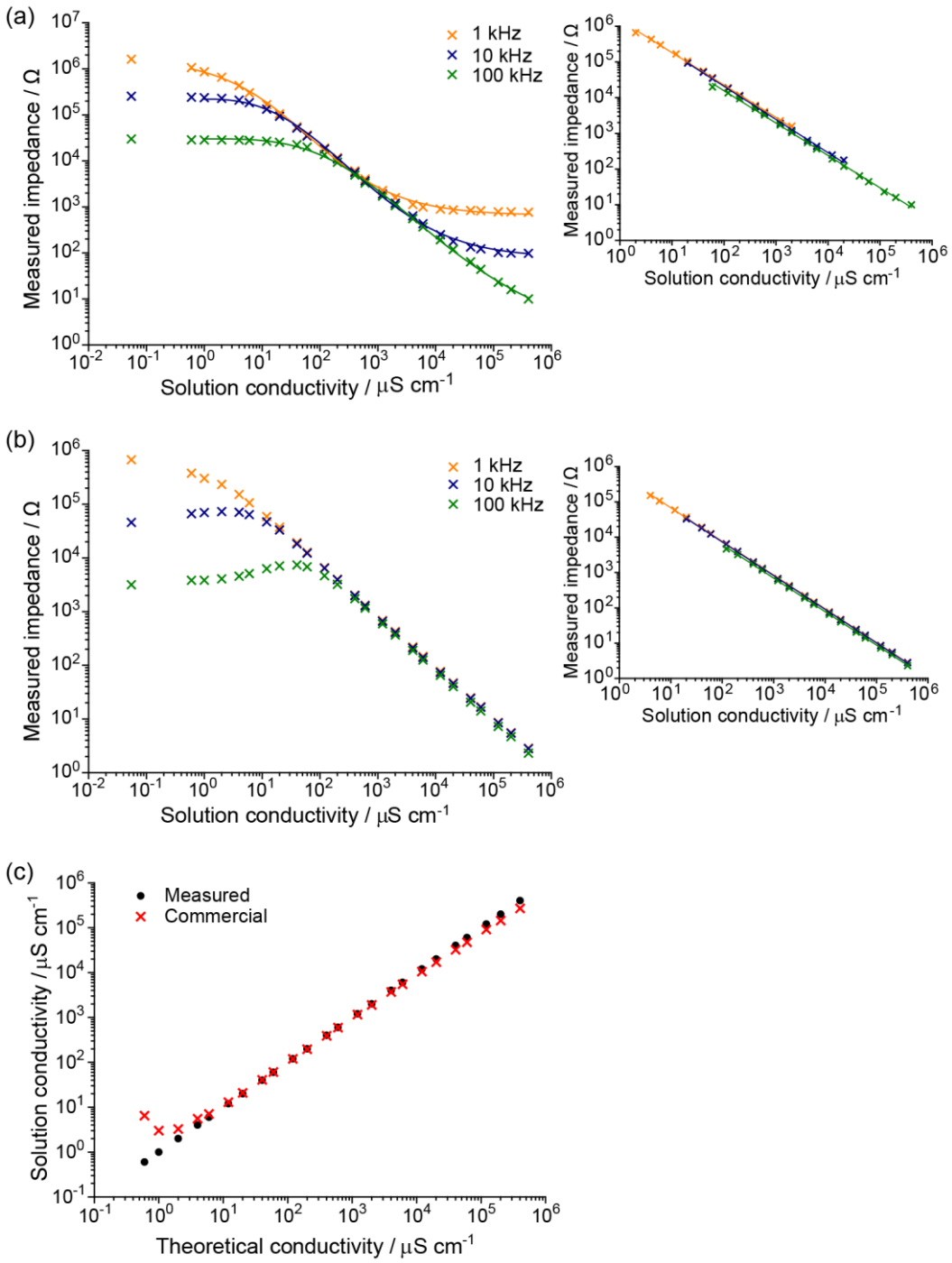

Figure 3.11. Seacon conductivity sensor calibration. (a) 2-point and (b) 4-point measured impedance of solutions of known conductivity, at applied AC frequencies of 1 (orange), 10 (blue) and 100 (green) kHz. Data points indicate experimental values, with fitted model. Inset shows the linear region of each calibration curve, including linear regression fitting. (c) Comparison of the measured solution conductivity by the Seacon sensor (●) and commercial sensor (×) against theoretical conductivity.

Similar to the Barcode sensor, we observe plateaus at either end of the conductivity range for the 2-point measurement, though at the critical ends (low κ, f = 1 kHz and high κ, f = 100 kHz) these have become less asymptotic. Fitted parameters for these calibration curves are listed in **Table 3.6**. Indeed, when we extract the linear portion of the calibration curve for all f values, we observe a wider working range than the Barcode sensor. For the Barcode sensor, the linear range was 10 – 100,000 µS cm^{-1} (**Figure 3.7**). A linear relationship between Z_{meas} and κ was observed for the Seacon sensor between 2 – 400,000 µS cm^{-1}. For the 4-point measurements, the working ranges for both sensors are similar: 5 – >200,000 µS cm^{-1} for Barcode and 4 – >400,000 µS cm^{-1} for Seacon. Equations for the linear fits are listed in **Table 3.7**.

Table 3.6. Fitted parameters for the 2-point calibration curves of the Seacon conductivity sensor.

Parameter	A_{min}	A_{max}	x_0	h	b	**Adjusted R^2**
1 kHz	650	1727945	64	−0.55	3.42	0.99857
10 kHz	83	220141	804	−2.57	11.8	0.99869
100 kHz	0.3	30092	18521	−3.36	0.96	0.99922

Table 3.7. Linear fit equations for the calibration curves of the Seacon conductivity sensor.

Frequency / kHz	**Linear fit equation**	R^2
2-point calibration		
1	$y = -0.908x + 10^{6.17}$	0.99852
10	$y = -0.930x + 10^{6.18}$	0.99879
100	$y = -0.906x + 10^{6.01}$	0.99846
4-point calibration		
1	$y = -0.954x + 10^{5.79}$	0.99989
10	$y = -0.954x + 10^{5.77}$	0.99987
100	$y = -0.948x + 10^{5.69}$	0.99975

To further the evaluation of Seacon sensor performance, the measured solution conductivities were compared with the commercial conductivity sensor (**Figure 3.11c**). Here, the experimentally measured Z_{sol} values were converted into κ values using the calibration curves (**Table 3.7**) and were plotted against the κ values theoretically calculated from KCl concentration. 2-point measurements were used, at f = 1 kHz for $\kappa < 10^2$ µS cm^{-1}, f = 10 kHz for $10^2 < \kappa < 10^4$ µS cm^{-1}, and f = 100 kHz for $\kappa > 10^4$ µS cm^{-1}. No significant difference was observed between the values measured by Seacon and the commercial sensor (paired t test, n = 24, p = 0.1). Overall, we have now demonstrated the efficacy of the Seacon conductivity sensor, and shown its ability to make accurate 2-point and 4-point simultaneous measurements of solution conductivity from 10^0 to >10^5 µS cm^{-1}.

3.4.3 Finite element method model of sensor

The conductivity of a solution is determined from the resistance through an electrolyte solution, which is measured by a conductivity sensor generating an electric field between electrodes.[32] For most sensors, where the electrodes are facing each other or are parallel to each other, the measurable volume of solution is that which is between the electrodes. However, for a planar arrangement of electrodes such as the Seacon conductivity sensor, the exact volume of solution probed by the sensor is most usefully determined by finite element method (FEM) modelling. Herein, we simulate two band electrodes in contact with a conducting block of aqueous solution. The structure of the 2-point Seacon conductivity sensor was defined in the appropriate geometry of the electrodes. A 2D plane through the centre of the sensor was considered in this model, where **Figure 3.12** shows the simulation domains. The block of solution and the intrinsic diamond are electrically isolated (boundary 3) and the two electrodes are connected as a current injection terminal and as ground, boundaries 1 and 2, respectively.

In order to develop an insight into the volumes of solution which the sensor is sensitive to, we add an occlusion (an air filled bubble) inside the block of solution in the model and then float it across the sensor in the *x* direction, in addition to a series of *z* positions. Consequently, there will be a drop in the apparent conductivity as a result of an increase in the measured impedance across the two electrodes due to the less conductive air bubble.

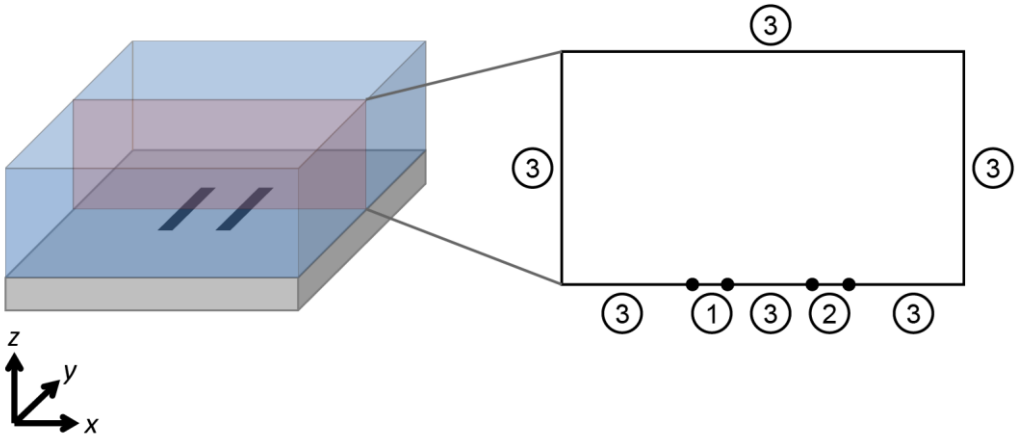

Figure 3.12. Schematic diagram of the 3D sensor system. A 2D section, shown in red, has been taken through the model, which is the face that has been simulated. The BDD band electrodes are shown in black, labelled as boundaries 1 and 2. The external surfaces that define the volume of solution shown in blue are labelled as boundary 3.

Typically ~50000 triangular mesh elements were used in the simulation with the greatest mesh resolution at the BDD-insulating diamond boundary where there are ~0.05 mesh elements per µm of electrode. Increasing the number of mesh elements was not found to considerably change the results obtained.

The model is solved using the Electric Currents interface and a Frequency Domain study step. This combination is useful for the modelling of AC problems when inductive effects are negligible.[33] Sufficient requirements for this are that the geometry is much smaller than the wavelength of the applied AC and that the skin depth (*i.e.* the depth from a conductor's surface that carries the majority of current density) is large compared to the size of the geometry. The skin depth, δ, is given by

$$\delta = \sqrt{\frac{2}{\omega\mu\kappa}} \tag{3.12}$$

where ω is the angular frequency, μ is the permeability, and κ is the conductivity.[34] This model uses nonmagnetic materials with a frequency of 100 kHz and a solution

conductivity of 1 S m^{-1}, giving a skin depth of approximately 1.6 m. The size of the geometry is 0.1 m, therefore the model used here is appropriate.

When induction is neglected, the electric field is curl free and can be expressed as the gradient of a scalar potential, *V*. The continuity equation for the conduction and displacement currents then becomes

$$-\nabla\cdot\left(\left(\kappa + j\omega\varepsilon_r\varepsilon_0\right)\nabla V\right) = 0 \tag{3.13}$$

where ε_0 is the permittivity of free space, and ε_r is the relative permittivity.[35,36] The electric field **E** and displacement field **D** are obtained from the gradient of *V*:[37]

$$\begin{aligned}\mathbf{E} &= -\nabla V\\ \mathbf{D} &= \varepsilon_0\varepsilon_r\mathbf{E}\end{aligned} \tag{3.14}$$

The set of boundary equations used in the model are given in **Table 3.8**. The condition for all edges is insulation, except at the two electrodes, where a current source of 1 mA is applied at the terminal electrode (boundary 1) with respect to ground potential (boundary 2).

Table 3.8. Set of equations governing current density into and out of the domain.

Boundary	**Description**	**Equation**
1	Terminal	$\int_{\partial\Omega}\mathbf{n}\cdot\mathbf{J}dS = I_0$
2	Ground	$V = 0$
3	Insulation	$\mathbf{n}\cdot\mathbf{J} = 0$

To simulate a bubble in the bulk solution, its position and extension are defined in the geometry and are described by coordinate dependent properties. Inside the bubble

centred at (x, z) with radius r the model assigns the properties of air, and outside of it the properties of the conducting solution. The results of the simulation are presented in **Figure 3.13**. Here, field lines indicate the electric potential distribution, whilst the surface plot is a logarithmic plot of the current distribution, 20log**J**, and the current density magnitude is represented by arrows.

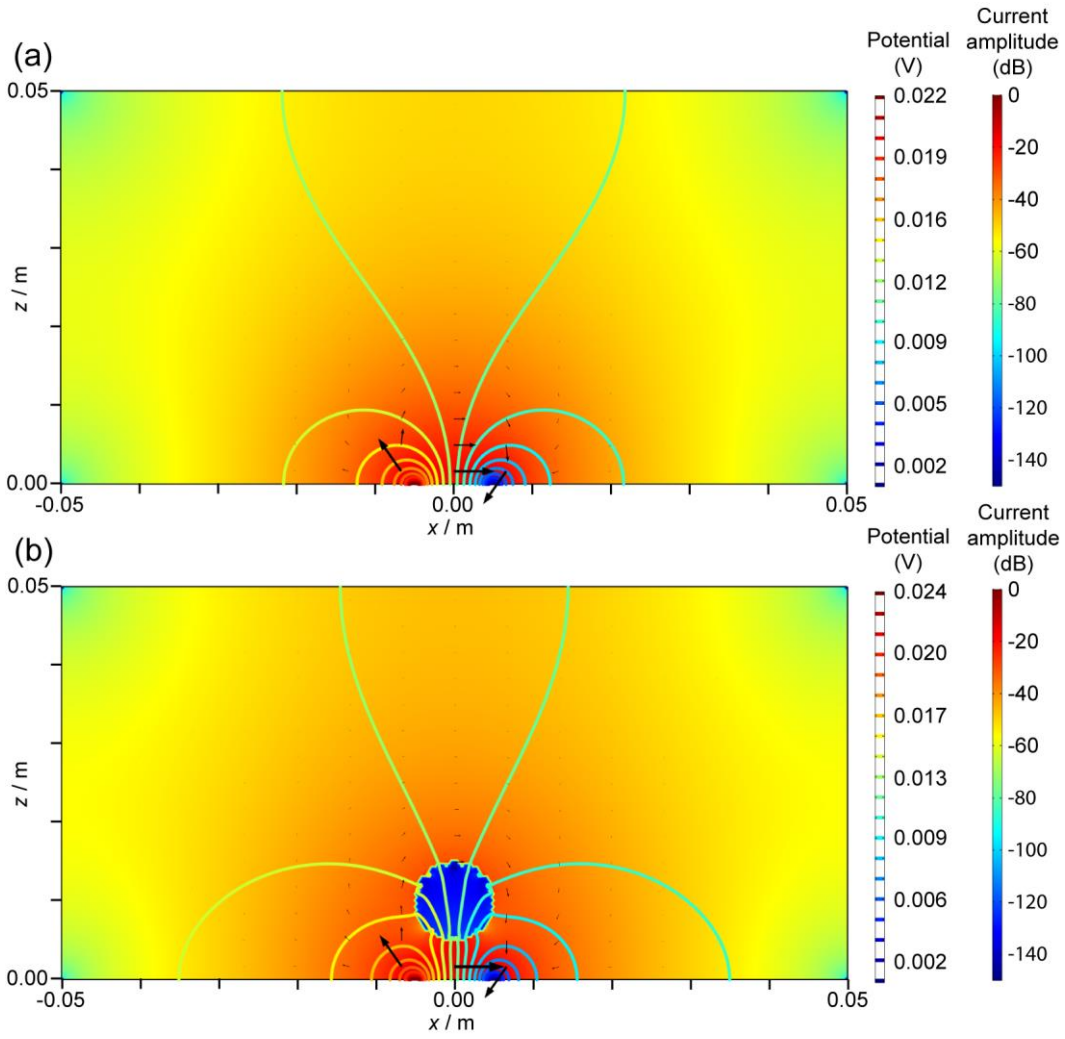

Figure 3.13. FEM simulation of the 2-point Seacon conductivity sensor, in the (a) absence and (b) presence of an air bubble. Two electrodes are exposed to bulk aqueous solution of 1 S m^{-1} with an applied AC of 0.001 A at f = 100 kHz. Field lines indicate the electric potential distribution. Arrows specify the current density magnitude, and the surface plot displays the amplitude of the current distribution (logarithmic). The air bubble in (b) has a radius of 0.005 m and is positioned at x = 0 m, z = 0.01 m.

The simulation is run in the absence of the air bubble (**Figure 3.13a**) where the conductivity sensor is exposed to bulk solution without any occlusion, and in the presence of an air bubble (**Figure 3.13b**) positioned centrally over the sensor at (x = 0 m, z = 0.01 m) with r = 0.005 m. Since a conductivity measurement is dependent on ion movement in a volume of solution between the electrodes, we would expect the sensor to be sensitive in proportion to the magnitude of the electric field. The relation between current density and electric field, $\mathbf{J} = \kappa\mathbf{E}$ allows us to express the field in terms of V.[38] As the simulation illustrates, in the presence of the air bubble the potential between the two electrodes increases by 2 mV than in its absence, representing an apparent change in solution conductivity as measured by the sensor because the resistance of the solution caused by the bubble is larger. This also gives rise to a slight change in the potential distribution between the two electrodes. Note that the current flowing through the bubble is approximately 100 dB lower in amplitude than the surrounding conductive aqueous solution.

Therefore, if either the position or dimension of the bubble are modified, this will cause changes in the solution resistance and consequently the electric potential between the electrodes and its distribution. Accordingly, this will change the measured impedance of the sensor. The analysis in **Figure 3.14** shows how the lateral and longitudinal position of the bubble, as well as the size of the bubble, affects the measured impedance. The simulation was run by performing a parametric sweep of x, from −0.1 m where the entire bubble is outside the solution domain, through the bulk solution in the x direction across the sensor, to +0.1 m, and then re-solving the simulation each time for different r or z values.

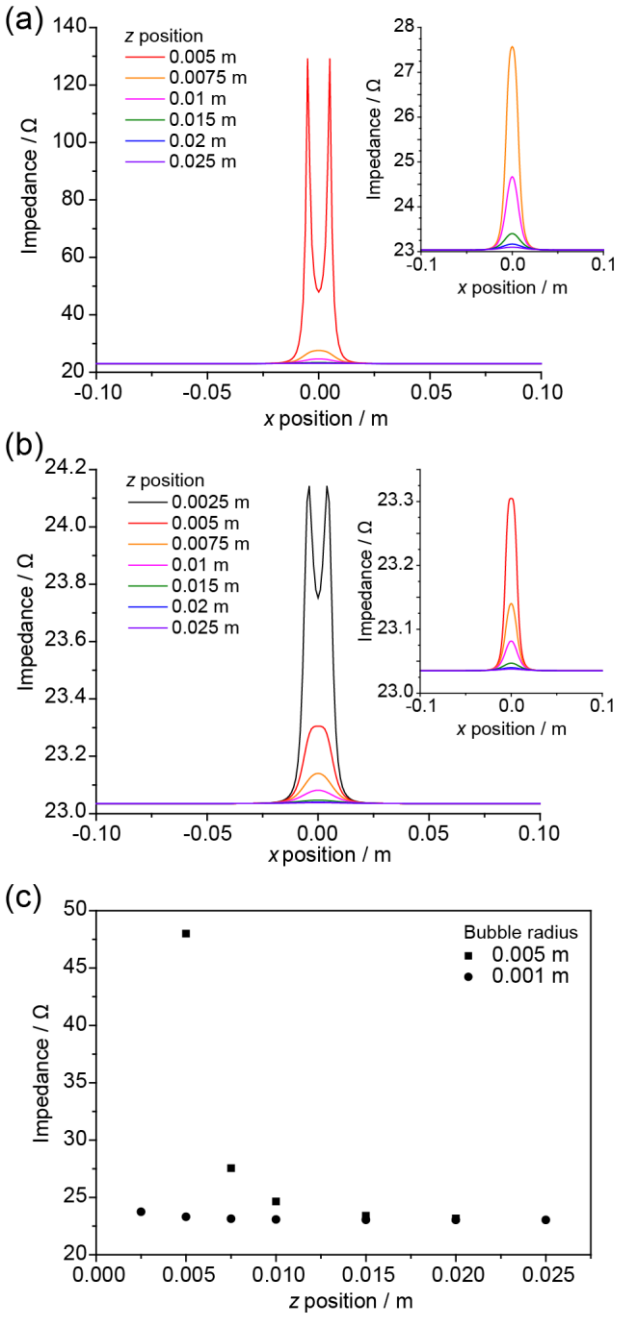

Figure 3.14. Analysis of FEM simulations of the 2-point Seacon conductivity sensor response to spatial variations of an air bubble. The impedance across the two electrodes of the FEM model in **Figure 3.13** is plotted as a function of the *x* coordinate of the centre of the air bubble, with radius of (a) 0.005 m and (b) 0.001 m. This simulation is then run at different *z* coordinates away from the sensor. (c) The peaks occur when the air bubble is directly over the sensor at $x = 0$.

Figure 3.14a–b demonstrates that the measured impedance of the sensor is a function of the *x* and *z* position of an air bubble with $r = 0.005$ and 0.001 m, respectively. Considering the *x* movement of the bubble, a peak appears when the air

bubble is placed centrally over the sensor, at $x = 0$. The inset plots show an enlarged part of the main graph. As the bubble moves into the region between the two electrodes, *i.e.* the measurable region, the impedance increases due to the presence of the non-conductive volume of air. However, this single peak occurs only when $z >$ 0.75 cm away from the sensor ($r = 0.005$ m) or $z > 0.5$ cm away ($r = 0.001$ m). When the bubble is closer than this, the peak splits into two and the maxima occurs when the bubble is directly above either electrode. For reference, the electrodes are 1 mm wide and their midpoints are at $x = \pm 0.005$ m.

When considering the z movement of the bubble (**Figure 3.14c**) at a fixed x position ($x = 0$), the measured impedance is highest when the bubble is closest to the sensor, then drops off as the bubble moves away from the sensor. The impedance reaches an asymptotic value of 23.035 Ω, and generally reaches this when $z > 0.02$ m, regardless of bubble radius.

For variations in both x and z position, the effect of bubble radius is considerable. The rate of change of the impedance increases much more rapidly as $z \rightarrow 0$ when $r =$ 0.005 m than 0.001 m. Moreover, the magnitude of the impedance is larger when r is larger, simply because the volume of non-conductive air is larger.

Therefore, the FEM simulation illustrates that occlusions close to the sensor (< ~2 cm), where the electric field strength is greatest, have a much larger effect on the electric potential than occlusions further away. By modelling in this way, we observe that the effective sensing region of the Seacon conductivity sensor is approximately 2 cm into bulk solution (in the z direction, normal to the electrode plane). Considering practical implications for a working device, this suggests that the sensor must be

placed at least 2 cm away from an external body to avoid impinging the electric field and hence substantially affecting the conductivity reading.

3.4.4 Incorporation of temperature measurements

The conductivity of a solution is strongly temperature dependent. Indeed, conductivity will increase with temperature due to the higher mobility of the ions present.[1] As a result, in most cases conductivity sensors will report a temperature corrected conductivity value, typically corrected to the value it would have been at a certain reference temperature, *e.g.* 25 °C.[18] The alternative is to report the conductivity measured at the sample temperature. Both of these methods require measurement of the temperature of the sample simultaneous to the conductivity measurement.

Two methods of integrating temperature sensing with the diamond conductivity sensor platform were investigated. Firstly, a commercially available Pt RTD was adhered to the rear face of the diamond substrate using Ag epoxy. However, this approach yields three interfaces between the RTD film and diamond substrate (**Figure 3.15a**), with materials that are less thermally conductive (**Table 3.9**). This may potentially lead to heat conduction losses through decreased heat flux and therefore time response errors, as well as inaccuracy through self-heating.[39] Consequently, the second method investigated was deposition of a Pt RTD film directly onto the rear face of the diamond substrate. This approach offers the advantage of only the one interface between RTD and diamond (**Figure 3.15a**).

Table 3.9. Thermal conductivities of the materials used in the RTD fabrication.[9]

Material	**Thermal conductivity / W m^{-1} K^{-1}**
Ag epoxy	1.6
Alumina	38
Diamond	1000
Epoxy resin	0.2

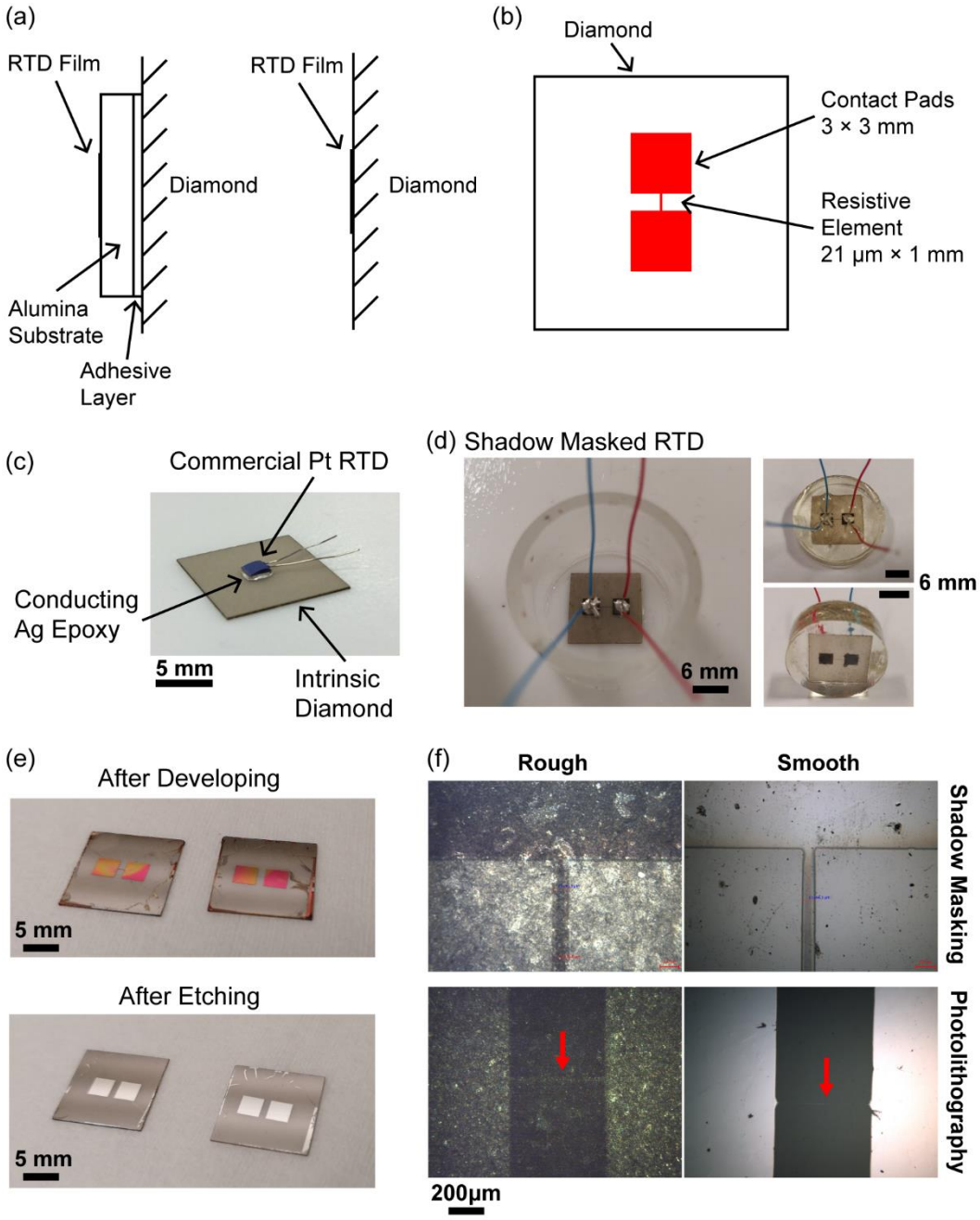

Figure 3.15. Integrated RTD design and fabrication for temperature sensing. (a) Two methods were investigated: (left) a commercial Pt RTD adhered to the diamond, and (right) depositing a Pt RTD film directly on the diamond surface. (b) Design of the deposited Pt RTD, highlighted in red. (c) Photograph of the commercial Pt RTD bonded to the surface of the intrinsic diamond substrate using Ag epoxy. (d) Photographs of the deposited Pt RTD by shadow masking, before (left) and after (right) encapsulating in epoxy resin. (e) Photographs of the process development for a deposited Pt RTD by photolithography. (top) After UV exposure developing, the masked photoresist layer is visible on top of the deposited Pt layer. (bottom) After acid etching, the contact pads remain but the resistive element has been removed. (f) Optical microscopy images of the designed Pt RTD deposited on the rough (lapped) and smooth (polished) sides of the diamond substrate, by shadow masking and by photolithography. Red arrows indicate the position of Pt in the resistive element.

Considering the first method using a commercial Pt RTD, a Pt100 RTD sensor (F2020-A) was adhered to the rear (lapped) face of an intrinsic diamond substrate (**Figure 3.15c**), before being encapsulated in epoxy resin with the front face exposed to solution. The RTD was operated using a cDAQ-9171 equipped with 9217 input module, which excites the Pt100 sensor with 1 mA constant current, and converts the measured resistance to a temperature through an internal calibration. Given this set-up, the total uncertainty is ±0.4 °C due to both the Pt100 RTD and DAQ device, with a specified response time of 0.2 ms.

For the deposited Pt RTD, a design was first created suitable for both shadow masking and photolithography processes. An RTD consists of a resistive element connected by two contact pads; the simplest design of the resistive element is a single rectilinear track, such that its resistance is 100 Ω at 0 °C (this is not mandatory but allows comparison with the commercial Pt100 RTD). Assuming a Pt resistivity, $\rho = 1.05\times10^{-7}$ Ω m,[9] the resistance of the resistive element is determined by the width (w), length (l), and thickness (d) of the track:[38]

$$R = \frac{\rho l}{wd} \tag{3.15}$$

Hence we can determine dimensions of the resistive element that will produce a target resistance by varying each of these three parameters (**Table 3.10**).

Table 3.10. Example dimensions of the resistive element that output a resistance of 100 Ω at 0 °C.

***l* / mm**	1	0.1	0.2	0.5	1	1
***w* / µm**	10	10	20	10	20	21
***d* / nm**	105	10.5	10.5	52.5	52.5	50

However, to obtain the most optimal design parameters of the resistive track, we considered which dimension offers better resolution and uniformity: either the machining/masking step (*xy* dimension) or the deposition step (*z* dimension). When considering the track thickness, the error in the deposition step is generally ±1 nm which results in a difference in the resistance of 2%. For the *xy* dimension, machining the shadow mask has an error of ±6 μm whereas the photomask offers an error of ±1 μm, resulting in resistance differences of 22% and 5%, respectively. Therefore variation in *w* and *l* have a larger effect than *d*, so maximising the former and minimising the latter will offer greater control; the final design for the deposited Pt pattern is shown in **Figure 3.15b**. For comparison, the width of the resistive track in the commercial Pt100 RTD sensor was determined to be 18 ± 2 μm. Note that the theoretically calculated resistance of the contact pads is 2.1 Ω, ensuring that the resistive element is indeed the most resistive part of the circuit.

Using this design, a shadow masked RTD was fabricated (**Figure 3.15d**) by Pt deposition through a Kapton film mask (negative image mask). Two wires were bonded to each contact pad to allow a 4-wire connection, and then the whole set-up was encapsulated in epoxy resin. However, when this device was tested there was no electrical connection (>10 MΩ resistance) found between the red and blue wires. Microscopy investigation (**Figure 3.15f**) revealed that there was a visible continuous Pt track present, and it appeared that connection between wire, Ag epoxy, and Pt contact pad was acceptable. Despite this, some component of the circuit was supplying a very high resistance causing the device to fail. Interestingly, observation of the Pt layer (**Figure 3.15d**) reveals the Pt to be a dull dark colour, instead of the shiny silver colour as expected; the reason for this may also be the cause which is contributing to the device failure.

For the photolithography procedure, standard techniques were used and summarised in **Figure 3.4**. Because the intrinsic diamond surface is hydrophilic, the primer HMDS was used as an adhesion promoting agent. This ensures that the photoresist forms a continuous film and that water does not interfere with subsequent stages of the process.[40] S1818 positive photoresist was spin coated onto the primed diamond substrate, and formed a visually homogeneous film. After UV exposure, the substrate was dipped in developer solution to solubilise the exposed resist, leaving the desired pattern of photoresist remaining (**Figure 3.15e**). Aqua regia was then used to etch away the unprotected Pt, heated to attain faster etch rates. At 80 °C, it took 15 min for the transparent diamond substrate to be revealed indicating the removal of the Ti/Pt layer, giving an etch rate of about 3.5 nm min^{-1} in accordance with previous observations.[41] However, whilst the contact pads were present after acid etching and photoresist removal, the critical resistive element was etched away (**Figure 3.15e**). Optical microscopy (**Figure 3.15f**) revealed that virtually no Pt remained in the resistive element. The most likely causes for this are either: (1) the photoresist layer was too thin due to being spin coated too rapidly, or (2) the substrate was over-developed, leading to some removal of unexposed photoresist, or (3) under etching where the acid etches Pt underneath the photoresist. Nevertheless, we believe that given further testing and process optimisation, the photolithography procedure has the potential to create working Pt RTDs that are deposited directly onto the diamond sensor surface.

We opted to move the study forward using the commercial Pt RTD sensor, assessing the performance of this diamond based temperature sensor simultaneously with the Seacon conductivity sensor. Given the strong temperature dependence of solution

conductivity, both sensors were tested in a calibration experiment (**Figure 3.16**) where only the temperature of the solution was altered.

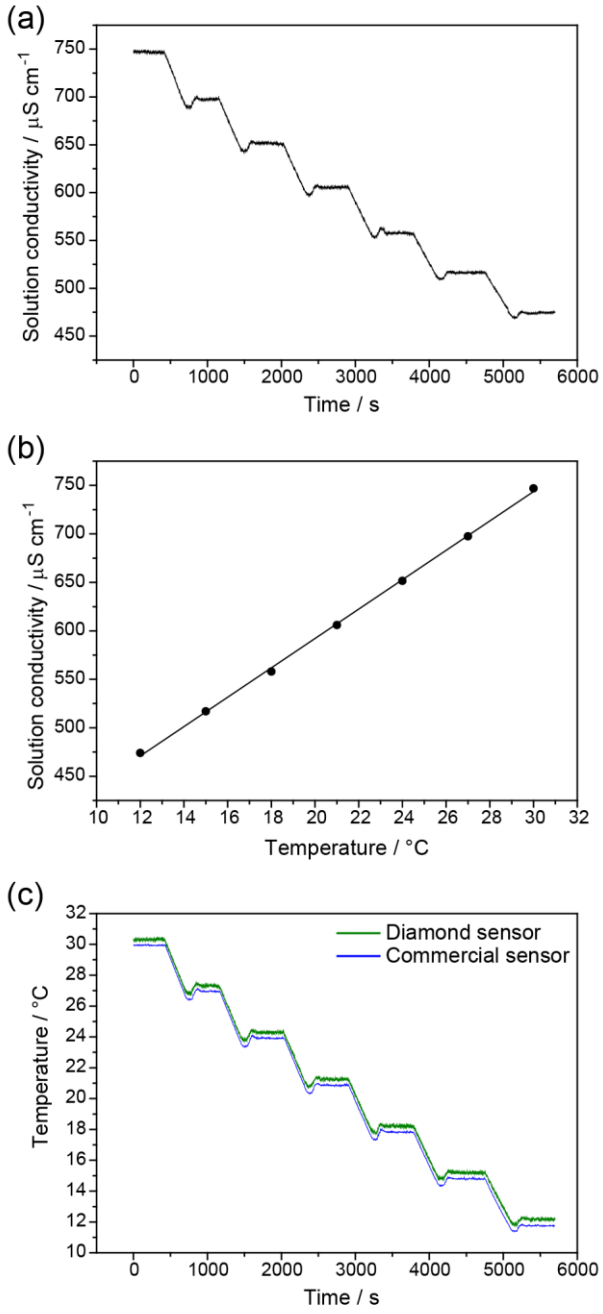

Figure 3.16. Conductivity *vs.* temperature experiment, measured in tap water in a temperature controlled water bath over a range of temperatures. (a) Conductivity measurements from the all-diamond sensor over time as the solution temperature is ramped downwards. (b) Plot of conductivity against temperature. (c) Temperature measurements from the diamond based sensor (—) and commercial sensor (—).

All sensors were measuring simultaneously in a temperature controlled (±0.15 °C) water bath. Both diamond sensors were measuring at a rate of 10 Hz, with the commercial temperature probe measuring at 1 Hz. Sample temperature was ramped downwards from 30–12 °C in intervals of 3 °C. Through monitoring the change in conductivity over time (**Figure 3.16a**), a calibration plot can be acquired (**Figure 3.16b**). A gradient of 15.2 ± 0.2 μS cm^{-1} $°C^{-1}$ was obtained.

The temperature coefficient of conductivity is given by equation (3.16):[17,18]

$$\alpha = \frac{1}{\kappa_{25}}\left(\frac{\kappa_\theta - \kappa_{25}}{\theta - 25}\right) \tag{3.16}$$

where 25 and θ °C are the temperatures at which the conductivities κ_{25} and κ_θ were measured, respectively. Temperature coefficients determined for the all-diamond conductivity sensor were 0.0230 ± 0.0006 $°C^{-1}$. This is equivalent to a change in conductivity of 2.3% $°C^{-1}$ in accordance with previous studies and generally accepted values of α = 2.0–2.2% $°C^{-1}$ for aqueous salt solutions.[42,43]

When comparing the two temperature sensors, the diamond based Pt100 sensor gave the same response as the commercial probe (**Figure 3.16c**), including detecting the overshoot in temperature change as a result of the water bath PID controller. Once the water temperature had stabilised, the mean difference in measured temperature by the diamond based sensor was +0.3 °C compared to the commercial probe.

3.4.5 Data acquisition and development of LabVIEW software

A LabVIEW VI consists of two parts: (1) a front panel, which provides a graphical user interface, and (2) a block diagram, where the code is programmed and executed.

The front panel consists of controls that allow the operator to input user-chosen properties or parameters that may be required by the software. The block diagram shows the flow of data and is generally read from left to right. Each icon represents code that executes a task, and data flows along the wires that connect the icons together.

In order to begin building a VI, we first considered the sequence of programming that was required. Firstly, we need to define the magnitude and frequency of the applied AC, as there are four options for both of these parameters in the AC conductance meter, as well as the voltage range measured by the differential voltmeter. In addition, the user must have the ability to start and stop the measurement, and specify the location of the resulting data file to be saved on the PC. Upon starting the measurement, the VI needs to instruct the instruments which settings to apply, and then begin acquiring and storing the voltage measurements from the instruments. Finally, when the user stops the measurement, the VI must stop taking readings and output the stored measurements into a data file.

Given that we can describe the programming steps using a flowchart, we opted to use a state machine design pattern. A state machine is a common program design architecture based on a state, an event, and an action.[44] It usually consists of a start-up and shut down state, along with other states, and the advantage of such a design pattern is that a different state may be called at different times (*i.e.* the states do not have to execute sequentially). In LabVIEW, a state machine is programmed using a case structure inside a while loop.[44] The case structure contains the functionality code which performs the main action of the state, and allows different code to be executed based on what is selected by its input terminal; note that only one case can execute at a time. The while loop provides the ability to continuously execute until a

given condition is met.[45] Therefore, each case in the case structure represents a state, and variations in which state is executed can be achieved until the while loop is stopped.

Screenshots of version 1 of the VI are shown in **Figure 3.17** and **Figure 3.18**. We have defined five states that the program can be in:

1. Idle. The user can select and input the required parameters. Measurement has not started.
2. Start. Initial safe conditions are output to the sensor instruments.
3. Check Panel. The user desired settings are output to the sensor instruments.
4. Acquire. Data is acquired from the sensor, stored in an array, and saved to a file.
5. Stop. The sensor instruments are returned to default safe conditions.

Figure 3.17 shows the front panel and the Acquire state of the block diagram, which is the key state that the VI will remain in during measurement acquisition. The block diagram for the four other states are shown in **Figure 3.18**.

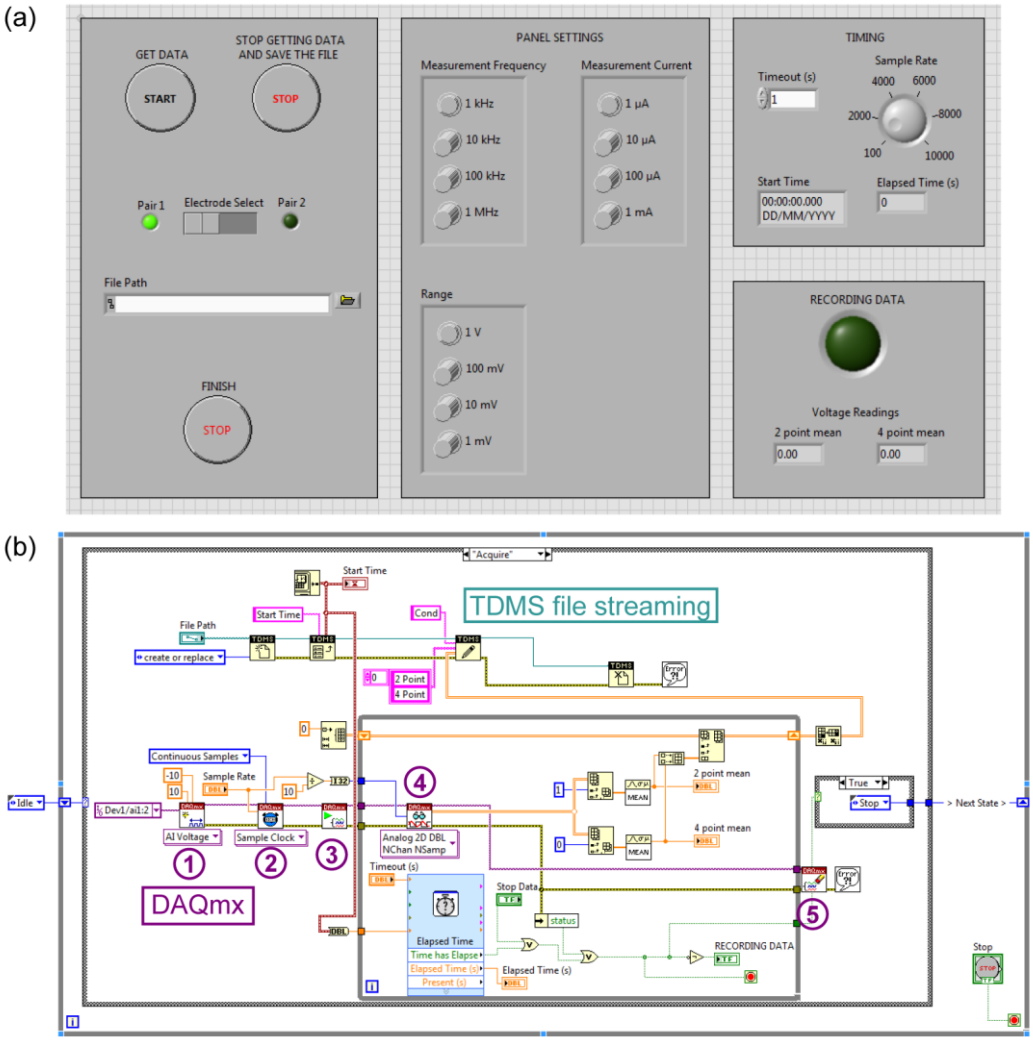

Figure 3.17. Screenshot of LabVIEW VI (version 1) to operate the conductivity sensor. (a) Front panel and (b) part of the block diagram of the VI showing the 'Acquire' case of the state machine, where the data acquisition, data handling, and file streaming occurs.

An advantage of the state machine architecture, in combination with the DAQ device, is that it allows for fast, continuous data acquisition. This is completed through a series of nodes called DAQmx, highlighted in purple in **Figure 3.17b** and described below:

1. Create Task – assigns the task to a physical channel. The DAQ device contains analogue input (AI) channels, where the measured voltage output from the sensor instruments is read from.

2. Configure Task – configures the timing of the task for reading samples. Samples of the analogue input are read by the DAQ device, and each sample represents one ADC conversion.
3. Start Task – starts the task.
4. Acquire (Read) – acquires data from the DAQ device. Data samples fill the FIFO buffer of the DAQ device, and are brought into the VI continuously until stopped.
5. Clear Task – stops the task.
6. Check for Errors – checks for and handles any errors that have occurred.

Once the VI enters the Acquire state, data from the sensor instruments begins to be acquired. The DAQmx Sample Clock node (node 2) controls the number of, and rate at which, samples acquired and put on the FIFO buffer (**Figure 3.3**). The DAQmx Read node (node 4) determines the transfer of data from the buffer into the software. This is done *via* USB bulk data transfer mechanism, and it is recommended that the number of samples is 0.1× less than the rate specified in DAQmx Sample Clock (the sample rate), which ensures that there are no PC buffer over- or under-write errors. The speed at which samples are transferred from the FIFO buffer to PC is independent of the execution speed of theVI, meaning that this is not the rate limiting step, ensuring that the FIFO buffer is not overrun.

Because we want to acquire continuous measurements, the DAQmx Read node is placed within a while loop. The DAQmx Sample Clock node is set to acquire continuous samples from the sensor instruments, but on execution the DAQmx Read node reads only a finite number of samples from the DAQ device buffer. Therefore, the while loop will repeat execution until stopped (by the user). Indeed, any code in this while loop will execute each time data samples are read, so here we begin data

handling. Outside the while loop, an array is initialised; each time the while loop executes, the voltage readings obtained are appended to the array.

We have used a NI USB-6002 DAQ device in our set-up, which is a 16-bit device with an input range of ±10 V. This means that the resolution of the ADC, *i.e.* the lowest amplitude signal change that the device can detect is 10 V ÷ 2^{16} = 0.15 mV. For input tasks, the device has a FIFO of 2047 samples. An input task with 2 channels (as used here) will acquire data at a maximum rate of 1024 samples per channel per second. The sample rate specifies how often the ADC converts data; this device has an aggregate rate of 50000 samples per second, so the sample rate is shared across all channels.

When the user decides to stop the measurement, after the final execution of the while loop, the array containing the voltage readings is streamed to a file on disk, highlighted in teal (**Figure 3.17b**). We opted to use save files using the TDMS file format, since it is optimised for saving large amounts of time series measurement data to disk. Also, it is capable of high speed streaming disk, and has an inherent hierachal structure meaning that channel data is automatically separated in the file. Other properties can also be included in the file, for example here the start time of the measurement is wrote to the file.

Alternate cases (states) of the state machine are shown in **Figure 3.18**. The Idle state contains a case structure which only advances to the next state, Start, when the start button is pressed.

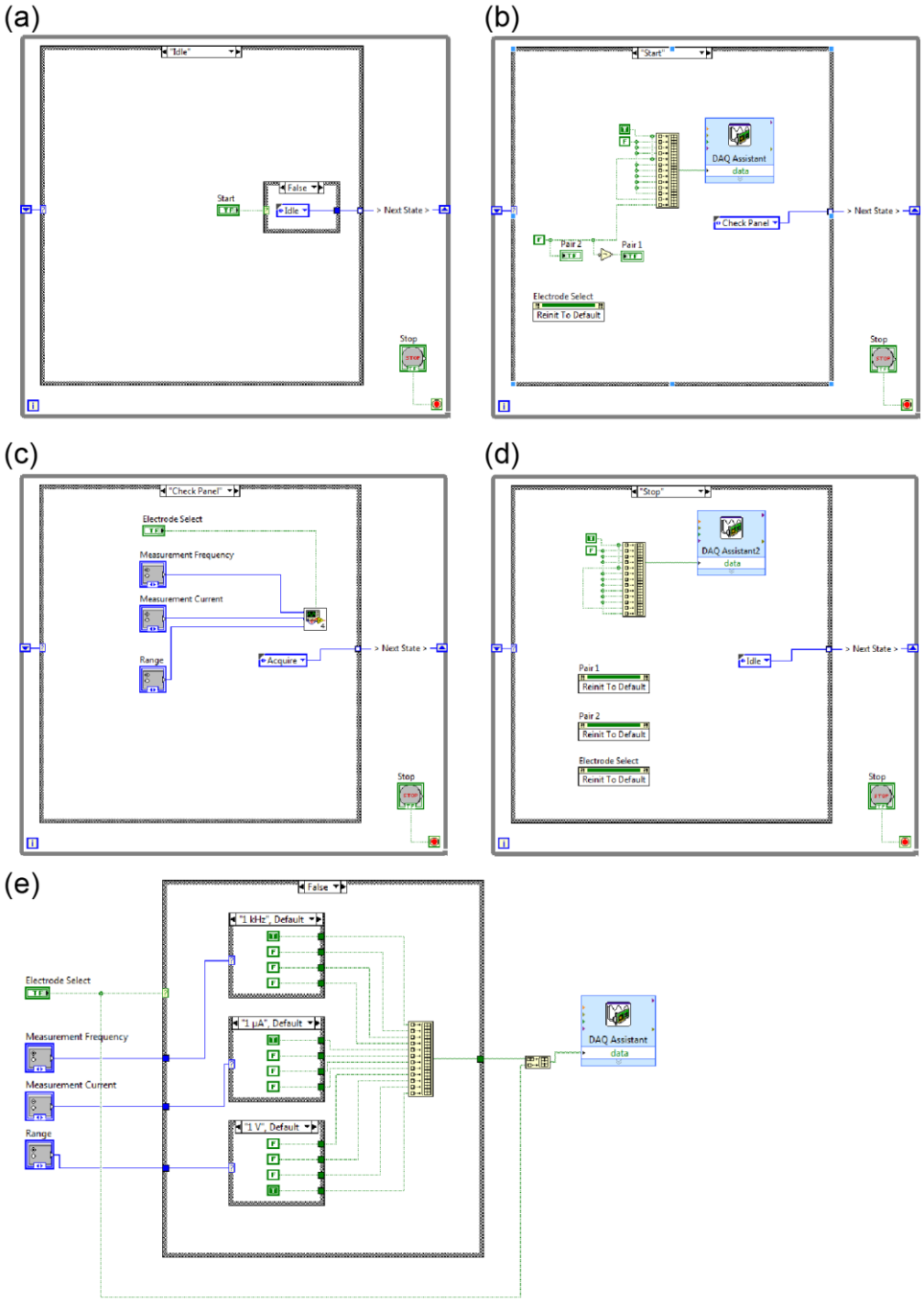

Figure 3.18. Screenshot of LabVIEW VI (version 1) to operate the conductivity sensor. (a–d) Alternate cases of the state machine, where initialisation of the instrument occurs before data acquisition, and where the instrument resets afterwards. (e) Block diagram of the sub-VI in (c) where the user desired parameters are output to the instrument.

The DAQ Assistant in the Start and Stop states, and in the sub-VI of the Check Panel state, is a high level function which is used to output digital signals to the DAQ device and sensor instruments. Essentially this is the same as the low level functions used in the Acquire state to read the analogue input, though the low level functions offer far more control over the process.

Each of the three settings for the sensor instruments—measurement AC frequency, measurement AC current, and range—has four independent options, which are wired into physical digital out channels on the DAQ device. This list of channels is defined in the DAQ Assistant. Therefore, if the user selects a measurement frequency of 1 kHz, a value of true is output to channel 1 and a value of false is output to channels 2−4, causing the setting of 1 kHz to be applied in the sensor instrument.

Currently the VI reads and saves to file only the raw voltage measurements from the sensor instruments. Version 2 of the VI (**Figure 3.19**) takes advantage of the DAQmx Read while loop in the Acquire state in order to display real-time conductivity readings to the user. Major changes regarding the development of the VI take place predominantly in the Acquire state, so from this point only the block diagram of this state along with the VI front panel will be shown in this chapter. Alternate cases of case structures can be found in Appendix C.

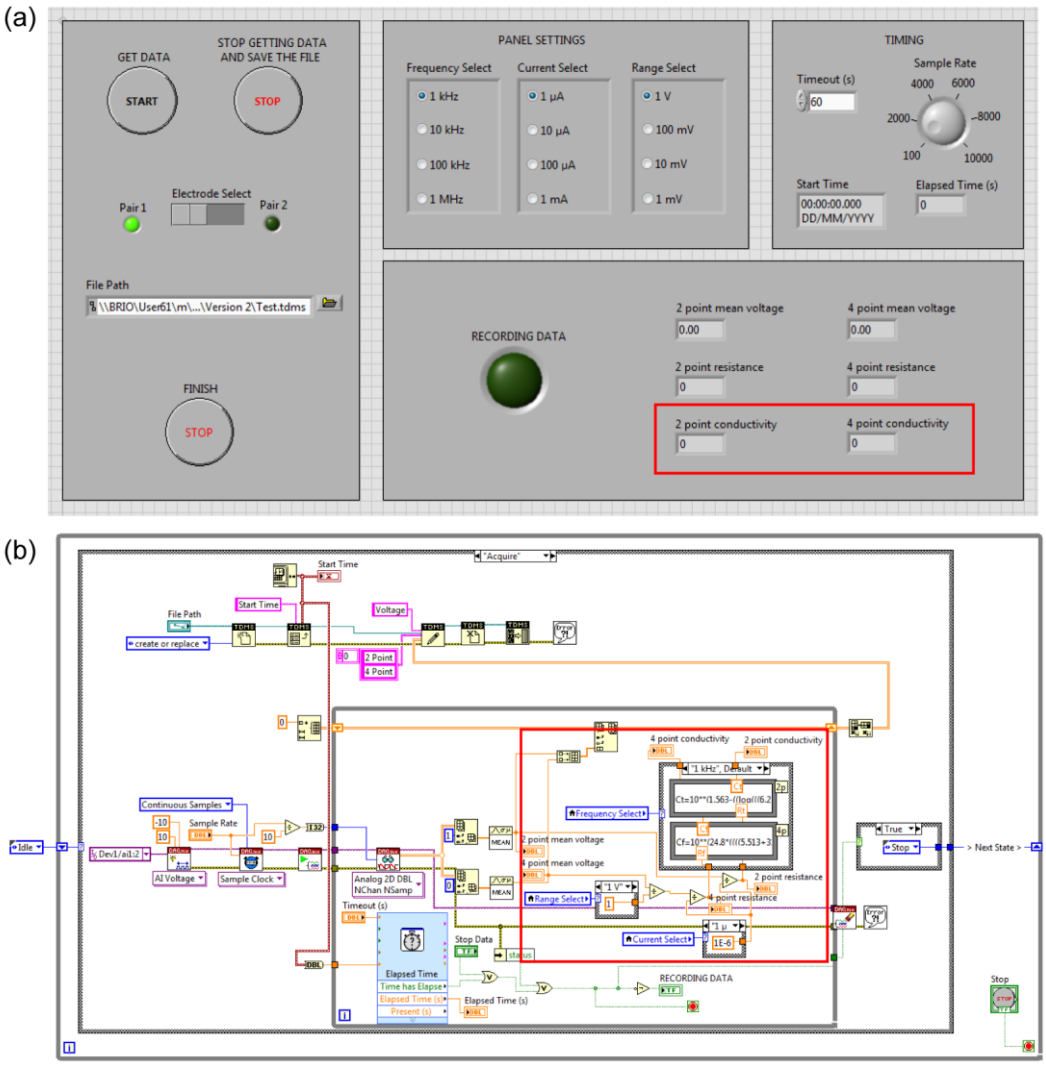

Figure 3.19. Screenshot of LabVIEW VI (version 2) to operate the conductivity sensor. (a) Front panel and (b) part of the block diagram of the VI showing the 'Acquire' case of the state machine where the data acquisition, data handling, and file streaming occurs. Major changes from version 1 are highlighted in the red boxes.

Using the fitted calibration curves for the Seacon conductivity sensor in **Figure 3.11** and **Table 3.6**, equation (3.10) is used to convert the voltage reading into a conductivity measurement. However, firstly knowledge of the selected sensor instrument settings is required in order to convert the voltage readings to resistance measurements, to select the calibration curve appropriate to the measurement AC frequency, and to ensure the correct voltage range is used. For this, we used local variables to read the value of the front panel objects for these three objects, wired to

case structures to ensure the appropriate functions are selected.[45] Indicators for both 2-point and 4-point measured resistance and conductivity now appear on the front panel to display to the user in real-time (also see the sub-VI block diagram in Appendix C).

Now the user can place the conductivity sensor in an electrolytic solution and attain an idea of its conductivity. However, the user must still manually select the right sensor instrument settings, and this requires starting and stopping the VI. Version 3 of the VI (**Figure 3.20**) allows the user to change these settings whilst the VI, and hence the measurement, remains running. For clarity, those parts of the VI relating to 4-point conductivity measurement have been omitted.

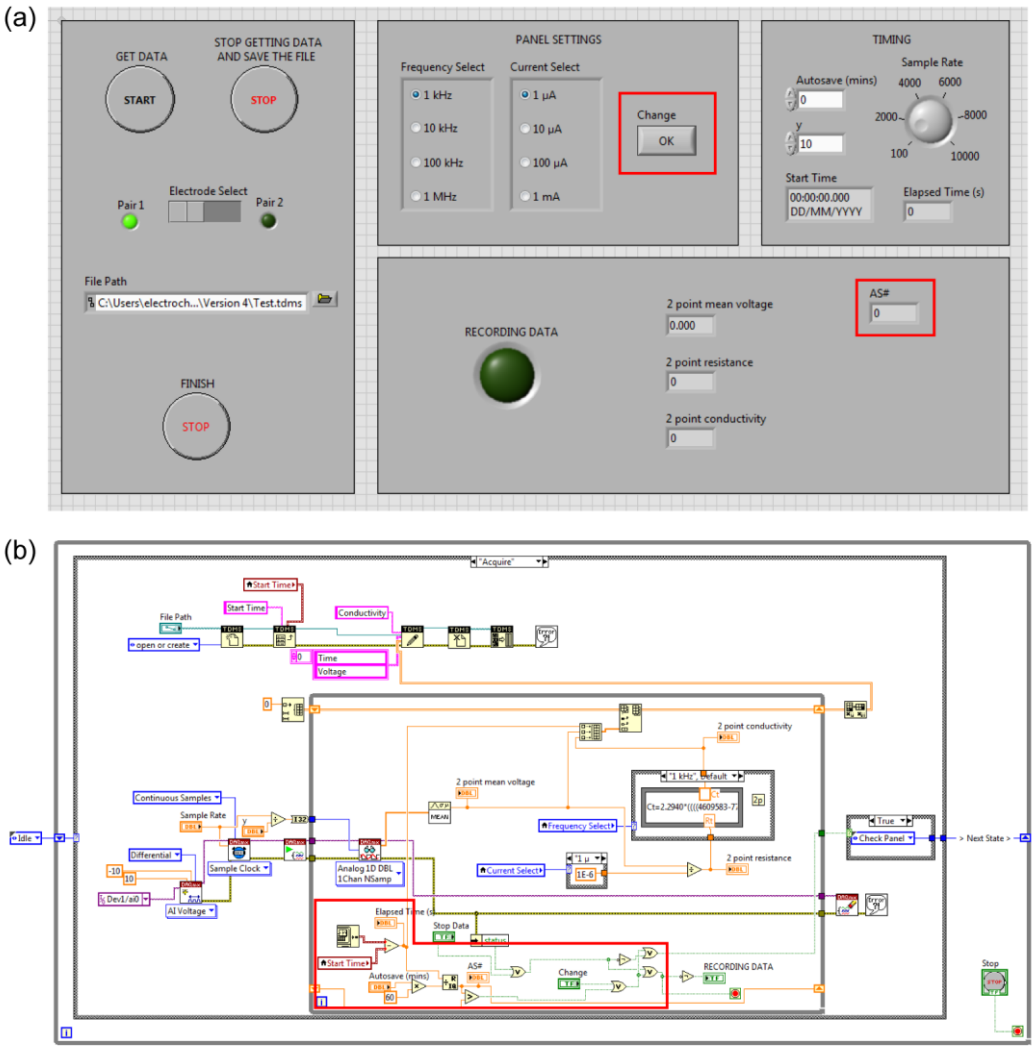

Figure 3.20. Screenshot of LabVIEW VI (version 3) to operate the conductivity sensor. (a) Front panel and (b) part of the block diagram of the VI showing the 'Acquire' case of the state machine where the data acquisition, data handling, and file streaming occurs. Major changes from version 2 are highlighted in the red boxes.

A new button control on the front panel (Change button) allows this function to be realised. Whilst the VI is running, the user can select different values of the radio buttons for measurement AC frequency and current, but this will not have any effect on the real-world sensor instrument. The Change button is linked to the conditional stop terminal of the DAQmx Read while loop, therefore when the Change button is pressed (*i.e.* its value is true), the while loop and hence the measurement is stopped. The true value is passed through to the state machine case structure, so that instead of

advancing to the Stop state, the VI moves to the Check Panel state. This results in the changed values of the controls on the front panel being read again, and output to the sensor instrument. After this, the VI advances to the Acquire state as usual and the measurement begins again. Note that at the end of the first execution of the Acquire state, the measurement data held in the array is streamed to a file. In the second execution of the Acquire state, the same file is opened and the newly generated array is appended to the existing data.

Additionally in version 3 of the VI, an autosave function was implemented. One of the disadvantages of the program design in the previous versions is that the measurement data was held locally in an array in the DAQmx Read while loop. Thus, if an error occurred or the PC crashed during the execution of the while loop, then all data acquired since starting the measurement would be lost as it would not been saved to disk at that moment in time; this is a significant problem for long-term measurement. In order to try to avoid this issue, an autosave function was implemented into the VI whereby data is streamed to disk periodically. This utilises the Get Date/Time In Seconds node.[19] In the Start state when the user begins the measurement, this node obtains the current time and writes it to a local variable. Each time the DAQmx Read while loop executes, the same node that is also present here obtains the current time and subtracts the start time local variable, which gives the elapsed time since the measurement began. Then, the elapsed time is compared to the user-desired Autosave time. If the elapsed time is a multiple of the autosave time, the while loop is stopped and therefore the data is streamed to disk. However, the code will then advance the VI to the Check Panel state; if the user has not changed the input for the sensor instrument, the VI will advance to the Acquire state and simply begin acquiring measurements again.

Next, we investigated the incorporation of simultaneous temperature measurements along with conductivity measurements. Version 4 of the VI (**Figure 3.21**) includes the ability to acquire temperature measurements from the diamond based temperature sensor (**Figure 3.15c**) and correct the measured κ_θ to κ_{25}. Therefore, we can now display a temperature corrected conductivity value and a measured temperature value in real-time to the user in addition to saving the time series recorded data to disk.

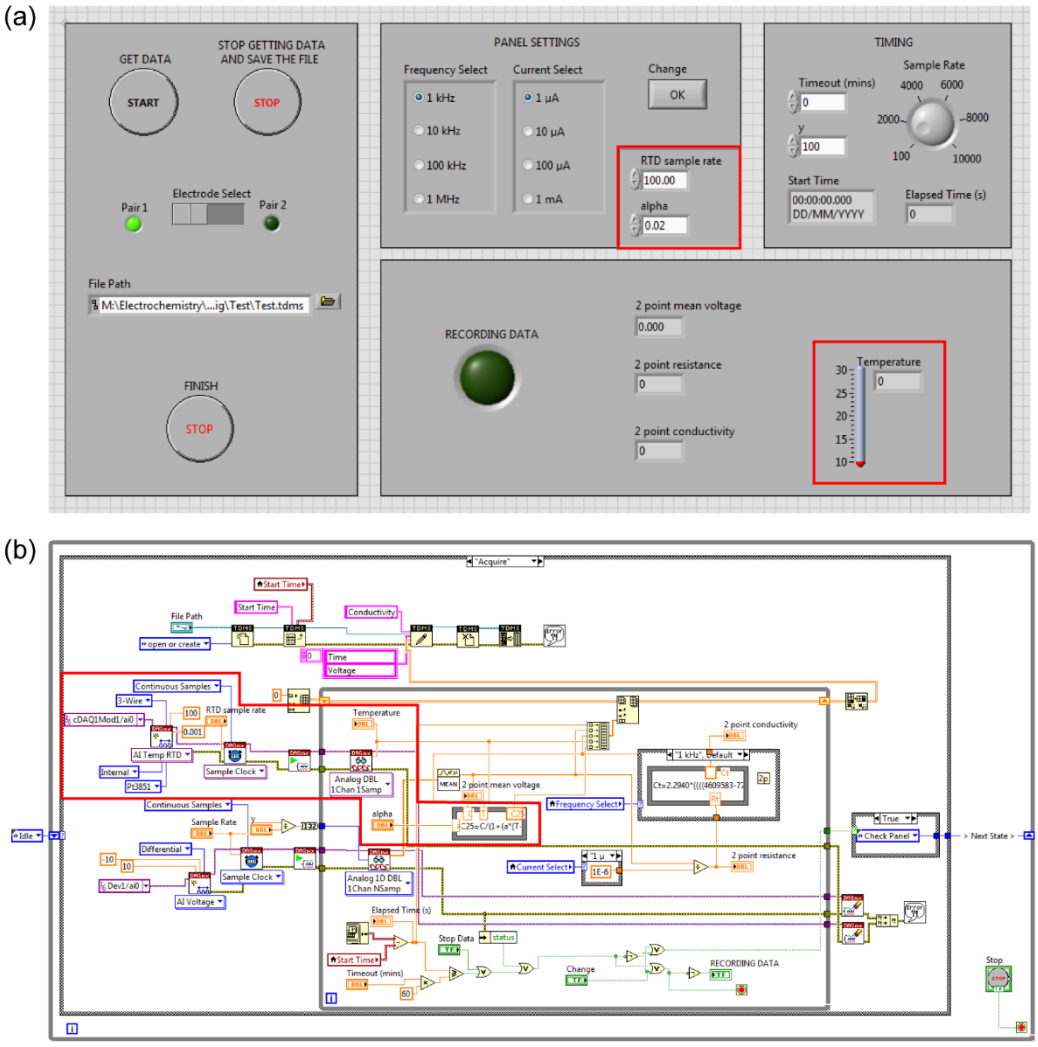

Figure 3.21. Screenshot of LabVIEW VI (version 4) to operate the conductivity sensor. (a) Front panel and (b) part of the block diagram of the VI showing the 'Acquire' case of the state machine where the data acquisition, data handling, and file streaming occurs. Major changes from version 3 are highlighted in the red boxes.

A number of significant modifications to the VI were required for this to be achieved. In terms of user input, two controls were added to the front panel to allow the user to specify a sample rate for the RTD (number of measurements per second) and a temperature coefficient for temperature correction.

A cDAQ-9171 device with 9217 input module was used to interface between the RTD and the VI. This DAQ device measures resistance from the RTD sensor and uses an internal calibration to output measured temperature values. In order to read data from this DAQ device, a second DAQmx series is required in the block diagram, similar to the conductivity sensor DAQ, which allows simultaneous readings from both devices. Code subsequent to the DAQmx Read nodes use the temperature values to correct the calibrated conductivity values. Consequently, the array which is streamed to disk once measurement has ceased contains the time, voltage (raw voltage from the sensor instrument), temperature, and conductivity.

3.4.6 Further design modifications

Having demonstrated the performance of the Seacon all-diamond conductivity sensor in both a 2-point and 4-point arrangement, we now explore possible modifications to the sensor design to either further improve the sensor response or to open new opportunities for sensor application.

We proposed two modified sensor designs (**Figure 3.22**) for a future diamond sensor fabrication run. Design 1 is a theoretically more ideal 4-point electrode configuration but tests the limitations of the laser micromachining and back contacting processes, whilst design 2 is a miniaturised form of the same design. The theoretical 2-point response curves of both designs are also shown.

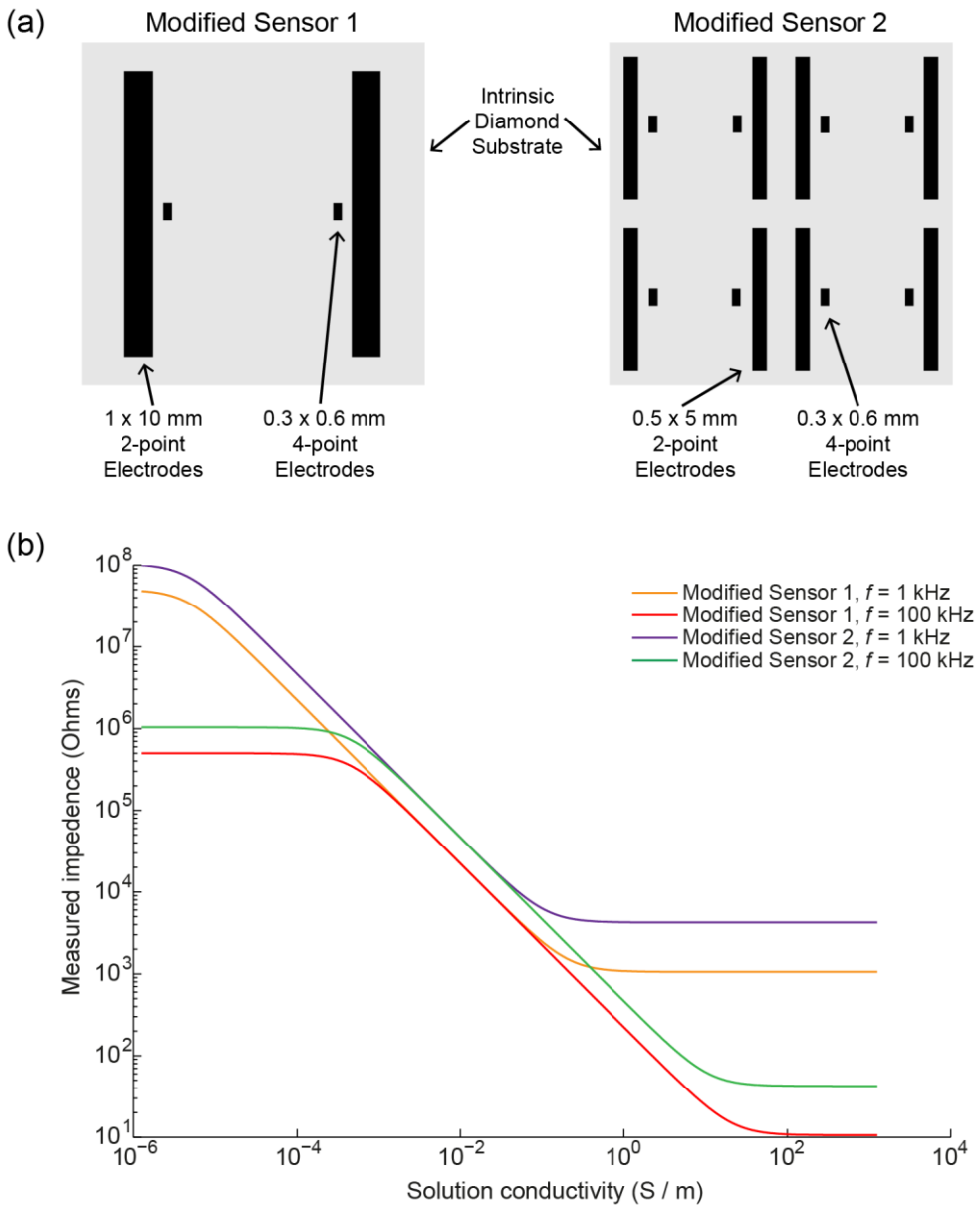

Figure 3.22. Design modifications for the all-diamond conductivity sensor. (a) Diagrams of two proposed modified sensor designs. (b) Theoretical response of the modified conductivity sensors to changing solution conductivities, at f = 1 and 100 kHz.

For a 4-point resistance (conductivity) measurement, in particular when the four electrodes are in a planar arrangement, ideally the potential sensing electrodes must be as close as possible to the current injection electrodes.[46] Though, they must also be sufficiently separated so that coupling of any stray fields and conductance currents does not occur.[30] In addition, the potential sensing electrodes must be as thin

as possible to ensure a uniform potential distribution across it, otherwise the electrode will be placed on a potential level different from the one it should register.[29] Ideally the potential sensing electrodes have a small surface area.

However, we must consider design limitations from a fabrication point of view. For laser micromachining, the minimum practical feature size is 10 µm. Previous research has shown that squares do not grow well in the BDD overgrowth stage, and additionally the minimum separation between inner and outer electrodes should be 200 µm.[47] For back contacting to the BDD electrodes, vias of 300 µm initial diameter are laser micro machined from the rear. Therefore, to avoid potential cross-talk between electrodes, to ease back contacting difficulties, and to ensure successful BDD overgrowth, the size of the potential sensing electrodes was w = 300 µm and l = 600 µm. Dimensions of the current injection electrodes remained the same as Seacon.

Furthermore, these design limitations also apply when considering miniaturisation of the device. Sensor design 1 potentially could work at a quarter of the size, but the inner sensing electrode size remains a constraint. Shrinking the conductivity cell much beyond that will get challenging if good performance is to remain. As a result, we proposed a design incorporating four conductivity sensor structures on the same 12 × 12 mm intrinsic diamond footprint. The size of the inner sensing electrode is the same as design 1, as this is what we consider to be the minimum feasible BDD band electrode size, whilst the size of the outer current injection electrodes are reduced.

3.5 Conclusions

The efficacy of a synthetic all-diamond 2-point conductivity sensor had been demonstrated previously,[5] but required further optimisation in order to be capable of making accurate measurements in higher conductivity aquatic environments, *e.g.* waste water, industrial process water, or sea water. Through an understanding of the cell design parameters, and by moving to a 4-point sensing configuration, a new sensor was designed that was optimised for this criteria. The Seacon device consists of four discrete band electrodes (two pairs of electrodes in a 4-point probe arrangement) fabricated from co-planar BDD electrodes on a synthetic diamond platform (12 mm × 12 mm). The sensor is shown to accurately determine solution conductivity over more than five orders of magnitude, from 10^1 to 4×10^5 μS cm^{-1}. Moreover, FEM simulation of the cell geometry enables us to establish that the effective sensing region of the Seacon sensor extends approximately 2 cm into bulk solution, a crucial factor when considering sensor placement and practical implications for a working device.

Importantly, we have established the capability to incorporate temperature sensing into the all-diamond platform, offering a distinct advantage given the importance of measuring sample temperature simultaneously with conductivity. Utilising a commercially available Pt100 RTD integrated into the sensor technology, we have demonstrated that accurate measurements of solution temperature can be made concurrent with conductivity measurements. In addition, we have explored the feasibility of fabricating a Pt RTD film directly onto the rear face of the diamond substrate, thus offering only one interface between RTD and diamond, hence obtaining more accurate measurements and faster response times.

Overall, the all-diamond sensor was shown to function reliably. The development of LabVIEW based software to operate the sensor offers the ability to obtain real-time measurements and a PC interface. This bodes well for the use of such sensors in natural aquatic environments and environments that require regular cleaning. Combining the all-diamond conductivity sensor presented herein with additional electrochemical sensors, such as for pH or heavy metals, also offers a multi-functional diamond based sensor. Furthermore, by packaging the sensor head with BDD electrodes suitable for ozone or hydroxyl generation, then a self-cleaning functionality can be added, with the aim of preventing accumulation of biofilms that hamper long term *in situ* placement of sensors for water and other process monitoring.

3.6 References

(1) Gray, J. R. Conductivity Analyzers and Their Application. In *Environmental Instrumentation and Analysis Handbook*; Down, R. D., Lehr, J. H., Eds.; John Wiley & Sons, Inc., 2004; pp 491–510.

(2) Lipták, B. G. *Instrument Engineers' Handbook. Volume I: Process Measurement and Analysis*, 4th ed.; CRC Press: Boca Raton, 2003.

(3) Macpherson, J. V. A Practical Guide to Using Boron Doped Diamond in Electrochemical Research. *Phys. Chem. Chem. Phys.* **2015**, *17* (5), 2935–2949.

(4) Joseph, M. B.; Bitziou, E.; Read, T. L.; Meng, L.; Palmer, N. L.; Mollart, T. P.; Newton, M. E.; MacPherson, J. V. Fabrication Route for the Production of Coplanar, Diamond Insulated, Boron Doped Diamond Macro- and Microelectrodes of Any Geometry. *Anal. Chem.* **2014**, *86* (11), 5238–5244.

(5) Joseph, M. B.; Colburn, A.; Mollart, T. P.; Palmer, N.; Newton, M. E.; Macpherson, J. V. A Synthetic Diamond Conductivity Sensor: Design Rules and Applications. *Sensors Actuators, B Chem.* **2017**, *238*, 1128–1135.

(6) Braunstein, J.; Robbing, G. D. Electrolytic Conductance Measurements and Capacitive Balance. *J. Chem. Educ.* **1971**, *48* (1), 52.

(7) Olthuis, W.; Streekstra, W.; Bergveld, P. Theoretical and Experimental

Determination of Cell Constants of Planar-Interdigitated Electrolyte Conductivity Sensors. *Sensors Actuators B. Chem.* **1995**, *24* (1–3), 252–256.

(8) Jacobs, P.; Varlan, A.; Sansen, W. Design Optimisation of Planar Electrolytic Conductivity Sensors. *Med. Biol. Eng. Comput.* **1995**, *33* (6), 802–810.

(9) Lide, D. R. *CRC Handbook of Chemistry and Physics*, 89th ed.; CRC Press: Boca Raton, 2008.

(10) Oldham, K.; Myland, J.; Spanier, J. *An Atlas of Functions*, 2nd ed.; Springer US: New York, 2009.

(11) Olthuis, W.; Volanschi, A.; Bomer, J. G.; Bergveld, P. A New Probe for Measuring Electrolytic Conductance. *Sensors Actuators B. Chem.* **1993**, *13* (1–3), 230–233.

(12) Hong, J.; Yoon, D. S.; Kim, S. K.; Kim, T. S.; Kim, S.; Pak, E. Y.; No, K. AC Frequency Characteristics of Coplanar Impedance Sensors as Design Parameters. *Lab Chip* **2005**, *5* (3), 270–279.

(13) Demierre, N.; Braschler, T.; Linderholm, P.; Seger, U.; Van Lintel, H.; Renaud, P. Characterization and Optimization of Liquid Electrodes for Lateral Dielectrophoresis. *Lab Chip* **2007**, *7* (3), 355–365.

(14) Holler, F. J.; Enke, C. G. Conductivity and Conductometry. In *Laboratory Techniques in Electroanalytical Chemistry*; Kissinger, P. T., Heineman, W. R., Eds.; Marcel Dekker: New York, 1996; pp 237–266.

(15) Robinson, R. A.; Stokes, R. H. *Electrolyte Solutions*, 2nd ed.; Butterworths Publications: London, 1965.

(16) Wu, Y. C.; Koch, W. F. Absolute Determination of Electrolytic Conductivity for Primary Standard KCl Solutions from 0 to 50°C. *J. Solution Chem.* **1991**, *20* (4), 391–401.

(17) Barthel, J.; Feuerlein, F.; Neueder, R.; Wachter, R. Calibration of Conductance Cells at Various Temperatures. *J. Solution Chem.* **1980**, *9* (3), 209–219.

(18) ISO-7888. *Water Quality - Determination of Electrical Conductivity. International Organization for Standardization: 6.*; Geneva, Switzerland, 1985.

(19) Johnson, G. W.; Jennings, R. *LabVIEW Graphical Programming*, 4th ed.; McGraw-Hill: New York, 2006.

(20) Muyskens, M. A.; Glass, S. V.; Wietsma, T. W.; Gray, T. M. Data Acquisition in the Chemistry Laboratory Using LabVIEW Software. *J. Chem. Educ.* **2009**, *73* (12), 1112.

(21) Krauß, A.; Weimar, U.; Göpel, W. LabView™ for Sensor Data Acquisition. *TrAC Trends Anal. Chem.* **1999**, *18* (5), 312–318.

(22) Sumathi, S.; Surekha, P. *LabVIEW Based Advanced Instrumentation Systems*; Springer-Verlag: Berlin, Heidelberg, 2007.

(23) Grahame, D. C.; Whitney, R. B. The Thermodynamic Theory of

Electrocapillarity. *J. Am. Chem. Soc.* **1942**, *64* (7), 1548–1552.

(24) Orazem, M. E.; Tribollet, B. *Electrochemical Impedance Spectroscopy*, 2nd ed.; John Wiley & Sons, Inc.: New Jersey, 2017.

(25) Pajkossy, T.; Jurczakowski, R. Electrochemical Impedance Spectroscopy in Interfacial Studies. *Curr. Opin. Electrochem.* **2017**, *1* (1), 53–58.

(26) Kerner, Z.; Pajkossy, T. On the Origin of Capacitance Dispersion of Rough Electrodes. *Electrochim. Acta* **2000**, *46* (2–3), 207–211.

(27) Pajkossy, T. Impedance of Rough Capacitive Electrodes. *J. Electroanal. Chem.* **1994**, *364* (1–2), 111–125.

(28) Volanschi, A.; Olthius, W.; Bergveld, P. Design of a Miniature Electrolyte Conductivity Probe Using ISFETs in a Four Point Configuration. *Sensors Actuators B Chem.* **1994**, *19* (1–3), 404–407.

(29) Schwan, H. P. Alternating Current Electrode Polarization. *Biophysik* **1966**, *3* (2), 181–201.

(30) Schwan, H. P.; Ferris, C. D. Four-Electrode Null Techniques for Impedance Measurement with High Resolution. *Rev. Sci. Instrum.* **1968**, *39* (4), 481–485.

(31) Gottschalk, P. G.; Dunn, J. R. The Five-Parameter Logistic: A Characterization and Comparison with the Four-Parameter Logistic. *Anal. Biochem.* **2005**, *343* (1), 54–65.

(32) Bockris, J. O.; Reddy, A. K. N. Ion Transport in Solutions. In *Modern Electrochemistry (1): Ionics*; Kluwer Academic Publishers: Boston, 2002; pp 361–600.

(33) Pryor, R. W. *Multiphysics Modeling Using COMSOL: A First Principles Approach*, 1st ed.; Jones and Bartlett Publishers: Massachusetts, 2011.

(34) Jordan, E. C.; Balmain, K. G. *Electromagnetic Waves and Radiating Systems*, 2nd ed.; Prentice-Hall, Inc.: New Jersey, 1968.

(35) Grant, I. S.; Phillips, W. R. *Electromagnetism*, 2nd ed.; John Wiley & Sons, Inc.: New Jersey, 1990.

(36) Purcell, E. *Electricity and Magnetism*, 2nd ed.; Cambridge University Press: Cambridge, 2011.

(37) Griffiths, D. J. *Introduction to Electrodynamics*, 3rd ed.; Prentice-Hall, Inc.: New Jersey, 1999.

(38) Young, H. D.; Freedman, R. A. *University Physics*, 11th ed.; Addison Wesley: San Francisco, 2004.

(39) Michalski, L.; Eckersdorf, K.; Kucharski, J.; McGhee, J. *Temperature Measurement*, 2nd ed.; John Wiley & Sons, Inc.: Chichester, 2001.

(40) Levinson, H. J. Photoresists. In *Principles of Lithography*; SPIE Press: Bellingham, 2011; pp 51–108.

(41) Williams, K. R.; Gupta, K.; Wasilik, M. Etch Rates for Micromachining Processing-Part II. *J. Microelectromechanical Syst.* **2003**, *12* (6), 761–778.

(42) Smith, S. H. Temperature Correction in Conductivity Measurements. *Limnol. Oceanogr.* **1962**, *7* (3), 330–334.

(43) Wagner, R. Temperaturkorrekturfaktoren Für Die Elektrischen Leitfähigkeit von Wässern. *Z. Wasser- Abwasserforsch.* **1980**, *2*.

(44) Bitter, R.; Mohiuddin, T.; Nawrocki, M. *LabVIEW Advanced Programming Techniques*, 1st ed.; CRC Press: Boca Raton, 2001.

(45) Travis, J. *LabVIEW For Everyone*, 2nd ed.; Prentice-Hall, Inc.: New Jersey, 2002.

(46) Bowler, J. R.; Bowler, N. Theory of Four-Point Alternating Current Potential Drop Measurements on Conductive Plates. *Proc. R. Soc. A Math. Phys. Eng. Sci.* **2007**, *463* (2079), 817–836.

(47) Bitziou, E.; Joseph, M. B.; Read, T. L.; Palmer, N.; Mollart, T.; Newton, M. E.; Macpherson, J. V. In Situ Optimization of PH for Parts-Per-Billion Electrochemical Detection of Dissolved Hydrogen Sulfide Using Boron Doped Diamond Flow Electrodes. *Anal. Chem.* **2014**, *86* (21), 10834–10840.

4 Boron doped diamond as a low biofouling material for sensing in aquatic environments by assessment of *Pseudomonas aeruginosa* biofilm formation

4.1 Aims

Boron doped diamond (BDD), given the robustness of the material, is becoming an electrode of choice for applications which require long term electrochemical monitoring of analytes in aqueous environments. However, despite the extensive work in this area there are no studies which directly assess the biofilm formation (biofouling) capabilities of the material, which is an essential consideration because biofouling often causes deterioration in sensor performance. *Pseudomonas aeruginosa* is one of the most prevalent bacterial pathogens linked to water-related diseases, with a strong capacity for forming biofilms on surfaces that are exposed to aquatic environments. In this study, we comparatively evaluate the biofouling capabilities of oxygen-terminated (O-)BDD against materials commonly employed as either the packaging or sensing element in water quality sensors, with an aim to identify factors which control biofilm formation on BDD. We assess the monospecies biofilm formation of *P. aeruginosa* in two different growth media, Luria-Bertani, a high nutrient source and drinking water, a low nutrient source, at two different temperatures (20 °C and 37 °C). Multispecies biofilm formation is also investigated. The performance of O-BDD, when tested against all other materials, promotes the lowest extent of *P. aeruginosa* monospecies biofilm formation, even with corrections made for total surface area (roughness). Importantly, O-BDD shows

the lowest water contact angle of all materials tested, *i.e.* greatest hydrophilicity, strongly suggesting that for these bacterial species, the factors controlling the hydrophilicity of the surface are important in reducing bacterial adhesion. This was further proven by keeping surface topography fixed and changing surface termination to hydrogen (H-), to produce a strongly hydrophobic surface. A noticeable increase in biofilm formation was found. Doping with boron also results in changes in hydrophobicity/hydrophilicity compared to the undoped counterpart, which in turn affects biofilm formation. For practical electrochemical sensing applications in aquatic environments, this study highlights the extremely beneficial effects of employing smooth, O-terminated (hydrophilic) BDD electrodes.

4.2 Introduction

In aquatic environments there is a critical need to monitor water quality, analysing parameters such as pH, dissolved gases, organic content, and heavy metals in order to fulfil quality control, environmental management, or regulatory compliance.[1] Monitoring typically involves the collection of discrete samples, followed by analysis in a laboratory or on-site if instrumentation permits.[2] The use of continuous *in situ* (or on-line) monitoring is considered most beneficial as it allows automatic, real-time measurements directly at the water source of interest.[1,2] However, one of the biggest challenges with *in situ* monitoring is deterioration of sensor performance over time because of biofouling, which provides a significant obstacle to obtaining reliable long-term measurements.[3–5] Biofouling is the accumulation of unwanted biological matter, and in aquatic environments this is often due to the formation of microbial biofilms.[6–8] Biofilms are complex and dynamic communities of

microorganisms attached to a surface.[9] Once adhered, the bacteria proliferate, produce an extracellular polymeric matrix, and form a matured biofilm.[10,11] Biofilm is not only a problem for *in situ* aquatic sensing, but also impacts detrimentally on a wide range of medical and industrial applications.[6,7,10,12–16]

Given the negative implications of biofilm formation, there is a vast amount of research into strategies for the prevention of surface biofouling. These surface modifications range from the development of surface coatings and anti-bacterial adhesion agents, to the incorporation of metal (silver and copper) nanoparticles and antimicrobial agents, and the engineering of nanostructured materials.[17–22] However, for sensing applications, it is not always possible to modify the sensor surface without adversely affecting the performance properties. This is especially true of devices where the sensing element, *e.g.* an electrode, is directly exposed to the solution.

As a sensor material, in particular for *in situ* and on-line applications, boron doped diamond (BDD) is being actively explored as a result of the superior properties of the material, such as hardness, chemical inertness, and corrosion resistance.[23] BDD is typically operated as an electrochemical sensor, packaged in either insulating undoped diamond[24] or a non-diamond material.[25] Undoped diamond is often claimed to be a low biofouling material;[26,27] however, the term biofouling is used loosely in the sensor literature and most biofouling studies investigate proteins[26] or neuronal cells.[28] However, these are not representative of a biofilm model of fouling, which is applicable under aquatic environmental conditions. Indeed, their mechanism of interaction is likely to be very different to that of a bacterial cell.[29] To date, there is no information on the interaction of bacterial cells with BDD, or indeed how doping may modify this interaction. Previous work focused only on the anti-adhesive

properties of nanocrystalline diamond, which itself contains significant non-diamond sp^2 carbon impurities.[30–32]

In this study, we investigate for the first time the bacterial biofilm formation capabilities of both oxygen terminated (O-) and hydrogen terminated (H-) BDD, and identify the possible factors[33–38] which play a role in adherence of bacteria to these surfaces. Biofilm formation is examined in relation to other electrode or packaging materials, including undoped diamond, stainless steel, screen printed carbon (SPC), alumina, copper, and polyvinyl chloride (PVC). We focus on *Pseudomonas aeruginosa* (five bacterial strains) as it is regarded as one of the most prevalent opportunistic bacterial pathogens linked to water-related diseases,[16] is a strong biofilm producer, and is commonly detected in both natural and man-made water ecosystems.[11] As this species is often part of a multispecies bacterial biofilm community,[39] we also combine *P. aeruginosa* with other relevant biofilm-producing bacterial species widely present in water systems (*Acinetobacter baumannii*, *Aeromonas hydrophila*, *Klebsiella pneumoniae*, and *Staphylococcus aureus*).[40–42] The biofilm-forming properties of the materials are directly compared using a range of complementary techniques, including crystal violet (CV) dye staining, scanning electron microscopy (SEM), and confocal laser scanning microscopy (CLSM).[8,43]

4.3 Experimental

4.3.1 Substrates

Substrate materials employed for biofilm growth were: unplasticised PVC (Goodfellow Cambridge, Huntingdon, UK), AISI 304 stainless steel (Goodfellow Cambridge, Huntingdon, UK), copper (Goodfellow Cambridge, Huntingdon, UK),

electrochemical processing grade BDD (polycrystalline and freestanding; Element Six, Didcot, UK), thermal grade intrinsic diamond (polycrystalline and freestanding; Element Six, Didcot, UK), alumina (CoorsTek, Fife, UK), and SPC (Gwent Electronic Materials, Pontypool, UK). The BDD is doped $>10^{20}$ B atoms cm^{-3}, which is above the metallic threshold.[23] All materials were cut to 4 mm diameter round discs using laser micromachining (E-355H-3-ATHI-O, Oxford Lasers, Didcot, UK), with the exception of copper and SPC, which were supplied pre-cut by the manufacturer. Diamond and BDD substrates were acid cleaned by exposure to a solution of 96% sulfuric acid (reagent grade; Sigma Aldrich, St. Louis, USA) saturated with potassium nitrate (reagent grade; Sigma Aldrich, St. Louis, USA) which was heated to a temperature of *ca*. 200 °C for 30 min; this process ensures that the surfaces were fully O-terminated prior to use, unless otherwise stated. All substrates were cleaned by sonication in acetone (≥99%; Sigma Aldrich, St Louis, USA), followed by isopropanol (≥99.5%; Sigma Aldrich, St Louis, USA), and Milli-Q ultrapure water (Merck Millipore, Watford, UK). Exceptions were PVC, which had the acetone step omitted, and SPC which was cleaned only by sonicating in ultrapure water. All cleaning steps had a duration of 10 min. Substrates were wiped with lint-free cloth between solvents and stored in 70% ethanol until further use.

4.3.2 Diamond substrate modification

Diamond and BDD substrates were H-terminated in a Seki Diamond 6500 series microwave plasma chemical vapour deposition system (Cornes Technologies, San Jose, USA). The substrates were evacuated to a base pressure of $>1\times10^{-6}$ mbar. Plasma hydrogenation was carried out at 500 sccm hydrogen flow, 1500 W microwave power, and 50 Torr pressure. Diamond and BDD substrates were surface

roughened using a laser micromachining approach (E-355H-3-ATHI-O, Oxford Lasers, Didcot, UK). Briefly, the laser was rastered over the surface of the substrates using a pulse density of 2×10^6 cm^{-2} and a fluence of 14 J cm^{-2}. Substrates were subsequently subjected to the acid cleaning procedure described above and then thermally oxidised in air at 600 °C for 5 h to remove any surface sp^2 carbon introduced from the laser micromachining process.

4.3.3 Substrate characterisation

Contact angle values were measured by the static sessile drop method, using a KRÜSS DSA100 drop shape analysis system (KRÜSS GmbH, Hamburg, Germany) at 20 °C with 3 µL droplets of Milli-Q ultrapure water (Merck Millipore, Watford, UK). Surface roughness measurements were made using atomic force microscopy (AFM; Bruker Innova, Coventry, UK) operating in tapping mode using an antimony doped silicon probe with a spring constant of 3 N m^{-1}. Images were obtained at a line scan rate of 0.3 Hz with a resolution of 512 lines and 512 points per line. For each substrate, three 5×5 µm areas were scanned (n = 3) and images analysed using Scanning Probe Image Processor (SPIP) software (v. 6.0.14, Image Metrology, Hørsholm, Denmark).

4.3.4 Bacterial strains, media, and growth conditions

Ten waterborne or water-based biofilm-producing bacterial strains were included in this study: *P. aeruginosa* MPAO1, *P. aeruginosa* NPAO1, *P. aeruginosa* PA14, *P. aeruginosa* LESB58, *P. aeruginosa* ΔwspF (hyperaggregative phenotype), *P. aeruginosa* ΔPsl ΔPel (non-biofilm producer phenotype), *Acinetobacter baumannii*

DSM 30008, *Aeromonas hydrophila* DSM 30187, *Klebsiella pneumoniae* DSM 30104, and *Staphylococcus aureus* ATCC 29213. All of these strains have been widely used for biofilm studies, are known to be moderate to strong biofilm producers, and are well characterised for genotype and phenotype.[44–47] All strains were stored as frozen stocks (−80 °C freezer) in Luria-Bertani (LB) broth (containing 10 g L^{-1} sodium chloride) with 20% glycerol until future use.

4.3.5 Inocula preparation and biofilm formation

Substrates were removed from 70% ethanol immersion and placed individually into the bottom of the wells of a polystyrene microtiter plate (Corning, Durham, USA). Three discs of each substrate were used per strain, in order to obtain triplicate measurements (n = 3). To confirm assay sterility, *i.e.* substrates are completely sterile, 200 µL of LB medium were added to each well and the microtiter plate incubated under static conditions at 37 °C for 24 h. Bacterial strains were transferred from the stock cultures to LB agar plates and incubated aerobically at 37 °C for 18 to 24 h. All strains were subcultured to LB broth and incubated at 37 °C, 120 rpm. The optical density of the bacterial cultures was monitored at 600 nm (OD_{600}) using a Jenway 7200 spectrophotometer (Cole-Parmer, Staffordshire, UK) to ensure that all cultures reached a mid-exponential growth phase, with an OD_{600} corresponding to approximately 10^8 cells mL^{-1} (strain-dependent OD_{600} range: 0.15–0.2). The strain *P. aeruginosa* ΔPsl ΔPel was used solely for validation of the microtiter plate biofilm assay, as this strain should not produce biofilm and therefore acts as a negative control. All other *Pseudomonas* strains were studied as monospecies biofilm producers. *P. aeruginosa* MPAO1 and the four non-*Pseudomonas* strains were used to generate multispecies biofilms.

Bacterial strains were tested for their ability to form biofilm on the substrates in the presence of two different media: LB broth (pH = 6.9 ± 0.1) and filtered tap drinking water (pH = 6.8 ± 0.1). The tap drinking water was collected from University of Warwick, Coventry, UK and filtered using a 0.2 μm pore size membrane filter (Sartorius Stedim Biotech, Göttingen, Germany). Free chlorine test strips (Fisher Scientific, Loughborough, UK) showed no free chlorine present in the drinking water (<0.05 ppm limit of detection). For the assay with LB growth medium, a 200 μL bacterial inoculum was added to each well (2×10^7 cells well^{-1}) after aspiration of LB previously added for sterility testing. For the assay with drinking water as the growth medium, the inoculum was centrifuged at 7,500 rpm for 10 min, the supernatant was removed and the bacterial pellet resuspended in the filtered tap water. The inoculum with a volume of 200 μL was then added to each well (2×10^7 cells well^{-1}).

For multispecies biofilms, a similar procedure was followed with equal cell concentrations of each strain being mixed together to attain the final inoculum of approximately 2×10^7 cells well^{-1}. For every assay, the microtiter plate was incubated under static conditions at either 37 °C or 20 °C for 2 days. For each substrate, negative controls (n = 3, medium only) were included. For each strain, positive growth controls (n = 3, absence of substrate) were also present in the analysis.

4.3.6 Microtiter plate biofilm formation quantitative assay

The assay was adapted from previously described protocols.[45,48,49] Briefly, after the 2 day-incubation, 150 μL of the liquid culture comprising planktonic cells were carefully aspirated from each well. Next, wells containing the substrate were washed once with sterile water, then the biofilm was fixed by incubation at 70 °C for 1 h.

Substrates were transferred using sterile tweezers to a new 96-well plate, before being stained with 200 µL of 0.1% crystal violet aqueous solution (1% in H_2O; Sigma Aldrich, St Louis, USA) for 15 min. The stain was removed from the wells and washed three times with sterile water to remove excess. Stained biofilm was solubilised in 200 µL of 30% acetic acid (≥99.7%; Fisher Scientific, Loughborough, UK) for 15 min. The solubilised stain was transferred to a new 96-well plate and the absorbance at 595 nm (A_{595}) measured using a Multiskan FC Microplate Photometer (Fisher Scientific, Loughborough, UK).

4.3.7 Confocal laser scanning and scanning electron microscopy

For all microscopy analysis, only MPAO1 monospecies and multispecies biofilms were investigated as MPAO1 is the most frequently studied *P. aeruginosa* strain. Processing of the substrates for microscopy analysis comprised different fixation and staining steps. The washing step was followed by chemical fixation with 200 µL of 1% glutaraldehyde (Grade I, 50% in H_2O; Sigma Aldrich, St Louis, USA) for 1 h. To remove excess glutaraldehyde, a three-step washing with 200 µL of sterile water was additionally performed. These sample pre-treatment steps were common to both microscopy techniques.

For CLSM, biofilm cells were stained by the addition of 150 µL of 0.1 mg mL^{-1} propidium iodide (≥94%; Sigma Aldrich, St Louis, USA) for 15 min at room temperature. A washing step with sterile water followed. Substrates were transferred using sterile tweezers onto a microscope slide. The dead stained biofilm cells were visualised on a Zeiss LSM710 microscope (Carl Zeiss Ltd., Cambridge, UK). A diode-pumped solid-state laser with maximum emission at 561 nm was used as the

excitation source, whilst the detection range was 566–718 nm. Triplicate images were obtained across two independent samples. Images were analysed using ImageJ software (v. 1.51n, National Institutes of Health, USA) by individually thresholding each image slice of the *z* stack, summing the slices, and calculating the mean fluorescence intensity across the resultant image.

For SEM, biofilms were dehydrated by a graded series of ethanol (50, 75, 90, 95, and 100%) for 10 min each. PVC substrates were carbon coated prior to imaging (Emitech K950X sputter coater, Quorum Technologies, Kent, UK). Images were obtained using the secondary electron detector on a Zeiss Gemini field emission (FE) instrument (Carl Zeiss Ltd., Cambridge, UK) operating at 1 kV. A minimum of 10 images were obtained on two independent samples.

4.3.8 Statistical analysis

Statistical analysis was performed using Past3 (v. 3.16, Oslo, Norway). To evaluate statistical correlations and identify trends in biofilm formation across substrates, Spearman's rank correlation (r_s) test was performed. To evaluate statistical differences in biofilm formation between substrates, either the paired *t* test was performed (for comparisons between two sets of observations), or the Kruskal-Wallis test with Dunn's post hoc adjusted for Bonferroni correction (for comparisons across all substrates). Data sets underwent the Shapiro-Wilk test for normal distribution prior to the aforementioned statistical tests. Differences were considered statistically significant at a probability $p < 0.05$.

4.4 Results and discussion

4.4.1 Optimisation of crystal violet assay

To quantify the extent of biofilm formation, a microtiter CV assay was used, whereby the absorbance of the solubilised CV stain (A_{595}) is considered proportional to the amount of biofilm biomass on the surface. Whilst the microtiter CV assay is now an established protocol, the procedure should be tested for optimisation of experimental conditions.[48–52] Firstly, growth curves of each of the *P. aeruginosa* strains used in this study were obtained to assess the optimal time for the bacterial cultures in the initial inocula to reach mid-exponential growth phase (**Figure 4.1**).

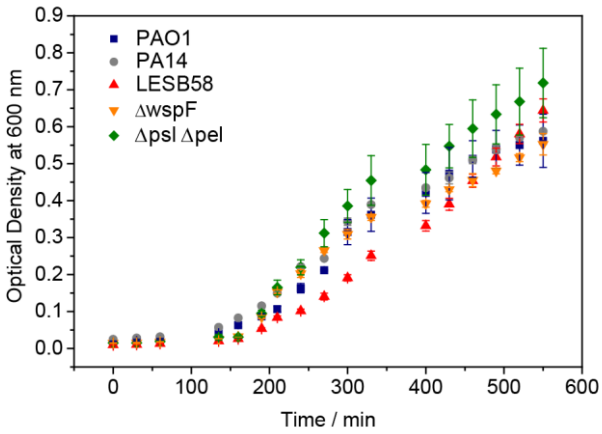

Figure 4.1. Growth curves of *P. aeruginosa* strains. Optical density at 600 nm was monitored as a function of time for growth suspensions of five individual *P. aeruginosa* strains (PAO1, PA14, LESB58, ΔwspF, and Δpsl Δpel). Data expressed as mean ± SD (n = 3).

By correlating the OD_{600} values with colony forming unit measurements ascertained from LB agar plate counting, for each bacterial strain this enables the determination of an OD_{600} corresponding to approximately 10^8 cells mL^{-1} (strain-dependent OD_{600} range: 0.15–0.2) along with the required growth time (*ca.* 4 h).[53] Therefore each biofilm formation experiment starts with a constant, known number of bacterial cells.

For the CV assay, there are a number of critical parameters that may affect the results. Consequently, we evaluated the biofilm formation assay under different conditions to optimise the outcome. Initially, experiments were conducted in the absence of substrates measuring the biofilm formed solely in the wells of the microtiter plate. After biofilm formation and CV staining, the stain solubilisation step has been reported using 30% acetic acid and 95% ethanol as solubilisation agents.[50,52] Both were tested (**Figure 4.2**) after biofilms formed using three individual strains of *P. aeruginosa* (ΔwspF, Δpsl Δpel, and LESB58).

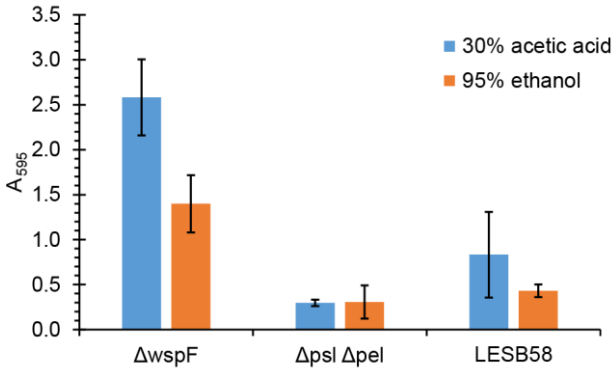

Figure 4.2. Extent of *P. aeruginosa* monospecies biofilm formation using different solubilisation agents. Data expressed as the absorbance of solubilised CV stain at 595 nm, using (■) 30% acetic acid and (■) 95% ethanol for solubilisation. Biofilm formation was assessed after 48 h at 37 °C in LB medium. Data from three individual strains (ΔwspF, Δpsl Δpel, LESB58) is presented as mean ± SD (n = 5).

Growth was performed at 37 °C for 48 h in LB medium, and the resultant biofilms were stained using a CV concentration of 0.1% v/v. Using 30% acetic acid, we observed that there was a larger differentiation in absorbance between strains: A_{595} range 0.30–2.58 using 30% acetic acid compared with A_{595} range 0.31–1.40 using 95% ethanol. Thus, 30% acetic acid allows for greater distinguishability between strains, so we opted for this solubilisation agent for all subsequent experiments.

Next, we assessed whether robust growth was found within the linear detection range of the assay set-up.[52] Biofilms were stained using CV concentrations of 0.1% and 0.01% v/v (**Figure 4.3**).

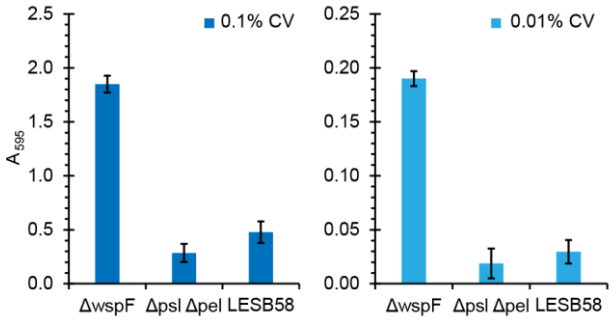

Figure 4.3. Extent of *P. aeruginosa* monospecies biofilm formation using different CV stain concentrations. Data expressed as the absorbance of solubilised CV stain at 595 nm, using (■) 0.1% and (■) 0.01% CV. Biofilm formation was assessed after 48 h at 37 °C in LB medium. Data from three individual strains (ΔwspF, Δpsl Δpel, LESB58) is presented as mean ± SD (n = 5).

Stain concentration of 0.1% CV showed an absorbance A_{595} > 1 for one strain (ΔwspF, hyperaggregative strain), whilst for the other strains the measured absorbance was within the range 0.1–1.0. A 1:10 dilution of the CV stain resulted in a 10 fold decrease in measured absorbance, which validates the method. However, the A_{595} range using 0.01% CV was considered too low (0.01–0.20), therefore a CV concentration of 0.1% was chosen for subsequent assay testing experiments.

Biofilm formation was also assessed in two different growth media, nutrient rich LB medium (high ionic strength) and low nutrient drinking water (low ionic strength) to mimic environmental conditions (**Figure 4.4**). Furthermore, two additional *P. aeruginosa* strains (PA14 and PAO1) were introduced for testing.

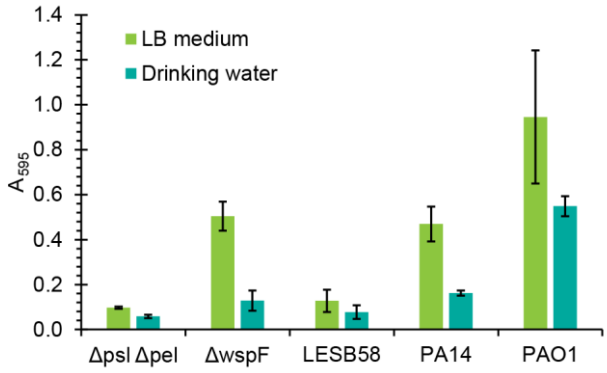

Figure 4.4. Extent of *P. aeruginosa* monospecies biofilm formation using different growth media. Data expressed as the absorbance of solubilised CV stain at 595 nm. Biofilm formation was assessed after 48 h at 37 °C in (■) LB medium and (■) drinking water. Data from five individual strains (Δpsl Δpel, ΔwspF, LESB58, PA14, PAO1) is presented as mean ± SD (n = 5).

All strains formed biofilm in drinking water as well as LB medium. We observed that the amount of biofilm formed in drinking water was significantly lower than in LB medium (paired t test, $p < 0.05$). Moreover, the same pattern in biofilm formation was observed between LB medium and drinking water ($r_s = 0.8$, $p < 0.1$).

Finally, the effect of the amount of time for growth of the biofilm cultures was examined (**Figure 4.5**). In all tests prior, 48 h growth time was allowed for biofilm formation, but 120 h growth time was also investigated.

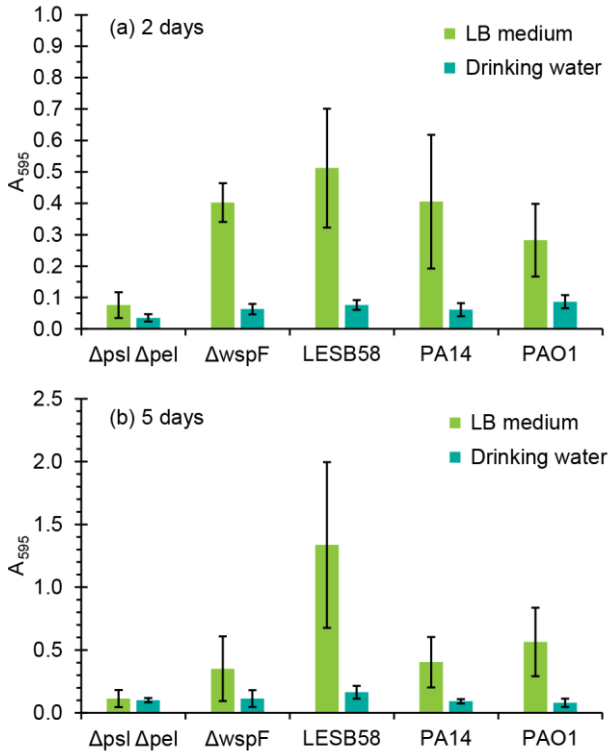

Figure 4.5. Extent of *P. aeruginosa* monospecies biofilm formation using different growth times. Data expressed as the absorbance of solubilised CV stain at 595 nm. Biofilm formation was assessed after (a) 48 h and (b) 120 h at 37 °C in (■) LB medium and (■) drinking water. Data from five individual strains (Δpsl Δpel, ΔwspF, LESB58, PA14, PAO1) is presented as mean ± SD (n = 5).

Biofilm formation after 5 days growth time was significantly higher than after 2 days growth time in both LB medium (paired t test, $p = 0.05$) and drinking water (paired t test, $p < 0.05$). However, after 5 days growth the resultant biofilm was very sticky and difficult to work with, meaning that some sample was lost. Measured absorbance values showed greater variability, therefore 2 days growth was selected.

4.4.2 *P. aeruginosa* monospecies biofilm formation on substrates

The ability of five different *P. aeruginosa* strains to form biofilms on the substrates under study was assessed. All measurements were carried out at one fixed growth time (48 h), thereby focusing predominantly on initial bacterial adhesion and the

early stages of biofilm development. After incubation, similar growth of free-floating bacteria in the medium (planktonic bacterial growth) was overall observed in the presence of all substrates, with the exception of copper where a comparatively lower planktonic bacterial growth was mostly detected.

To quantify the extent of biofilm formation on each substrate, a microtiter CV assay was used, whereby the absorbance of the solubilised CV stain (A_{595}) is considered proportional to the amount of biofilm biomass on the surface. CV absorbance data for these monospecies biofilms are summarised in box plot form in **Figure 4.6**, and the individual CV absorbance data of each strain used is detailed in **Figure 4.7**. The absorbance data has been normalised with respect to geometric surface area. All substrates, except for SPC, had the same geometric surface area. All substrates, except for SPC, had the same geometric surface area. The approach was employed in two different growth media, nutrient rich LB medium (high ionic strength) and low-nutrient drinking water (low ionic strength) to mimic environmental conditions, under two different temperature conditions, 37 °C (optimum bacterial growth temperature) and 20 °C (closer to environmental water temperature).

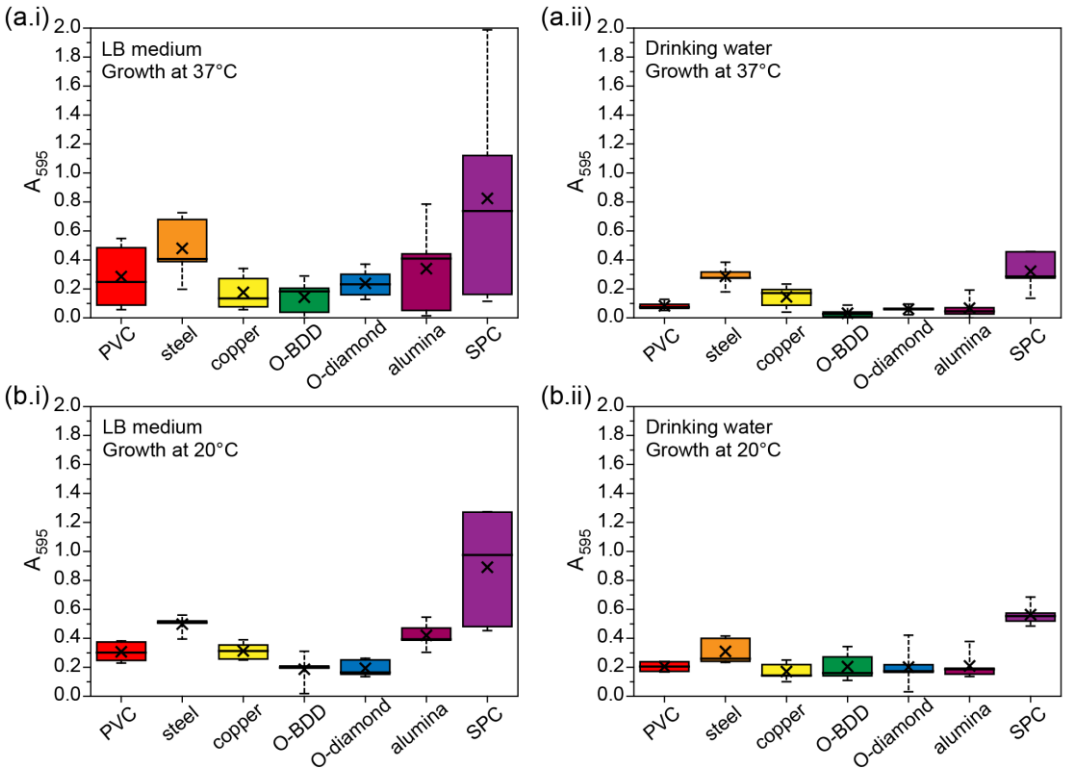

Figure 4.6. Extent of *P. aeruginosa* monospecies biofilm formation on different substrates. Data expressed as the absorbance of solubilised CV stain at 595 nm. Biofilm formation was assessed after 48 h under the following growth conditions: (a) 37 °C and (b) 20 °C, in (i) LB medium and (ii) drinking water. Data from five individual strains (MPAO1, NPAO1, PA14, LESB58, ΔwspF) is presented as a boxplot where crosses and bars indicate mean and median absorbance values respectively, and whiskers extend to minimum and maximum data points.

The CV data in **Figure 4.6** comprises A_{595} values from five separate strains of *P. aeruginosa* monospecies biofilms. **Figure 4.7** presents these A_{595} values individually in more detail.

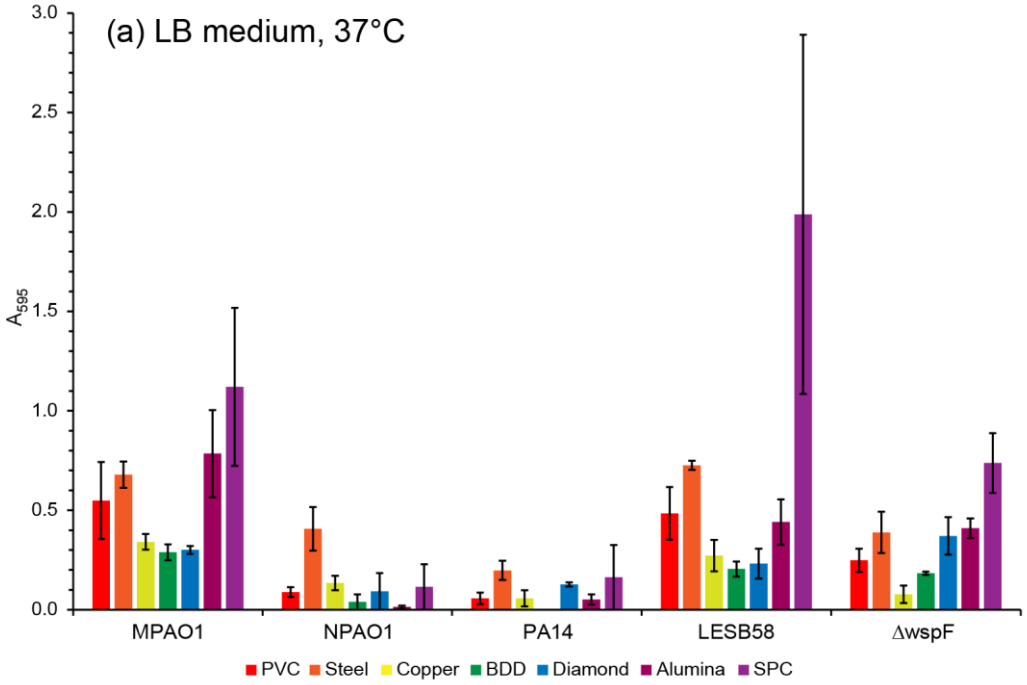
(a) LB medium, 37°C
A_{595}
3.0
2.5
2.0
1.5
1.0
0.5
0.0
MPAO1
NPAO1
PA14
LESB58
ΔwspF
PVC
Steel
Copper
BDD
Diamond
Alumina
SPC

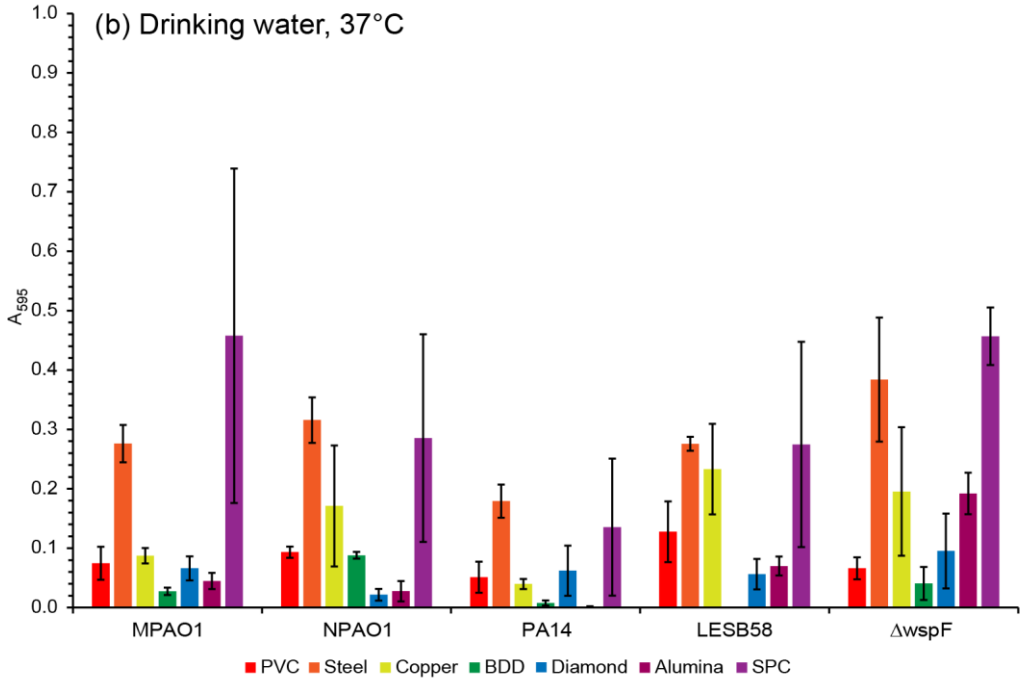
(b) Drinking water, 37°C
A_{595}
1.0
0.9
0.8
0.7
0.6
0.5
0.4
0.3
0.2
0.1
0.0
MPAO1
NPAO1
PA14
LESB58
ΔwspF
PVC
Steel
Copper
BDD
Diamond
Alumina
SPC

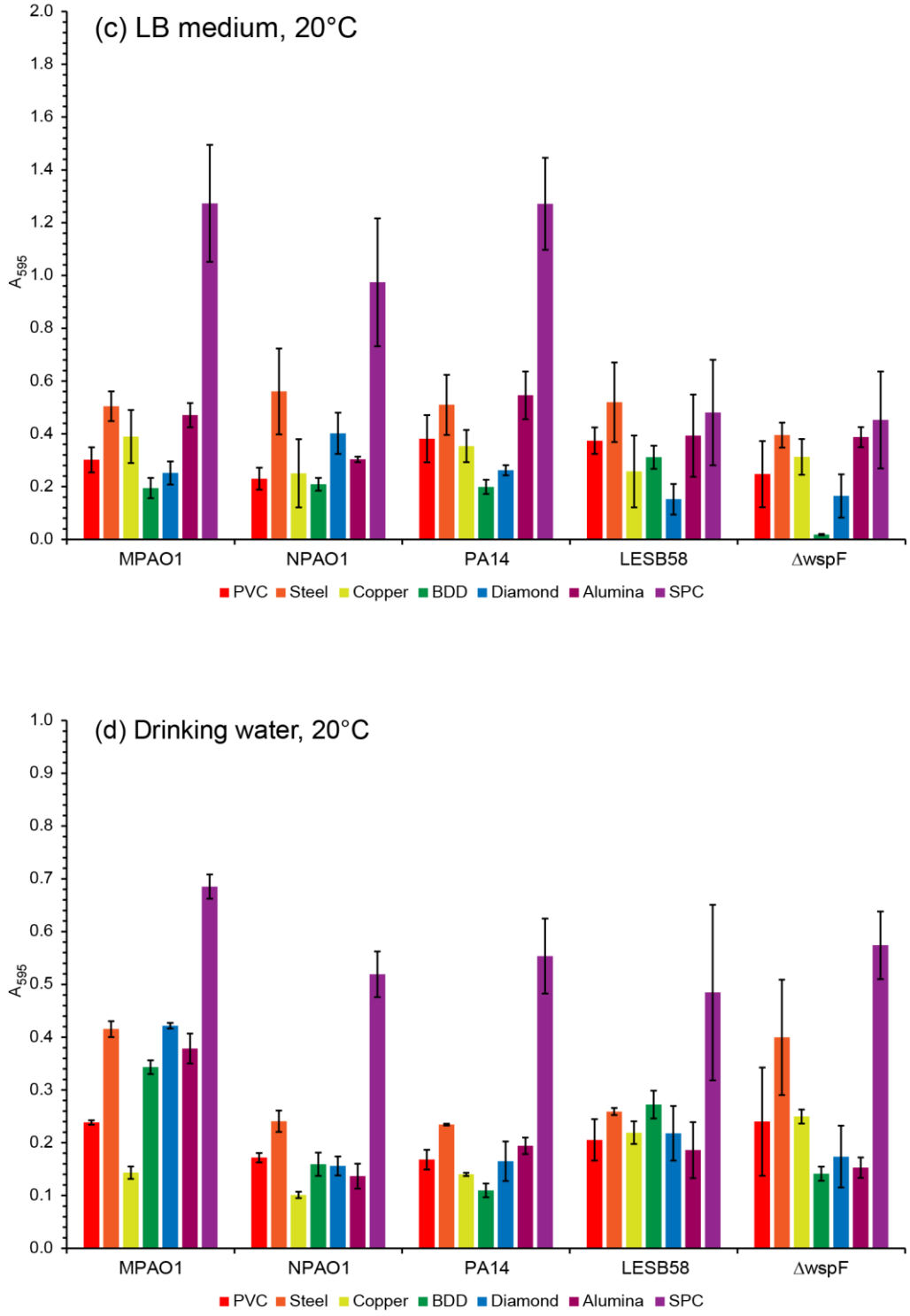

Figure 4.7. Extent of individual strain *P. aeruginosa* monospecies biofilm formation on different substrates. Data expressed as the absorbance of solubilised CV stain at 595 nm. Biofilm formation was assessed after 48 h under the following growth conditions: (a) LB medium at 37 °C, (b) drinking water at 37 °C, (c) LB medium at 20 °C, and (d) drinking water at 20 °C. Bars represent the mean ± standard error of the mean.

Comparison of the extent of *P. aeruginosa* monospecies biofilm formation at both 37 °C and 20 °C revealed no significant differences in the quantity of biofilm formed on each substrate in LB medium (paired *t* test, $p = 0.1$). A rank-order analysis of biofilm formation across all substrates showed a strong correlation ($r_s = 0.89$, $p < 0.05$), indicating a similar trend in biofilm formation across substrates independent of temperature. In drinking water, significantly higher biofilm biomass was observed at 20 °C compared to 37 °C (paired *t* test, $p < 0.05$) for each substrate. As biofilm formation is often a response to unfavourable environmental conditions or stresses,[11,54] it appears that the restricted nutrient content of drinking water in combination with a sub-optimal growth temperature has actively promoted biofilm formation under these more hostile conditions. Also, the same trend in biofilm formation across substrates at 37 °C and 20 °C was not observed ($r_s = 0.46$, $p = 0.3$). This is mostly explained by a comparatively higher biofilm formation on the copper substrate at 37 °C.

When comparing if nutrient content could have an impact on the results obtained, we observed that the amount of biofilm formed on substrates in drinking water was significantly lower than in LB medium, regardless of temperature (paired *t* test, $p < 0.05$). This data confirms that for *P. aeruginosa* biofilm formation, nutrient content is important.[11,54] Comparing data for biofilm formation across all substrates, the trends between the substrates in the two different growth media were more similar at 37 °C ($r_s = 0.75$, $p = 0.07$) than at 20 °C ($r_s = 0.67$, $p = 0.07$). The substrate that showed the biggest difference in biofilm formation was alumina, showing a comparatively higher biofilm formation on its surface in the LB medium than that in drinking water (for both growth temperatures).

Examining individual substrates, the amount of biofilm formed on SPC was the highest in all conditions tested, reported as a mean A_{595} throughout (A_{595} = 0.65 ± 0.26). Conversely, the lowest amount of biofilm formed was observed on O-BDD (A_{595} = 0.14 ± 0.08). Between these extremes, steel was the substrate on which the second highest amount of biofilm was quantified (A_{595} = 0.39 ± 0.11), followed by alumina (A_{595} = 0.26 ± 0.15), PVC (A_{595} = 0.22 ± 0.10), copper (A_{595} = 0.20 ± 0.08), and O-diamond (A_{595} = 0.17 ± 0.08). Statistical analysis also highlighted significant differences across the substrates studied (Kruskal-Wallis, $p < 0.05$), with significantly lower biofilm formation on (1) both O-BDD and O-diamond compared to SPC and steel in LB medium at 20 °C and 37 °C; (2) O-BDD compared to SPC and steel in drinking water at 37 °C; and (3) copper against SPC in drinking water at 20 °C (post-hoc Dunn's test, $p < 0.05$). Regarding individual *P. aeruginosa* strain biofilm formation, the measured range was substrate-specific and showed intra-species variability, with the highest overall variation in biofilm formation among strains being observed on SPC. Nonetheless, in three out of the four growth conditions employed, the highest amount of biofilm across all five strains was observed on SPC (**Figure 4.7**).

In addition to the quantitative CV analysis, FE-SEM was used as a complementary technique to image the biofilms formed on the substrates (**Figure 4.8**). FE-SEM investigation of the *P. aeruginosa* monospecies biofilms formed on all the substrates at 37 °C in LB medium qualitatively corroborated the findings of the CV assay, *i.e.* the lowest levels of biofilm formation were observed on O-BDD. On SPC a dense, uniform coating of biofilm over the entire substrate results, whereas for alumina the majority of the substrate is coated. On the other hand, whilst formation of biofilm on copper and steel is prevalent, it is heterogeneously distributed across the surface.

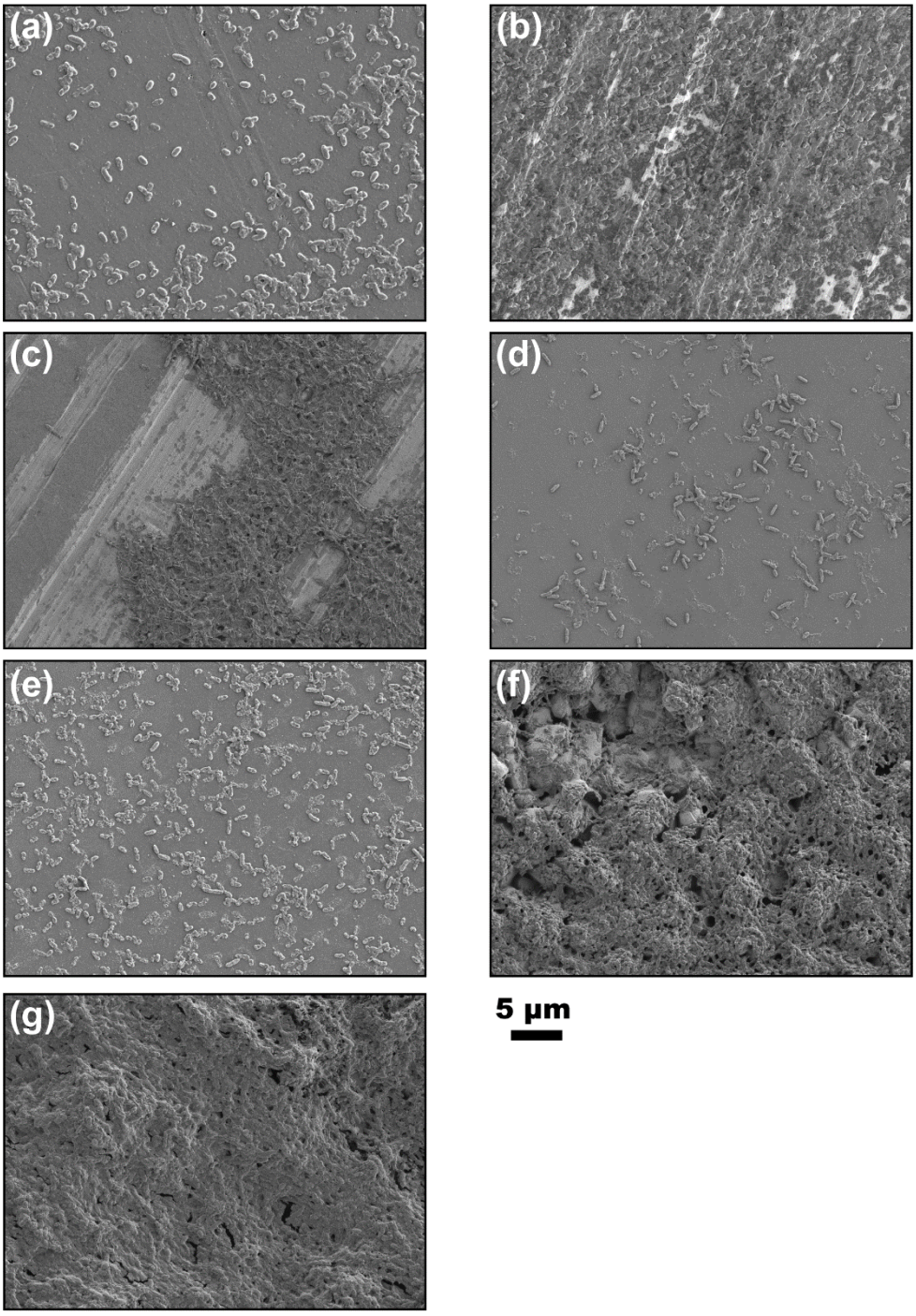

Figure 4.8. FE-SEM images of *P. aeruginosa* MPAO1 monospecies biofilms formed on (a) PVC, (b) steel, (c) copper, (d) O-BDD, (e) O-diamond, (f) alumina, and (g) SPC after 48 h bacterial growth in LB medium.

Figure 4.9 shows FE-SEM images of *P. aeruginosa* MPAO1 monospecies biofilms formed on the substrates in drinking water. When using drinking water as the growth

medium, biofilm formation on all substrates was visibly lower than in LB medium, with the most visually noticeable difference was observed on alumina (compare **Figure 4.8f** with **Figure 4.9f**), corroborating the observations from the CV assay.

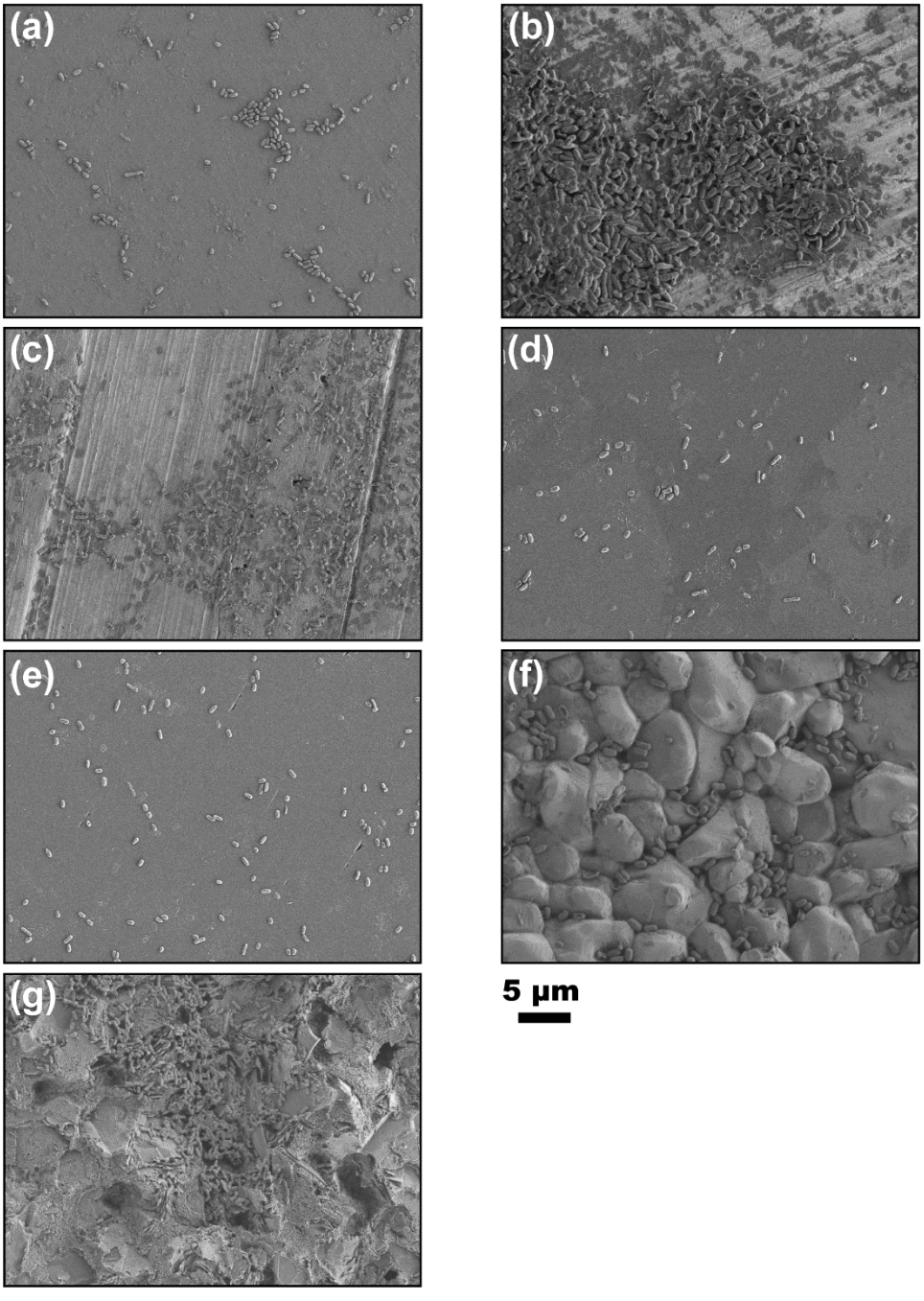

Figure 4.9. FE-SEM images of *P. aeruginosa* MPAO1 monospecies biofilms formed on (a) PVC, (b) steel, (c) copper, (d) BDD, (e) diamond, (f) alumina, and (g) SPC after 48 h bacterial growth in drinking water.

On PVC, O-BDD, and O-diamond substrates, in both LB medium and drinking water, biofilm formation is sparse with only individual bacteria, with typical dimensions of *ca.* 1 μm length, visible. Whilst the biofilm formation on PVC appeared heterogeneous in distribution (**Figure 4.10**), interestingly on both O-diamond and O-BDD no preferential growth behaviour was observed across the two surfaces, which are polycrystalline in nature.

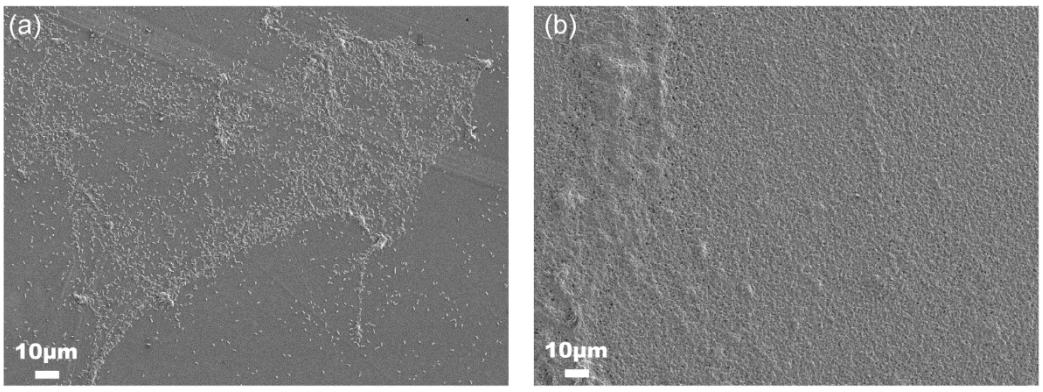

Figure 4.10. FE-SEM images of P. aeruginosa MPAO1 monospecies biofilms formed on PVC after 48 h bacterial growth in LB medium, illustrating (a) low and (b) high coverage.

Figure 4.10 shows two FE-SEM images of *P. aeruginosa* MPAO1 monospecies biofilms formed on PVC in LB medium. This substrate qualitatively showed heterogeneity in biofilm formation across its surface. As illustrated in **Figure 4.10**, areas of both relatively lower and higher extents of biofilm formation were observed.

Surface roughness is often considered an important factor in biofilm formation, though the extent to which this property influences the process is dependent on the material, type of roughness, environmental conditions and bacterial species.[33,35–38] Substrate surface roughness (arithmetical mean roughness, R_a) was determined by AFM image analysis (**Figure 4.11**) and is listed in **Table 4.1**. O-BDD (and O-diamond) substrates presented the smoothest surfaces, having a sub-nanometre level

roughness, whilst alumina and SPC were more than two orders of magnitude rougher. FE-SEM images of the bare surfaces are presented in **Figure 4.12**.

Table 4.1. Surface roughness, surface area, and contact angles of the substrates used. Surface roughness, total surface area, and contact angle values listed as mean ± SD (n = 3).

Substrate	**Surface roughness, R_a / nm**	**Geometric surface area / mm^2**	**Total surface area / mm^2**	**Contact angle / °**
PVC	4.76 ± 0.78	12.6	12.8 ± 0.15	73.7 ± 1.2
Steel	23.7 ± 3.0	12.6	12.9 ± 0.06	68.5 ± 1.8
Copper	23.0 ± 5.0	12.6	13.3 ± 0.47	74.3 ± 4.5
O-BDD	0.49 ± 0.04	12.6	12.6 ± 0.03	25.5 ± 1.7
O-Diamond	0.72 ± 0.16	12.6	12.6 ± 0.06	34.2 ± 0.3
Alumina	208 ± 50	12.6	21.5 ± 2.7	30.4 ± 0.6
SPC	204 ± 35	10.0	17.8 ± 2.2	64.4 ± 6.6

Table 4.1 summarises both the geometric surface area of the substrates, the total surface area (incorporating surface roughness), and contact angles. The total surface area for each substrate was calculated using equations (4.1) and (4.2):

$$\text{Total surface area} = \text{Geometric area} \times \left(1 + \text{Area factor}\right) \tag{4.1}$$

$$\text{Area factor} = \frac{\text{Projected area - Cross sectional area}}{\text{Cross sectional area}} \tag{4.2}$$

where the projected area and cross sectional area refers to the mean value (n = 3) recorded from the individual AFM scan of each substrate (**Figure 4.11**). The projected scan area was determined from the AFM images by calculating the sum of

the area of all the triangles formed by three adjacent data points. The cross sectional scan area was 25 μm^2 for all scans.

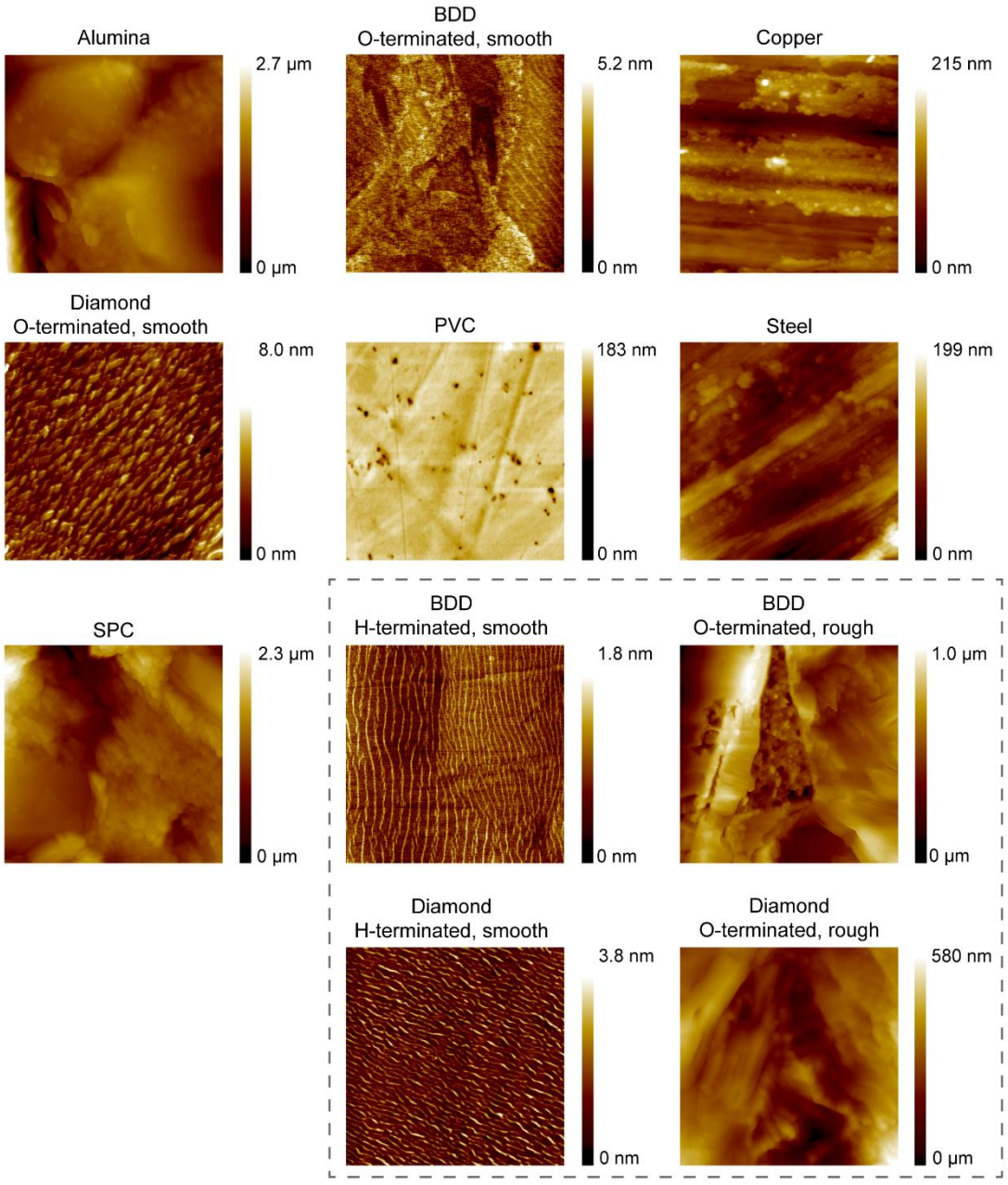

Figure 4.11. AFM images of the substrates used in this study. Modified diamond substrates are distinguished by the dashed box. The size of each image is 5×5 µm.

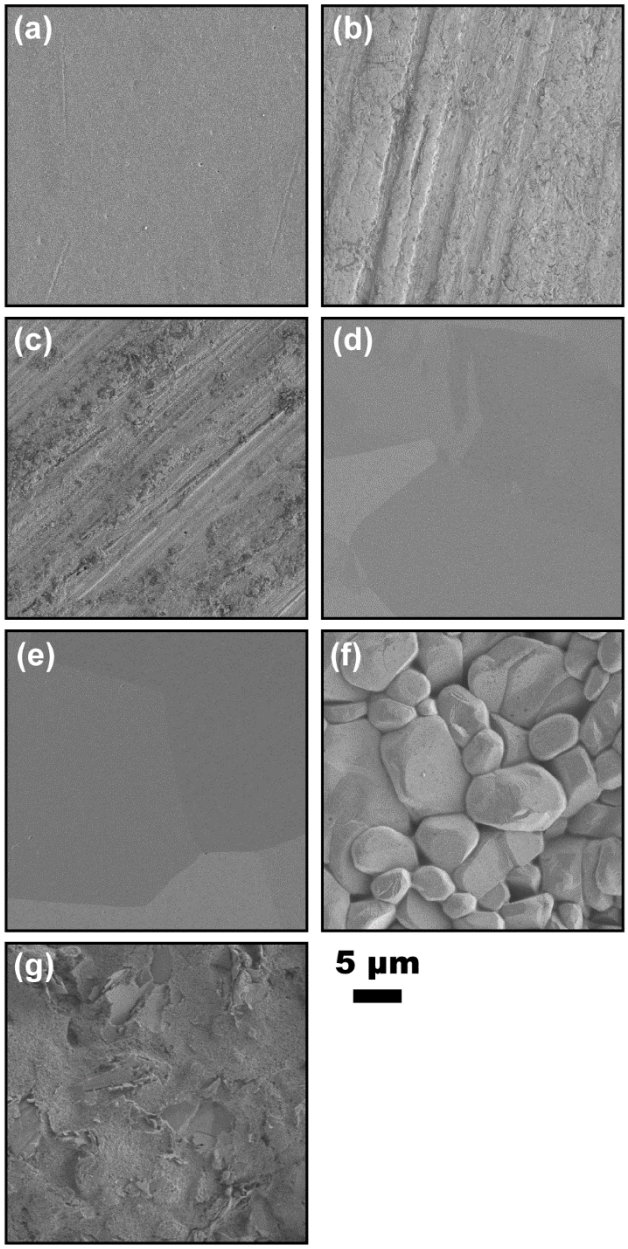

Figure 4.12. FE-SEM images of the bare surface of (a) PVC, (b) steel, (c) copper, (d) O-BDD, (e) O-diamond, (f) alumina, and (g) SPC substrates.

Both O-BDD and O-diamond substrates offer a flat and featureless surface, corresponding to their low R_a values. Whilst PVC also has a relatively low surface roughness, there are a number of small circular wells, pinholes, and grooves covering the entire surface (more clearly visible in the AFM image, **Figure 4.11**). These features are approximately 0.05–0.2 µm in size. The metal surfaces, *i.e.* steel and

copper, contain ridges and grooves that are ~1 μm in width. The alumina substrate consists of particles ranging approximately 2–20 μm in diameter that are compacted together to form a ceramic boulder-like structure. SPC comprises carbon particles that have been screen printed as an emulsion onto an alumina base and then dried, resulting in a surface that is layered and slightly porous.

The extent of *P. aeruginosa* monospecies biofilm formation was highest on SPC, which has the highest surface roughness (comparable with alumina), most likely due to the increased number of attachment sites.[33,36,37,55] In contrast, the lowest biofilm formation observed, under almost all conditions, was with O-BDD which exhibited the lowest surface roughness. In this case the smooth surfaces are likely to be presenting lower obstacle densities, enabling the bacteria to spread more[56,57] and making it more difficult for the bacteria to find each other to begin building a community (biofilm),[11,58–60] as observed in the FE-SEM images (**Figure 4.8d** and **e**).

To better account for surface roughness, the CV absorbance data was normalised against total surface area, as determined from the AFM image analysis (**Table 4.1**), and is shown in **Figure 4.13**. Even after total surface area normalization, similar trends are still revealed. SPC (A_{595} = 0.037 ± 0.015 mm^{-2}) consistently shows the highest amount of biofilm, whilst O-BDD showed the lowest amount of biofilm (A_{595} = 0.011 ± 0.006 mm^{-2}). Thus, surface roughness alone cannot be responsible for the differences observed as even when correcting for total surface area, O-BDD outperforms SPC in terms of minimising biofilm formation on the surface.

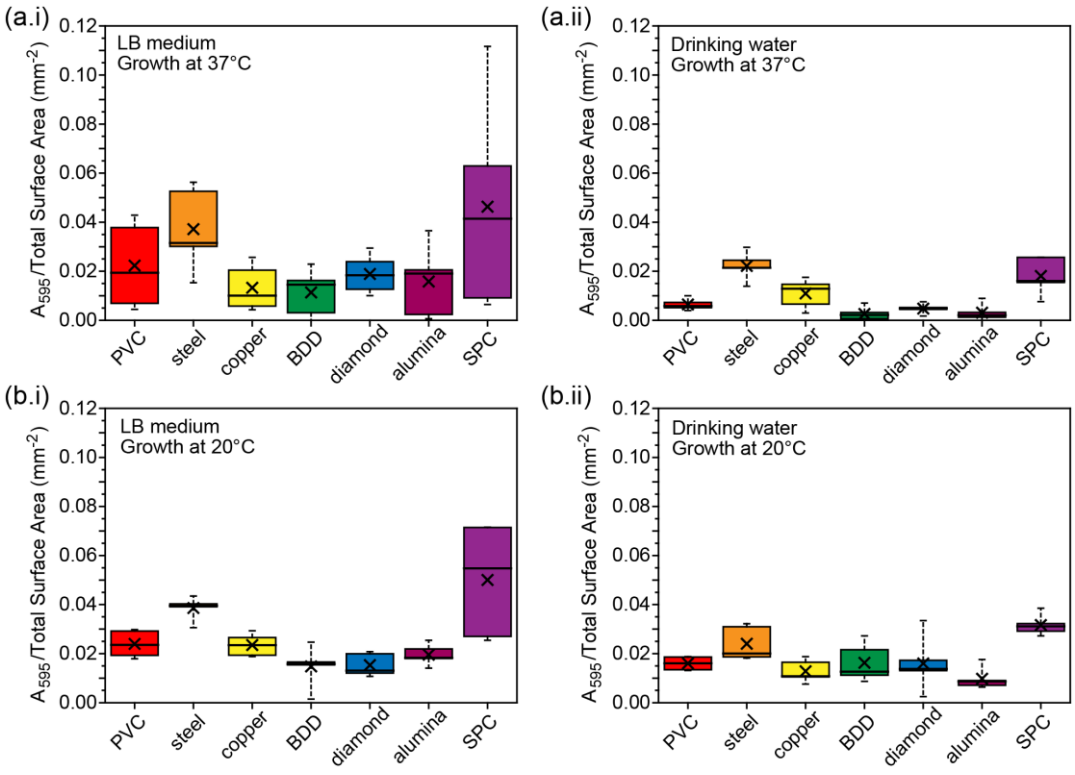

Figure 4.13. Extent of P. aeruginosa monospecies biofilm formation on different substrates. Data expressed as the absorbance of solubilised CV stain at 595 nm, divided by the total surface area of the substrate. Biofilm formation was assessed after 48 h under the following growth conditions: (a) 37 °C and (b) 20 °C, in (i) LB medium and (ii) drinking water. Data from five individual strains (MPAO1, NPAO1, PA14, LESB58, ΔwspF) is presented as a boxplot where crosses and bars indicate mean and median absorbance values respectively (n = 3 for each strain), and whiskers extend to minimum and maximum data points.

4.4.3 Multispecies biofilm formation on substrates

In order to ensure a greater ecological relevance, the extent of multispecies biofilm formation on the seven substrates was investigated. Four different bacterial species (*A. baumannii*, *A. hydrophila*, *K. pneumoniae* and *S. aureus*) along with *P. aeruginosa* MPAO1 were co-cultured. Incubation in the presence of all substrates under study was conducted at 37 °C in both LB medium and drinking water. The microtiter assay absorbance values of the solubilised CV of destained biofilms were determined as a quantitative measurement (five technical replicates) of the multispecies biofilm formed (**Figure 4.14**). Accordingly, the absorbance values

represent total biofilm biomass formed and no information can be extracted regarding the species dependence (the proportion of each bacterial species that make up the total multispecies biofilm) of each substrate.

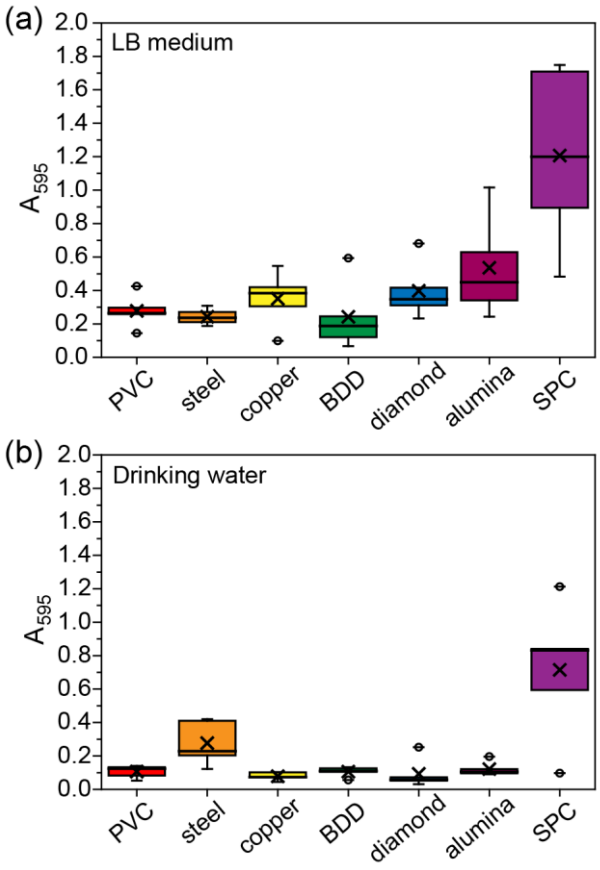

Figure 4.14. Extent of multispecies biofilm formation on different substrates. Data expressed as the absorbance of solubilised CV stain at 595 nm. Biofilm formation was assessed after 48 h at 37 °C in (a) LB medium and (b) drinking water. Data from five replicates is presented as a boxplot, where crosses and bars indicate mean and median absorbance values respectively, whiskers extend to values within 1.5 times the interquartile range, and circles specify outliers.

Comparison of the overall amount of multispecies biofilm formed with the overall amount of *P. aeruginosa* MPAO1 monospecies biofilm revealed that there was no significant difference in the quantity (biomass) of biofilm formed in either LB medium or drinking water (paired *t* test, p = 0.2 and 0.1, respectively). These findings suggest that interspecific interactions of cooperative or competitive nature

between bacterial species did not substantially impact biofilm formation over the duration of the experiment.[61,62] Similar to the *P. aeruginosa* monospecies biofilm data, the amount of multispecies biofilm formed in the presence of drinking water was significantly lower than in LB medium (paired *t* test, $p < 0.05$). A rank-order comparative analysis of the multispecies biofilm formation across substrates also revealed a statistical dependence on the growth media ($r_s = 0.11$, $p = 0.78$). When performing the experiments in LB, the lowest amount of multispecies biofilm was detected on O-BDD ($A_{595} = 0.24 \pm 0.21$) while the highest biofilm biomass was detected on SPC ($A_{595} = 1.21 \pm 0.54$), corroborating the results of *P. aeruginosa* MPAO1 monospecies biofilm (**Figure 4.6**). The amount of biofilm on SPC was approximately three times higher than most other substrates, but was only statistically significantly higher than BDD (Kruskal-Wallis, $p < 0.05$; post-hoc Dunn's test, $p < 0.05$). The experiments in drinking water similarly showed the highest amount of multispecies biofilm biomass on SPC ($A_{595} = 0.72 \pm 0.41$). The substrate with the second highest multispecies biomass was steel ($A_{595} = 0.28 \pm 0.13$), with all other substrates showing comparable values ($A_{595} = 0.10 \pm 0.02$).

4.4.4 *P. aeruginosa* biofilm formation on modified diamond substrates

To obtain insight into the role surface roughness and hydrophobicity plays in biofilm formation, quantitative measurements of surface roughness and hydrophobicity (**Table 4.1**) were plotted against *P. aeruginosa* monospecies and multispecies biomass formed (**Figure 4.15**). The area of each bubble depicts the mass of biofilm formed on each of the substrates.

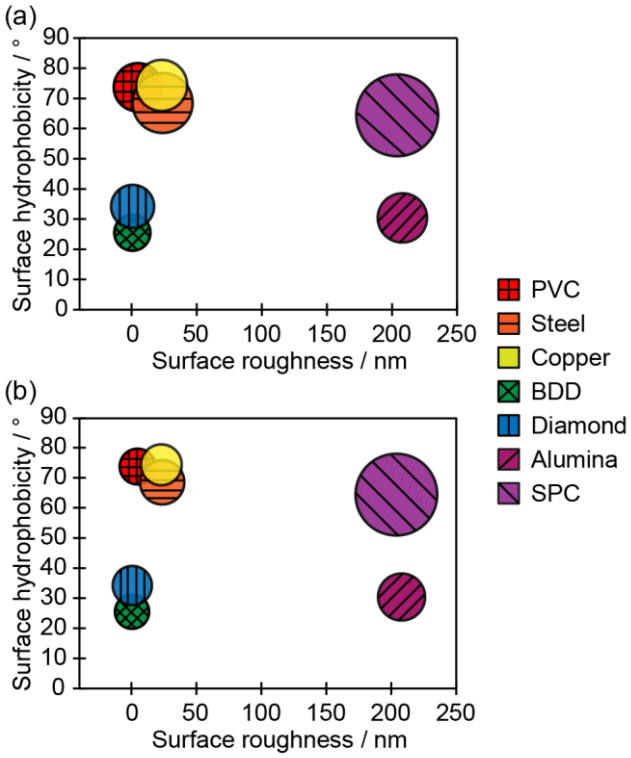

Figure 4.15. Bubble plot correlating substrate surface roughness and hydrophobicity with the overall extent of (a) P. aeruginosa MPAO1 monospecies and (b) multispecies biofilm formation. The area of the bubbles depict the mass of biofilm formed on each of the substrates, for all conditions studied, as assessed by CV, where values are expressed as the average normalised absorbance of solubilised CV stain at 595 nm (n = 3 for (a) and n = 5 for (b)).

In order to understand the origins of the low biofouling characteristics of O-BDD, further studies were carried out to assess the impact of both boron doping and surface termination on biofilm formation at 37 °C in LB medium on modified BDD substrates. The surface roughness of the BDD/diamond substrates employed for these studies was kept very similar, in order to exclude roughness effects (**Table 2**). Undoped and metal-like doped BDD substrates were employed along with O- and H-terminated BDD/diamond. The O-terminated polycrystalline surface presents a variety of different oxygen functional groups including C=O, C–O–C and C–OH.[23] Experiments also explored the effect of deliberately increasing the surface roughness

of O-terminated BDD/diamond, using a laser roughening approach. FE-SEM images of the bare substrates are found in **Figure 4.16**.

Table 4.2. Physical properties of the diamond and BDD substrates. Contact angle, surface roughness, and total surface area values listed as mean ± SD (n = 3). *Data for these substrates are repeated from Table 4.1 for ease of comparison.

Substrate	**Contact angle / °**	**Surface roughness, R_a / nm**	**Geometric surface area / mm^2**	**Total surface area / mm^2**
O-BDD (smooth)*	25.5 ± 1.7	0.49 ± 0.04	12.6	12.6 ± 0.03
O-BDD (rough)	22.6 ± 4.9	118 ± 11	12.6	16.3 ± 2.7
H-BDD (smooth)	117.5 ± 6.5	0.18 ± 0.01	12.6	12.6 ± 0.01
O-Diamond (smooth)*	34.2 ± 0.3	0.72 ± 0.16	12.6	12.6 ± 0.06
O-Diamond (rough)	26.7 ± 7.0	100 ± 30	12.6	13.8 ± 0.46
H-Diamond (smooth)	96.3 ± 5.3	0.63 ± 0.21	12.6	12.6 ± 0.01

Figure 4.16 shows FE-SEM images of the bare surface of the diamond substrates after modification. H-terminated substrates are smooth; Rough substrates are O-terminated.

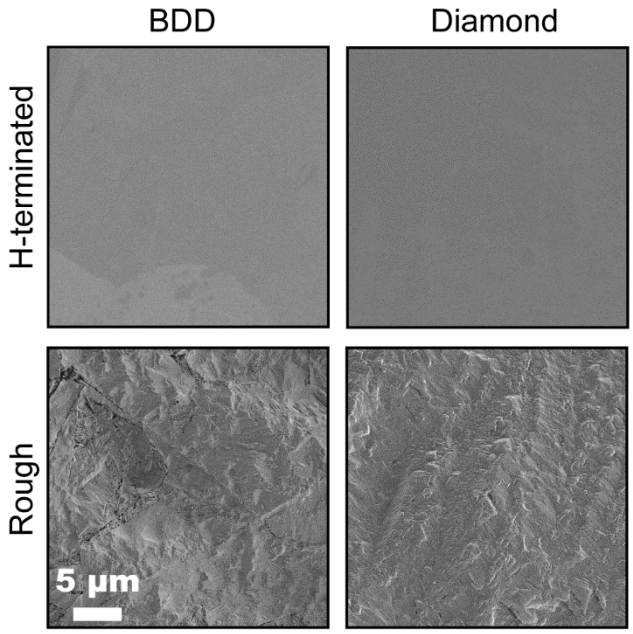

Figure 4.16. FE-SEM images of the bare surface of the modified diamond substrates.

Water contact angle measurements, which represent the interplay between polar and dispersion substrate-water interactions,[63] were recorded on all of the BDD and diamond substrates to provide information on the hydrophobicity/hydrophilicity of the surface (**Table 4.2**). Interestingly, O-BDD shows the lowest contact angle of all surfaces examined, including those of the other materials investigated (**Table 4.1**), indicating that it is the most hydrophilic. In contrast, the H-BDD surface presents the most hydrophobic surface, demonstrating the huge changes in wettability possible on a BDD/diamond surface simply by changing the surface termination. Importantly, this can take place under conditions which leave the substrate topography[23] and mechanical properties (stiffness)[36] unchanged.

To determine the quantity of biofilm formed on the surface of the modified diamond and BDD substrates, CLSM was applied.[8,43] Whilst CV assays are useful, the values obtained for the destained *P. aeruginosa* monospecies and multispecies biofilm on BDD (and diamond) were close to the detection limit of the technique. Thus, to more

precisely assess the impact of the surface roughness and hydrophobicity on biofilm formation, quantitative analysis of the fluorescence intensity from the CLSM images was undertaken for the modified diamond substrates in addition to the original substrates (**Figure 4.17**). A strong positive correlation was observed between CLSM and CV assay results for both *P. aeruginosa* monospecies and multispecies biofilm formation on all substrates (r_s = 0.8, p < 0.1), largely supporting the use of either of the quantitative methods for comparative studies.

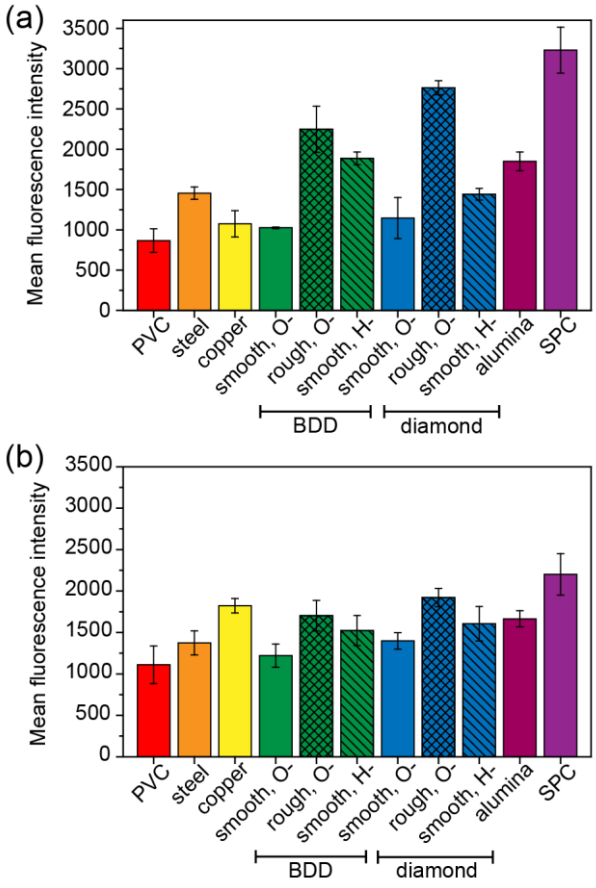

Figure 4.17. Fluorescence intensity of propidium iodide stained (a) P. aeruginosa monospecies and (b) multispecies biofilms formed on all substrates. BDD and diamond substrates were modified to have three different surface characteristics: O-terminated (hydrophilic) and smooth, O-terminated and rough, and H-terminated (hydrophobic) and smooth. Biofilm formation determined after 48 h bacterial growth at 37 °C in LB medium. CLSM images of the biofilms were obtained, and each image was analysed to record the mean fluorescence intensity of propidium iodide at 566–718 nm. Bars represent mean ± SD after triplicate analysis.

For O-termination, when evaluating the rough O-BDD and rough O-diamond with their smooth analogues, the extent of *P. aeruginosa* monospecies biofilm formation was significantly greater (*t* test, $p < 0.05$) on the rough compared to smooth surfaces. The mean fluorescence intensity was approximately 2.2 and 2.4 times higher, for O-BDD and O-diamond, respectively, compared to the smooth O-surfaces. Previous *P. aeruginosa* SEM studies with nanocrystalline and microcrystalline diamond (same surface termination) found the numbers of adhering bacteria were greater for microcrystalline diamond than nanodiamond (rms roughness 88.9 nm and 49.9 nm, respectively).[30] On the basis of our studies, we speculate that our observations are most likely due to surface roughness increasing attachment sites on the surface. However, there may also be changes in substrate chemical functionality, occurring as a result of the roughening process, which can also influence bacterial adhesion.[36,64] This could account for the slightly increased hydrophilicity of the rough O-BDD and O-diamond compared to their smooth counterparts.

When comparing the smooth H-terminated BDD and smooth H-diamond with their O-terminated smooth equivalents, the amount of biofilm formed was significantly higher (*t* test, $p < 0.05$) on H-terminated substrates, clearly showing the role that this factor plays under conditions independent of surface roughness. The average fluorescence intensity was 1.8 times and 1.3 higher on H-terminated smooth BDD and H-diamond, respectively, compared to their O-terminated counterparts. Note that the hydrophobicity of H-BDD was greater than H-diamond (**Table 4.2**).

The extent of multispecies biofilm formation on the modified diamond substrates was also significantly greater on the rough O-BDD and rough O-diamond substrates than on the smooth O-BDD and O-diamond surfaces (*t* test, $p < 0.05$), with the mean fluorescence intensity 1.4 times higher for both rougher substrates. The extent of

multispecies biofilm formation on the H-BDD and H-diamond smooth substrates was marginally greater than the O-terminated smooth BDD and diamond surfaces (*t* test, $p = 0.08$ for BDD, $p = 0.2$ for diamond).

FE-SEM performed on all BDD and diamond substrates largely supports the CLSM data, and representative images are shown in **Figure 4.18** for *P. aeruginosa* monospecies. Further FE-SEM imaging of multispecies biofilm formation on all the substrates used in this study are shown in **Figure 4.19**. As shown by **Figure 4.18**, biofilm formation on the rough O-BDD and rough O-diamond substrates resulted in a thicker, uniform biofilm structure. Conversely, the O-terminated smooth substrates showed adhesion of individual bacteria but little evidence of biofilm formation and colonisation. Biofilms on the smooth H-BDD and H-diamond were heterogeneous across the substrates, but have noticeably increased bacterial cell density compared to their O-smooth counterparts though are not as dense as the O-rough diamond and BDD surfaces.

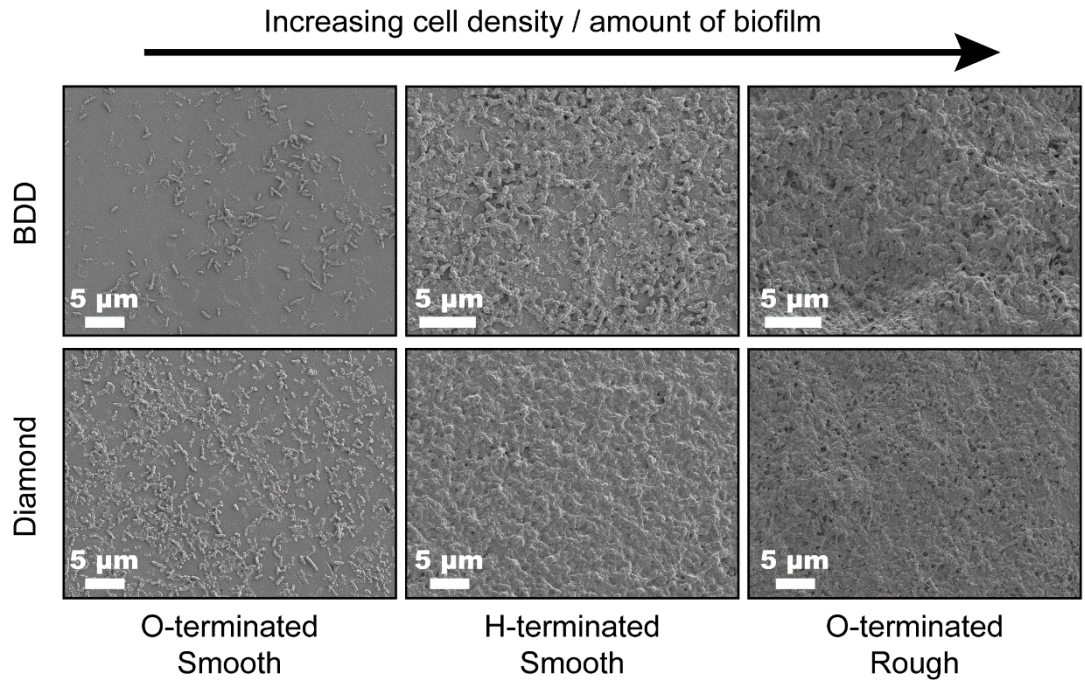

Figure 4.18. FE-SEM images of P. aeruginosa monospecies biofilms formed on BDD and diamond, with three different surface characteristics: O-terminated (hydrophilic) and smooth, H-terminated (hydrophobic) and smooth, and O-terminated and rough.

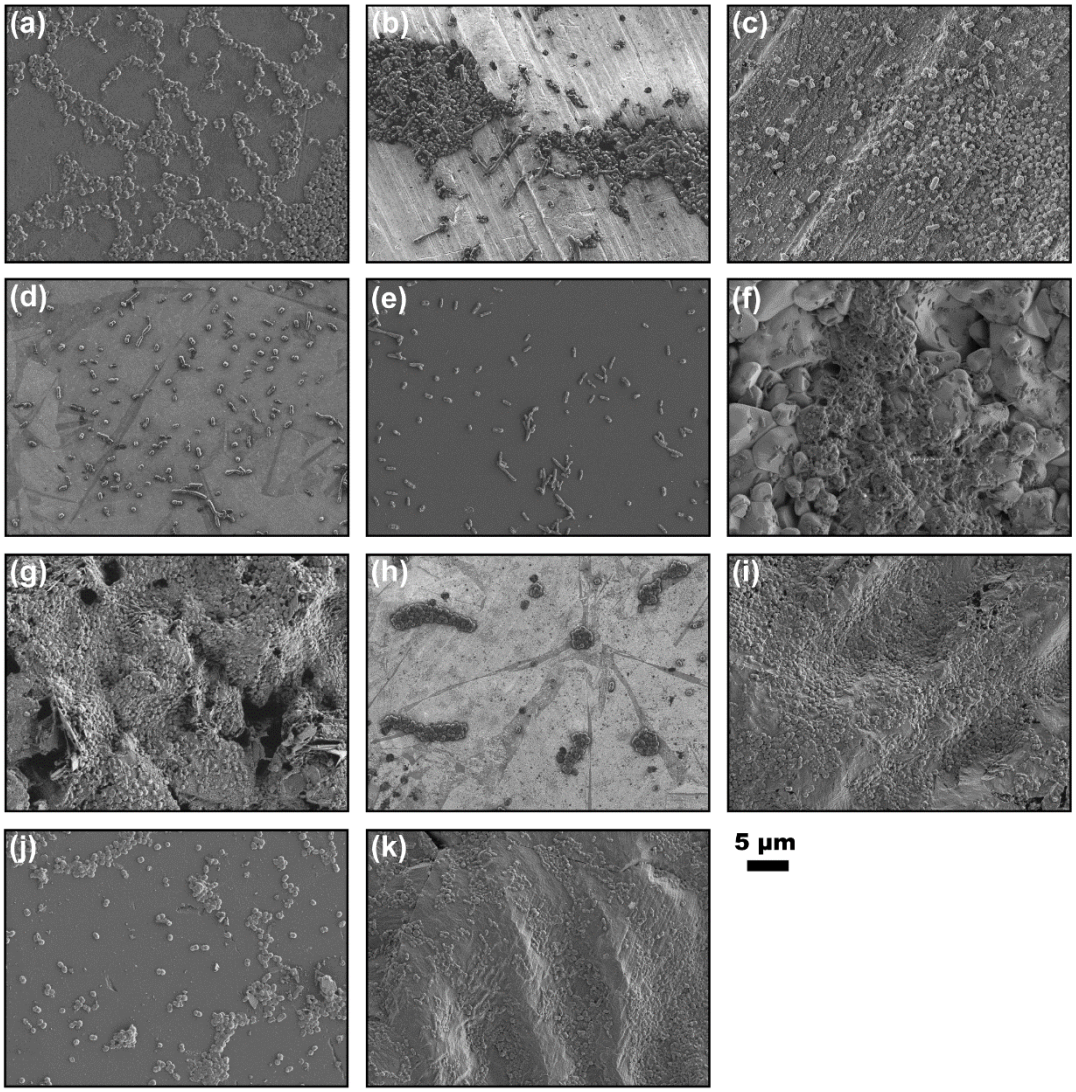

Figure 4.19. FE-SEM images of multispecies biofilms formed on (a) PVC, (b) steel, (c) copper, (d) O-BDD (smooth), (e) O-diamond (smooth), (f) alumina, (g) SPC, (h) H-BDD (smooth), (i) O-BDD (rough), (j) H-diamond (smooth), and (k) O-diamond (rough) after 48 h bacterial growth in LB medium at 37 °C.

It is clear from the results presented that surface termination on BDD and diamond plays a significant role in influencing bacterial attachment and biofilm formation capabilities, with H-termination strongly favouring biofilm formation. This suggests that *P. aeruginosa* and the multispecies bacteria are presenting a more hydrophobic outer cell wall to the surface, resulting in favourable hydrophobic and non-polar interactions, along with weak van der Waals interactions.[33,34,38,59,65–67] For water on

H-diamond, simulations[68] have shown that although the C–H bond on diamond is polarised ($C^{\delta-}$—$H^{\delta+}$), it only acts as a weak hydrogen bond donor with water. It is the dispersion forces that dominate significantly over any electrostatic contribution, leading to low adsorption energies for water and a high contact angle. In contrast, for O-diamond the bond polarity is reversed ($C^{\delta+}$—$O^{\delta-}$)[23,69] and strong electrostatic hydrogen bonding effects are now significant, leading to much greater water adsorption energies and a lower contact angle. It is these extreme properties that are likely to be disfavouring adhesion of the hydrophobic bacteria to the O-terminated surface.[70] Additionally, since bacterial cell walls are mostly negatively charged,[55] we also believe that bond polarity (dipole) of the C–O bond plays a role in reducing adhesion of the bacteria on O-BDD (and O-diamond). This repulsive effect is likely to be affected by the ionic strength of the growth medium.[38,55] Considering the application of BDD to electrochemical sensing in aquatic environments,[6,71] in future work we aim to investigate extensively the roles that electrostatics and surface potential have on bacterial adherence and biofilm formation on BDD, especially as a route to minimise biofouling even further.

Importantly, we also show that doping diamond with boron affects bacterial attachment. For example, comparing O-BDD with O-diamond, qualitative FE-SEM investigation (**Figure 4.18**) and quantitative CLSM analysis (**Figure 4.17**) both indicate a lower bacterial cell density on the boron doped surface, whilst the opposite is true for the H-terminated BDD surface. We find that doping with BDD renders the O-terminated surface more hydrophilic (lower contact angle, **Table 4.2**), and the H-terminated more hydrophobic (higher contact angle, **Table 4.2**), highlighting again the role that hydrophobicity (and associated factors) plays for diamond/BDD substrates. Although we cannot be sure of the exact origin of the changes in

wettability due to boron doping, there are a variety of possible influences which affect the way that water interacts with the BDD surface, which in turn affects bacterial adhesion. These include the role of boron in withdrawing electron density between surface C and –O or –H bonds, as well as surface electrolyte potential and electron charge distribution (density of states) differences.[72] Future studies will look to model the BDD-water interface to determine the exact origin of this phenomenon.

4.5 Conclusions

A comprehensive, systematic study of bacterial biofilm formation has been carried out using five different strains of *P. aeruginosa*, in order to compare monospecies biofilm formation on O-BDD with PVC, stainless steel, copper, O-diamond, alumina, and SPC as a function of the growth medium (LB *vs.* drinking water) and temperature (37 °C *vs.* 20 °C). Further studies also investigated *A. baumannii*, *A. hydrophila*, *K. pneumoniae* and *S. aureus* bacterial multispecies biofilm formation. SPC was consistently found to have the highest amount of biofilm formation, whereas O-BDD was found to have the relatively lowest levels. Similar trends were observed even after correcting for total surface area, indicating that surface roughness is not the only factor controlling bacterial adhesion and biofilm formation.

Analysis of surface hydrophobicity revealed that O-BDD was the most hydrophilic surface due to strong electrostatic interactions with water, providing evidence for hydrophilicity (and associated factors) being very important in reducing biofilm formation for these bacteria on this surface. This was further confirmed by keeping surface topography fixed and switching surface termination to H-, which is strongly hydrophobic, and observing increased biofouling. Importantly, boron doping was

also found to play a role with boron presence resulting in either increased (if O-terminated) or decreased (if H-terminated) hydrophilicity, compared to undoped diamond, which in turn resulted in decreased or increased biofilm formation, respectively.

This study highlights the importance of O-BDD as a low biofouling electrode for long-term electrochemical monitoring in aquatic environments. Whilst the high hydrophilic properties are clearly advantageous, to fully realise O-BDD's low biofouling capabilities the surface should also be prepared as smooth as possible, conclusions that can also be extended to other materials used as electrodes or electrode packaging, for this bacterial system. We anticipate that further reductions in the low biofouling attributes of O-BDD will be possible by exploiting biasing at an electrochemical potential during rest periods in the electrochemical sensing procedure, to prevent bacterial adhesion via electrostatic repulsion.

4.6 References

(1) *In Situ Monitoring of Aquatic Systems: Chemical Analysis and Speciation*, 1st ed.; Buffle, J., Horvai, G., Eds.; John Wiley & Sons, Inc.: Chichester, 2001.

(2) Howell, K. A.; Achterberg, E. P.; Braungardt, C. B.; Tappin, A. D.; Worsfold, P. J.; Turner, D. R. Voltammetric in Situ Measurements of Trace Metals in Coastal Waters. *TrAC - Trends Anal. Chem.* **2003**, *22* (11), 828–835.

(3) Prien, R. D. The Future of Chemical in Situ Sensors. *Mar. Chem.* **2007**, *107* (3), 422–432.

(4) Delauney, L.; Compère, C.; Lehaitre, M. Biofouling Protection for Marine Environmental Sensors. *Ocean Sci.* **2010**, *6* (2), 503–511.

(5) Klahre, J.; Flemming, H. C. Monitoring of Biofouling in Papermill Process Waters. *Water Res.* **2000**, *34* (14), 3657–3665.

(6) Flemming, H. C. Microbial Biofouling: Unsolved Problems, Insufficient Approaches, and Possible Solutions. In *Biofilm Highlights*; Flemming, H. C., Wingender, J., Szewzyk, U., Eds.; Springer-Verlag: Berlin, 2011; pp 81–110.

(7) Flemming, H. C. Biofouling in Water Systems - Cases, Causes and Countermeasures. *Appl. Microbiol. Biotechnol.* **2002**, *59* (6), 629–640.

(8) Lewandowski, Z.; Beyenal, H. *Fundamentals of Biofilm Research*, 2nd Ed.; CRC Press: Boca Raton, 2017.

(9) Donlan, R. M. Biofilm Formation: A Clinically Relevant Microbiological Process. *Clin. Infect. Dis.* **2001**, *33* (8), 1387–1392.

(10) Costerton, J. W.; Cheng, K.-J.; Greesy, G. G.; Ladd, T. I.; Nickel, J. C.; Dasgupta, M.; Marrie, T. J. Bacterial Biofilms in Nature and Disease. *Ann. Rev. Microbiol.* **1987**, *41*, 435–464.

(11) O'Toole, G.; Kaplan, H. B.; Kolter, R. Biofilm Formation as Microbial Development. *Annu. Rev. Microbiol.* **2000**, *54* (1), 49–79.

(12) Bixler, G. D.; Bhushan, B. Biofouling: Lessons from Nature. *Philos. Trans. R. Soc. A Math. Phys. Eng. Sci.* **2012**, *370* (1967), 2381–2417.

(13) *Biofilms - Science and Technology*, 1st Ed.; Melo, L. F., Bott, T. R., Fletcher, M., Capdeville, B., Eds.; Plenum Publishing Corporation, 1992.

(14) Carpentier, B.; Cerf, O. Biofilms and Their Consequences, with Particular Reference to Hygiene in the Food Industry. *J. Appl. Bacteriol.* **1993**, *75* (6), 499–511.

(15) Garrett, T. R.; Bhakoo, M.; Zhang, Z. Bacterial Adhesion and Biofilms on Surfaces. *Prog. Nat. Sci.* **2008**, *18* (9), 1049–1056.

(16) Wingender, J.; Flemming, H. C. Biofilms in Drinking Water and Their Role as Reservoir for Pathogens. *Int. J. Hyg. Environ. Health* **2011**, *214* (6), 417–423.

(17) Kostakioti, M.; Hadjifrangiskou, M.; Hultgren, S. J. Bacterial Biofilms: Development, Dispersal, and Therapeutic Strategies in the Dawn of the Postantibiotic Era. *Cold Spring Harb. Perspect. Med.* **2013**, *3* (4), a010306–a010306.

(18) Chen, M.; Yu, Q.; Sun, H. Novel Strategies for the Prevention and Treatment of Biofilm Related Infections. *Int. J. Mol. Sci.* **2013**, *14* (9), 18488–18501.

(19) Banerjee, I.; Pangule, R. C.; Kane, R. S. Antifouling Coatings: Recent Developments in the Design of Surfaces That Prevent Fouling by Proteins, Bacteria, and Marine Organisms. *Adv. Mater.* **2011**, *23* (6), 690–718.

(20) Gu, H.; Ren, D. Materials and Surface Engineering to Control Bacterial Adhesion and Biofilm Formation: A Review of Recent Advances. *Front. Chem. Sci. Eng.* **2014**, *8* (1), 20–33.

(21) Tripathy, A.; Sen, P.; Su, B.; Briscoe, W. H. Natural and Bioinspired Nanostructured Bactericidal Surfaces. *Adv. Colloid Interface Sci.* **2017**, *248*, 85–104.

(22) Chamsaz, E. A.; Mankoci, S.; Barton, H. A.; Joy, A. Nontoxic Cationic Coumarin Polyester Coatings Prevent Pseudomonas Aeruginosa Biofilm Formation. *ACS Appl. Mater. Interfaces* **2017**, *9* (8), 6704–6711.

(23) Macpherson, J. V. A Practical Guide to Using Boron Doped Diamond in

Electrochemical Research. *Phys. Chem. Chem. Phys.* **2015**, *17* (5), 2935–2949.

(24) Joseph, M. B.; Bitziou, E.; Read, T. L.; Meng, L.; Palmer, N. L.; Mollart, T. P.; Newton, M. E.; MacPherson, J. V. Fabrication Route for the Production of Coplanar, Diamond Insulated, Boron Doped Diamond Macro- and Microelectrodes of Any Geometry. *Anal. Chem.* **2014**, *86* (11), 5238–5244.

(25) Ayres, Z. J.; Borrill, A. J.; Newland, J. C.; Newton, M. E.; Macpherson, J. V. Controlled sp2 Functionalization of Boron Doped Diamond as a Route for the Fabrication of Robust and Nernstian pH Electrodes. *Anal. Chem.* **2016**, *88* (1), 974–980.

(26) Meijs, S.; Alcaide, M.; Sørensen, C.; McDonald, M.; Sørensen, S.; Rechendorff, K.; Gerhardt, A.; Nesladek, M.; Rijkhoff, N. J. M.; Pennisi, C. P. Biofouling Resistance of Boron-Doped Diamond Neural Stimulation Electrodes Is Superior to Titanium Nitride Electrodes in Vivo. *J. Neural Eng.* **2016**, *13* (5), 56011.

(27) Wilson, R. E.; Stoianov, I.; O'Hare, D. Biofouling and in Situ Electrochemical Cleaning of a Boron-Doped Diamond Free Chlorine Sensor. *Electrochem. commun.* **2016**, *71*, 79–83.

(28) Chong, K. F.; Loh, K. P.; Vedula, S. R. K.; Lim, C. T.; Sternschulte, H.; Steinmüller, D.; Sheu, F. S.; Zhong, Y. L. Cell Adhesion Properties on-Photochemically Functionalized Diamond. *Langmuir* **2007**, *23* (10), 5615–5621.

(29) Kloss, F. R.; Gassner, R.; Preiner, J.; Ebner, A.; Larsson, K.; Hächl, O.; Tuli, T.; Rasse, M.; Moser, D.; Laimer, K.; et al. The Role of Oxygen Termination of Nanocrystalline Diamond on Immobilisation of BMP-2 and Subsequent Bone Formation. *Biomaterials* **2008**, *29* (16), 2433–2442.

(30) Medina, O.; Nocua, J.; Mendoza, F.; Gómez-Moreno, R.; Ávalos, J.; Rodríguez, C.; Morell, G. Bactericide and Bacterial Anti-Adhesive Properties of the Nanocrystalline Diamond Surface. *Diam. Relat. Mater.* **2012**, *22*, 77–81.

(31) Budil, J.; Matyska Lišková, P.; Artemenko, A.; Ukraintsev, E.; Gordeev, I.; Beranová, J.; Konopásek, I.; Kromka, A. Anti-Adhesive Properties of Nanocrystalline Diamond Films against *Escherichia Coli* Bacterium: Influence of Surface Termination and Cultivation Medium. *Diam. Relat. Mater.* **2018**, *83*, 87–93.

(32) Jakubowski, W.; Bartosz, G.; Niedzielski, P.; Szymanski, W.; Walkowiak, B. Nanocrystalline Diamond Surface Is Resistant to Bacterial Colonization. *Diam. Relat. Mater.* **2004**, *13* (10), 1761–1763.

(33) Merritt, K.; An, Y. H. Factors Influencing Bacterial Adhesion. In *Handbook of Bacterial Adhesion: Principles, Methods, and Applications*; An, Y. H., Friedman, R. J., Eds.; Humana Press: Totowa, 2000; pp 53–72.

(34) Cerca, N.; Pier, G. B.; Vilanova, M.; Oliveira, R.; Azeredo, J. Quantitative Analysis of Adhesion and Biofilm Formation on Hydrophilic and Hydrophobic Surfaces of Clinical Isolates of *Staphylococcus Epidermidis*.

Res. Microbiol. **2005**, *156* (4), 506–514.

(35) Hsu, L. C.; Fang, J.; Borca-Tasciuc, D. A.; Worobo, R. W.; Moraru, C. I. Effect of Micro- and Nanoscale Topography on the Adhesion of Bacterial Cells to Solid Surfaces. *Appl. Environ. Microbiol.* **2013**, *79* (8), 2703–2712.

(36) Song, F.; Koo, H.; Ren, D. Effects of Material Properties on Bacterial Adhesion and Biofilm Formation. *J. Dent. Res.* **2015**, *94* (8), 1027–1034.

(37) Donlan, R. M. Biofilms: Microbial Life on Surfaces. *Emerg. Infect. Dis.* **2002**, *8* (9), 881–890.

(38) Tuson, H. H.; Weibel, D. B. Bacteria-Surface Interactions. *Soft Matter* **2013**, *9* (17), 4368–4380.

(39) Røder, H. L.; Sørensen, S. J.; Burmølle, M. Studying Bacterial Multispecies Biofilms: Where to Start? *Trends Microbiol.* **2016**, *24* (6), 503–513.

(40) Emmerson, A. M. Emerging Waterborne Infections in Health-Care Settings. *Emerg. Infect. Dis.* **2001**, *7* (2), 272–276.

(41) Liu, S.; Gunawan, C.; Barraud, N.; Rice, S. A.; Harry, E. J.; Amal, R. Understanding, Monitoring, and Controlling Biofilm Growth in Drinking Water Distribution Systems. *Environ. Sci. Technol.* **2016**, *50* (17), 8954–8976.

(42) Szewzyk, U.; Szewzyk, R.; Manz, W.; Schleifer, K.-H. Microbiological Safety of Drinking Water. *Annu. Rev. Microbiol.* **2000**, *54* (1), 81–127.

(43) Azeredo, J.; Azevedo, N. F.; Briandet, R.; Cerca, N.; Coenye, T.; Costa, A. R.; Desvaux, M.; Di Bonaventura, G.; Hébraud, M.; Jaglic, Z.; et al. Critical Review on Biofilm Methods. *Crit. Rev. Microbiol.* **2017**, *43* (3), 313–351.

(44) Kukavica-Ibrulj, I.; Bragonzi, A.; Paroni, M.; Winstanley, C.; Sanschagrin, F.; O'Toole, G. A.; Levesque, R. C. In Vivo Growth of *Pseudomonas Aeruginosa* Strains PAO1 and PA14 and the Hypervirulent Strain LESB58 in a Rat Model of Chronic Lung Infection. *J. Bacteriol.* **2008**, *190* (8), 2804–2813.

(45) Andreozzi, E.; Barbieri, F.; Ottaviani, M. F.; Giorgi, L.; Bruscolini, F.; Manti, A.; Battistelli, M.; Sabatini, L.; Pianetti, A. Dendrimers and Polyamino-Phenolic Ligands: Activity of New Molecules Against *Legionella Pneumophila* Biofilms. *Front. Microbiol.* **2016**, *7* (289), 1–16.

(46) Rendueles, O.; Ghigo, J. M. Multi-Species Biofilms: How to Avoid Unfriendly Neighbors. *FEMS Microbiol. Rev.* **2012**, *36* (5), 972–989.

(47) Mah, T. C.; O'Toole, G. A. Mechanisms of Biofilm Resistance to Antimicrobial Agents. *Trends Microbiol.* **2001**, *9* (1), 34–39.

(48) Merritt, J. H.; Kadouri, D. E.; O'Toole, G. A. Growing and Analyzing Static Biofilms. *Curr. Protoc. Microbiol.* **2005**, *0* (1), 1B.1.1-1B.1.17.

(49) Chandra, J.; Mukherjee, P. K.; Ghannoum, M. A. In Vitro Growth and Analysis of Candida Biofilms. *Nat. Protoc.* **2008**, *3* (12), 1909–1924.

(50) Toole, G. A. O.; Kolter, R. Initiation of Biofilm Formation in Pseudomonas Fluorescens WCS365 Proceeds via Multiple, Convergent Signalling Pathways: A Genetic Analysis. *Mol. Microbiol.* **1998**, *28* (3), 449–461.

(51) O'Toole, G. A. Microtiter Dish Biofilm Formation Assay. *J. Vis. Exp.* **2011**, No. 47, 10–11.

(52) Kwasny, S. M.; Opperman, T. J. Static Biofilm Cultures of Gram-Positive Pathogens Grown in a Microtiter Format Used for Anti-Biofilm Drug Discovery. *Curr. Protoc. Pharmacol.* **2010**, 1–27.

(53) Monod, J. The Growth of Bacterial Cultures. *Annu. Rev. Microbiol.* **1949**, *3* (1), 371–394.

(54) O'Toole, G. A. Jekyll or Hide? *Nature* **2004**, *432* (7018), 680–681.

(55) Renner, L. D.; Weibel, D. B. Physiochemical Regulation of Biofilm Formation. *MRS Bull* **2011**, *36* (5), 347–355.

(56) Volpe, G. G.; Volpe, G. G. The Topography of the Environment Alters the Optimal Search Strategy for Active Particles. *Proc. Natl. Acad. Sci.* **2017**, *114* (43), 11350–11355.

(57) Bechinger, C.; Di Leonardo, R.; Löwen, H.; Reichhardt, C.; Volpe, G. G.; Volpe, G. G. Active Particles in Complex and Crowded Environments. *Rev. Mod. Phys.* **2016**, *88* (4), 45006.

(58) Watnick, P.; Kolter, R. Biofilm, City of Microbes. *J. Bacteriol.* **2000**, *182* (10), 2675–2679.

(59) Dunne, W. M. Bacterial Adhesion: Seen Any Good Biofilms Lately? *Clin. Microbiol. Rev.* **2002**, *15* (2), 155–166.

(60) MacEachran, D. P.; O'Toole, G. A. Do Not Fear Commitment: The Initial Transition to a Surface Lifestyle by Pseudomonads. In *The Biofilm Mode of Life: Mechanisms and Adaptations*; Kjelleberg, S., Givskov, M., Eds.; Horizon Bioscience, 2007; pp 23–35.

(61) Burmølle, M.; Ren, D.; Bjarnsholt, T.; Sørensen, S. J. Interactions in Multispecies Biofilms: Do They Actually Matter? *Trends Microbiol.* **2014**, *22* (2), 84–91.

(62) Lee, K. W. K.; Periasamy, S.; Mukherjee, M.; Xie, C.; Kjelleberg, S.; Rice, S. A. Biofilm Development and Enhanced Stress Resistance of a Model, Mixed-Species Community Biofilm. *ISME J.* **2014**, *8* (4), 894–907.

(63) Bos, R.; Mei, H. C. Van Der; Busscher, H. J. Physico-Chemistry of Initial Microbial Adhesive Interactions - Its Mechanisms and Methods for Study. *FEMS Microbiol. Rev.* **2017**, *23*, 179–230.

(64) Oh, Y. J.; Lee, N. R.; Jo, W.; Jung, W. K.; Lim, J. S. Effects of Substrates on Biofilm Formation Observed by Atomic Force Microscopy. *Ultramicroscopy* **2009**, *109* (8), 874–880.

(65) Berne, C.; Ellison, C. K.; Ducret, A.; Brun, Y. V. Bacterial Adhesion at the Single-Cell Level. *Nat. Rev. Microbiol.* **2018**, *16* (10), 616–627.

(66) Fletcher, M.; Loeb, G. I. Influence of Substratum Characteristics on the Attachment of a Marine Pseudomonad to Solid Surfaces. *Appl. Environ. Microbiol.* **1979**, *37* (1), 67–72.

(67) Pringle, J. H.; Fletcher, M. Influence of Substratum Wettability on Attachment of Freshwater Bacteria to Solid Surfaces. *Appl. Environ. Microbiol.* **1983**, *45* (3), 811–817.

(68) Mayrhofer, L.; Moras, G.; Mulakaluri, N.; Rajagopalan, S.; Stevens, P. A.; Moseler, M. Fluorine-Terminated Diamond Surfaces as Dense Dipole Lattices: The Electrostatic Origin of Polar Hydrophobicity. *J. Am. Chem. Soc.* **2016**, *138* (12), 4018–4028.

(69) Kondo, T.; Honda, K.; Tryk, D. A.; Fujishima, A. AC Impedance Studies of Anodically Treated Polycrystalline and Homoepitaxial Boron-Doped Diamond Electrodes. *Electrochim. Acta* **2003**, *48* (19), 2739–2748.

(70) Rumbo, C.; Tamayo-Ramos, J. A.; Caso, M. F.; Rinaldi, A.; Romero-Santacreu, L.; Quesada, R.; Cuesta-López, S. Colonization of Electrospun Polycaprolactone Fibers by Relevant Pathogenic Bacterial Strains. *ACS Appl. Mater. Interfaces* **2018**, *10* (14), 11467–11473.

(71) Sultana, S. T.; Babauta, J. T.; Beyenal, H. Electrochemical Biofilm Control: A Review. *Biofouling* **2015**, *31* (9–10), 745–758.

(72) Zhao, S.; Larsson, K. Theoretical Study of the Energetic Stability and Geometry of Terminated and B-Doped Diamond (111) Surfaces. *J. Phys. Chem. C* **2014**, *118* (4), 1944–1957.

5 The application of all-diamond conductivity sensors towards sensing in real world aquatic environments

5.1 Aims

Solution conductivity is one of the chief parameters to measure when monitoring water quality in a variety of industrial and environmental applications. These aquatic environments can encompass a wide range of natural waters or manufacturing process fluids, where the state of flow in these conditions is generally turbulent. *In situ* conductivity sensors that allow automatic, real-time measurement directly at the water source of interest are highly advantageous for process monitoring in these applications. The ability to measure local spatial and temporal variations in fluid composition and conductivity is of interest in many industrial and environmental processes, where turbulence is present to bring about the transport of matter and the mixing and reaction of components.

In this study, we evaluate the performance properties of an all-diamond conductivity sensor (comprised of two conducting boron doped diamond electrodes embedded in an insulating diamond platform) under real world aquatic environments. Specifically, two sensor applications were investigated. Firstly, natural environmental conditions were considered using river water in an artificial river flume, to assess potential for long-term continuous *in situ* monitoring. Then, the ability of the conductivity sensor for measuring local concentration variations (changes in conductivity) for use in an industrial setting were analysed by means of a circular pipe flow rig with an external marker fluid introduced into a flowing stream of ambient fluid, to determine the

response of the sensor to marked fluctuations in conductivity under turbulent flow conditions.

5.2 Introduction

5.2.1 Conductivity and aquatic environments

Solution conductivity measurements have found widespread use in a variety of industrial and environmental applications.[1] In such aquatic environments there is a critical need to monitor water quality, of which conductivity is one of the chief parameters to analyse in addition to properties such as pH, dissolved gases, organic content, and heavy metals.[2,3] For environmental applications in particular, there are a plethora of motives for measuring conductivity (water quality) in a wide range of natural waters, such as ground and surface water, seawater and coastal waters, spring water, mine waters, and river water.[3,4] Most of these motives revolve around the monitoring of human activities or natural processes in order to assess the impact of these and instigate any appropriate remedial actions.[5–7]

Monitoring in natural environments presents various problems. The classic problem is delay between sampling and analysis, but this is being addressed through the development of *in situ* analytical sensors that allow automatic, real-time measurement of variables directly at the water source of interest.[2,8] Indeed, the first *in situ* analyser for the marine environment was aimed at measuring conductivity and this is considered to be a turning point in marine chemistry.[9] However, one of the current limitations is the density of sampling available. The scales of variability in the natural environment are vast, as both spatial and temporal changes in a property can occur over short and long ranges.[5] For example, oceans cover large areas but

complex currents and tides can cause shifts in conductivity over the short-term (a tidal cycle) or the long-term (seasons or years). In addition, for conductivity sensing the ionic composition of natural waters can vary substantially. The ionic composition of river water arises predominantly from the bicarbonate anion, HCO_3^-, and Ca^{2+} cation, but also minor constituents being SO_4^{2-}, Cl^-, Mg^{2+}, and Na^+.[10] Whilst this can aid water quality analysis (*e.g.* effect of acid rain, surface water runoff), the drawback is the need for advanced temperature correction techniques.[11]

In addition to the natural environment, conductivity sensing is important for a wide variety of industrial applications, including pharmaceuticals,[12] textiles,[13] and food processing such as dairy, fruit juice, and wine.[14,15] Conductivity measurements are often used for process analysis, control, and optimisation, where there is a need for the measurement of both regular and varying point compositions.[16,17]

In both environmental and industrial monitoring situations, water quality characteristics fluctuate in response to changes caused by a host of factors.[18] Such changes may be either deliberate or unintentional. Therefore, conductivity sensors that are continuously monitoring will be expected to respond to the measurement of concentration fluctuations.[19,20]

5.2.2 Turbulent flows

The state of flow in rivers, oceans, and the atmosphere of our planet is generally turbulent. Hence, all associated problems such as erosion, migration of marine life, dispersion of pollutants, and atmospheric convection are dependent on the structure of turbulence.[21] Turbulence is difficult to define precisely, but can be observed

ubiquitously in the environment, for example in the movement of clouds, or smoke plumes rising upwards.[22]

The physical nature of turbulence is that of a random process. Turbulent flow is of a chaotic, unpredictable nature which is highly time and space dependent with a very large number of degrees of freedom.[23] Consider the injection of an external dye fluid into a circular pipe (**Figure 5.1a**) through which water is flowing through. This could, for example, represent the dispersion of some pollutant into a sewage pipe.[24] The dispersal and distribution of chemicals, pollutants, sediments, or particulate matter in drinking water systems and other flowing waters is also synonymous.[25,26] In other industrial and engineering applications turbulent flows are also prevalent, such as the processing of liquids, pipe lines, flows around vehicles (*e.g.* airplanes, ships, automobiles) and the mixing of reactants in chemical reactors, engines, furnaces, *etc.*[22]

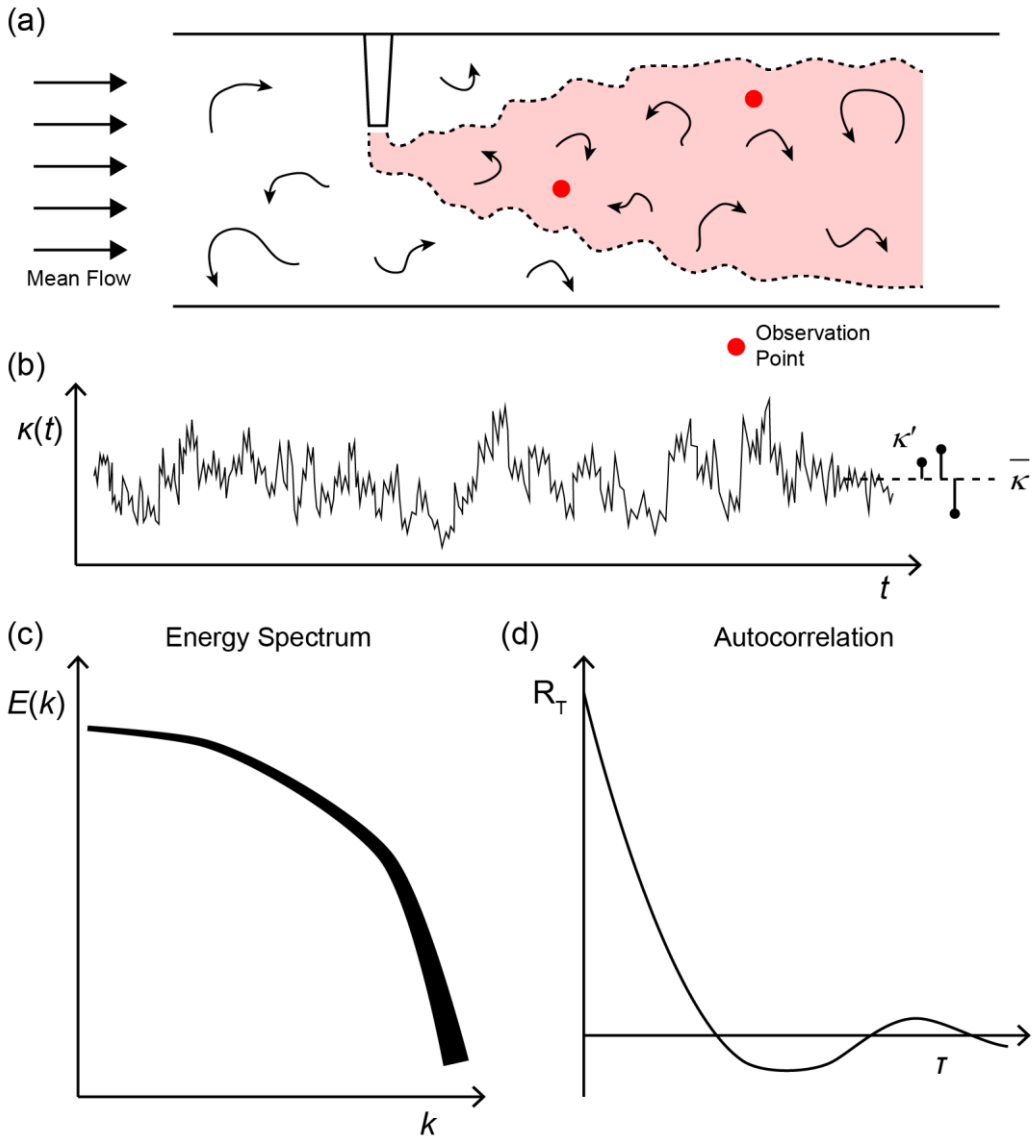

Figure 5.1. (a) Illustration of marker fluid injection into turbulent pipe flow. Thick black arrows indicate streamlines parallel to the mean flow direction of fluid through a pipe. Small black arrows indicate turbulent eddies of varying sizes. Red dotted area displays the marker fluid. (b) Sample of a measured conductivity trace in turbulent flow. This random process is characterised by a time average conductivity, $\overline{\kappa}$, and fluctuations about this value, κ'. (c) Typical energy spectrum, relating the energy content, *E*, contained in a particular frequency, *k*. Note that this is a logarithmic plot. (d) Typical autocorrelation function (R_T) with lag time, τ. Adapted from Pope, and Mathieu and Scott.[22,23]

Close to the injection point, the dye streak will begin to be agitated by the turbulent motions, becoming progressively less distinct with downstream distance. Eventually, mixing with the surrounding water will reduce the dye concentration to the extent that it is no longer visible.[22] Indeed, experiments of this nature hark back to those

conducted by Reynolds[27] and Taylor[28] when laying the foundations of the subject of turbulence.

A sensor measuring at a given observation point will produce a signal with a distinct "furriness" as a function of time (**Figure 5.1b**).[23] This not only reflects the random fluctuations present in turbulent flow, but also the existence of a continuum of different spatial and time scales in the dynamics of turbulence. Instabilities present in turbulent flow are responsible for the generation of large scale eddies (intense, random variations in space and time) which are unstable, giving rise to smaller scale eddies, and so on and so forth. Consequently, this cascade process results in a continuum of spatial scales, and considering the dye injection example, will range from the large scale bulk advection through the pipe through to the smallest dissipation scales of the external dye fluid.[23] If the dye was a markedly different conductivity than the ambient fluid, then the signal from a conductivity sensor placed in the flow would experience fluctuations proportional to the fluctuations in electrolyte concentration.[19]

The loss of randomness can be physically seen in the dependence of a flow property (*e.g.* conductivity, velocity, temperature) at a point in space ($\mathbf{x}$) at a given instance in time (t) compared to its value in the immediate neighbourhood ($\mathbf{x} \pm \Delta\mathbf{x}$, $t \pm \Delta t$). The quantities $\Delta\mathbf{x}$ and Δt over which a meaningful relationship exists are called the length and time scales of turbulence.[21,29] Experiments pertaining to measurement of local turbulent quantities are subject to difficulty, including limited probe response to high frequency fluctuations, and the need for rapid sampling of data to follow fast variation in flow properties and capture sufficiently long signals.[21]

5.2.3 Measures of turbulence

Although flow variables under turbulence are unpredictable in their detail, the statistical properties are reproducible and independent of time, and consequently we must consider the averages and probability distributions of flow properties.[22,23]

5.2.3.1 Intensity of turbulence

Any instantaneous flow quantity that is being measured (here, we use conductivity) can be written in the following form with respect to its mean and its fluctuating quantity:

$$\kappa_i(t) = \overline{\kappa_i} + \kappa'_i(t) \tag{5.1}$$

where $\overline{\kappa}$ is the time average of the conductivity and κ' is the superimposed conductivity fluctuations (**Figure 5.1b**). However, a measurement trace is made by taking *n* samples periodically. Then, if fluctuations in κ are being sampled:

$$\kappa_{\text{mean}} = \overline{\kappa} = \frac{1}{n}\sum_{i=1}^{n}\kappa_i \tag{5.2}$$

If the individual fluctuations about $\overline{\kappa}$ are $\kappa'_1 = \kappa_1 - \overline{\kappa}$, $\kappa'_2 = \kappa_2 - \overline{\kappa}$, *etc*. then the average value of κ' will be zero. However, the mean of the squares of the fluctuations is not equal to zero (since all are positive):

$$\overline{(\kappa')^2} = \frac{1}{n}\sum_{i=1}^{n}(\kappa'_i)^2 \tag{5.3}$$

The root mean square (RMS) of this quantity is the measure of the magnitude of the conductivity fluctuations about the mean value, and is known as the intensity of

turbulence.[30] The mean, $\overline{\kappa}$, and RMS of the fluctuations, $\frac{\sqrt{\overline{(\kappa')^2}}}{\overline{\kappa}}$, are two of the simplest and essential statistical quantities that must be determined from the signal.[31]

5.2.3.2 Energy spectrum

Flow property fluctuations are complex functions of time, and turbulence is composed of a superposition of eddies of varying sizes. The distribution of length and time scales is presented in terms of frequencies ($\kappa/\Delta\mathbf{x}$ Hz, for example). A particular turbulent field can be described in terms of the distribution of the fluctuations as a function of frequency, k.[21] Therefore, the signal obtained from a turbulent flow may have different strengths for different frequencies. For example, the low frequency portion of the κ trace may contain little energy whilst the high frequency portion contains much more. Hence, the spectrum of turbulence relates the energy content to the frequency.[30] Consider the band of frequencies between k and $k + dk$. Then, define E such that $E(k)dk$ is the contribution to $\overline{\kappa'^2}$ of the frequencies in this band. The mean squared fluctuation covering all frequencies is therefore:

$$\overline{\kappa'^2} = \int_0^\infty E(k)dk \tag{5.4}$$

where E is the spectral density function for the $\overline{\kappa'^2}$ component.[22,30]

Power spectral density (PSD) is a measure of how the power in a random signal is distributed amongst these different frequencies, therefore different shapes of the curve will indicate different distributions of the energy as a function of frequency.[32] The microscale of turbulence is chiefly determined by the higher frequencies.[30] Large frequencies correspond to small eddy sizes. Thus, very small eddy sizes result

in dissipation of the flow property, making the turbulence spectrum have a finite (though broad) bandwidth.[21] A truly random field such as white noise will have a flat uniform spectrum over both small and large frequencies. A useful representation for measurement and noise signals is a non-uniform power spectral density up to a cut-off frequency k' and becomes flat for higher frequencies.[32]

5.2.3.3 Spatial representation of turbulence

In the direction of bulk advection, if we define k to be the frequency observed at a point at a fixed location, then the spatial statistics of a measured flow property can be determined, assuming that this function is frozen in time. Therefore, if $\boldsymbol{k}$ is the wavenumber:

$$\boldsymbol{k} = \frac{k}{u} \tag{5.5}$$

we can observe the statistics as functions of k (*i.e.* the energy spectrum) and convert them to functions of $\boldsymbol{k}$. In general, $\boldsymbol{k}$ is a vector with three components in the x, y, and z directions.[33]

5.2.3.4 Autocorrelation

Given N observations of conductivity κ_1, …, κ_N in a time series, we can form $N-1$ pairs of observations separated by one time interval, τ. The quantity defined by Equation (5.2) converges to a unique function of τ that is independent of t for any particular steady turbulent flow. Because this correlation is all within a single measurement trace, it is called an autocorrelation function, R_T.[30] We can measure the correlation coefficient between adjacent observations κ_t and $\kappa_{t+\tau}$ using:

$$r_{\mathrm{T}} = \frac{\sum_{t=1}^{N-\tau}\left(\kappa_t - \bar{\kappa}\right)\left(\kappa_{t+\tau} - \bar{\kappa}\right)}{\sum_{t=1}^{N}\left(\kappa_t - \bar{\kappa}\right)^2} \tag{5.6}$$

This is the autocorrelation coefficient at lag τ.[34,35] The autocorrelation function R_T of the signal is found by evaluating the set of autocorrelation coefficients from 1–*N*, and it may have a wide variety of shapes; the one illustrated in **Figure 5.1d** is typical.[30,32]

The ability to measure local spatial and temporal variations in fluid composition (*i.e.* conductivity) is of interest in relation to many industrial processes that rely on turbulence to bring about the transport of matter, or the mixing and reaction of components. Usually such variations are distributed randomly about mean values and require reduction of results to statistical expression.[17] In order to characterise a random signal in turbulent flow, we can determine the mean and RMS fluctuation to specify amplitude behaviour, and PSD and autocorrelation to specify frequency and time behaviour.[32] In this study, we aim to investigate the performance properties of the all-diamond conductivity sensor developed in Chapter 3, evaluating its applicability towards environmental and industrial applications. For the former, the sensor is placed into river water flowing through an artificial flume; for the latter, the sensor is exposed to turbulent pipe flow into which an external marker fluid of differing characteristics is injected.

5.3 Experimental

5.3.1 Artificial river flume

A rectilinear open channel flume was constructed from PVC coated wood with dimensions 2 m length × 10 cm width × 28 cm depth, as shown in **Figure 5.2**. At the

upstream end of the flume, a layer of glass beads covering a 10 × 10 cm area was present over the inlet to act as a calming measure and dissipate flow. At the downstream end of the flume, a weir was inserted 14 cm away from the end to control the flow rate and ensure a more constant flow through the flume. Flow was driven by a centrifugal brass body water pump (CEB103, Clarke Pumps, London, UK) which drained water from the weir and recirculated it upstream.

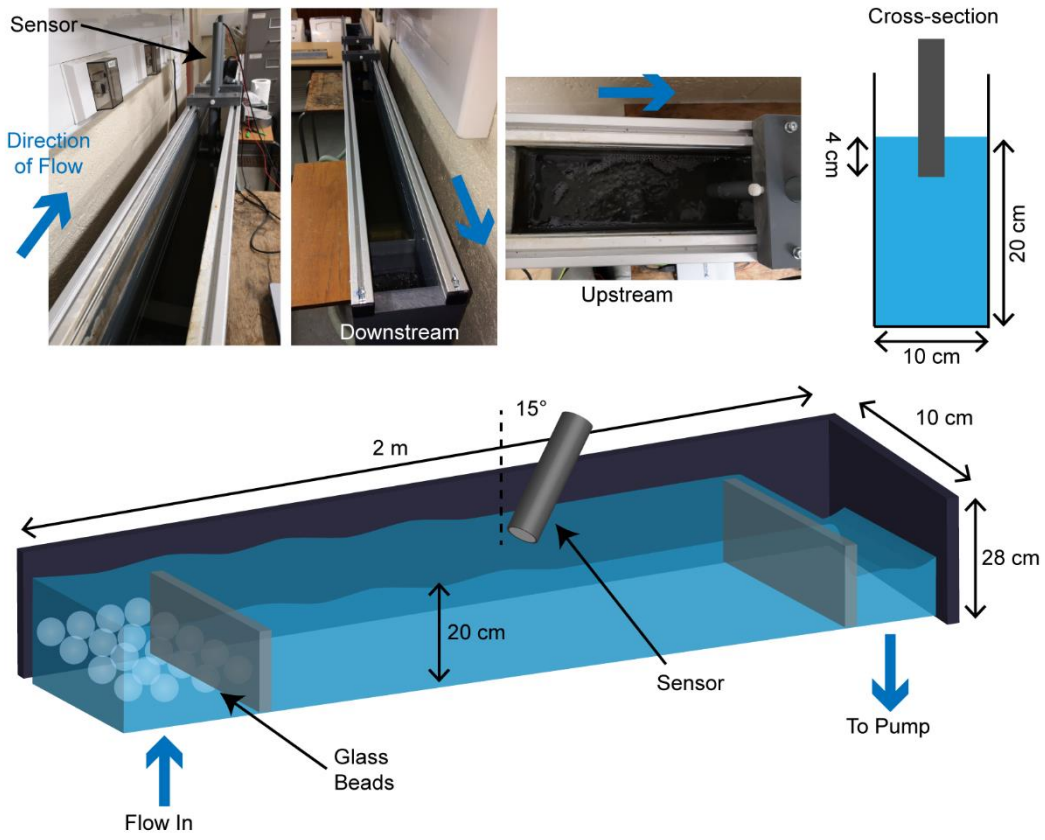

Figure 5.2. Artificial river flume setup.

River water was collected from the River Sowe, Warwickshire, UK (coordinates: 52.354775; −1.514451) in 10 L high-density polyethylene jerry cans (Azpack, Loughborough, UK). The flume was filled with river water (approximately 50 L) and allowed to recirculate for 48 h for flow to stabilise. Remaining river water was stored at room temperature (~15 °C).

An all-diamond conductivity sensor and a diamond based temperature sensor were both fabricated as described in Chapter 3, and individually mounted in the end of a PVC tube (Durapipe, Cannock, UK). Sensors were placed in the centre of flow (*i.e.* the midpoint of the flume width) at a depth of 4 cm beneath the water surface, and at an angle of 15° facing the flow. The diamond based temperature sensor was positioned 10 cm behind the all-diamond conductivity sensor. Before measurements were started, the flume was covered in aluminium foil to prevent evaporation losses. River water was added periodically when the water level in the weir dropped too low.

Operation of the sensors were described in Chapter 3. The AC conductance meter applied an AC of 100 μA at f = 100 kHz. A commercial Pt RTD temperature probe (HH376, Omega Engineering, Manchester, UK) was also employed.

For electrochemical characterisation of the electrodes, cyclic voltammetry (CVM) was employed using a CHI760E potentiostat (CH Instruments, Texas, USA). A three electrode setup was used, with one of the sensor BDD bands as working electrode, a saturated calomel electrode (SCE) as reference electrode, and a coiled Pt wire as counter electrode. To study the electrochemistry of an outer-sphere redox couple, a solution of 1 mM hexaammineruthenium(III) chloride (99%; Strem Chemicals, Cambridge, UK) in 0.1 M potassium nitrate (≥99.0%, Sigma-Aldrich, St. Louis, USA) was prepared. Cyclic voltammograms (CVMs) were recorded between +0.2 – −0.5 V *vs.* SCE, at scan rates of 0.1, 0.5, and 1.0 V s^{-1}. Capacitance C_{dl} was obtained by cycling the potential around 0 ± 0.01 V *vs.* SCE at scan rates of 0.1, 0.5, 1.0, 5.0, and 10.0 V s^{-1} (equivalent to 0.25, 1.25, 2.5, 12.5, and 25 Hz, respectively). The average of the current magnitude at 0 V *vs.* SCE was taken and divided by the scan rate.

5.3.2 Pipe flow rig

Experimental work involving turbulent flow was undertaken on a recirculating pipe flow system, consisting of extruded PVC pipe (Pipestock, Romsey, UK) with an internal diameter of 5 cm, as shown in **Figure 5.3**. Tap water was recirculated from a ~3000 L reservoir tank, driven by a vertical centrifugal pump (IPN80-125/0.55-4, Wilo Salmson Pumps, Dortmund, Germany). Flow velocity was kept constant by maintaining a constant volumetric flow rate (±0.02 L s^{-1}) measured by a flow meter.

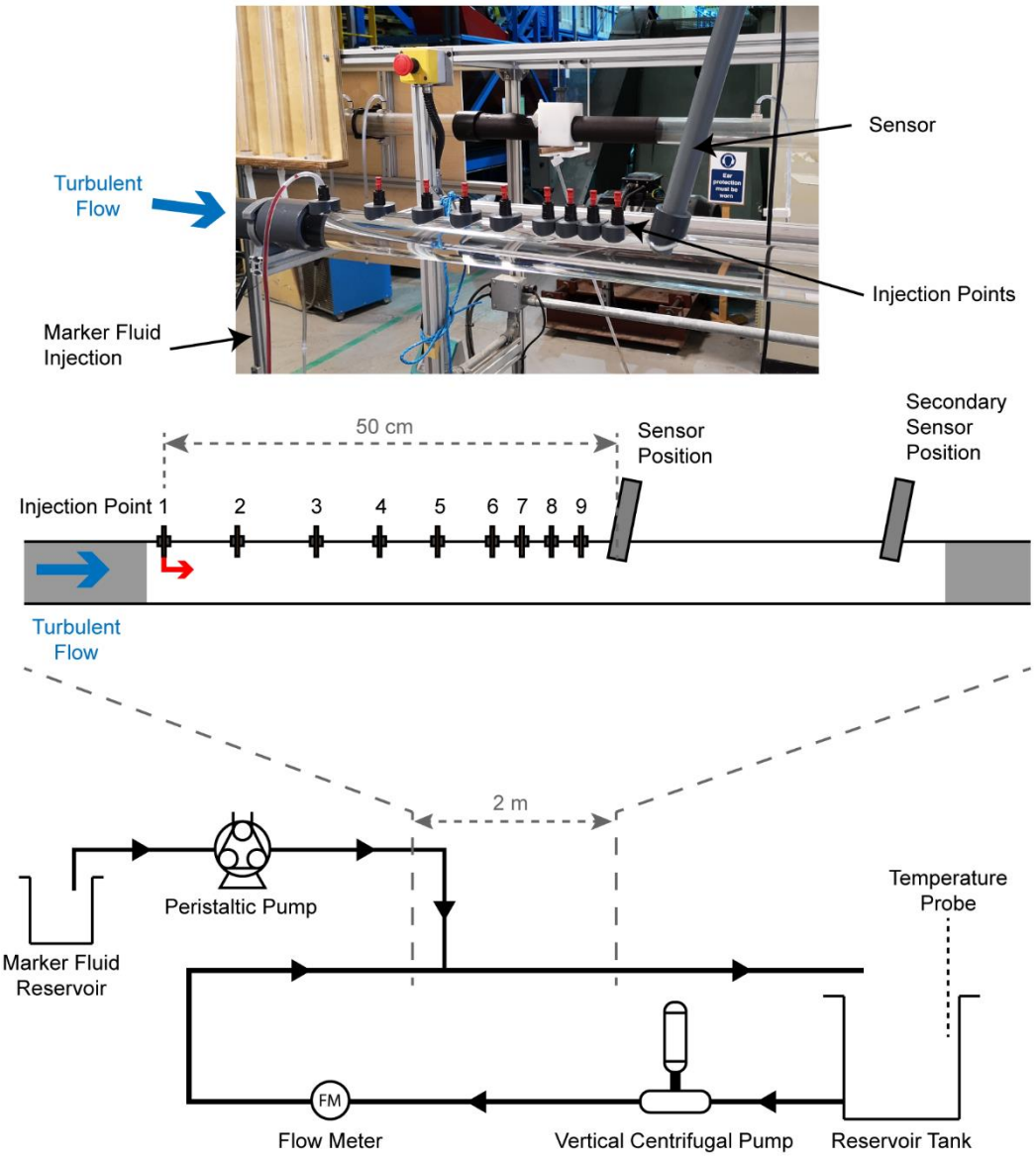

Figure 5.3. Pipe flow rig setup.

A test section was incorporated into the flow system, consisting of transparent extruded PVC pipe (Pipestock, Romsey, UK) to allow visualisation of mixing when an external marker fluid was injected into the main pipe flow. The all-diamond conductivity sensor was inserted vertically into the test section to a depth of 2 cm and at an angle of 15° facing the flow. A secondary position was located behind this initial primary position to allow for simultaneous temperature measurements with the diamond based temperature sensor. Nine injection points were located at positions 5, 8, 11, 14, 20, 26, 32, 40, and 50 cm in front of the primary sensor position to allow marker fluid injection.

Marker fluid was prepared by dissolving 5 g L^{-1} KCl (>99%; Acros Organics, Geel, Belgium) and 10 mL L^{-1} dark red colouring (Brake Bros, Ashford, UK) in tap water (University of Warwick, Coventry, UK). Conductivity of the marker fluid was measured to be 8.1 ± 0.3 mS cm^{-1} (InLab 731, Mettler Toledo, Leicester, UK). For experiments involving a change in marker fluid conductivity, KCl (>99%; Acros Organics, Geel, Belgium) was added to tap water such that four different solution conductivities were attained: 325 ± 3 µS cm^{-1} (no KCl added), 980 ± 1 µS cm^{-1}, 3.46 ± 0.01 mS cm^{-1}, and 10.42 ± 0.01 mS cm^{-1}. In addition, KCl (>99%; Acros Organics, Geel, Belgium) was also added to the reservoir tank to increase its conductivity to 1.9 ± 0.05 mS cm^{-1}. For experiments testing the diamond based temperature sensor, the marker fluid employed was solely tap water with 10 mL L^{-1} Acid Blue 9 dye (Cole-Parmer Instruments, Illinois, USA) added to allow visualisation of mixing. Here, the marker fluid was elevated to a temperature of 60 °C using a hotplate.

For all experiments, reservoir water was recirculated at the desired flow velocity for at least 60 s prior to injection to ensure stable flow (*i.e.* following the initial “spin-

up" stage after which flow is assumed to be fully turbulent). Marker fluid was injected from a 4 L reservoir by a peristaltic pump (505Di, Watson Marlow, Falmouth, UK) through flexible PVC tubing into the main pipe *via* the injection point (4 mm diameter stainless steel tube). The remaining eight injection points were capped off. In order to establish a baseline for each experiment, sensor measurement started and finished 15 s before and after the marker fluid injection period, respectively. During marker fluid injection, 100 mL of marker fluid was pumped at a constant rate of 4.0, 6.2, or 12.5 mL s^{-1}. Operation of the all-diamond conductivity sensor and diamond-based temperature sensor were described in Chapter 3. The AC conductance meter applied an AC of 1 mA at f = 100 kHz. For experiments acquiring data at a high sample rate, a USB-6289 DAQ card (National Instruments, Austin, USA) was employed. A commercial Pt RTD temperature probe (HH376, Omega Engineering, Manchester, UK) was monitoring the reservoir tank temperature throughout.

5.3.3 Data analysis and statistical analysis

Data analysis was conducted using OriginPro (v. 9.1, OriginLab Corporation, Massachusetts, USA) and MATLAB (v. 2018b, MathWorks, Massachusetts, USA).

Statistical analysis was performed using Past3 (v. 3.16, Oslo, Norway). To evaluate statistical correlations, Pearson's product moment correlation (r) was performed. To evaluate statistical differences, t test was performed. Data sets underwent the Shapiro-Wilk test for normal distribution prior to the aforementioned tests. Differences were considered statistically significant at a probability $p < 0.05$.

5.4 Results and discussion

5.4.1 Conductivity sensing in natural waters

Open-channel flow denotes flow where there exists a free surface at the interface between the atmosphere and fluid, such as a river or canal,[36] as is the case with the artificial river flume used herein. Open-channel flows are three dimensional, and generally turbulent. To characterise the nature of the flow that the conductivity sensor was placed into, the local Reynolds number (Re) was calculated as applicable to open-channel flow:

$$\mathrm{Re} = \frac{4au\rho}{P\eta} \tag{5.7}$$

where a is the cross-sectional area, u is average flow velocity in the streamwise direction, ρ is the fluid density, and η is the dynamic viscosity of the fluid. The wetted perimeter, P, includes the sides and bottom of the channel, but not the free surface or parts above water level.[36] For the flume used in this study, a = 0.02 m^2, P = 0.5 m, ρ = 997 kg m^{-3}, and η = 8.9×10^{-4} kg m^{-1} s^{-1}. Given that the surface flow velocity (u) was approximately 0.1 m s^{-1}, this results in Re ≈ 18000 which indicates turbulence conditions on the order of a slow-flowing natural river.[37]

As an initial trial, the all-diamond conductivity sensor, diamond based temperature sensor, and commercial temperature probe were placed in the flume for a duration of 7 days (**Figure 5.4**). The sensors were placed in the area of maximum flow velocity (the midplane at around 20% below the surface).[36]

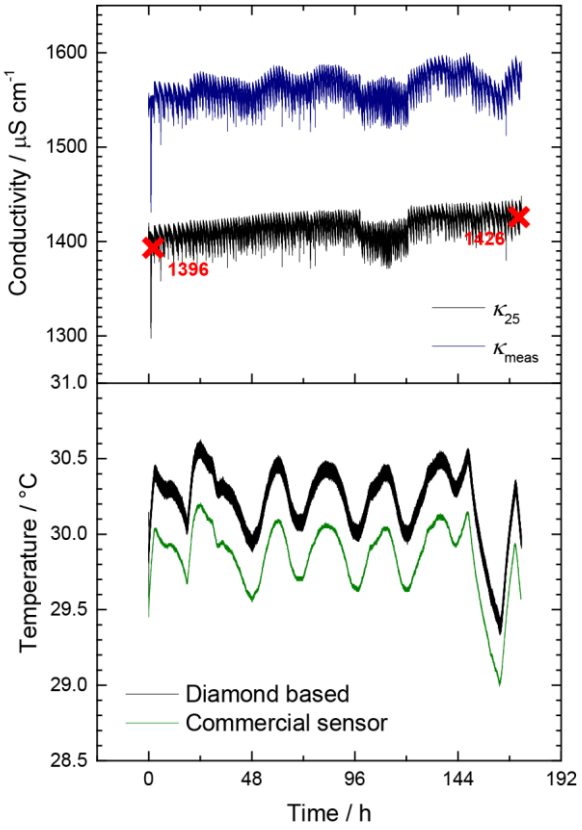

Figure 5.4. Continuous conductivity and temperature measurements taken simultaneously in artificial river flume. (Top) Conductivity measurements using the all-diamond conductivity sensor, showing measured data (κ_{meas}, —) and temperature corrected data (κ_{25}, —). Red crosses indicate mean values (n = 3) measured using the commercial conductivity probe. (Bottom) Temperature measurements using the diamond based Pt RTD sensor (—) compared to the commercial sensor (—).

Continuous measurements were acquired from all sensors in natural river water; both the diamond sensors were acquiring measurements at 10 Hz, whilst the commercial temperature probe was 1 Hz. Considering the temperature measurements, both sensors produce a similar measurement trace over the 7-day period, with an offset of around ±0.3 °C as observed previously (Chapter 3). Water temperature showed daily oscillation, as the temperature rose and fell over 24 h cycles.

Both the measured conductivity, κ_{meas}, and conductivity corrected to 25 °C, κ_{25}, traces from the all-diamond sensor are shown in **Figure 5.4**. The daily variability in

temperature can also be observed in κ_{meas}, due to the temperature dependence of κ. When temperature corrected, this effect is removed resulting in values of $\bar{\kappa}$ = 1413 µS cm^{-1} and $\overline{(\kappa')^2}$ = 10 µS cm^{-1}. Around day 4, a sudden slight drop in κ was observed (over a 24 h period) which may have been caused by foreign matter or suspended sediment, returning to its initial value when removed by the mean flow.[38]

Over the 7-day period, there appears to be a steady increase in κ_{25} of about 20 µS cm^{-1}. This could be due to either stability of the sensor (surface fouling, measurement drift) or changes in the natural conditions that affect the sensor response.[39] Though, the increase in κ was also observed when compared to samples drawn from the flume at the start and finish of the measurement period and determined using a commercial conductivity sensor, suggesting the latter explanation rather than the former. Therefore, this shows promise for the use of the all-diamond conductivity sensor for long-term monitoring in natural aquatic environments.

To further investigate any effect of possible biofouling on the all-diamond conductivity and diamond based temperature sensors, the sensors were cleaned and then placed into the river flume for a longer 36-day duration (**Figure 5.5**). CVM and capacitance measurements were also used to compare the sensor electrodes at the start and finish of the measurement period.

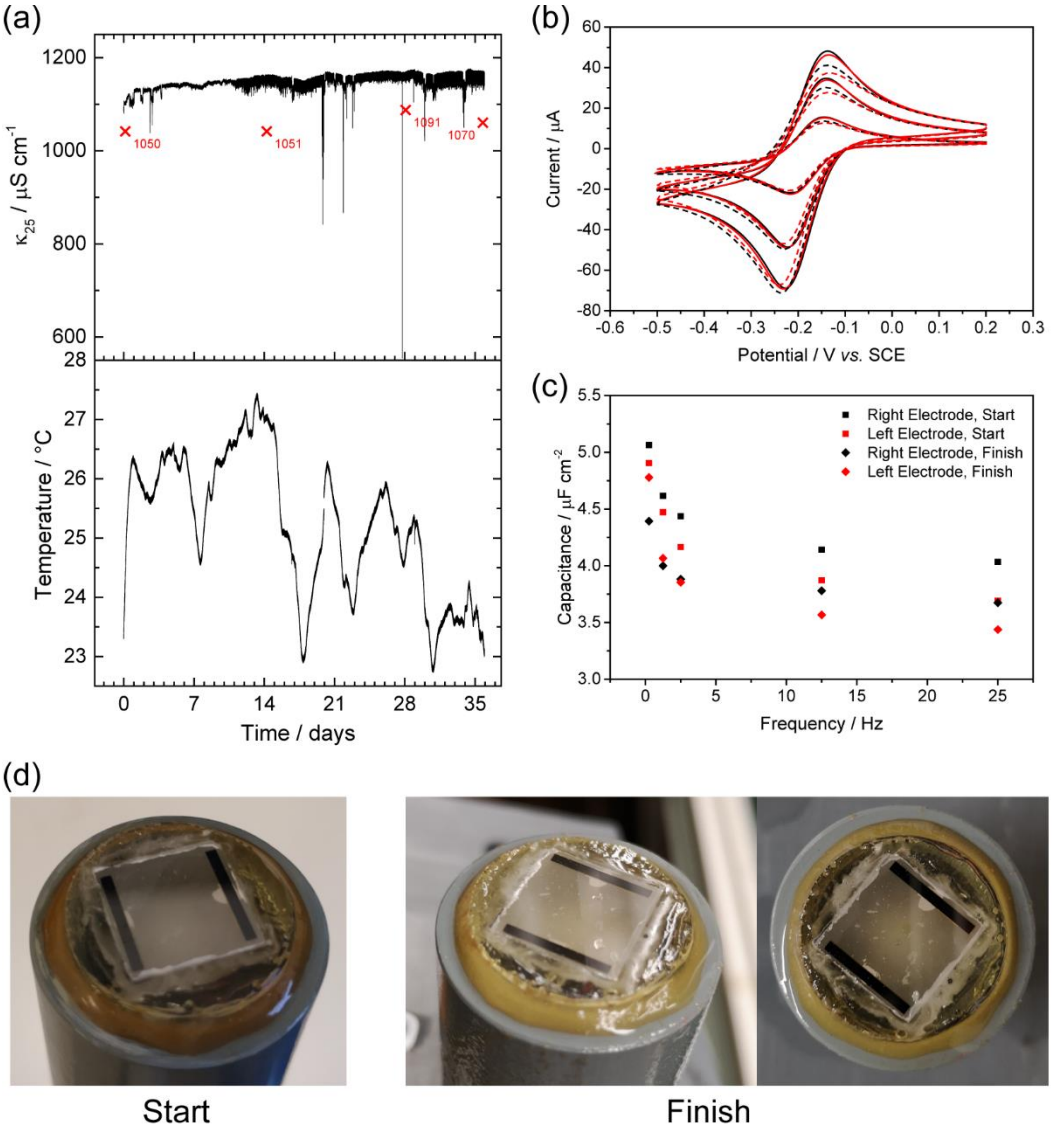

Figure 5.5. 36-day performance data for the all-diamond conductivity sensor and diamond based temperature sensor in the artificial river flume. (a) Measurement data for (top) κ_{25} values using the all-diamond conductivity sensor, and (bottom) temperature values using the diamond based Pt RTD sensor. Red crosses indicate mean values (n = 3) measured using the commercial conductivity probe. (b) Cyclic voltammograms of 1 mM $Ru(NH_3)_6^{3+}$ in 0.1 M KNO_3 at scan rates of 0.1, 0.5, and 1.0 V s^{-1} on the left (red) and right (black) sensor electrodes, at the start (—) and finish (---) of the 36-day period. (c) Capacitance C_{dl} *vs.* frequency of the left (red) and right (black) sensor electrodes, at the start (■) and finish (♦) of the 36-day period. (d) Photographs of the conductivity sensor at the start and finish of the 36-day period.

Figure 5.5a shows the measurement traces of both κ_{25} and temperature obtained from the all-diamond conductivity and diamond based temperature sensors, respectively. Both sensors were obtaining simultaneous measurements at 10 Hz over

the 36-day period. Similar to the 7-day data, there is a slight overall increase in κ of the river water from 1100 to 1150 µS cm^{-1} (also observed with the commercial sensor). This trend appears to be a real effect, probably due to changes in biological activity, carbon dioxide content, and salt content occurring in the river water over time.[10,40] Spikes present in the output signal trace, as discussed previously, are most likely due to foreign matter or air bubbles interacting with the sensor, since the spikes are always in an increasing voltage (increasing *R*) direction.[38] After *ca.* day 14, conductivity signal fluctuations become noticeably larger, from ~8 µS cm^{-1} to ~20 µS cm^{-1}, most likely due to change in suspended sediment properties or fouling.[38,41]

This minor increase in sensor noise could indicate the initial onset of fouling on the electrode surface. From the electrochemistry of an outer-sphere redox couple, ruthenium(II/III) hexaammine (**Figure 5.5b**) we observe some evidence for biofouling on the sensor electrodes. Comparing the results with both electrodes at the start with the finish, peak separation increased by 6 mV, but this was not statistically significant (*t* test, $p = 0.4$). However, the ratio of peak current magnitudes decreased significantly (*t* test, $p < 0.05$) by 0.103. Considering the capacitance of both electrodes (**Figure 5.5c**), a decrease in capacitance was observed at the finish when compared to the start, suggesting either a reduction in actual effective surface area, or a change in the surface properties of the electrode. But, this difference was not statistically significant on either the left (*t* test, $p = 0.4$) or right (*t* test, $p = 0.05$) electrode. Overall, these results show the limited impact of biofouling on the measurement of conductivity with BDD electrodes, over the duration of this experiment.[42,43] Visual inspection of the sensor (**Figure 5.5d**) further corroborates the electrochemical data, since minimal accumulation of biological matter can be

observed across the sensor surface. Thus, even after one month monitoring river water *in situ*, with the exception of a ~2.5× increase in noise, the all-diamond conductivity sensor appears resilient to loss in performance, biofouling, and drift.

We now consider the effect of turbulent river flow on the sensor performance (**Figure 5.6**). The all-diamond conductivity was placed into the river flume at varying positions (30, 50, 70, and 90 cm) away from the flow inlet, *i.e.* 30 cm is furthest upstream, whilst 90 cm is furthest downstream. In all cases, the diamond based temperature sensor was positioned 10 cm behind the conductivity sensor.

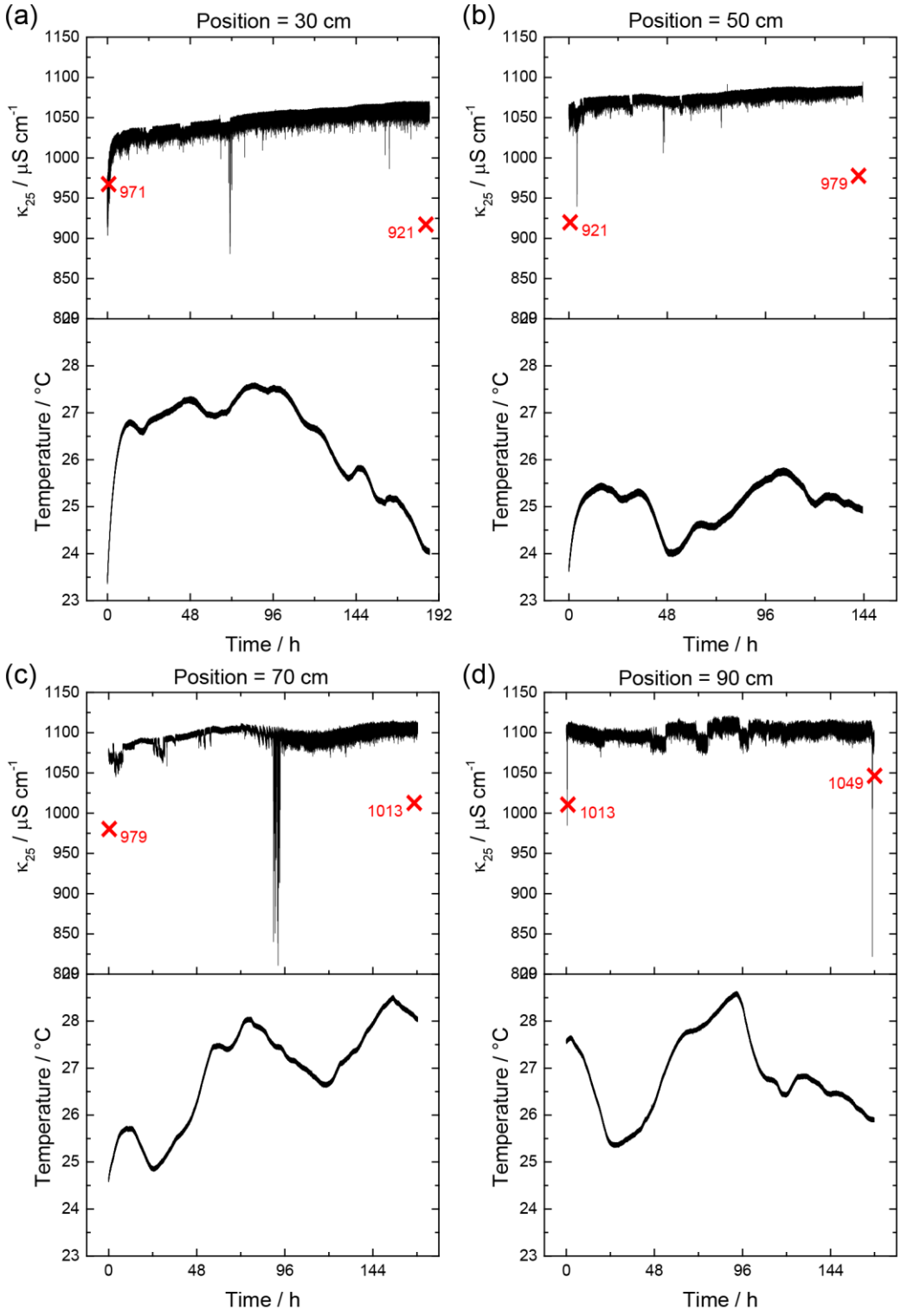

Figure 5.6. Performance data for the all-diamond conductivity sensor and diamond based temperature sensor in the artificial river flume. Measurement data for (top) κ_{25} values using the all-diamond conductivity sensor, and (bottom) temperature values using the diamond based Pt RTD sensor. Conductivity sensor was located at positions of (a) 30 cm, (b) 50 cm, (c) 70 cm, and (d) 90 cm from the front of the flume. Red crosses indicate mean values (n = 3) measured using the commercial conductivity probe.

Both sensors were recording data for 7 days in each position, acquiring measurements at 10 Hz. The measurement trace for each sensor position was analysed to obtain the statistical turbulence quantities $\bar{\kappa}$, $\overline{(\kappa')^2}$, and $\frac{\sqrt{\overline{(\kappa')^2}}}{\bar{\kappa}}$ (**Table 5.1**).

Table 5.1. Turbulence characteristics measured by the all-diamond conductivity sensor in **Figure 5.6.**

Position / cm	$\bar{\kappa}$ / μS cm^{-1}	$\overline{(\kappa')^2}$ / μS cm^{-1}	$\frac{\sqrt{\overline{(\kappa')^2}}}{\bar{\kappa}}$
30	1046	14	0.0036
50	1076	7	0.0025
70	1095	10	0.0029
90	1101	7	0.0024

The measured $\bar{\kappa}$ increases as the sensor position moves downstream, however this is most likely a real effect of increasing κ over time, as observed previously (and this is also seen with commercial conductivity sensor measurements). Nevertheless, the square of the turbulent fluctuations and the RMS of this quantity about the mean revealed more information about the turbulent nature of this open-channel flow. A weak correlation was observed between sensor position and both $\overline{(\kappa')^2}$ ($r = -0.70$, $p = 0.3$) and $\frac{\sqrt{\overline{(\kappa')^2}}}{\bar{\kappa}}$ ($r = -0.76$, $p = 0.24$). The strongest fluctuations in ionic composition and overall intensity of turbulence, as measured by the conductivity sensor, are at the most upstream position (30 cm, **Table 5.1**). When the sensor is further downstream (≥50 cm), there appears to be little change in turbulent characteristics. This is not overall unexpected, because it has been found that vertical

turbulence contributes to the dynamic behaviour of river flow, and dominates over longitudinal turbulence.[44–46] In fact, the fluctuations measured in the upstream position may be due to a velocity component, *i.e.* a higher velocity nearer to the flow inlet. For a further investigation into river analysis, it will be interesting to consider variation along the vertical axis in addition to the longitudinal axis, in particular when forces near the bed (bottom) of the flume will be considerably different.[44] This has application in transport and dispersion in natural streams.[37,45]

5.4.2 Conductivity sensing in an industrial setting

5.4.2.1 Turbulent pipe flow

In order to assess the performance capabilities of the all-diamond conductivity sensor in an industrial application, conductivity experiments were conducted in a pipe flow rig. Piping systems are encountered extensively in practical fluids engineering applications, with a variety of flow velocities, fluids, and pipe shapes.[36] In these experiments, the measurement response of the conductivity sensor was investigated in reaction to marked changes in fluid composition.

Circular pipe flow is based on average velocity, u, to calculate Reynolds number (Re):

$$\mathrm{Re} = \frac{u d_\mathrm{p} \rho}{\eta} \tag{5.8}$$

where d_p is the pipe diameter.[36] For the setup used here, d_p = 0.05 m, ρ = 997 kg m^{-3}, and η = 8.9×10^{-4} kg m^{-1} s^{-1}. Given that the minimum and maximum flow velocities (u) used were 0.5 and 2.5 m s^{-1} respectively, this results in Re ≈ 28000–140000. Generally, for Re > 2000−2500, flow is fluctuating and agitated, *i.e.* turbulent.[36]

Initially, both the all-diamond conductivity sensor and diamond based temperature sensor were placed into the turbulent pipe flow of a single ambient fluid: tap water (**Figure 5.7**). The resultant κ_{25} measurement traces are shown where the pipe flow velocity, u, was 1 and 2 m s^{-1}, each for 30 min duration.

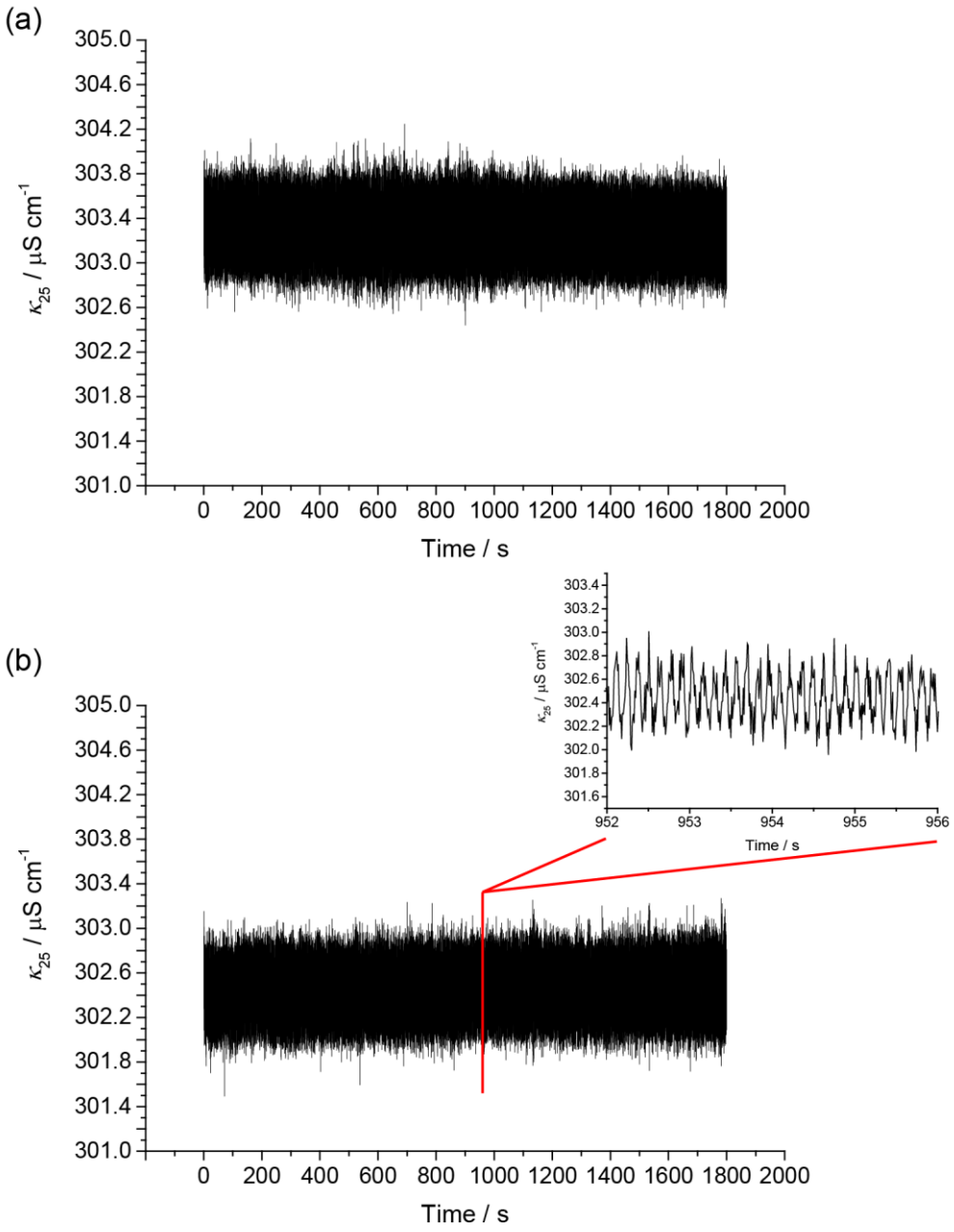

Figure 5.7. Conductivity measurement, κ_{25}, in turbulent pipe flow of tap water. Flow velocity was (a) 1 and (b) 2 m s^{-1} in a 5 cm diameter pipe. Measurements obtained at 100 Hz.

From the inset shown in **Figure 5.7**, we can see that the fluctuations are not strictly periodic, but encompass a continuous range of frequencies; coupled with the sufficiently high Re, this indicates that the system is under a fully turbulent flow condition.[36] The statistical turbulence quantities $\bar{\kappa}$, $\overline{(\kappa')^2}$, and $\frac{\sqrt{\overline{(\kappa')^2}}}{\bar{\kappa}}$ were determined from both measurement traces. At u = 1 m s^{-1}, $\bar{\kappa}$ = 303.30 µS cm^{-1}, $\overline{(\kappa')^2}$ = 0.22 µS cm^{-1}, and $\frac{\sqrt{\overline{(\kappa')^2}}}{\bar{\kappa}}$ = 0.0015. At u = 2 m s^{-1}, $\bar{\kappa}$ = 302.44 µS cm^{-1}, $\overline{(\kappa')^2}$ = 0.21 µS cm^{-1}, and $\frac{\sqrt{\overline{(\kappa')^2}}}{\bar{\kappa}}$ = 0.0015. The statistical characteristics are the same at both flow velocities, since the conductivity measurement was of a single fluid with a regular, point composition; the quantities derived here are essentially due to the sensor noise. The periodic component of the noise may be attributed to the pump, in operation during the measurement.

5.4.2.2 Marker fluid injection experiments

The ability to measure variation in fluid composition is attractive in many industrial processes, in particular the introduction of a secondary fluid into an ambient flow, *e.g.* for mixing, reaction, or dispersion of components.[17,28,47] The remainder of this study is concerned with the performance capabilities of the all-diamond conductivity sensor for measuring local concentration variation by means of the fluctuation in conductivity, when a tracer substance (marker fluid) is injected into a flowing stream of tap water (**Figure 5.8**). Varying experimental parameters were investigated: the pipe flow velocity, u; the marker fluid injection flow rate, v; and the injection position/distance away from the sensor, j. Marker fluid was of high conductivity (8.1

± 0.3 mS cm^{-1}), injected through a 4 mm inlet into pipe ambient fluid flow of tap water (260 µS cm^{-1}). The length of the inlet and depth of the sensor were kept constant, and chosen to ensure that the sensor was always within the turbulent plume.

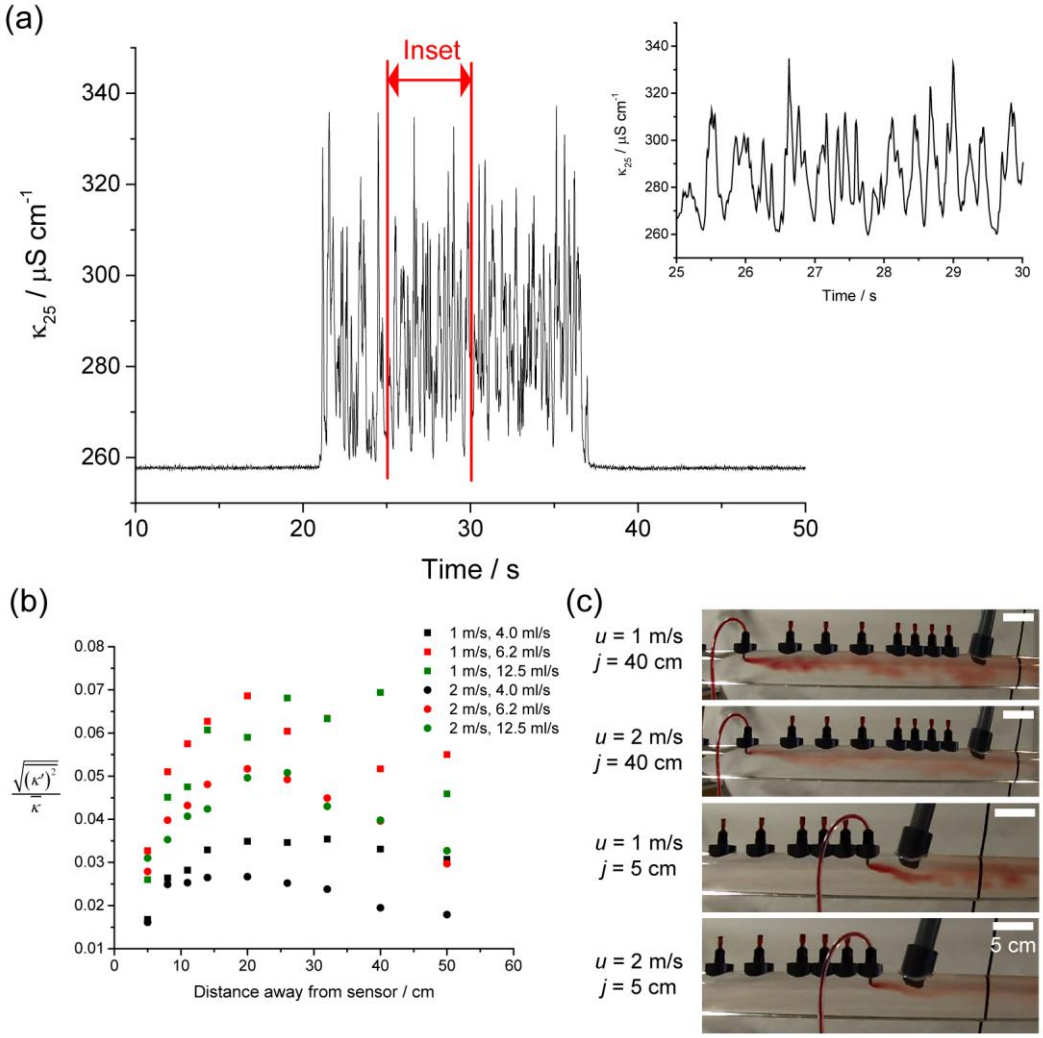

Figure 5.8. Marker fluid injection into turbulent pipe flow. High conductivity (8.1 mS cm^{-1}) marker fluid was injected at varying positions upstream of the all-diamond conductivity sensor into tap water (260 µS cm^{-1}) flowing through a 5 cm diameter pipe. (a) Conductivity measurement, κ_{25}, with time. Marker fluid injection occurred at 21 s. Inset shows a zoomed in portion of the turbulent region. (b) Intensity of turbulence measured by the conductivity sensor, at varying marker fluid injection positions (j) away from the sensor. Experimental parameters changed were pipe flow velocity, u = 1 m s^{-1} (squares) and u = 2 m s^{-1} (circles), and the marker fluid injection flow rate, v = 4.0 mL s^{-1} (black), v = 6.2 mL s^{-1} (red), and v = 12.5 mL s^{-1} (green). (c) Still photographs showing an instantaneous representation of the turbulent region (marker fluid injection) under given experimental parameters. For all images, v = 6.2 mL s^{-1}.

Figure 5.8a shows the continuous measurement trace of κ_{25} recorded by the all-diamond conductivity sensor. The turbulent region where the marker fluid injection occurs (21–37 s) is clearly visible, contrasting with the baseline measurement of solely tap water. By examining only the turbulent region, statistical quantities can be extracted regarding the marker fluid injection period. To do this, the time period over which to average must be adequate, generally defined as > 5 s;[36] since injections are generally 15–30 s in duration, this assumption is valid for our analyses.

The key statistical measure is the intensity of turbulence, $\frac{\sqrt{\overline{(\kappa')^2}}}{\overline{\kappa}}$ (**Figure 5.8b**). When considering the longitudinal variation, *i.e.* distance between sensor and injection, the intensity of turbulence is relatively small when the injection is very close to the sensor (< 10 cm) because the profile of the injected marker fluid remains laminar and is relatively unaffected by the mainstream turbulence.[29,48] This can be observed visually in the photographs in **Figure 5.8c**: where j = 5 cm, the sensor is measuring little variation in κ. At distances of 10–15 cm the intensity of turbulence peaks, before slowly decreasing as j increases. At this point, large scale vortex structures are the dominant component contributing to the mixing and lateral growth of the marker fluid as it moves downstream.[29] Here the concentration distribution is highly non-uniform, and becomes progressively more uniform with increasing distance as the marker fluid becomes more mixed with the ambient fluid.[49,50]

Figure 5.8b also shows that turbulence intensity increases with marker fluid injection flow rate. When the injection flow rate is larger, the injected marker fluid jet becomes well mixed with the mainstream, as a result of a larger turbulence scale; at slower flow rates, the injected jets are well preserved with less effect of vortex motion.[48]

Finally, considering the mainstream pipe flow velocity, as velocity increased the turbulence intensity decreased. Similar studies regarding fluid mixing in pipes note an inverse relation with velocity.[51] We reason that this lower measure of turbulence for a faster flow may be because we are measuring the injected plume at a lower time than if the mainstream were slower. In other words, for a given time interval, the same volume of marker fluid has been injected into double the volume of mainstream fluid at $u = 2$ m s^{-1} than at $u = 1$ m s^{-1}, and this can be seen in **Figure 5.8c**.

Of course, this statistical treatment only reveals limited information about the turbulent measurements. Given that the turbulent fluctuations span a range of frequencies (inset, **Figure 5.8a**), spectral analysis yields more information on the strength of the signal in turbulent flow for different frequencies.[30] **Figure 5.9** through **Figure 5.12** show the spectral distribution functions obtained from the analysis of the turbulent region of the sensor signal from marker fluid injection experiments. **Figure 5.9** investigates the effect of varying the distance between the injection and the sensor, from $j = 5$ cm to $j = 50$ cm, at a constant $u = 1$ m s^{-1} and $v = 6.2$ mL s^{-1}.

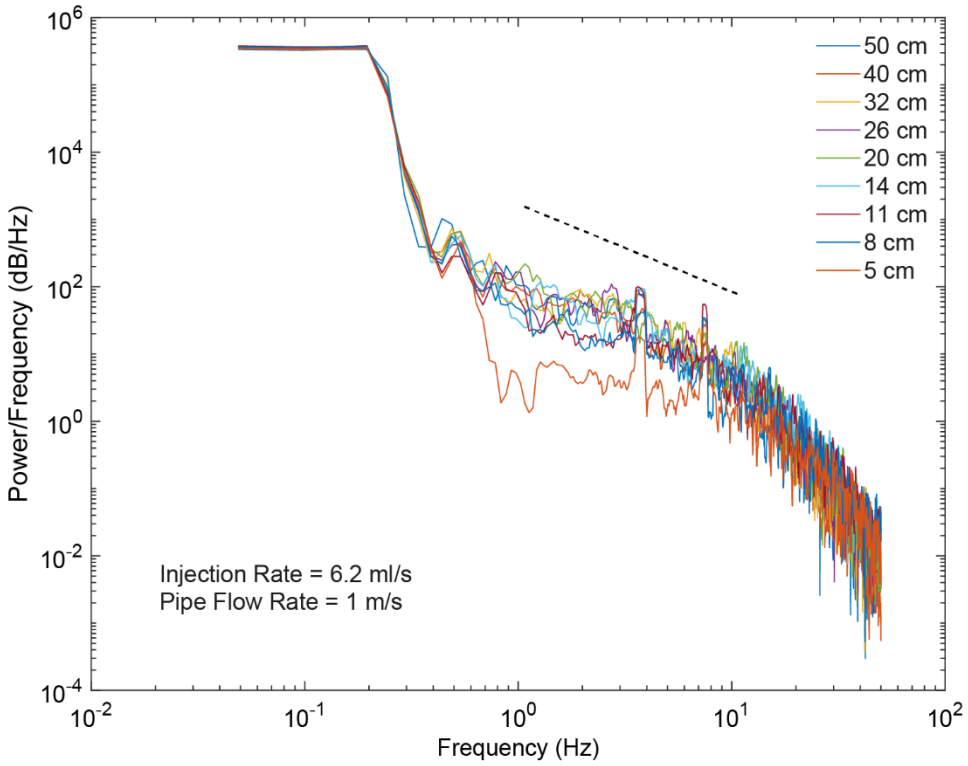

Figure 5.9. Power spectral density function showing the effect of varying marker fluid injection position (j). High conductivity (8.1 mS cm^{-1}) marker fluid was injected at j = 5, 8, 11, 14, 20, 26, 32, 40, and 50 cm upstream of the all-diamond conductivity sensor into tap water (260 µS cm^{-1}) flowing through a 5 cm diameter pipe. For all experiments, u = 1 m s^{-1} and v = 6.2 mL s^{-1}. Black dotted line marks the Kolmogorov −5/3 gradient.

As expected, in all cases we observe the Kolmogorov cascade, where turbulent κ fluctuations are transferred from higher to lower length and energy-containing scales (low to high k), and at $k \approx 10^1$ Hz the spectrum drops off as the fluctuations dissipate away.[23,52] The sensor was able to detect turbulent κ fluctuations up to 50 Hz (half the sampling rate[53]) at all injection positions. However, at the closest position j = 5 cm, we see that the magnitude of power in the spectrum for the larger turbulent fluctuation scales (lower k) is smaller compared to all other positions, with a larger change from bulk advection,[23,52] further suggesting that mixing from the initial marker fluid jet is minimal at this injection position. This correlates with the earlier

observation (**Figure 5.8b**) that the statistical intensity of turbulence was smallest at this position.

Figure 5.10 explores the effect of increasing the mainstream pipe flow velocity from 1 m s^{-1} to 2 m s^{-1}. The two extreme injection positions are shown, j = 5 and 50 cm, at injection flow rates v = 4.0, 6.2, and 12.5 mL s^{-1}.

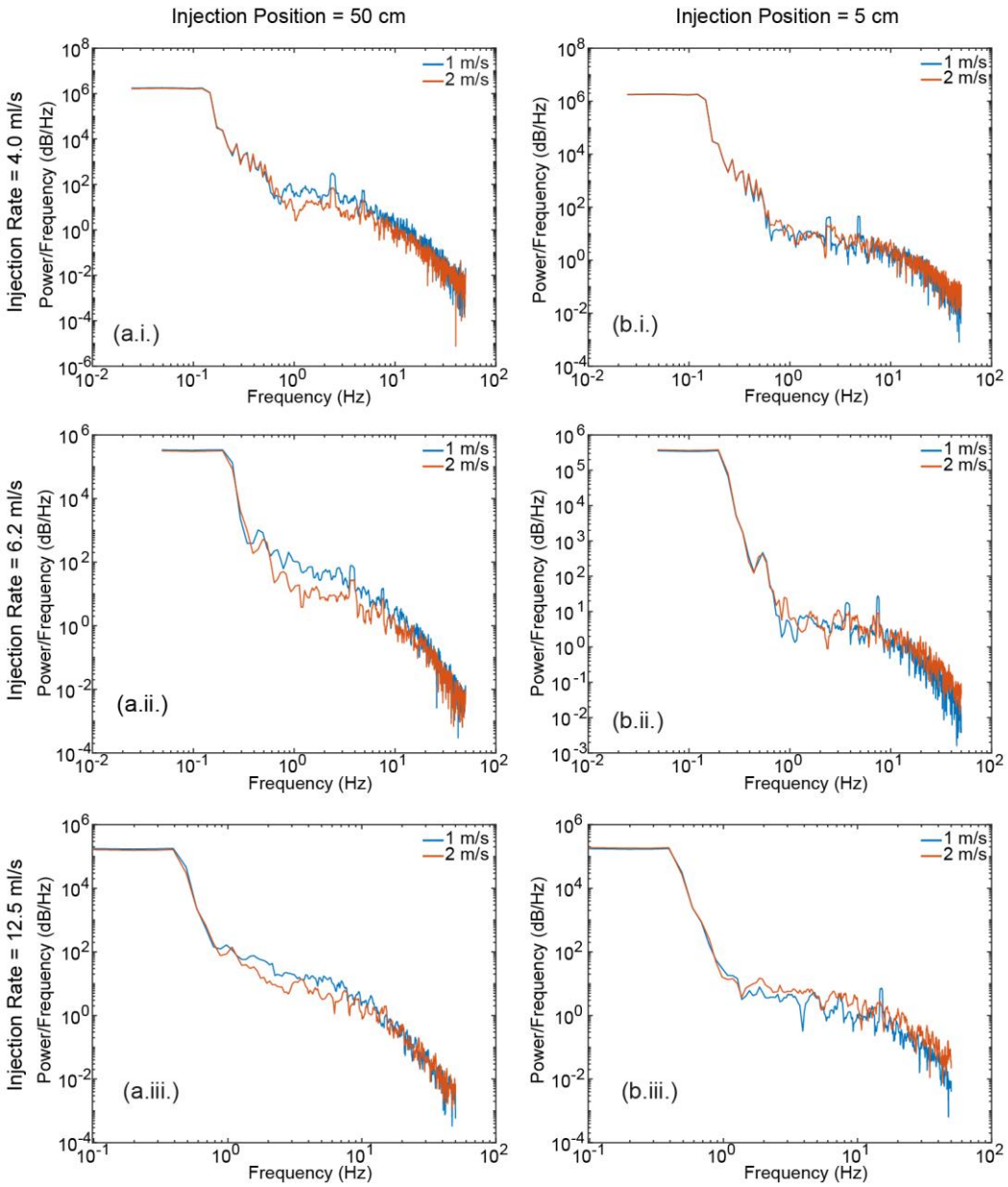

Figure 5.10. Power spectral density function showing the effect of varying pipe flow velocity (u). High conductivity (8.1 mS cm^{-1}) marker fluid was injected at (a) j = 50 cm and (b) j = 5 cm upstream of the all-diamond conductivity sensor into tap water (260 µS cm^{-1}) flowing at velocity, u = 1 m s^{-1} (—) and 2 m s^{-1} (—) through a 5 cm diameter pipe. Injection flow rate was (i) v = 4.0 mL s^{-1}, (ii) v = 6.2 mL s^{-1}, and (iii) v = 12.5 mL s^{-1}.

At j = 5 cm, there is no observable difference in the PSD regardless of pipe flow velocity or injection flow rate. The magnitude of power in the inertial subrange of the spectrum was around 10^1 dB/Hz. In contrast, at j = 50 cm a slight difference in the inertial subrange was observed at all injection flow rates, whereby the power

magnitude was larger (by approximately one order of magnitude) under u = 1 m s^{-1} compared to 2 m s^{-1}. As the higher mainstream velocity (higher Re) turbulent mixing is greater,[54] the sensor is therefore detecting a smaller distribution of concentration fluctuations, since the turbulence is dominated more by smaller eddies.[55] Conversely, at the lower velocity (u = 1 m s^{-1}), there is a wider distribution of concentration fluctuations and therefore more power per frequency.

We can extend this analysis further by investigating the time domain through the autocorrelation function of the turbulent region of marker fluid injection. **Figure 5.11** shows the autocorrelation function of the injection experiment where j = 50 cm and v = 6.2 mL s^{-1} for both u = 1 and 2 m s^{-1}.

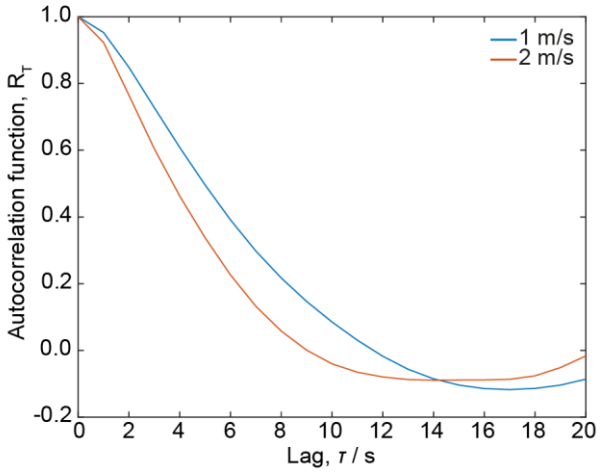

Figure 5.11. Autocorrelation function of the turbulent pipe flow during marker fluid injection experiment, at u = 1 m s^{-1} (—) and 2 m s^{-1} (—). For both, j = 50 cm, v = 6.2 mL s^{-1}.

The shape of this function is typical of turbulent flow where low frequency terms predominate.[30,35] A value of R_T close to 1 indicates that a conductivity with a certain value tends to be followed by one near that same value, and R_T tends towards approximately 0 at longer lag times.[34,35] We observe that at the higher mainstream velocity (u = 2 m s^{-1}), the autocorrelation functions drops to a random series at

shorter lag time, suggesting again that turbulent mixing is greater (at a faster timescale, since the integral time scale is smaller[56]) and that the turbulence is dominated by smaller eddies of more uniform size.[57,58]

Finally, the effect of marker fluid injection flow rate is investigated (**Figure 5.12**), at 4.0, 6.2, and 12.5 mL s^{-1}. The two extreme injection positions are shown, j = 5 and 50 cm, at mainstream flow velocities u = 1 and 2 m s^{-1}.

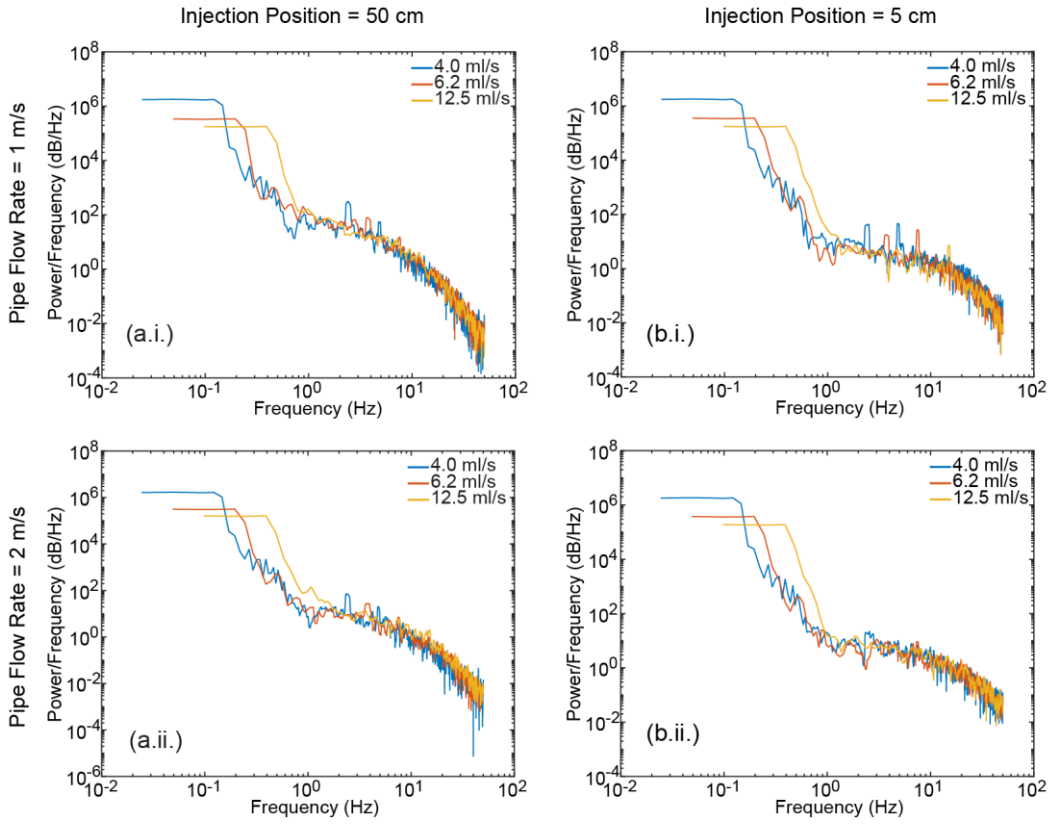

Figure 5.12. Power spectral density function showing the effect of varying marker fluid injection flow rate (v). High conductivity (8.1 mS cm^{-1}) marker fluid was injected at (a) j = 50 cm and (b) j = 5 cm upstream of the all-diamond conductivity sensor at a flow rate of v = 4.0 mL s^{-1} (—), v = 6.2 mL s^{-1} (—), and v = 12.5 mL s^{-1} (—) into tap water (260 µS cm^{-1}) through a 5 cm diameter pipe. Pipe flow velocity was (i) u = 1 m s^{-1}, and (ii) u = 2 m s^{-1}.

There appears to be no observable dependence of the injection flow rate on the PSD of measured κ fluctuations, and this has also been found in previous work.[59] At faster

flow rates, we are not able to resolve the low frequency terms since they occur on slower timescales.[60] This can be further analysed by the autocorrelation function (**Figure 5.13**).

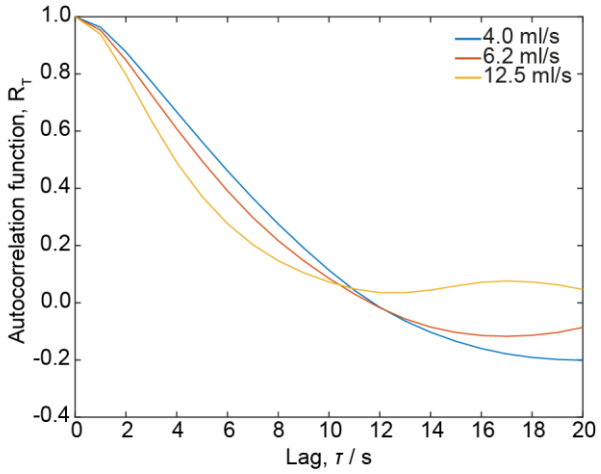

Figure 5.13. Autocorrelation function at varying injection flow rates, v = 4.0 mL s^{-1} (—), 6.2 mL s^{-1} (—), and 12.5 mL s^{-1} (—). For both, u = 1 m s^{-1}, j = 50 cm.

Here, we observe that as injection flow rate increases, the integral time scale decreases. The integral time scale is the time over which a turbulent fluctuation is correlated with itself.[56] For v = 12.5 mL s^{-1} in particular this is noticeable, as for this curve the high frequency terms begin to predominate, causing oscillations in the autocorrelation function with an amplitude that decreases rapidly in the first few lags.[35]

Whilst others[59] did not find a dependence on injection flow rate, a dependence on concentration was observed. Consequently, we investigated the effect of changing the conductivity of the marker fluid (**Figure 5.14**). The conductivity of the ambient mainstream fluid was increased to 1.9 mS cm^{-1} by addition of KCl, and the conductivity of the marker fluid was adjusted to allow for both an increase and a decrease in measured conductivity to be realised.

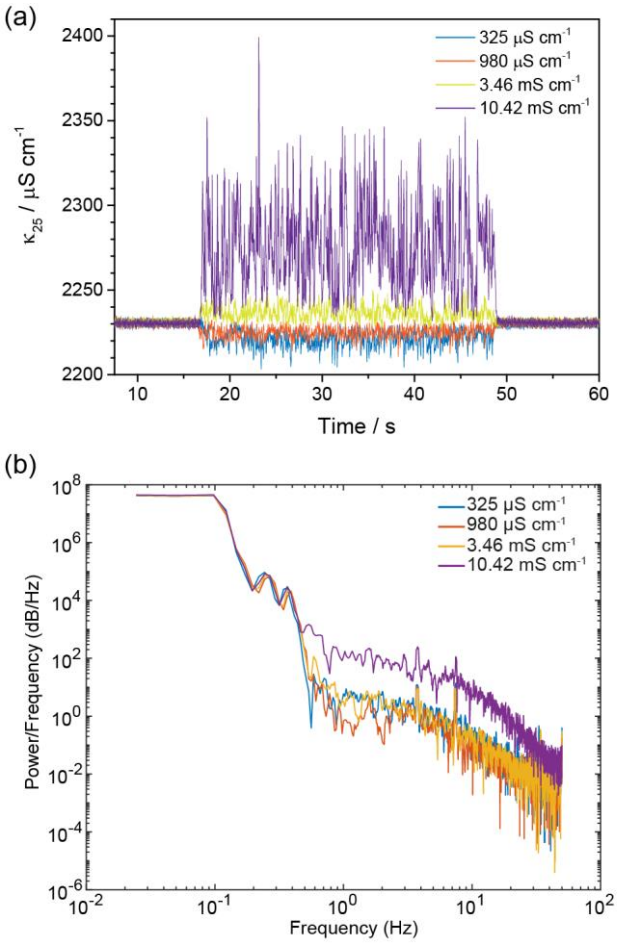

Figure 5.14. Effect of changing conductivity of marker fluid injected into ambient fluid. (a) Continuous conductivity measurement, κ_{25}, with time. (b) Power spectral density function of the turbulent region. Marker fluid with conductivity of 325 µS cm^{-1} (—), 980 µS cm^{-1} (—), 3.46 mS cm^{-1} (—), and 10.42 mS cm^{-1} (—) was injected into ambient fluid (1.9 mS cm^{-1}) pipe flow. u = 1 m s^{-1}, v = 6.2 mL s^{-1}, j = 50 cm.

Figure 5.14a shows the κ_{25} measurement traces where the marker fluid injected was either a lower (325 and 980 µS cm^{-1}) or a higher (3.46 and 10.42 mS cm^{-1}) conductivity than the mainstream ambient fluid. Visual inspection alone of the traces reveals that as the marker fluid concentration increases away from ambient, the strength of the κ fluctuations measured by the sensor increases. This is most noticeable for the 10.42 mS cm^{-1} conductivity, which represents a 420% change in κ, whereas the other conductivities amount to a ±83% change.

In the power spectrum (**Figure 5.14b**), we observe a higher power for the 10.42 mS cm^{-1} conductivity. Firstly, the spectrum itself is at a higher power (*i.e.* shifted upwards) from 5×10^{-1} dB/Hz, the inertial subrange, to higher frequencies, most likely as a result of the increased change in magnitude of κ. Secondly, the spectrum rolls off at a higher power: 10^{-1}–10^{-2} dB/Hz compared to ~10^{-3} dB/Hz for the other conductivities. This may be because the fluid viscosity becomes important at the dissipative range scales,[23] and the higher conductivity solution (≈0.07 mol dm^{-3} KCl) will show an increase in viscosity.[61]

Whilst the physical nature of turbulence is a continuum phenomenon, there often also exists a marked boundary layer between the turbulent region and the ambient surroundings.[23] Up to now, the conductivity sensor and the injection source have been positioned such that the sensor is always within the turbulent plume upon marker fluid injection. We now consider the effect of varying the injection depth, which is the distance between the source of injection (outlet) and the pipe wall (**Figure 5.15**). The depth of the sensor remains constant, whilst the position of the injection outlet varies across the pipe radially, from nearside pipe wall (17 mm) to far side (42 mm). Note that for all experiments prior, the injection depth was 22 mm.

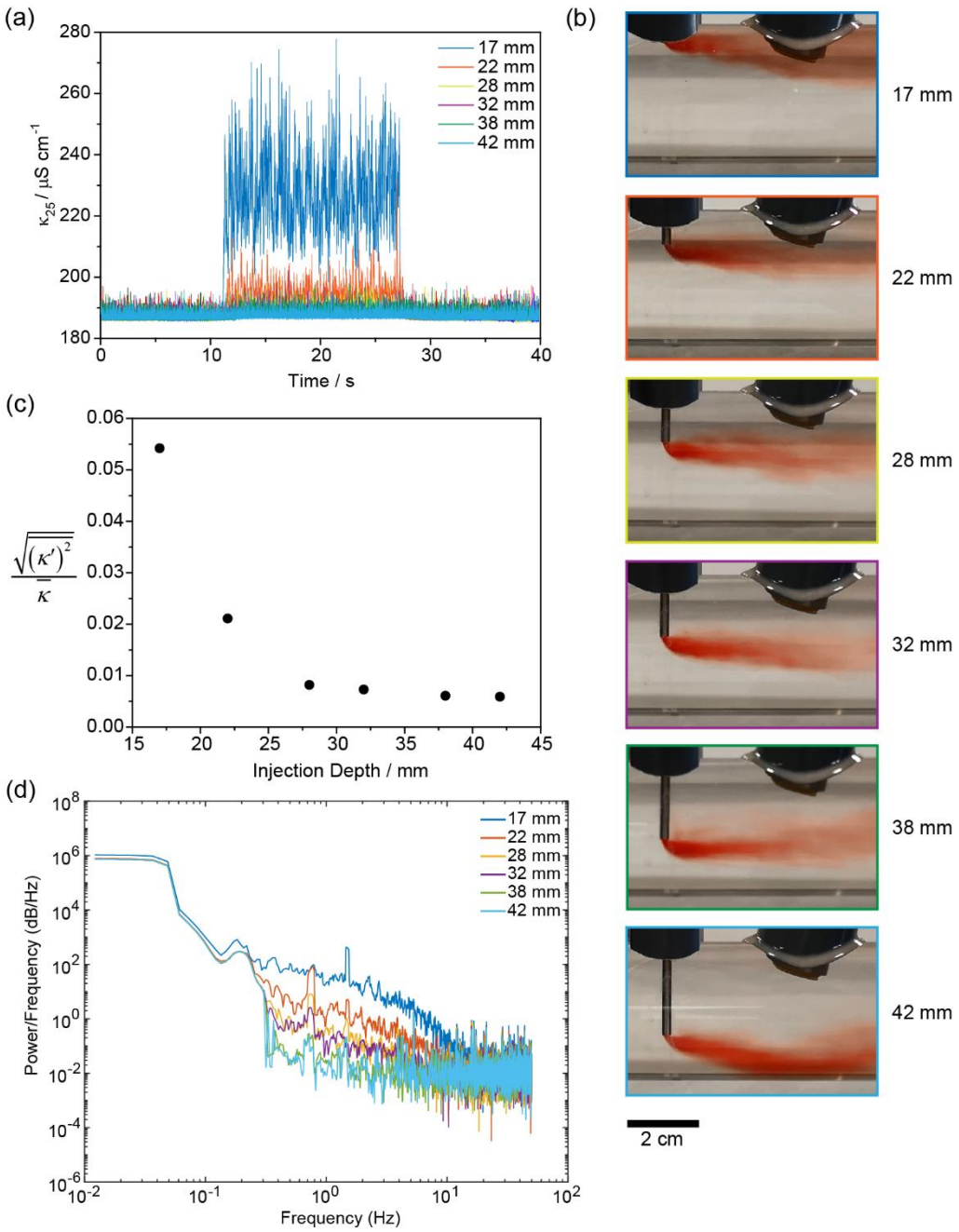

Figure 5.15. Effect of varying injection depth (distance of injection outlet from pipe wall). (a) Continuous conductivity measurement, κ_{25}, with time. (b) Still photographs showing an instantaneous representation of the marker fluid injection. (c) Intensity of turbulence measured by the conductivity sensor of different injection depths. (d) Power spectral density function of the turbulent region. For all, high conductivity (8.1 mS cm^{-1}) marker fluid was injected at a distance of (—) 17 mm, (—) 22 mm, (—) 28 mm, (—) 32 mm, (—) 38 mm, and (—) 42 mm away from the pipe wall. u = 1 m s^{-1}, v = 6.2 mL s^{-1}, j = 5 cm.

Figure 5.15a shows the κ_{25} measurement traces during marker fluid injection through the varying length outlets. The scale of measured κ fluctuations is highest at the shortest injection depth (17 mm) and decreases as the injection depth increases. This is corroborated by the statistical intensity of turbulence values determined from the turbulent region of the traces (**Figure 5.15c**). We observe that at an injection depth > 28 mm, the sensor is not detecting any κ fluctuations and so the intensity of turbulence reaches a minimum. From the photographs (**Figure 5.15b**), it can be seen that at 17 mm the sensor is positioned at the centreline of the turbulent plume, and at 22 mm the sensor is near to the boundary layer whilst still within the turbulent plume. Beyond 28 mm, the sensor becomes outside the turbulent plume and therefore there are no detectable changes in κ.

In Chapter 3, it was revealed by finite element method simulation that the measurable range of the conductivity sensor extends approximately 2 cm into solution. The experimental results here (**Figure 5.15d**) correspond well with the simulation results, suggesting that the sensing volume of the sensor is ~2–2.5 cm (normal to the sensor face). Here, we observe that as injection depth increases, the power magnitude drops substantially and sequentially at the onset of the inertial subrange (3×10^{-1} dB/Hz). At injection depths 38 and 42 mm, the spectra is essentially a flat line over the whole frequency range ($>3\times10^{-1}$ dB/Hz), indicating that only the ambient fluid pipe flow is being detected.[21]

For all of the marker fluid injection power spectra illustrated, the spectra roll off at the dissipative range where lower length and energy-containing scales dominate.[23,52] However, as a result of the measurement acquisition rate being 100 Hz, the upper k bound is limited to 50 Hz yet the spectra appear to still roll off by visual extrapolation, indicating that up to a measurement rate of 100 Hz the sensor remains

sensitive to detecting κ fluctuations. This is equivalent to ~1 cm length scale of measurement (at u = 1 m s^{-1}) which makes sense given that the sensor electrodes are spaced 9 mm apart.

In order to further assess the performance of the conductivity sensor, we investigate its sensitivity at higher frequencies where noise obscures the desired signal. To increase the measurement acquisition rate we changed to a higher specification NI USB 6289 DAQ card, with the capability to acquire data at 10 kHz, instead of 100 Hz as previously used. Marker fluid injection experiments were conducted at 2 and 10 kHz sample rate, at varying mainstream flow velocities (u = 0.5–2.5 m s^{-1}) since this parameter allows for analysis of spatial scales (**Figure 5.16**).

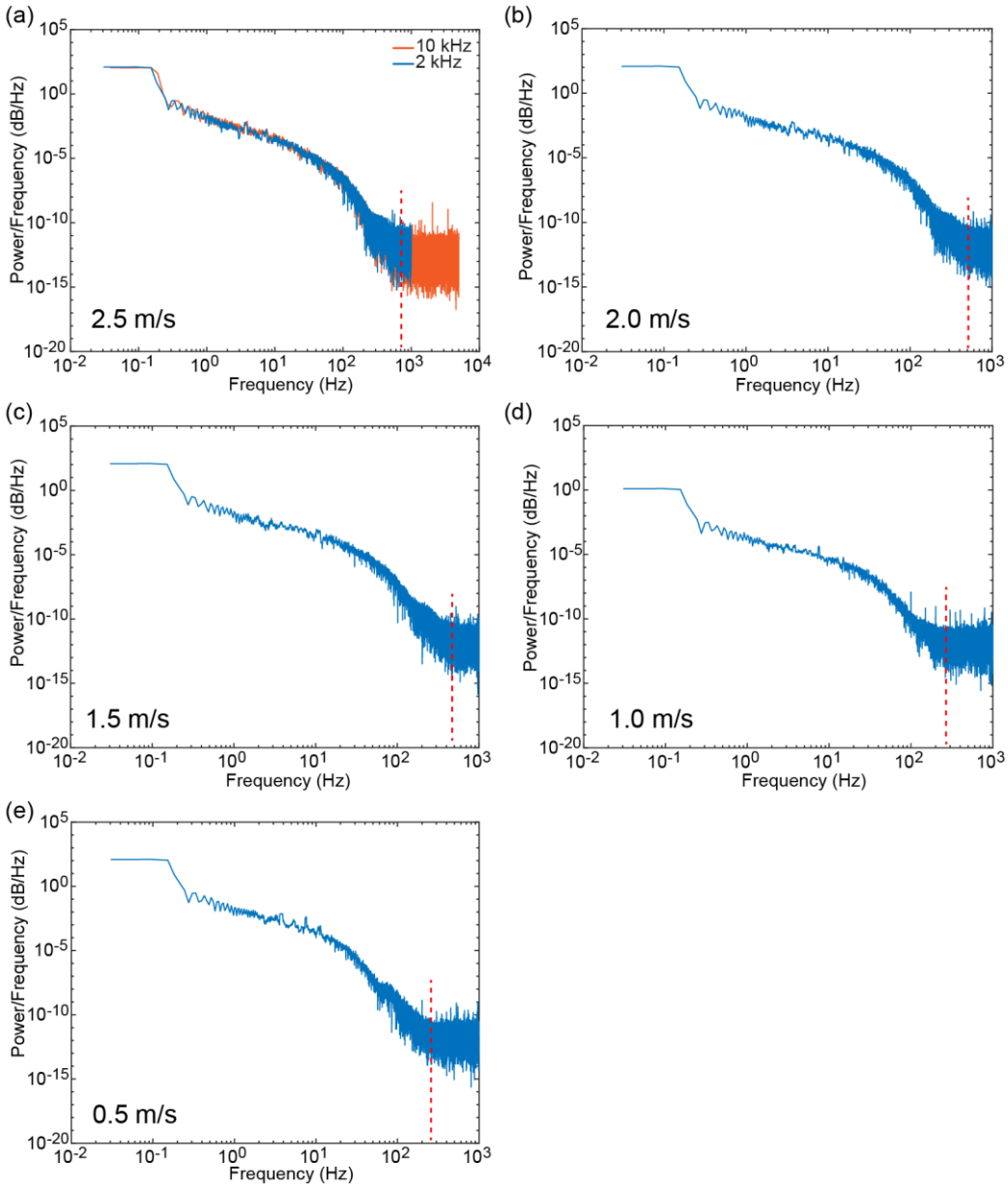

Figure 5.16. Varying mainstream pipe flow velocity with measurements obtained at high sample rate. Power spectral density function of the turbulent region of marker fluid injection experiments, where (a) u = 2.5 m s^{-1}, (b) u = 2.0 m s^{-1}, (c) u = 1.5 m s^{-1}, (d) u = 1.0 m s^{-1}, and (e) u = 0.5 m s^{-1}. Measurement sample rate was (—) 2 kHz or (—) 10 kHz. Red dotted line indicates location of the noise floor. v = 6.2 mL s^{-1}, j = 14 cm.

At u = 2.5 m s^{-1} (**Figure 5.16a**), the experiment was conducted using a measurement sample rate of 2 and 10 kHz. The power spectra rolls off to a frequency of $k' \approx$ 600–700 Hz, where it hits the noise floor. At $k > k'$, the system is only detecting white noise, where the power spectral density is independent of frequency.[62] Therefore, at

10 kHz sample rate the spectra merely extends the noise floor to higher frequencies. For clarity, **Figure 5.16b–e** show only the 2 kHz sample rate since k' and the noise floor are observable, and the higher sample rate adds no more information.

Comparison of the power spectra and the noise floor at the different mainstream flow velocities (**Table 5.2**) reveals a correlation between the roll-off frequency and the pipe flow velocity ($r = 0.992$, $p < 0.05$).

Table 5.2. Dependence of roll-off frequency on pipe flow velocity.

u / m s^{-1}	k' / Hz
2.5	600–700
2.0	500–600
1.5	400–500
1.0	~300
0.5	200–300

The change in k' with flow velocity suggests that the conductivity sensor is spatially limited on the length scale.[55] At the highest $u = 2.5$ m s^{-1}, the spatial resolution of the sensor is ~0.38 cm. This indicates that even at high flow velocities (high Re) the sensor can detect changes in conductivity at fast timescales (up to 700 Hz).

Leading on from this, we investigated the effect of gradually diluting the marker fluid concentration, to monitor the change in the power spectra and determine the sensitivity and detection limits of the conductivity sensor. Marker fluid injection experiments were conducted, decreasing its conductivity from 7.80 mS cm^{-1} by serial dilution with tap water (**Figure 5.17**). These experiments were performed at the highest flow velocity ($u = 2.5$ m s^{-1}) at a sample rate of 2 kHz. The injection depth was 22 mm, $v = 6.2$ mL s^{-1}, and $j = 14$ cm.

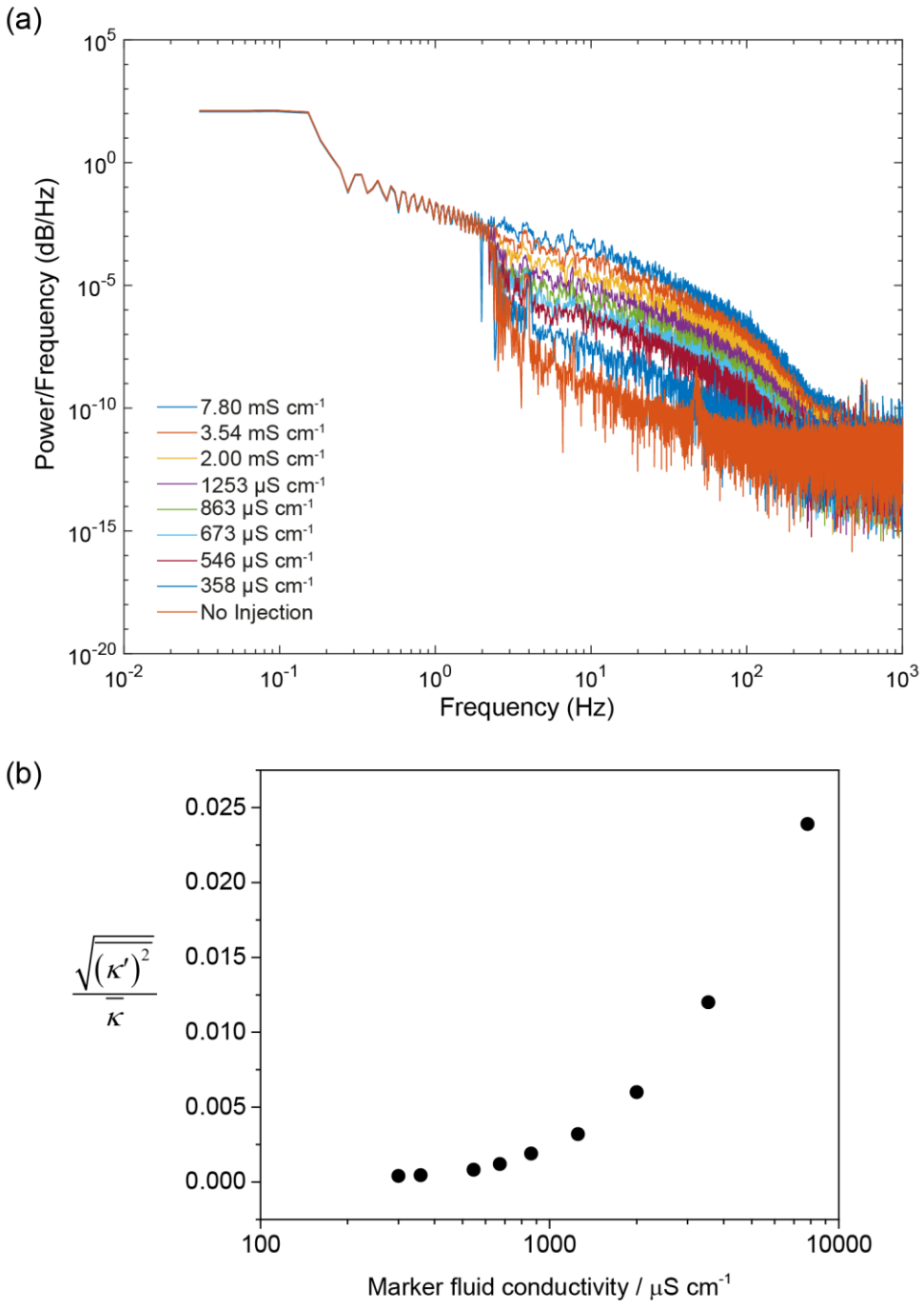

Figure 5.17. Marker fluid injection experiments showing marker fluid concentration dependence. (a) Power spectral density function of the turbulent region, and (b) intensity of turbulence measured by the conductivity sensor. Marker fluid was serially diluted from (—) 7.80 mS cm^{-1} through (—) 3.54 mS cm^{-1}, (—) 2.00 mS cm^{-1}, (—) 1253 µS cm^{-1}, (—) 863 µS cm^{-1}, (—) 673 µS cm^{-1}, (—) 546 µS cm^{-1}, to (—) 358 µS cm^{-1} injected into turbulent pipe flow of tap water (300 µS cm^{-1}). u = 2.5 m s^{-1}, v = 6.2 mL s^{-1}, j = 14 cm.

As the conductivity of the marker fluid decreases, the fluctuations in κ that are detected by the sensor become less. This is present in both the power spectra and the overall statistical intensity of turbulence. Across all k, the PSD drops as a function of marker fluid conductivity. No injection represents the background ambient fluid flow of the tap water (300 µS cm^{-1}) where no marker fluid was injected. Notice in this spectrum we observe a small noise peak at 50 Hz (most likely due to power line[62]) that is not observable at the lowest marker fluid conductivity or above (>358 µS cm^{-1}), signifying that stray fluctuations in sensor output (noise observed *e.g.* in **Figure 5.7**) are not appreciably correlated with the true signal, *i.e.* the κ fluctuations within a sensing volume surrounding the sensor.[63]

5.4.2.3 Diamond based temperature sensor

For all the turbulence experiments described in this Chapter, the diamond based temperature sensor was also positioned in the pipe setup (situated in the secondary position, **Figure 5.3**) recording temperature measurements simultaneously to the conductivity measurements from the all-diamond conductivity sensor, in order to attain temperature corrected conductivity (κ_{25}) values. A commercial temperature probe was used to monitor the reservoirs for ambient fluid and marker fluid, and no appreciable temperature change was detected (<0.1°C) over the timescale of the experiments (min). Therefore the κ fluctuations measured were not a function of temperature. However, because turbulent temperature fluctuations may accompany κ fluctuations when measuring in real world environments (*e.g.* for atmospheric measurement[33,64]), we investigated the performance of the diamond based temperature sensor with respect to the detection of fluctuations in temperature arising in turbulent flow.

Using the same pipe flow setup as previous (**Figure 5.3**), the diamond based temperature position was located in the primary position. In these experiments, marker fluid was the same composition as the ambient fluid (tap water) but was maintained at a high temperature (60 °C) and injected into low temperature ambient fluid (15 °C). Measurement traces obtained were similar to those illustrated earlier, and the turbulent regions during marker fluid injection were analysed by PSD (**Figure 5.18**).

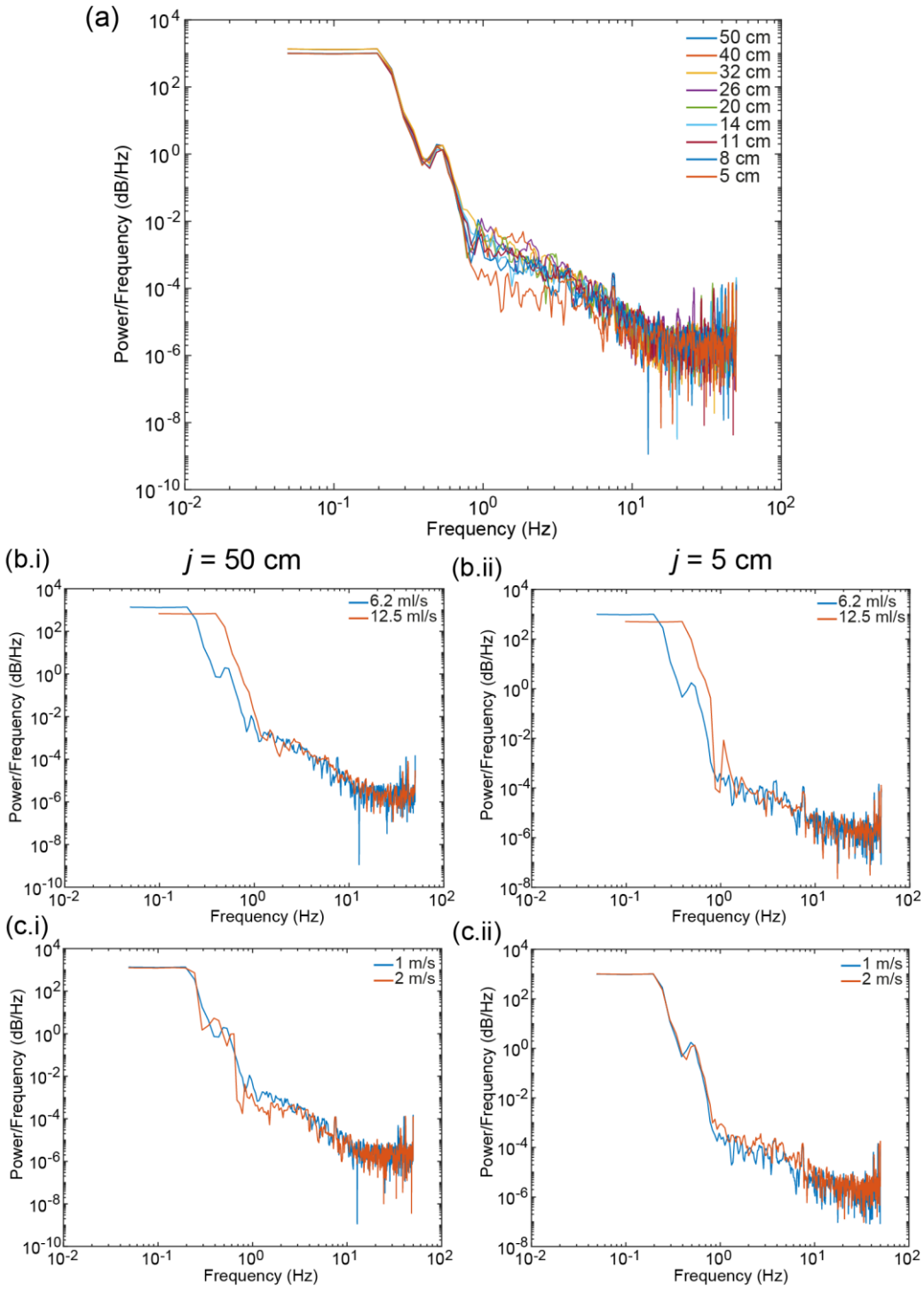

Figure 5.18. Power spectral density functions from marker fluid injection experiments measured using diamond based temperature sensor. High temperature (60 °C) marker fluid was injected into low temperature (15 °C) pipe flow. (a) Varying marker fluid injection position at a constant u = 1 m s^{-1}, v = 6.2 mL s^{-1}. (b) Varying marker fluid injection flow rate at constant u = 1 m s^{-1} for (i) j = 50 cm and (ii) j = 5 cm. (c) Varying mainstream pipe flow velocity at constant v = 6.2 mL s^{-1} for (i) j = 50 cm and (ii) j = 5 cm.

Since temperature is a scalar flow property, as well as conductivity, the shape of the PSD curves are the same as we have seen previously. Measurements were obtained at 100 Hz, thereby giving an upper k bound of 50 Hz. However, in all experimental conditions the noise floor of the diamond based temperature sensor was found to be $k' \approx$ 10–11 Hz. This indicates that the sensor can only respond to turbulent temperature fluctuations on time scales larger than ~0.1 ms.

The decaying behaviour of the PSD depends on the temperature dissipation rate, χ,[65,66]

$$\chi = 2D\int_0^\infty k^2 E(k)dk \tag{5.9}$$

where D is the thermal diffusivity of water (1.43×10^{-7} m^2 s^{-1}).[67] When comparing flow velocity, $\chi = 3.6\times10^{-5}$ K s^{-1} for u = 1 m s^{-1} and $\chi = 4.0\times10^{-5}$ K s^{-1} for u = 2 m s^{-1}. Both of these are constant v = 6.2 mL s^{-1}; at the faster injection flow rate (v = 12.5 mL s^{-1}) $\chi = 6.8\times10^{-5}$ K s^{-1}. These observations are in accordance with previously calculated values, and suggest that the sensor was measuring temperature fluctuations at spatial scales short enough for diffusion to become dominant (under the experimental conditions used here).[65,66]

5.5 Conclusions

For monitoring solution conductivity in real world aquatic environments, a conductivity sensor is generally exposed to turbulent flow conditions, and may be expected to measure changes in conductivity over both short and long spatial and temporal ranges. In this study, the performance properties of the all-diamond conductivity sensor were evaluated under such situations. Specifically, two sensor

applications were investigated: environmental, using river water in an artificial river flume; and industrial, using a circular pipe flow rig.

To simulate monitoring in the natural environment, the all-diamond conductivity sensor and diamond based temperature sensor were placed in natural river water flowing through an artificial flume. Both were shown to be capable of measuring accurate conductivity and temperature values simultaneously in this environment. Moreover, even after 36 days continuous monitoring river water *in situ*, with the exception of a ~2.5× increase in noise, the all-diamond conductivity sensor appears resilient to loss in performance, biofouling, and drift.

In order to analyse the performance capabilities of the conductivity sensor regarding measurement under spatial and time scales in the dynamics of turbulence, the sensor was placed in a circular pipe with an external fluid introduced into the turbulent flow. This has application in many industrial and engineering processes. The response of the conductivity sensor to marked changes in conductivity under turbulent flow conditions was assessed as a function of varying experimental parameters: pipe flow velocity, marker fluid injection flow rate, and the injection position/distance away from the sensor. Through analysis using various statistical measures of turbulence, we show that the all-diamond conductivity sensor is able to detect fluctuations in conductivity overall under all conditions tested. The highest spatial resolution of the sensor was found to be ~0.38 cm, indicating that even at high flow velocities (high Re) the sensor is capable of detecting changes in conductivity due to turbulent motion at fast timescales (up to 700 Hz).

Overall, this study has shown that the all-diamond conductivity sensor offers the capacity for *in situ* monitoring of solution conductivity in a range of real world

aquatic environments. The ability to measure changes in conductivity at high spatial resolution and fast timescales will afford the sensor opportunity in a host of environmental, industrial, and engineering applications.

5.6 References

(1) Lipták, B. G. *Instrument Engineers' Handbook. Volume I: Process Measurement and Analysis*, 4th ed.; CRC Press: Boca Raton, 2003.

(2) *In Situ Monitoring of Aquatic Systems: Chemical Analysis and Speciation*, 1st ed.; Buffle, J., Horvai, G., Eds.; John Wiley & Sons, Inc.: Chichester, 2001.

(3) McCleskey, R. B.; Kirk Nordstrom, D.; Ryan, J. N. Electrical Conductivity Method for Natural Waters. *Appl. Geochemistry* **2011**, *26* (SUPPL.), S227–S229.

(4) de Sousa, D. N. R.; Mozeto, A. A.; Carneiro, R. L.; Fadini, P. S. Electrical Conductivity and Emerging Contaminant as Markers of Surface Freshwater Contamination by Wastewater. *Sci. Total Environ.* **2014**, *484* (1), 19–26.

(5) Mills, G.; Fones, G. A Review of in Situ Methods and Sensors for Monitoring the Marine Environment. *Sens. Rev.* **2012**, *32* (1), 17–28.

(6) Hyldgård, A.; Mortensen, D.; Birkelund, K.; Hansen, O.; Thomsen, E. V. Autonomous Multi-Sensor Micro-System for Measurement of Ocean Water Salinity. *Sensors Actuators A Phys.* **2008**, *147* (2), 474–484.

(7) Bartram, J.; Ballance, R. *Water Quality Monitoring*, 1st ed.; Chapman & Hall: London, 1996.

(8) Howell, K. A.; Achterberg, E. P.; Braungardt, C. B.; Tappin, A. D.; Worsfold, P. J.; Turner, D. R. Voltammetric in Situ Measurements of Trace Metals in Coastal Waters. *TrAC - Trends Anal. Chem.* **2003**, *22* (11), 828–835.

(9) Wangersky, P. J. Methods of Sampling and Analysis and Our Concepts of Ocean Dynamics. *Sci. Mar.* **2005**, *69*, 75–84.

(10) Livingstone, D. A. Chemical Composition of Rivers and Lakes. In *Data of Geochemistry*; Fleischer, M., Ed.; United States Government Printing Office: Washington, 1963.

(11) Talbot, J. D. R.; House, W. A.; Pethybridge, A. D. Prediction of the Temperature Dependence of Electrical Conductance for River Waters. *Water Res.* **1990**, *24* (10), 1295–1304.

(12) Gangarosa, L. P.; Park, N. H.; Fong, B. C.; Scott, F.; Hill, J. M. Conductivity of Drugs Used for Iontophoresis. *J. Pharm. Sci.* **1978**, *67* (10), 1439–1443.

(13) Lin, S. H.; Chen, M. L. Treatment of Textile Wastewater by Chemical

Methods for Reuse. *Water Res.* **1997**, *31* (4), 868–876.

(14) Palaniappan, S.; Sastry, S. K. Electrical Conductivity of Selected Juices: Influences of Temperature, Solids Content, Applied Voltage, and Particle Size. *J. Food Process Eng.* **1991**, *14* (4), 247–260.

(15) Colombié, S.; Latrille, E.; Sablayrolles, J. M. Interest of On-Line Monitoring Electrical Conductivity during Wine Fermentation. *Eur. Food Res. Technol.* **2008**, *226* (6), 1553–1557.

(16) Mohammadi, A. R.; Graham, T. C. M.; Madden, J. D. W.; Bennington, C. P. J. Toward a Flow Following Ionic Conductivity and Temperature Sensor Package. *Ind. Eng. Chem. Res.* **2012**, *51* (6), 2738–2746.

(17) Lamb, D. E.; Manning, F. S.; Wilhelm, R. H. Measurement of Concentration Fluctuations with an Electrical Conductivity Probe. *AIChE J.* **1960**, *6* (4), 682–685.

(18) Maupin, T. P.; Agouridis, C. T.; Warner, R. C. Conductivity Sensor Accuracy and Temporal Stability: A Laboratory and Field Study. In *Environmental Considerations in Energy Production*; Crayton, J. R., Ed.; Society for Mining, Metallurgy, and Exploration, Inc.: Englewood, 2013.

(19) Weidman, P. D. Measurement Techniques in Laboratory Rotating Flows. In *Advances in Fluid Mechanics*; Gad-el-Hak, M., Ed.; Springer-Verlag: Berlin, 1989.

(20) Smol'yakov, A. V.; Tkachenko, V. M. *The Measurement of Turbulent Fluctuations*, 1st ed.; Springer-Verlag: Berlin, 1983.

(21) Muralidhar, K. Introduction to Turbulence. In *Turbulent Flows*; Biswas, G., Eswaran, V., Eds.; Alpha Science International: Pangbourne, 2002; pp 1–40.

(22) Pope, S. B. *Turbulent Flows*, 1st ed.; Cambridge University Press: Cambridge, 2000.

(23) Mathieu, J.; Scott, J. *An Introduction to Turbulent Flow*, 1st ed.; Cambridge University Press: Cambridge, 2000.

(24) Robinson, D. I. Multi-Scale Modelling of Effluent Dispersion in the Marine Environment, Imperial College London, 2016.

(25) Reynolds, C. S.; White, M. L.; Clarke, R. T.; Marker, A. F. Suspension and Settlement of Particles in Flowing Water: Comparison of the Effects of Varying Water Depth and Velocity in Circulating Channels. *Freshw. Biol.* **1990**, *24* (1), 23–34.

(26) Czernuszenko, W.; Rowinski, P. *Water Quality Hazards and Dispersion of Pollutants*, 1st ed.; Springer Science & Business Media: New York, 2005.

(27) Reynolds, O. An Experimental Investigation of the Circumstances Which Determine Whether the Motion of Water Shall Be Direct or Sinuous, and of the Law of Resistance in Parallel Channels. *Philos. Trans. R. Soc. London* **1883**, *174* (1883), 935–982.

(28) Taylor, G. The Dispersion of Matter in Turbulent Flow through a Pipe. *Proc. R. Soc. London. Ser. A. Math. Phys. Sci.* **1954**, *223* (1155), 446–468.

(29) Kleinstreur, C. *Engineering Fluid Dynamics*, 1st ed.; Cambridge University Press: Cambridge, 1997.

(30) Cebeci, T. *Analysis of Turbulent Flows*, 2nd ed.; Elsevier Ltd: Oxford, 2004.

(31) Subbarao, P. M. V. Measurement of Turbulent Fluctuations. In *Turbulent Flows*; Biswas, G., Eswaran, V., Eds.; Alpha Science International: Pangbourne, 2002; pp 179–218.

(32) Bentley, J. P. *Principles of Measurement Systems*, 4th ed.; Pearson Education: Harlow, 2005.

(33) Blackadar, A. K. *Turbulence and Diffusion in the Atmosphere*, 1st ed.; Springer-Verlag: Heidelberg, 1998.

(34) Chatfield, C. *The Analysis of Time Series: An Introduction*, 6th ed.; CRC Press: Boca Raton, 2003.

(35) Percival, D. P.; Walden, A. T. *Spectral Analysis for Physical Applications*, 1st ed.; Cambridge University Press: Cambridge, 1993.

(36) White, F. M. *Fluid Mechanics*, 7th ed.; McGraw-Hill: New York, 2010.

(37) Malverti, L.; Lajeunesse, E.; Métivier, F. Small Is Beautiful: Upscaling from Microscale Laminar to Natural Turbulent Rivers. *J. Geophys. Res. Earth Surf.* **2008**, *113* (4), 1–14.

(38) McQuivey, R. S. *Principles and Measuring Techniques of Turbulence Characteristics in Open-Channel Flows*; Washington, 1973.

(39) Hanrahan, G.; Patil, D. G.; Wang, J. Electrochemical Sensors for Environmental Monitoring: Design, Development and Applications. *J. Environ. Monit.* **2004**, *6* (8), 657.

(40) Edmondson, W. T. Measurements of Conductivity of Lake Water in Situ. *Ecology* **1956**, *37* (1), 201–204.

(41) Navratil, O.; Esteves, M.; Legout, C.; Gratiot, N.; Nemery, J.; Willmore, S.; Grangeon, T. Global Uncertainty Analysis of Suspended Sediment Monitoring Using Turbidimeter in a Small Mountainous River Catchment. *J. Hydrol.* **2011**, *398* (3–4), 246–259.

(42) Trouillon, R.; O'Hare, D. Comparison of Glassy Carbon and Boron Doped Diamond Electrodes: Resistance to Biofouling. *Electrochim. Acta* **2010**, *55* (22), 6586–6595.

(43) Trouillon, R.; Combs, Z.; Patel, B. A.; O'Hare, D. Comparative Study of the Effect of Various Electrode Membranes on Biofouling and Electrochemical Measurements. *Electrochem. commun.* **2009**, *11* (7), 1409–1413.

(44) Yokosi, S. The Structure of River Turbulence. *Bull. Disaster Prev. Res. Inst.* **1967**, *17* (2), 1–29.

(45) Fischer, H. B. Longitudinal Dispersion and Turbulent Mixing in Open-Channel Flow. *Annu. Rev. Fluid Mech.* **1973**, *5* (1), 59–78.

(46) West, J. R.; Oduyemi, K. O. K. Turbulence Measurements of Suspended

Solids Concentration in Estuaries. *J. Hydraul. Eng.* **1989**, *115* (4), 457–474.

(47) McComb, W. D.; Rabie, L. H. Local Drag Reduction Due to Injection of Polymer Solutions into Turbulent Flow in a Pipe. Part I: Dependence on Local Polymer Concentration. *AIChE J.* **1982**, *28* (4), 547–557.

(48) Kadotani, K.; Goldstein, R. J. On The Nature of Jets Entering A Turbulent Flow: Part A—Jet–Mainstream Interaction. *J. Eng. Power* **1979**, *101* (3), 459.

(49) Fitzgerald, S. D.; Holley, E. R. *Jet Injections for Optimum Mixing in Pipe Flow*; 1979.

(50) Usui, H. Drag Reduction Caused by the Injection of a Polymer Solution into a Pipe Flow. In *Structure of Turbulence and Drag Reduction*; Gyr, A., Ed.; Springer-Verlag: Berlin, Heidelberg, 1990; pp 257–274.

(51) Levenspiel, O. Longitudinal Mixing of Fluids Flowing in Circular Pipes. *Ind. Eng. Chem.* **1958**, *50* (3), 343–346.

(52) Phillips, O. M. The Kolmogorov Spectrum and Its Oceanic Cousins: A Review. *Proc. R. Soc. A Math. Phys. Eng. Sci.* **1991**, *434* (1890), 125–138.

(53) Thomson, D. J. Spectrum Estimation and Harmonic Analysis. *Proc. IEEE* **1982**, *70* (9), 1055–1096.

(54) Dimotakis, P. E. Turbulent Mixing. *Annu. Rev. Fluid Mech.* **2005**, *37* (1), 329–356.

(55) Guilkey, J. E.; Kerstein, A. R.; McMurtry, P. A.; Klewicki, J. C. Mixing Mechanisms in Turbulent Pipe Flow. *Phys. Fluids* **1997**, *9* (3), 717–723.

(56) Kundu, P. K.; Cohen, I. M.; Dowling, D. R. *Fluid Mechanics*, 5th ed.; Academic Press: Waltham, 2012.

(57) O'Neill, P. L.; Nicolaides, D.; Honnery, D. R.; Soria, J. Autocorrelation Functions and the Determination of Integral Length with Reference to Experimental and Numerical Data. In *15th Australasian Fluid Mechanics Conference*; 2004.

(58) Garde, R. J. *Turbulent Flow*, 1st ed.; Wiley Eastern: New Delhi, 1994.

(59) Usui, H.; Maeguchi, K.; Sano, Y. Drag Reduction Caused by the Injection of Polymer Thread into a Turbulent Pipe Flow. *Phys. Fluids* **1988**, *31* (9), 2518–2523.

(60) Soulsby, R. L. Selecting Record Length and Digitization Rate for Near-Bed Turbulence Measurements. *J. Phys. Oceanogr.* **1980**, *10* (2), 208–219.

(61) Goldsack, D. E.; Franchetto, R. C. The Viscosity of Concentrated Electrolyte Solutions. II. Temperature Dependence. *Can. J. Chem.* **2006**, *56* (10), 1442–1450.

(62) Munroe, D. M. Signal-to-Noise Ratio Improvement. In *Handbook of Measurement Science*; Sydenham, P. H., Ed.; John Wiley & Sons, Inc.: Chichester, 1982; pp 431–488.

(63) Lapointe, M. F.; De Serres, B.; Biron, P.; Roy, A. G. Using Spectral Analysis

to Detect Sensor Noise and Correct Turbulence Intensity and Shear Stress Estimates from EMCM Flow Records. *Earth Surf. Process. Landforms* **1996**, *21*, 195–203.

(64) Lumley, J. L.; Panofsky, H. A. *The Structure of Atmospheric Turbulence*, 1st ed.; John Wiley & Sons, Inc.: New York, 1964.

(65) Grant, H. L.; Hughes, B. A.; Vogel, W. M.; Moilliet, A. The Spectrum of Temperature Fluctuations in Turbulent Flow. *J. Fluid Mech.* **1968**, *34* (3), 423–442.

(66) Hill, R. J. Models of the Scalar Spectrum for Turbulent Advection. *J. Fluid Mech.* **1978**, *88* (03), 541.

(67) Lide, D. R. *CRC Handbook of Chemistry and Physics*, 89th ed.; CRC Press: Boca Raton, 2008.

6 Design and development of a biofilm activity sensor for monitoring biofilm formation

6.1 Aims

Biofouling and biofilm formation problems are usually detected by the deterioration of process performance or product quality. Following this, an antifouling countermeasure is applied in the hope of restoring process parameters. Alternatively, the blind application of biocides is employed. Both of these constitute expensive ways of monitoring of biofilm formation and treatment. Clearly, early warning systems which indicate the site and extent of biofilm formation in water systems are of crucial significance for timely and optimal countermeasures against biofouling. Here, we explore initial work into the fabrication and testing of three possible prototype small-scale devices for the detection of biofilm formation. These have been designed to be suitable for placement in a variety of water based environments, for example in medical or environmental applications.

6.2 Introduction

Biofouling is the accumulation of unwanted biological matter upon a surface, most commonly through the development of microbial biofilms. Biofouling impacts negatively on a wide variety of medical, environmental and industrial contexts. Industrial biofouling affects a range of applications from water utility systems and food production, to power plants and industrial processes.[1–11] Biofilms in aquatic ecosystems pose environmental concerns and a significant threat to human health,

since they can act as reservoirs for antibiotic resistance, and aid the transmission of human pathogens. In humans, biofilms can lead to persistent and life-threatening infections, often through the contamination of medical devices, catheters, implants, and prosthetics.[11,12]

Despite the huge costs of biofouling and biofilm formation, one problem in conventional antifouling measures still remains: there is no early warning system to monitor or identify the onset of biofilm formation. Typically, biofouling is only detected by losses in process performance or product quality. Consequently, any biofilm countermeasure is either proactive (*e.g.* regular dosing of disinfectant) or reactive (*e.g.* cleaning once performance has dropped) but these are often expensive ways of monitoring, and neither can provide an optimal biofilm control strategy.[7,13]

As a result, early warning systems which indicate the site and extent of biofilm formation in water systems are of crucial significance for timely and optimal countermeasures against biofouling. Some research has gone into the development of optical fibre sensors for this purpose.[14–16] However, these typically require the turbidity of the water system to be quite low so as to avoid interferences.

One of the only current commercially available biofilm activity sensors (**Figure 6.1**) works similarly to a conductivity sensor, effectively making a resistance measurement.[17,18] It applies a small positive potential across alternating electrodes for a short time, then applies zero potential for the remainder, measuring the current continuously. This system uses metal (stainless steel or titanium) electrodes, and is around 6−10 cm in size as it is designed for in-line process control.

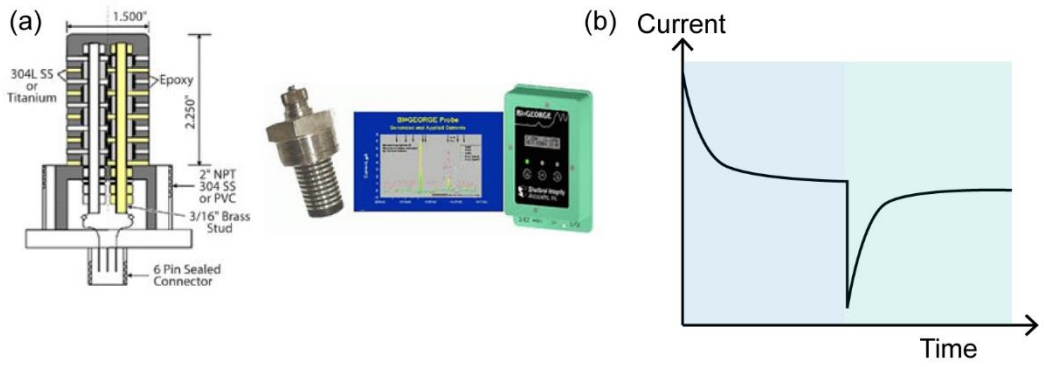

Figure 6.1. Current commercially available biofilm activity sensor. (a) Schematic showing the alternating electrodes (left) and photograph of the sensor (right). (b) Example sensor response, following the measured current with time, upon the application of a small positive potential (blue region) and then zero potential (green region).

As a result of each applied potential step change, there is a current spike arising from the change in double layer capacitance, which equates to the charging or discharging of a capacitor when a potential step is applied.[19] This decays to a certain baseline current value (termed "active baseline" following step from 0 to positive potential, and "passive baseline" following step back to 0 mV, both measured at the end of the respective periods). It is thought that the presence of a biofilm on the sensor will result in a change in both the baseline current levels; generally, as biofilm forms on the sensor surface, the active baseline increases whilst the passive baseline decreases.[17] The origin of the current changes is currently not understood, but we offer some suggestions later on in this chapter.

In this work, we investigate the production of devices based on a similar concept, which are smaller in size and can thus ultimately be placed in a variety of smaller-scale environments, as opposed to *e.g.* large scale plants. Such devices would be required in a range of medical applications, for example in dental unit waterlines[20] or renal dialysis units[21]. We explore different fabrication procedures along with three

different electrode materials, from low cost where the device is likely to be disposable, to more robust devices which are reusable.

6.3 Experimental

Biofilm activity sensor designs were based on a current commercial biofilm activity sensor, [17,18] and consisted of a series of electrode pairs alternating in an interdigitated fashion. Three sensors were fabricated for testing using different materials (**Figure 6.2**), which overall represent different levels of cost, reusability, and ease of fabrication. A 3D printed sensor was custom designed and printed in-house (Process Instruments, Burnley, UK) using electrically conductive acrylonitrile butadiene styrene (ABS) to create 12 layers (6 electrode pairs) embedded in a housing of insulating ABS. A screen printed sensor was fabricated by a commercial manufacturer (Gwent Electronic Materials, Pontypool, UK) using a carbon/graphite paste to create four electrode pairs screen printed onto an alumina substrate. An all-diamond sensor was fabricated as described previously,[22] and in Chapter 2, to create four boron doped diamond (BDD) electrode pairs embedded in an insulating diamond substrate. After an acid cleaning treatment, the BDD surface was O-terminated (O-BDD). Electrical contact was made to each sensor from dedicated contact areas with Ag conductive epoxy and Cu wires. For ease of manufacture, the 3D printed sensor was assembled as a flow-through device, whilst the screen printed and diamond sensors were planar.

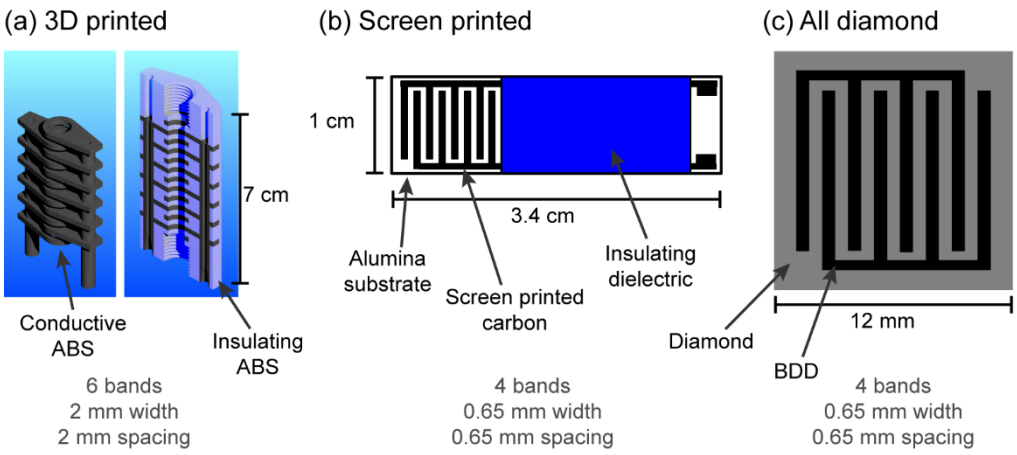

Figure 6.2. Designs of the three prototype biofilm activity sensors: (a) 3D printed, (b) screen printed, and (c) all diamond.

All three sensors were placed in-line in a flow system (**Figure 6.3**) driven by a small centrifugal pump (HD601, Hidom Electric Co., China). The 3D printed sensor was connected directly in-line, whilst the all-diamond sensor was sited in-line using a tee plug and connector; the screen printed sensor was positioned in a small PVC sub-reservoir. A commercial biofilm activity sensor (Biosense; Process Instruments, Burnley, UK) was also employed. The system was recirculating rain water that was collected and spiked with 1 g L^{-1} glucose (Sigma-Aldrich, St Louis, USA) to encourage bacterial growth. Using custom-built electronics (Process Instruments, Burnley, UK) for each sensor, a potential of 200 mV was applied between each of the alternating electrode pairs, for a duration of 30 min every 6 h. For the remainder of the time, a potential of 0 mV was applied, and the current monitored throughout.

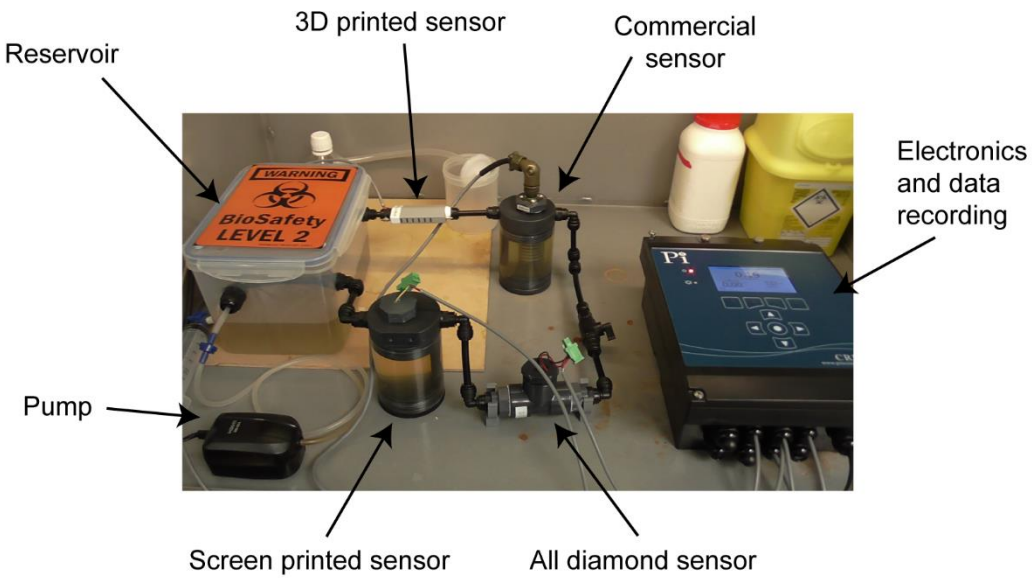

Figure 6.3. Experimental flow system set-up for biofilm activity sensor trials.

Chronoamperometry experiments were conducted using a CHI760A potentiostat (CH Instruments, Texas, USA). One side of the alternating electrode pairs was connected as working electrode, with the other side as reference and counter electrode. Step pulses of 200 mV and 0 mV were alternately applied each for 1000 s duration, and the current measured as a function of time. 1 g of sodium alginate (Vickers Laboratories, Pudsey, UK) was dissolved in 100 mL ultrapure water, which formed a clear, transparent gel. This gel was applied approximately uniformly across the surface of the biofilm activity sensor to simulate a biofilm matrix.

Data analysis was conducted using OriginPro (v. 9.1, OriginLab Corporation, Massachusetts, USA).

6.4 Results and discussion

Images of the three potential sensors each manufactured using different electrode materials: (1) using the all-diamond platform consisting of BDD electrodes embedded in an insulating diamond substrate, (2) a screen printed electrode consisting of carbon ink screen printed onto an alumina substrate, and (3) a 3D printed sensor consisting of conducting ABS embedded into insulating ABS, are shown in **Figure 6.4a**. In order to assess the feasibility as a biofilm activity sensor, all three test sensors were placed in-line in a recirculating flow system for 3 days, following a sensing procedure similar to the commercial sensor: application of 200 mV for 30 min duration applied every 6 h, with 0 mV applied for the remainder. The current-time data is shown in **Figure 6.4b**.

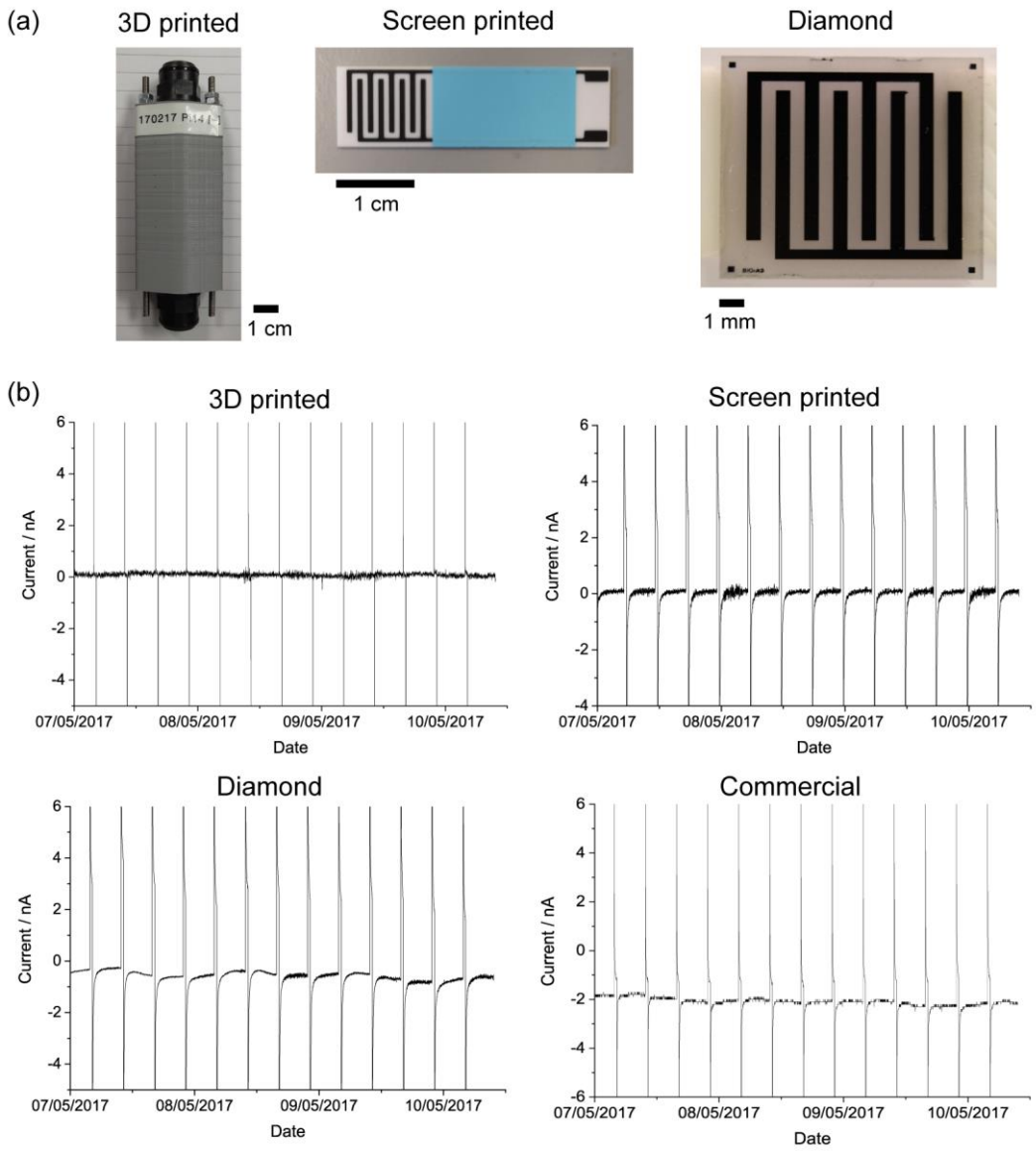

Figure 6.4. Design and trial data from 3D printed, screen printed, and diamond biofilm activity sensors. (a) Photographs of the fabricated sensors are shown alongside (b) an 86 hour measurement trace, in addition to the commercial sensor for comparison. All sensors were placed in-line in a flow system recirculating rain water spiked with 1 g L^{-1} glucose. Current across the interdigitated electrodes was measured following the application of 200 mV for 30 min duration applied every 6 h, with 0 mV applied for the remainder.

From the initial trial data, for the 3D printed sensor it is not possible to observe a baseline current following the 200 mV application, nor is it possible to observe the current decay; the signal appears to be one continuous noisy baseline. This may be due to the material not being conductive enough. For the screen printed sensor,

performance started well as baseline current levels were stable and clearly defined. However, after a few days the signal became progressively worse/noisier, due to the degradation of ink/polymer (small flakes of the black ink were visually observed occasionally coming off). When the sensor was removed from the system following the trial, the remaining ink peeled directly off the substrate. Finally, the all-diamond sensor gave average performance fairly consistently, due to the robust nature of diamond surface. Note that this 3-day trial period was not intended to detect any signs of biofilm activity, but rather to assess general performance properties of each sensor design.

Of all the three sensors, the all-diamond appears to be the most stable, though this is the most expensive design and fabrication process. Additionally, as shown in Chapter 4, O-BDD offers a very low biofouling surface. Due to this, a bare O-BDD based sensor may not respond to biofilm formation quickly enough in the system of interest. However, also shown in Chapter 4 was that it is possible to modify the surface properties of diamond, for example by using a laser micromachining approach to increase the surface roughness of BDD. Using this procedure, the resultant surface was shown to significantly increase levels of biofilm formation (**Figure 4.18**). Consequently, a fourth prototype was constructed based on the all-diamond design, but taking into account cost and increased biofilm formation properties of the surface.

In particular, six individual BDD bands of dimensions 1 × 10 mm were laser roughened, electrically connected in an alternating arrangement, and then encapsulated in epoxy. This sensor, which represents a lower cost version of the all-diamond sensor, was tested in the flow system for 14 days. The current-time profiles are shown in **Figure 6.5a**.

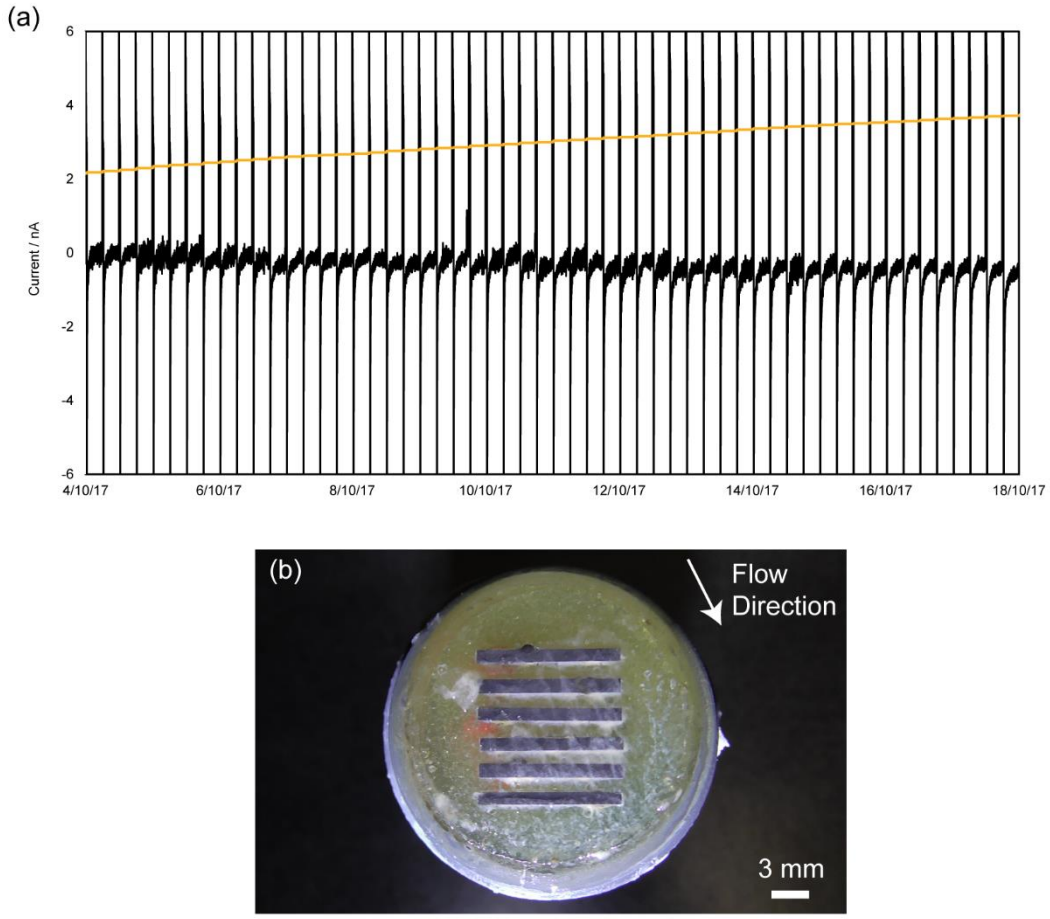

Figure 6.5. 14 day measurement data from the laser roughened BDD biofilm activity sensor. (a) Sensor was placed in a flow system recirculating rain water spiked with 10 g L^{-1} glucose. Current across the interdigitated electrodes was measured following the application of 200 mV for 30 min duration applied every 6 h, with 0 mV applied for the remainder. Orange line indicates the cumulative moving average of the current value at the end of each 30 min application.[§§] (b) Photograph of the sensor at the end of the test period.

Two key points can be observed from the measurement trace. First, the baseline current following 200 mV application increased from 2.1 nA to 3.9 nA over the 14 day period (orange line, **Figure 6.5a**) along with the passive baseline current (following 0 mV application) decreasing from 0 nA to −1 nA. Both of these are attributed to biofilm formation on the roughened BDD bands.[17] Interestingly, it is

[§§] The current magnitude at the end of each 30 min period of 200 mV application is used to calculate an equally weighted average of the sequence of current values up to the present time.

also possible to observe optically some form of biofouling on the sensor surface (**Figure 6.5b**).

Moreover, it is possible to observe that the shape of the passive current curve (0 mV application) changing over the 14 day period. We believe that this is a result of the presence of biofilm changing either the double layer capacitance or creating an additional system resistance. Furthermore, the application of +200 mV may induce bacterial attachment and biofilm formation on the electrode surface (due to the net negative charge on a bacterial cell).[23,24] Moreover, an active biofilm may also release species that are redox active (can be oxidised/reduced) such as pyocyanin[25] or other biomarkers[26], which may be possible to detect *via* a Faradaic current flow.

To begin to understand why this result is occurring, and to investigate whether the shape of the passive current-time curves can inform whether levels of biofilm formation are increasing, we looked at the curve shapes under different conditions. Using chronoamperometry, potentials of 0 mV and 200 mV were applied to the laser roughened BDD band sensor to simulate the biofilm activity measurement (**Figure 6.6**).

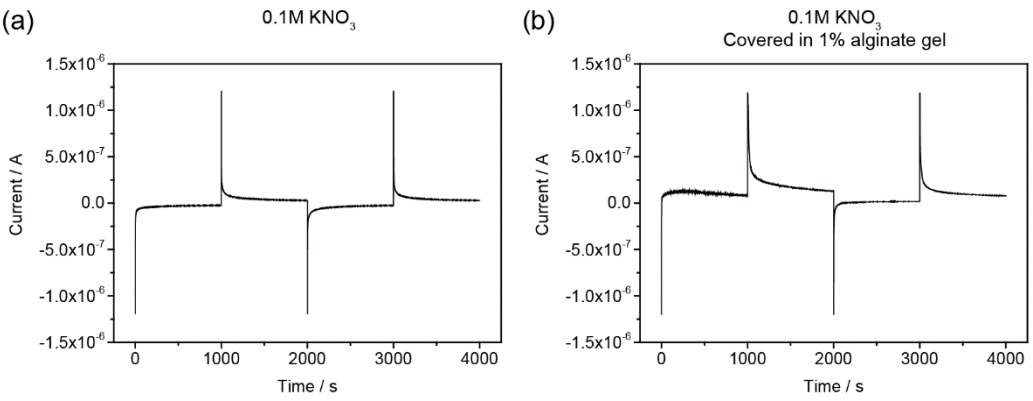

Figure 6.6. Chronoamperometry experiment using the laser roughened BDD biofilm activity sensor when (a) clean, and (b) covered in 1% alginate gel. 0 mV and 200 mV are alternately applied across the interdigitated electrodes for 1000 s duration each, in a solution of 0.1M KNO_3.

The experiment was performed in 0.1M KNO_3 as the background electrolyte solution, initially with the roughened BDD electrodes (**Figure 6.6a**). Alginate is a polysaccharide produced by bacteria in biofilms and is a major component of the extracellular polymeric substance.[27,28] After coating the sensor surface with an alginate gel, we observe that the shape of curve does change (**Figure 6.6b**) resulting in a slower current decay and a higher current baseline level compared to the absence of the alginate gel. It will be interesting for future work to investigate the effect of other insulating films (*e.g.* polystyrene), as well as preconcentrating the film with an electroactive species to mimic a biofilm.

6.5 Conclusions

The fabrication of a small-scale biofilm activity sensor was investigated, from low cost where the device is likely to be disposable, to more robust devices which are reusable. Three different electrode materials were explored, namely 3D printed ABS, screen printed carbon, and BDD. Only BDD proved suitable over an initial trial timescale (3 days). The 3D printed ABS used did not appear to be conductive enough, resulting in high noise; the performance of the screen printed sensor started well, but after the trial was observed to irreversibly degrade. Due to the low biofouling nature of BDD, this material may not provide the early warning signal that is necessary. Nonetheless, using a laser roughening approach, the BDD band electrodes can be modified in order to promote biofilm formation on the surface. Using a biofilm activity sensor fabricated from these electrodes, over a 14 day trial period the sensor response was observed to change which was attributed to biofilm formation. The use of laser roughened, boron doped diamond band electrodes hence

proves promising for a biofilm activity sensor. However, considerable further work is required in order reach proof-of-concept stage, to understand why this result is occurring, and to establish whether fouling activity can be distinguished (*i.e.* biofilm formation *vs.* inorganic fouling).

6.6 References

(1) Bixler, G. D.; Bhushan, B. Biofouling: Lessons from Nature. *Philos. Trans. R. Soc. A Math. Phys. Eng. Sci.* **2012**, *370* (1967), 2381–2417.

(2) Walker, J.; Surman, S.; Jass, J. *Industrial Biofouling: Detection, Prevention and Control*, 1st Ed.; Wiley: Chichester, 2000.

(3) *Biofilms - Science and Technology*, 1st Ed.; Melo, L. F., Bott, T. R., Fletcher, M., Capdeville, B., Eds.; Plenum Publishing Corporation, 1992.

(4) Liu, S.; Gunawan, C.; Barraud, N.; Rice, S. A.; Harry, E. J.; Amal, R. Understanding, Monitoring, and Controlling Biofilm Growth in Drinking Water Distribution Systems. *Environ. Sci. Technol.* **2016**, *50* (17), 8954–8976.

(5) Costerton, J. W.; Cheng, K.-J.; Greesy, G. G.; Ladd, T. I.; Nickel, J. C.; Dasgupta, M.; Marrie, T. J. Bacterial Biofilms in Nature and Disease. *Ann. Rev. Microbiol.* **1987**, *41*, 435–464.

(6) Klahre, J.; Flemming, H. C. Monitoring of Biofouling in Papermill Process Waters. *Water Res.* **2000**, *34* (14), 3657–3665.

(7) Flemming, H. C. Microbial Biofouling: Unsolved Problems, Insufficient Approaches, and Possible Solutions. In *Biofilm Highlights*; Flemming, H. C., Wingender, J., Szewzyk, U., Eds.; Springer-Verlag: Berlin, 2011; pp 81–110.

(8) Carpentier, B.; Cerf, O. Biofilms and Their Consequences, with Particular Reference to Hygiene in the Food Industry. *J. Appl. Bacteriol.* **1993**, *75* (6), 499–511.

(9) Flemming, H. C. Biofouling in Water Systems - Cases, Causes and Countermeasures. *Appl. Microbiol. Biotechnol.* **2002**, *59* (6), 629–640.

(10) Garrett, T. R.; Bhakoo, M.; Zhang, Z. Bacterial Adhesion and Biofilms on Surfaces. *Prog. Nat. Sci.* **2008**, *18* (9), 1049–1056.

(11) Wingender, J.; Flemming, H. C. Biofilms in Drinking Water and Their Role as Reservoir for Pathogens. *Int. J. Hyg. Environ. Health* **2011**, *214* (6), 417–423.

(12) Balcázar, J. L.; Subirats, J.; Borrego, C. M. The Role of Biofilms as Environmental Reservoirs of Antibiotic Resistance. *Front. Microbiol.* **2015**, *6*, 1–9.

(13) Costerton, J. W. *Marine and Industrial Biofouling*, 4th ed.; Flemming, H.-C., Murthy, P. S., Venkatesan, R., Cooksey, K., Eds.; Springer Series on Biofilms; Springer-Verlag: Berlin, Heidelberg, 2009; Vol. 4.

(14) Tamachkiarow, A.; Flemming, H. C. On-Line Monitoring of Biofilm Formation in a Brewery Water Pipeline System with a Fibre Optical Device. *Water Sci. Technol.* **2003**, *47* (5), 19–24.

(15) Strathmann, M.; Mittenzwey, K. H.; Sinn, G.; Papadakis, W.; Flemming, H. C. Simultaneous Monitoring of Biofilm Growth, Microbial Activity, and Inorganic Deposits on Surfaces with an in Situ, Online, Real-Time, Non-Destructive, Optical Sensor. *Biofouling* **2013**, *29* (5), 573–583.

(16) Philip-Chandy, R.; Scully, P. J.; Eldridge, P.; Kadim, H. J.; Grapin, M. G.; Jonca, M. G.; D'Ambrosio, M. G.; Colin, F. Optical Fiber Sensor for Biofilm Measurement Using Intensity Modulation and Image Analysis. *IEEE J. Sel. Top. Quantum Electron.* **2000**, *6* (5), 764–772.

(17) Bruijs, M. C. M.; Venhuis, L. P.; Jenner, H. A.; Daniels, D. G.; Licina, G. J. Biocide Optimisation Using an on-Line Biofilm Monitor. *J. Power Plant Chem.* **2001**, *3* (7), 400.

(18) Fallon, H.; Licina, G. J. Optimization of Biofilm Control Using an On-Line Monitor: Case Studies from around the World. *J. Power Plant Chem.* **2010**, *12* (12), 722–735.

(19) Bard, A. J.; Faulkner, L. R. *Electrochemical Methods, Fundamentals and Applications*, 2nd ed.; John Wiley & Sons, Inc.: New York, 2001.

(20) Wirthlin, M. R.; Marshall, G. W.; Rowland, R. W. Formation and Decontamination of Biofilms in Dental Unit Waterlines. *J. Periodontol.* **2003**, *74* (11), 1595–1609.

(21) Stickler, D. J.; Jones, S. M.; Adusei, G. O.; Waters, M. G.; Cloete, J.; Mathur, S.; Feneley, R. C. L. A Clinical Assessment of the Performance of a Sensor to Detect Crystalline Biofilm Formation on Indwelling Bladder Catheters. *BJU Int.* **2006**, *98* (6), 1244–1249.

(22) Joseph, M. B.; Bitziou, E.; Read, T. L.; Meng, L.; Palmer, N. L.; Mollart, T. P.; Newton, M. E.; MacPherson, J. V. Fabrication Route for the Production of Coplanar, Diamond Insulated, Boron Doped Diamond Macro- and Microelectrodes of Any Geometry. *Anal. Chem.* **2014**, *86* (11), 5238–5244.

(23) Shim, S.; Hong, S. H.; Tak, Y.; Yoon, J. Prevention of *Pseudomonas Aeruginosa* Adhesion by Electric Currents. *Biofouling* **2011**, *27* (2), 217–224.

(24) Sultana, S. T.; Babauta, J. T.; Beyenal, H. Electrochemical Biofilm Control: A Review. *Biofouling* **2015**, *31* (9–10), 745–758.

(25) Lau, G. W.; Hassett, D. J.; Ran, H.; Kong, F. The Role of Pyocyanin in *Pseudomonas Aeruginosa* Infection. *Trends Mol. Med.* **2004**, *10* (12), 599–606.

(26) Bassler, B. L. Regulation of Gene Expression by Quorum Sensing. *Curr. Opin. Microbiol.* **1999**, *2*, 582–587.

(27) Gacesa, P.; Russell, N. J. *Pseudomonas Infection and Alginates: Biochemistry, Genetics and Pathology*, 1st ed.; Chapman & Hall: London, 1990.

(28) Donlan, R. M. Biofilms: Microbial Life on Surfaces. *Emerg. Infect. Dis.* **2002**, *8* (9), 881–890.

7 Conclusions

7.1 Conclusions

The use of boron doped diamond (BDD) as an electrode material is of great interest in the analytical sensing field due to its many desirable qualities such as chemical and mechanical resistance as well as antifouling properties, making it advantageous for use in a variety of environmental and industrial applications. This thesis has explored the development of an all-diamond conductivity sensor, comprised of BDD electrodes encapsulated in an insulating diamond substrate, which is capable of making accurate measurements of solution conductivity in a host of natural aquatic environments.

Chapter 3 discusses the design and fabrication of an all diamond conductivity sensor. Through optimisation of the sensor cell design parameters, using a 4-point sensing configuration the Seacon conductivity sensor was demonstrated to make accurate measurements over more than five orders of magnitude, in particular the higher conductivity range that is relevant for aquatic and marine waters. In addition, finite element method simulation was utilised to understand some practical implications for the placement of this sensor device. Finally, by exploiting the high thermal conductivity of diamond it was shown to be able to integrate a temperature sensing element into the all-diamond platform. This enables the real-time simultaneous measurement of both conductivity and temperature, facilitating accurate conductivity measurement with temperature correction. Along with the development of a LabVIEW program to operate the sensor and offer a PC interface, we have produced a complete working conductivity sensor device suitable for natural aquatic environments.

However, for long-term measurement in such applications, biofouling is a major issue faced by sensors as it often causes deterioration in stability and performance. This was investigated further as discussed in Chapter 4. O-terminated BDD was found to be a low biofouling material compared to other common electrode and packaging materials. The extent of biofilm formation on BDD was assessed, and the surface properties that affect bacterial attachment explored on O-terminated BDD. This more fundamental study offers, for the first time, an insight into the interaction of microbial biofilms with BDD, which is an important consideration when utilising this material as an electrode for an applied sensor in real-world aquatic environments.

Chapter 5 looked towards applying the all-diamond conductivity sensor in flow environments and real water systems. For over a month the sensor was recording accurate conductivity measurements *in situ* in natural river water, and was found to be resilient to the detrimental effects of biofouling. Additionally, the performance properties of the sensor were fully tested under the dynamics of turbulent flow using a test pipe rig. Through analysis using various statistical measures of turbulence, the spatial and temporal resolution of the sensor was investigated, along with its response to marked rapid changes in conductivity. Overall, the sensor was found to offer valuable performance capability for a wide range of environmental, industrial, and engineering applications.

Though, for many industrial processes biofouling causes loss in performance and product quality, it is typically often only discovered once performance has been detrimentally affected. A sensor which provides an early warning indicator to biofilm formation activity, and a signal for when treatment is required, would have wide ranging economic benefits to many industries by providing timely and optimal

antifouling countermeasures. Chapter 6 explored the production of a biofilm activity sensor that enabled the detection of biofilm formation. The use of three electrode materials was discussed, and we highlighted that laser roughened BDD shows potential for this purpose due to its ability to promote microbial attachment.

In summary, this thesis explored the development of a synthetic all-diamond conductivity sensor from proof-of-concept through to validation in both laboratory and simulated environments, providing a greater understanding of BDD electrodes for real-world sensor applications. Specifically, we demonstrated the capability of the sensor as a working device allowing accurate measurements of solution conductivity with temperature correction, not only for a wide range of natural aquatic environments, but due to the extreme chemical robustness of diamond it also opens up application in more challenging corrosive or abrasive environments. Moreover, we investigated the low biofouling properties of BDD in relation to microbial biofilm formation, which has favourable implication when utilising this material as an electrode in real-world aquatic environments. Finally, we progressed from laboratory to simulated environments by assessment of the performance of the all-diamond conductivity sensor in both an environmental natural river water system as well as a pilot test rig suitable for industrial application, thus establishing the capacity for long term *in situ* placement of this all-diamond conductivity sensor for monitoring in a range of aquatic environments.

7.2 Future outlook

In addition to the work presented herein, there is considerable scope and opportunity for future work and the further development of the technologies and concepts discussed. Some ideas for future directions are now considered.

In Chapter 3, we began to explore possible modifications to the design of the all-diamond conductivity sensor to either further improve the sensor response or to open up new opportunities for sensor application. In particular, the possibility for miniaturisation of the conductivity sensor is incredibly exciting, as it allows for extensive biological application. This might prove an effective tool for both *ex vivo* testing (compatibility with small sample volumes) and *in vivo* monitoring, given the inert nature of diamond and its antifouling properties regarding *e.g.* organics and proteins.

Whilst conductivity is one of the essential testing parameters for water quality analysis, it is not the only one: pH, dissolved oxygen, and heavy metals are also common indicators of water quality. Recent work has seen the development of not only a BDD based pH sensor,[1] but has also shown the possibility for simultaneous detection of dissolved oxygen and pH (in buffered aqueous solution).[2] A natural step forward would be to create a combined conductivity and pH sensor utilising the all-diamond platform. The outcome here would be one robust, multifunctional device with the advantage that this sensor could survive in challenging environments, making it attractive to various applications such as deep sea monitoring.

Following the more fundamental study of the extent of bacterial attachment and biofilm formation on BDD in Chapter 4, there remains scope for further investigation in this area. All biofilm formation experiments in this thesis were performed under

static conditions, but since many of the desired applications for BDD electrodes encompass some form of fluid flow, it would be interesting to examine if BDD remains a low biofouling material under flow conditions. In addition, since a BDD electrode would often experience different electric potentials during operation, it would be noteworthy to study the effect of applied potential to attract or retard bacterial attachment. We anticipate that further reductions in the low biofouling attributes of BDD will be possible by exploiting biasing at an electrochemical potential during rest periods in the electrochemical sensing procedure, to prevent bacterial adhesion via electrostatic repulsion. Furthermore, BDD electrodes are suitable for ozone or hydroxyl generation,[3–5] meaning that a relatively non-toxic, self-cleaning functionality can be added, with the aim of preventing accumulation of biofilm or the utilisation of electrochemical cleaning procedures to remove established biofilm.

Chapter 6 started an initial exploration into the feasibility of a biofilm activity sensor. This would be extremely beneficial to a biofouling monitoring system to provide information on the site and extent of biofilm formation, ideally on-line and in real-time. Laser roughened BDD electrodes showed potential for this purpose, but requires considerable further work in order to get to proof-of-concept stage. Analysis of the sensor response could be improved so as to positively identify biofilm formation, and possibly discriminate biofilm against other forms of fouling. This would have major industrial application in any antifouling countermeasure strategy, as it could be used as feedback to apply biocide (or any other cleaning measure) in an efficient manner.

7.3 References

(1) Ayres, Z. J.; Borrill, A. J.; Newland, J. C.; Newton, M. E.; Macpherson, J. V. Controlled sp2 Functionalization of Boron Doped Diamond as a Route for the Fabrication of Robust and Nernstian pH Electrodes. *Anal. Chem.* **2016**, *88* (1), 974–980.

(2) Read, T. L.; Cobb, S. J.; Macpherson, J. V. An Sp 2 Patterned Boron Doped Diamond Electrode for the Simultaneous Detection of Dissolved Oxygen and pH. *ACS Sensors* **2019**, *4* (3), 756–763.

(3) Arihara, K.; Terashima, C.; Fujishima, A. Electrochemical Production of High-Concentration Ozone-Water Using Freestanding Perforated Diamond Electrodes. *J. Electrochem. Soc.* **2007**, *154* (4), 71–75.

(4) Honda, Y.; Ivandini, T. A.; Watanabe, T.; Murata, K.; Einaga, Y. An Electrolyte-Free System for Ozone Generation Using Heavily Boron-Doped Diamond Electrodes. *Diam. Relat. Mater.* **2013**, *40*, 7–11.

(5) Heim, C.; Ureña de Vivanco, M.; Rajab, M.; Müller, E.; Letzel, T.; Helmreich, B. Rapid Inactivation of Waterborne Bacteria Using Boron-Doped Diamond Electrodes. *Int. J. Environ. Sci. Technol.* **2015**, *12* (10), 3061–3070.

Appendix

A: Instrument circuit diagrams

Circuit diagrams of the instrumentation used in the operation of the conductivity sensor.

RMS to DC converter

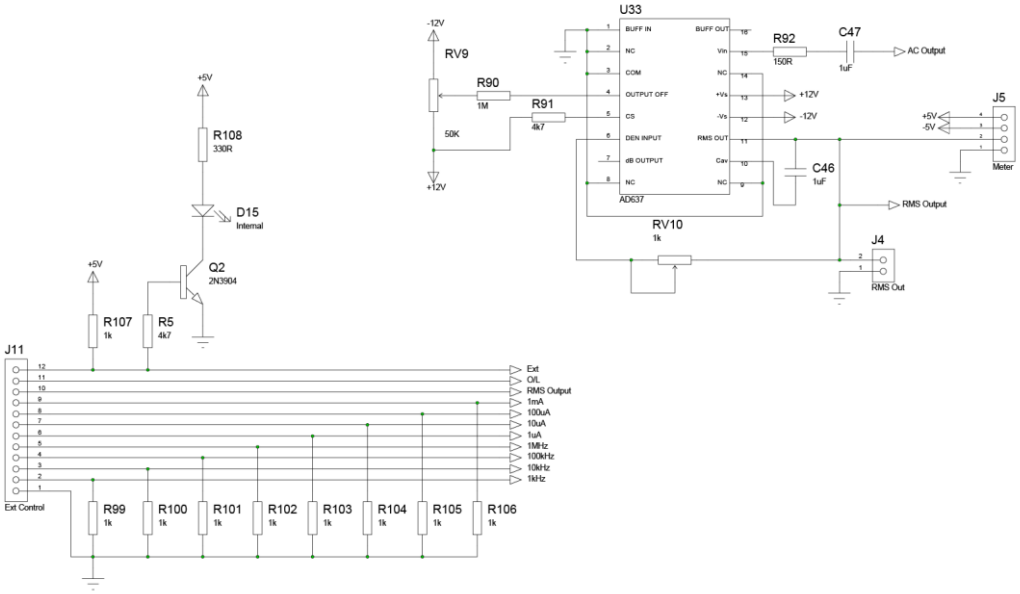

Conductance cell

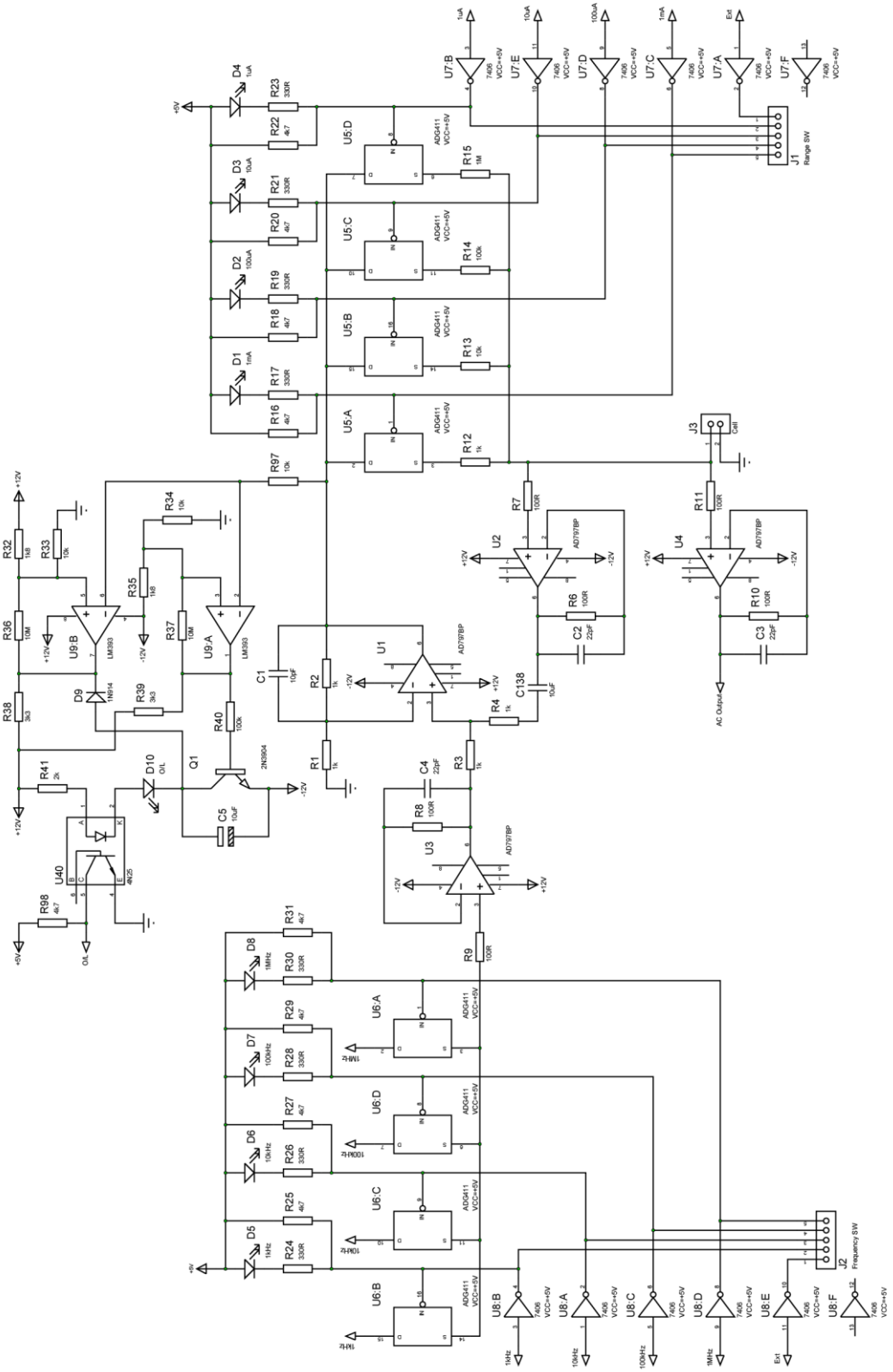

Current pump

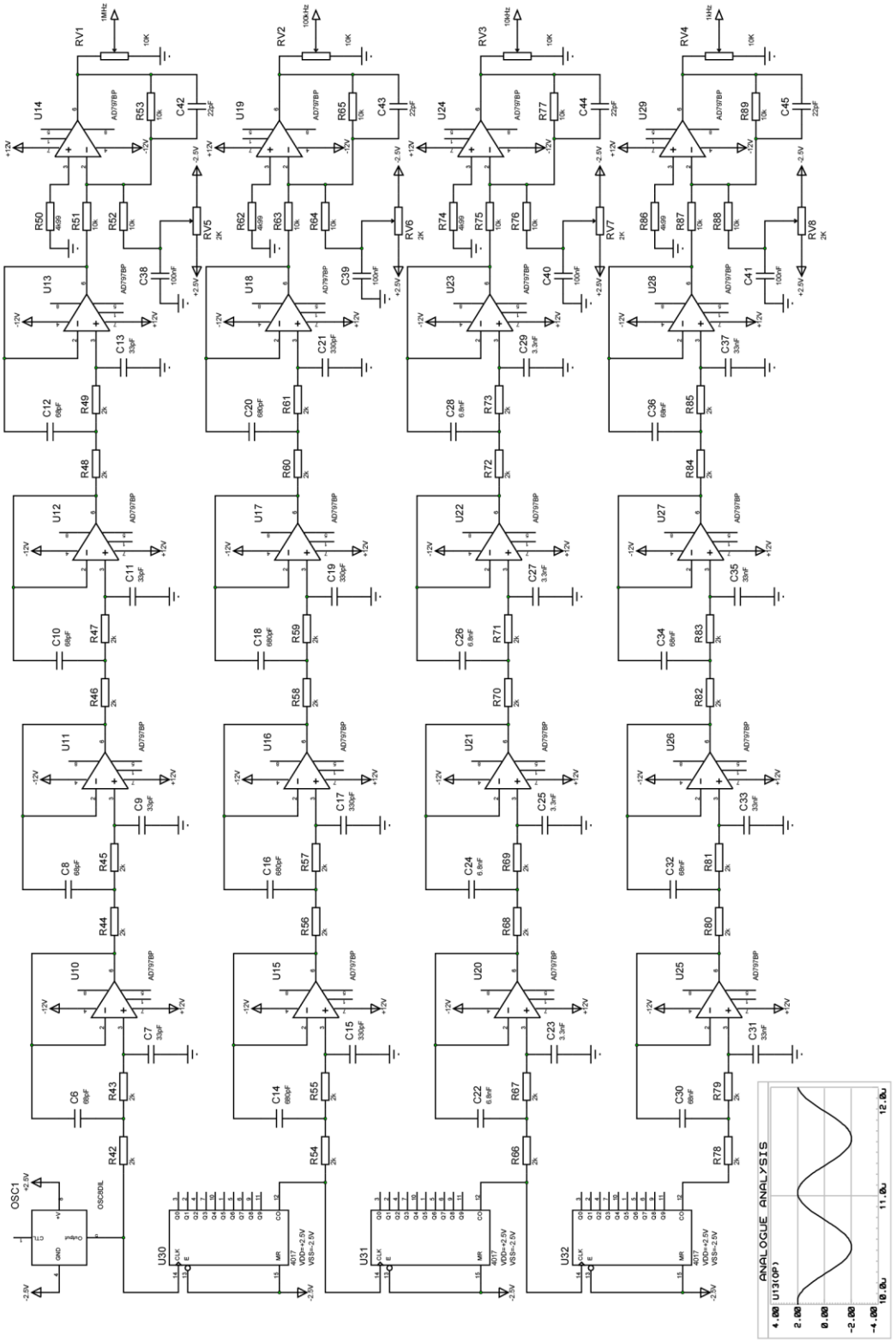

Differential amplifier

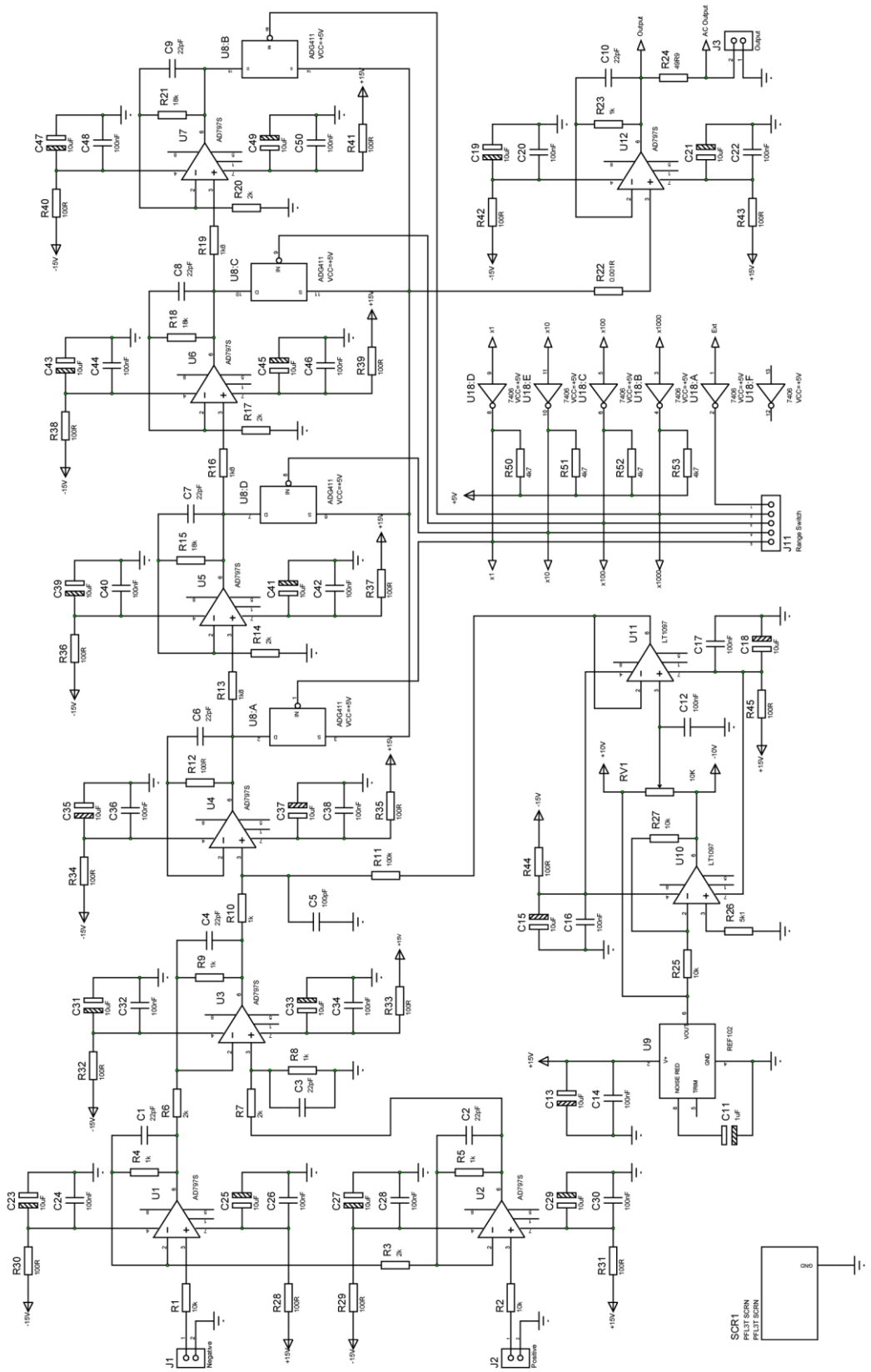

Power supply

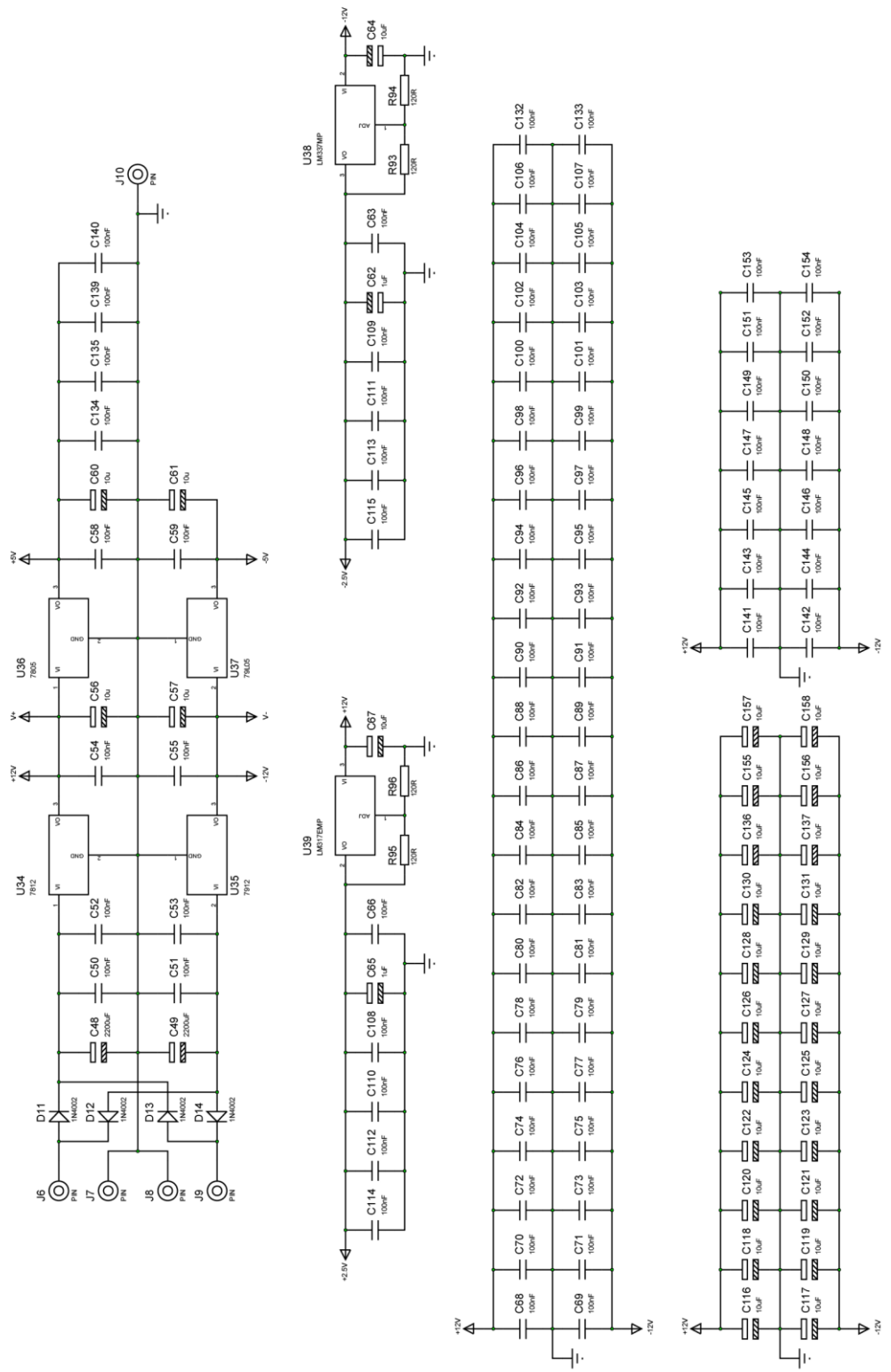

B: MATLAB Script

Full MATLAB script to model the theoretical conductivity sensor behaviour, which produces the plots presented in Chapter 3.

```
clear all
close(figure(1));  % clears everything and resets matlab
%script that simulates the behaviour of the electrode geometries in
different solutions.
%set the applied frequency. then change the concentration (i.e.
conductivity) and watch what happens to the impedance measured by
each sensor

%% Sensors definitions
Sensor1.w = 100e-6;
Sensor1.s = 10000e-6;
Sensor1.L = 5000e-6;
Sensor1.f = 10000;
Sensor1.n = 2;
Sensor1.C = 3;

Sensor2.w = 100e-6;
Sensor2.s = 10000e-6;
Sensor2.L = 5000e-6;
Sensor2.f = 10000;
Sensor2.n = 2;
Sensor2.C = 10;

Sensor3.w = 100e-6;
Sensor3.s = 10000e-6;
Sensor3.L = 10000e-6;
Sensor3.f = 10000;
Sensor3.n = 2;
Sensor3.C = 3;

Sensor4.w = 100e-6;
Sensor4.s = 1000e-6;
Sensor4.L = 10000e-6;
Sensor4.f = 100000;
Sensor4.n = 2;
Sensor4.C = 7;

Sensor5.w = 1000e-6;  % width of band
Sensor5.s = 6000e-6;  % separation between bands
Sensor5.L = 10000e-6;  % length of band
Sensor5.f = 100000;  % frequency of AC
Sensor5.n = 2;  % number of bands
Sensor5.C = 7;  % capacitance of electrode

%% other definitions
NumSens = 2;  % number of sensors to run

%%
```

```
Concentrations = -4:6/1000:5; % from 1uM to 1M
Concentrations = 10.^Concentrations;  % defining a range of
concentrations from 10^-4 to 10^4

SpecCond = 5.011+7.634; % conductivity of Na+ and Cl- ions in mS
SpecCond = SpecCond/1000; % S m^2 mol^-1

Conductivities = Concentrations*SpecCond;  % conductivity equation

RimpStore = zeros(3,length(Concentrations));  % RimpStore is a
matrix of zeros of size 3 x however many concentrations there are
for l = 1:NumSens  % FOR when l is 1 to NumSens
    eval(['w=Sensor' int2str(l) '.w;']);  % eval executes the
    expression as a string
    eval(['s=Sensor' int2str(l) '.s;']);  % int2str converts integer
    to a string
    eval(['L=Sensor' int2str(l) '.L;']);
    eval(['f=Sensor' int2str(l) '.f;']);
    eval(['n=Sensor' int2str(l) '.n;']);
    eval(['C=Sensor' int2str(l) '.C;']);

    if n==2
        k = s/(s+2*w);  % if n=2 then calculate k with this equation
    elseif n>2
        k = cos(pi/2*w/(s+w));  % if n>2 then calculate k with this
      equation
    else
        fprintf('%s\n','You chose a silly number for n... try n >
      1');  % otherwise write this phrase
    end

   RimpVector = zeros(length(Concentrations),1);  % RimpVector is a
    vector of length however many concentrations there are, initally
    filled with zeros
    for m = 1:length(Concentrations)
        conc = Concentrations(m);
        cond = SpecCond*conc;  % conductivity
        Rho = 1/cond;  % resistivity

        % returns the calculated impedance for a given k and
        frequency combination
        % k = measure of geometry, effectively ratio between s and w

        %% physical constants
        e0 = 8.85e-12;
        er = 80.22;

        % Capacitance per unit area
        BDDCapacitance = C; % uF cm^-2
        BDDCapacitance = BDDCapacitance*0.01; % F m^-2

        %% obtain the impedance

        % A = area of 1 electrode
        A = w*L;
        % wTotal = total width of whole device
        wTotal = n*w+(n-1)*s;

        CellConstant = 2/((n-1)*L)*ellipke(k)/ellipke(sqrt(1-k^2));
```

```
        % Cdl = capacitance of the double layer
        Cdl = BDDCapacitance*A*(n/2);
        % Ccell = Capacitance due to the geometry of the cell
        Ccell = (e0*er)/CellConstant;
        % Rsol = resistance of the solution under this geometry
         (Hong 2005,eqn8)
        Rsol = CellConstant*Rho;

        a = Cdl*Rsol;
        b = 2*Ccell+Cdl;
        c = Cdl*Ccell*Rsol;

        Sigma = 2*pi*f;
        Rimp = sqrt(Sigma^4*(a*b-
2*c)^2+(2*Sigma*b+Sigma^3*a*c)^2)/(Sigma^2*b^2+Sigma^4*c^2);

        RimpVector(m) = Rimp;
    end
    RimpStore(l,:) = RimpVector;
end

%% plotting

colours = 'brkgm';  % defines the colours of lines
hold on  % retains plots so that new plots are added to existing
plots
figure(1)  % creates figure window
for m = 1:NumSens
    colour = colours(m);
    plot(Conductivities,RimpStore(m,:),colour);  % plots
     conductivity vs impedance

    set(gca,'YScale','log');
    set(gca,'XScale','log');
end
xlabel('Solution conductivity (S / m)','FontSize',14);  % formatting
the axes
ylabel('Measured impedence (Ohms)','FontSize',14)
set(gcf,'Color','w');
set(gca,'FontSize',12);
set(gcf,'Position',[200 200 900 600]);
legend('S1','S2','S3','S4','S5');
hold off

RimpColumns=transpose(RimpStore);
```

C: LabVIEW VIs

Screenshots of the LabVIEW VIs described in Chapter 3, showing all cases of case structures where applicable.

Version 2

(a)

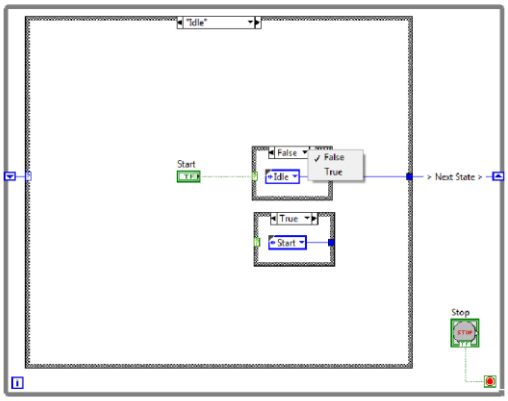

(b)

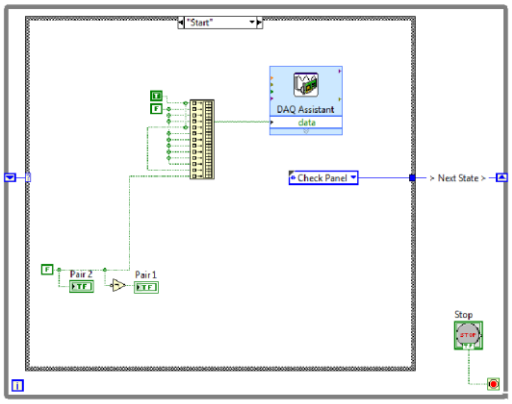

(c)

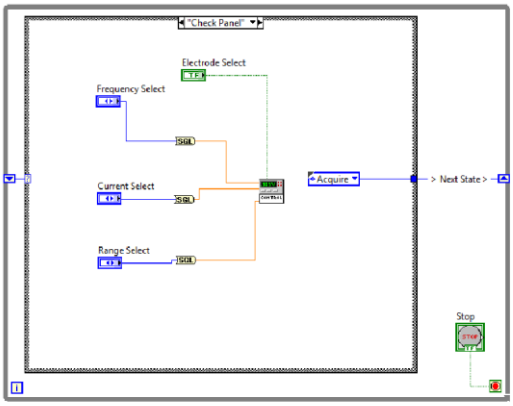

(d)

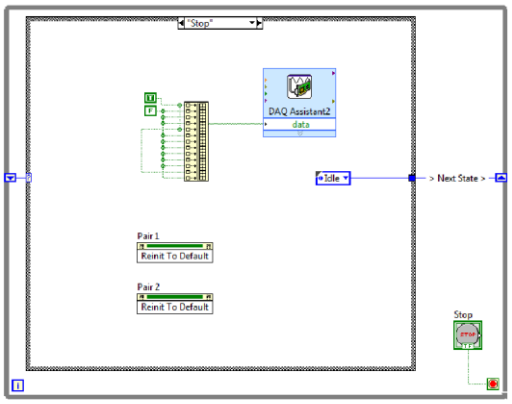

(e) Cases in 'Acquire' state

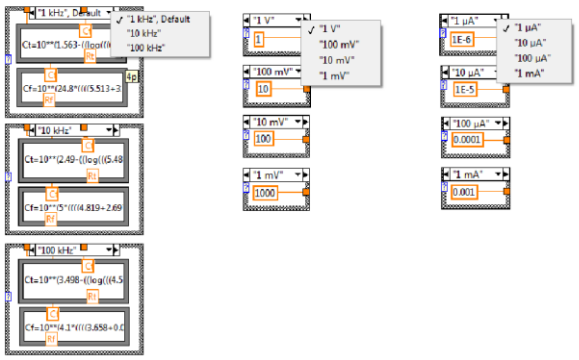

Block diagram of the Sub-VI in (c)

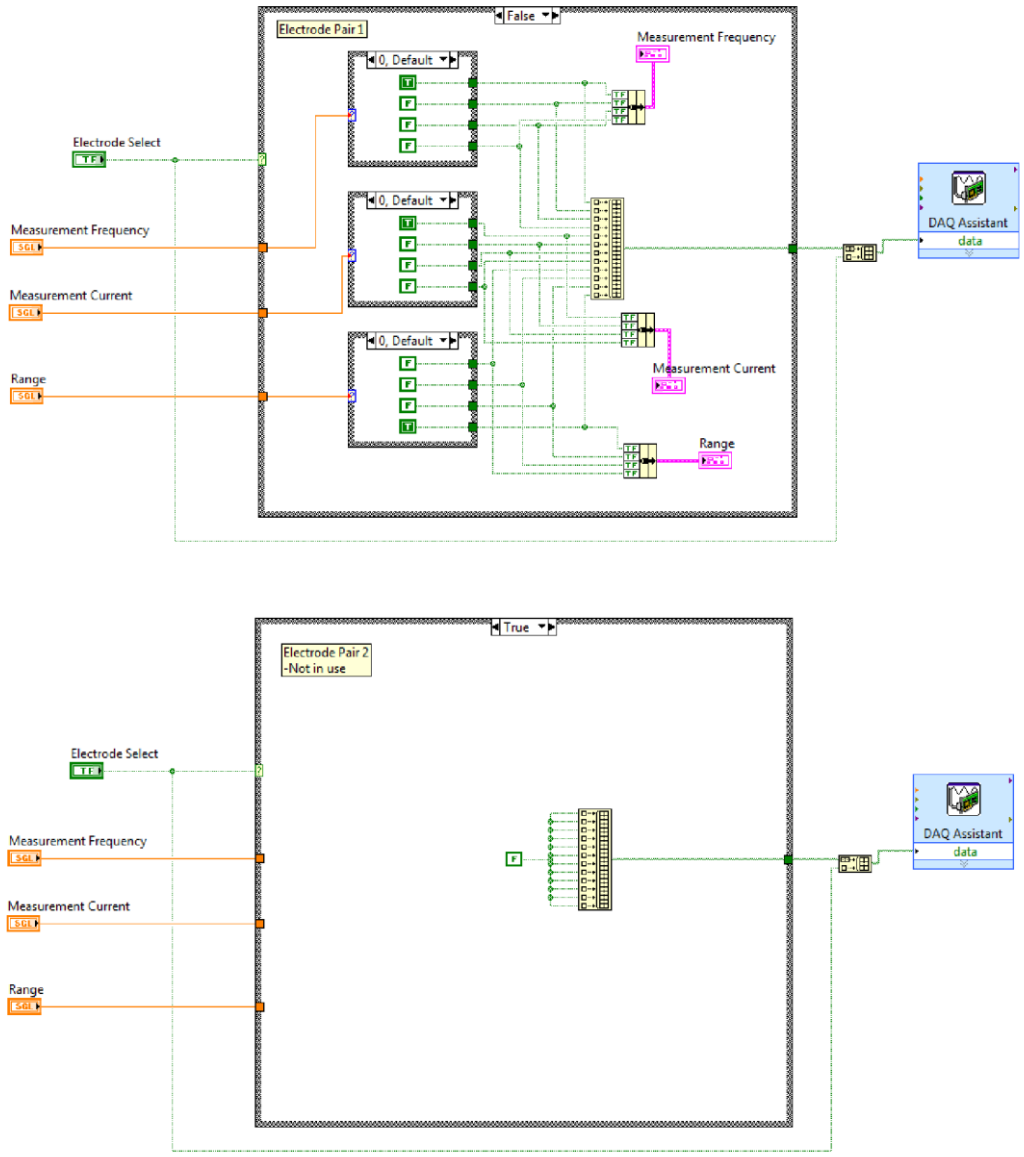

Version 3

(a)

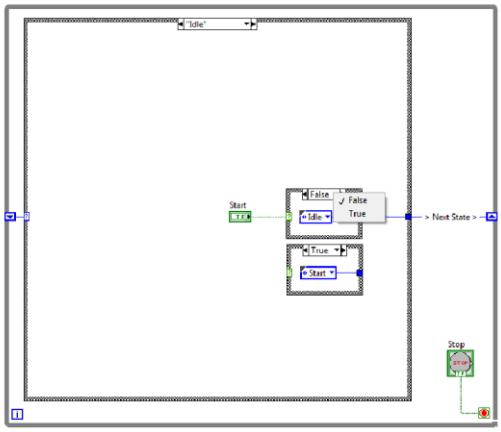

(b)

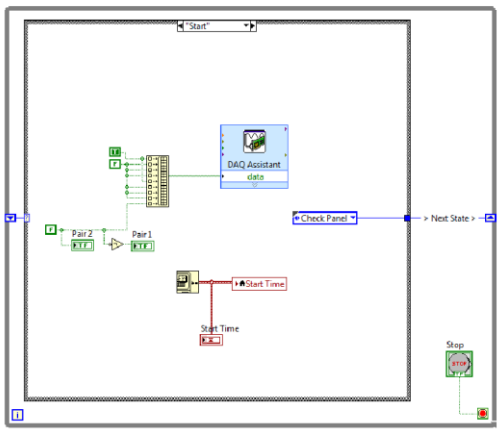

(c)

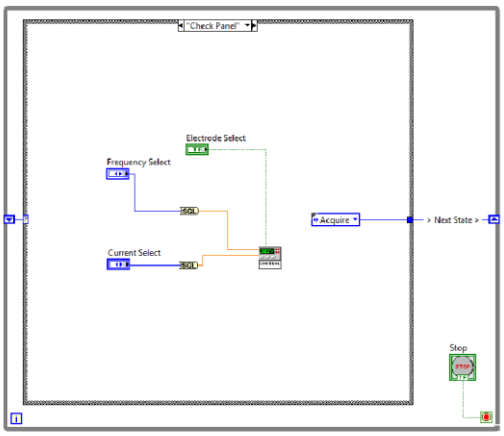

(d)

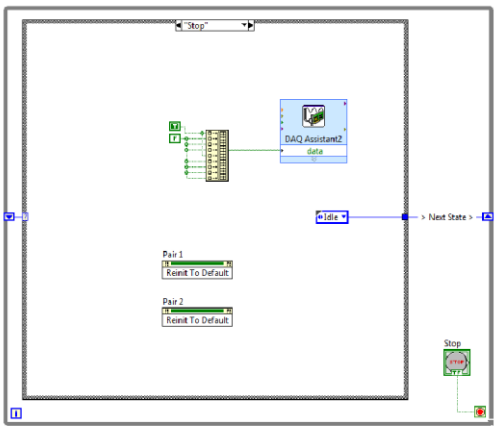

(e) Cases in 'Acquire' state

“...to the last I grapple with thee;

from hell's heart I stab at thee;

for hate's sake I spit my last breath at thee.”

— Herman Melville, *Moby-Dick, or, the Whale*